Electron Attachment To Small Molecular Clusters

Thesis

Electron Attachment to Small Molecular Clusters

Agnieszka Sieradzka

Supervisor:
Jimena D. Gorfinkiel

A Thesis presented for the degree of Doctor of Philosophy
in the discipline of Physics

The Open University
Department of Physical Sciences

Milton Keynes
March, 2017

Electron attachment to small molecular clusters

Agnieszka Sieradzka

Submitted for the degree of Doctor of Philosophy
January, 2017

Abstract

A large number of secondary electrons with low energies (< 20 eV) is produced during irradiation of biological matter. It is known that such electrons lead to fragmentation of DNA via dissociative electron attachment (DEA). DEA happens via the formation of a resonance (transient negative ion). Studying the properties of the resonances (energy and lifetime) is the first step to describe and understand DEA. Although isolated DNA constituents have been studied broadly, DEA is likely to be affected by the environment. The goal of this research is a theoretical investigation of the influence of the environment on resonance formation. The object of this study is low-energy collision with pyridine (prototype of biological molecule) and thymine (one of the DNA nucleobases), both in gas-phase and surrounded by water (forming small clusters). We provide a comparison of pyridine and pyridine-H_2O calculations for various standard scattering models (Static Exchange, Static Exchange plus Polarization and Close-Coupling). For pyridine-$(H_2O)_n$, n = 2, 3, 5, calculations have been performed using the Static Exchange method, whereas thymine and thymine-$(H_2O)_n$, n = 2, 3, 5, were studied using the Static Exchange and Static Exchange plus Polarization methods. This research gives an insight into how the water environment changes resonance properties. The presence of water does not have the same effects in all systems studied. We confirmed that the effects depend on the character of water as a proton donor or acceptor. We showed that the resonance shift depends on the water binding site to the molecule and that it does not shift all resonances in one system equally strongly. Additionally, isolated pyridine has been investigated in more detail, in order to compare it with diazines, studied previously in our group. We found that the resonance formation in both system is similar.

ACKNOWLEDGEMENTS

First of all I would like to thank Dr. Jimena D. Gorfinkiel for widespread and excellent help and guidance through all these years of my PhD studies. There is a lot to be grateful and thank you for. Thank you for your astonishing understanding, incredible patience, kindness and for passing on so much wisdom, knowledge and experience. I have learned very much from you.

The person who also taught me a lot during me PhD time is Zdenek Mašín. Thank you for sharing with me your experience and knowledge and for your guidance at the beginning of my PhD study.

I also want thank Prof. J. Kohanoff and Prof. I. I. Fabrikant for providing the thymine and thymine clusters geometries and S. Caprasecca for providing the thymine modified orbitals (described using the polarized continuum model). Without all of them chapter 5 of my thesis could not exist in the form as it is now. I am also very grateful for providing pyridine data and formic acid geometries by the Schwinger multichannel group in Brazil lead by Prof. H. F. Bettega.

I would like to thank my friends for the great and not great time spent in MK, especially Dan (thanks a lot for your incredible support, for our talks and for being so extremely nice to me, even if I was so mean to you; all that means a lot to me!), Joe (for many developing talks), George (who after one year of sharing an office and great time there left me alone to look for a better life on the south cost) and Alex (for sharing frustration of not working OU computers and many other much nicer moments). And many thanks to Olimpia, for the support just from the beginning of my PhD and much before, for always being there when I needed you. And many thanks to all my friends and family. Dziękuję!

Finally, I would like to thank my Marvuś. There is so much to thank you for and not enough words and time to express how much I am grateful for you being always so incredible helpful, supporting, understanding, comforting, patient and wonderful. Thank you for always being perfect for me. Danke schön!

CONTENTS

Abstract ii

Acknowledgements v

List of acronyms xi

1 Introduction 1

1.1 Systems studied . . . 3

1.2 Low-energy electron processes . . . 7

1.2.1 Resonances . . . 8

1.3 Prior research . . . 11

1.4 Layout of the thesis . . . 13

2 Theory 15

2.1 Introduction to Electronic Structure Theory . . . 15

2.2 Introduction to scattering theory . . . 18

2.3 S-matrix theory . . . 20

2.3.1 Single channel case . . . 20

2.3.2 Scattering amplitude . . . 23

2.3.3 Analytic properties of the S-matrix: bound states and resonances . . . 24

2.3.4 Cross section . . . 28

2.3.5 Phase shift . . . 29

2.3.6 Multichannel case . . . 30

2.3.7 Time-delay . . . 31

2.4 R-matrix theory . . . 32

2.4.1 Potential scattering . . . 33

2.4.2 Electron-molecule scattering . . . 36

2.5 Scattering models . . . 39
2.6 UKRmol+ suite and complementary tools . . . 41

3 Electron collisions with pyridine **47**
3.1 Pyridine characteristics . . . 48
3.2 Calculation details . . . 49
3.2.1 Target . . . 49
3.2.2 Scattering . . . 54
3.3 Cross sections . . . 54
3.3.1 SE model . . . 54
3.3.2 SEP model . . . 56
3.3.3 CC model . . . 61
3.4 Resonances . . . 65
3.4.1 Shape resonances . . . 66
3.4.2 Core-excited resonances . . . 69
3.4.2.1 Time-delay analysis . . . 69
3.4.2.2 Cross sections . . . 71
3.5 Summary . . . 74

4 Electron collisions with pyridine-water **75**
4.1 Calculation details . . . 77
4.1.1 Targets . . . 77
4.1.2 Scattering . . . 78
4.1.3 Polarizability . . . 79
4.2 Differential cross section . . . 81
4.3 Resonances in Pyr-H_2O . . . 85
4.3.1 SE model . . . 86
4.3.1.1 Indirect effects . . . 87
4.3.1.2 Direct effects . . . 88
4.3.1.3 Total effects . . . 90
4.3.2 SEP model . . . 91
4.3.3 CC model . . . 94
4.4 Resonances in Pyr-$(H_2O)_n$ . . . 98
4.5 Summary . . . 102

5 Electron collisions with thymine-$(H_2O)_5$ **103**

5.1 Thymine characteristics . . . 105

5.2 Calculation details . . . 106

5.2.1 Target geometries . . . 106

5.2.2 Target details . . . 110

5.2.3 Scattering . . . 111

5.3 Resonances . . . 113

5.3.1 Thymine . . . 113

5.3.2 Thymine-H_2O . . . 115

5.3.3 Thymine-$(H_2O)_n$, n = 1, 2, 3 . . . 119

5.4 Thymine-$(H_2O)_5$ . . . 123

5.4.1 Indirect effects . . . 124

5.4.2 Direct effects . . . 127

5.4.3 Total effects . . . 130

5.4.4 Comparison with prior research . . . 133

5.4.5 Thymine with polarized orbitals . . . 135

5.5 Summary . . . 137

6 Conclusions and outlook **139**

A Software **145**

A.1 UKRmol suite . . . 145

A.2 Running the UKRmol and UKRmol+ suite . . . 146

B Benzene, pyridine, pyrimidine **149**

B.1 Benzene, pyridine and pyrimidine HF orbitals . . . 149

B.2 Comparison of cross sections . . . 155

C Pyridine-water **159**

C.1 Pyr-H_2O, Pyr and water HF orbitals . . . 159

C.2 Polarizability . . . 168

D Thymine-water **171**

D.1 Thy and Thy-$(H_2O)_5$ HF orbitals . . . 171

Bibliography **183**

LIST OF ACRONYMS

Acronym	Meaning
DNA	Deoxyribonucleic acid
SEs	Secondary electrons
LEEs	Low-energy electrons
SSBs	Single strand breaks
DSBs	Double strand breaks
TNIs	Transient negative ions
DEA	Dissociative electron attachment
AD	Autodetachment
ETS	Electron transmission spectroscopy
HF	Hartree-Fock
SCF	Self-Consistent Field
CSFs	Configuration State Functions
GTOs	Gaussian-type orbitals
FCI	Full Configuration Interaction
MCSCF	Multi Configuration Self Consistent Field
CAS	Complete Active Space
CASSCF	Complete Active Space Self Consistent Field
SA-CASSCF	State-Averaged CASSCF
SE	Static Exchange
SEP	Static Exchange plus Polarization
CC	Close-Coupling
LUMO	Lowest unoccupied molecular orbital
HOMO	Highest occupied molecular orbital
IECS	Integral elastic cross section
EDCS	Elastic differential cross section
DCS	Differential cross section
IECS	Integral elastic cross sections
TICS	Total inelastic cross sections
ESCS	Excited state cross section
ESECS	Elastic cross section for excited state
ESTCS	Excited state total cross section
v.o.	Virtual orbitals
FA	Formic acid
VEA	Vertical electron attachment

Table 1: Glossary of important acronyms.

1

INTRODUCTION

One of the main motivations for studying electron scattering from polyatomic molecules is the effects of radiation damage on DNA (deoxyribonucleic acid) and other cell constituents. Knowledge of DNA behaviour under radiation is essential to detailed understanding of radiation damage in living organisms. It is a well-known fact that the exposure of living beings to high energy radiation may result in very serious problems. These effects could (and still can) be directly observed after the dropping of the nuclear bombs in Hiroshima and Nagasaki in 1945 or after the Chernobyl disaster at the nuclear power plants in 1986. Those disasters (and many other similar ones) caused the local dosage of radiation received by living beings to be sufficiently high to bring about fatal effect, i.e. death, grave physical injuries and genetic mutations passed to descendants.

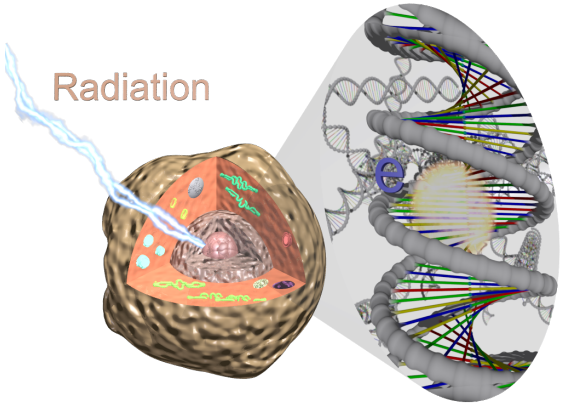

Figure 1.1: Simplified illustration of the structure of a cell. Generated using POV-Ray, a fragment of the picture was created based on source [1].

Beyond the extreme occurrences, every living body is constantly exposed to some dosage of radiation due to the presence of ubiquitous cosmic radiation and the existence of radioactive isotopes on the earth (e.g. radon, uranium). In additional, during specific medical treatment and imaging, radiation is used in positive ways. Particularly, nowadays, radiotherapy is a very powerful medical tool to deal with diseases. Therefore, in order to use radiation effectively, it is necessary to have detailed knowledge of the processes taking place in the human body during exposure to radiation. Especially in the cell nucleus

where DNA is placed, because DNA is the element of a cell which is most sensitive for radiation (figure 1.1). Damage of the DNA can lead to fatal and long-term effects. Understanding biological radiation damage can help to design better treatments, safer imagining and to improve radiation protection.

Radiation may interact with biological matter by direct and indirect action. *Direct action* is any form of radiation in biological material interacting directly with the targets (e.g. DNA) in the cells. The target atoms may be ionized or excited, initiating the chain of events leading to biological changes. It is the main process when radiation consists of neutrons or α-particle. *Indirect action* happens when radiation interacts with other atoms or molecules (not being the target atoms or molecules, i.e. mainly water) mostly leading to the production of free radicals that are able to diffuse far enough to reach and damage the target. This indirect process is responsible for 67% of the biological damage.

The chain of events is a sequence of events which is induced by the interaction of fast primary particles with cellular constituents. The events can be divided into three major groups: *primary*, *secondary* and *radioactive* [2, 3]. This sequence of events is still unknown but crucial to accomplish a complete description of the effects of ionizing radiation in living cells.

All electrons originating from ionization by primary fast charged particles are called secondary electrons (SEs) [4, 5]; including those coming from multiple ionizations or Auger events. The energy of SEs ranges from $\sim$ 0 eV to $\sim$ 1 keV. Most SEs have low energies with a distribution that lies essentially below 70 eV, with the most probable energy $\sim 9 - 10$ eV [6]. SEs create the majority of the reactive species, i.e. ions, excited molecules, free radicals and low-energy electrons (LEEs), which initiate further chemical reactions.

Low-energy electrons are SEs with energy $E < 30$ eV [4, 5], that can mainly be generated by water ionization. LEEs, through exchange of energy with the medium, finally become trapped by electrostatic interactions with induced and permanent dipole moments of the surrounding molecules and become thermalized. Thermal ($E \sim 0.025$ eV) and epithermal ($E < 5$ eV) electrons disappear mostly by recombination with ions, attachment to molecules or diffusion.

It has been known for a long time that ionizing radiation can induce mutagenic or lethal effects, initiated by structural and chemical modifications of the nucleic acid bases [7] or the deoxyribose sugar moiety [8]. But only since the pioneering study by Boudaïffa *et al.* [9] in 2000, it has been confirmed that the low-energy (E < 20 eV), secondary electrons can also contribute to DNA damage. The secondary electrons together with the neutral radicals and ions are produced along the radiation track in a cell and afterwards interact with the constituents of DNA [10] (this is further explained below). These were unexpected findings, because until then it was believed that only electrons at energies above the ionization threshold could cause DNA breaking.

Figure 1.2 shows results by Boudaïffa *et al.* [9]. As expected, single strand breaks (SSBs) and double strand breaks (DSBs) appear at energies above the ionization threshold, i.e. above 10 eV. And their intensity continuously rises with electron energy in the investigated energy range, i.e. close to the ionization threshold. But below the ionization threshold, surprisingly, the presence of SSBs and DSBs does not disappear and a broad peak is centered at about 10 eV. Further work by this group after extending their experiment to the electron energy range below 3 eV gave results manifesting additional resonances, but only for SSB formation [11]. The observed low-energy peaks are due to the fact that electrons can be captured by the molecule, as a result of that transient negative ions (TNIs) are created which can lead to decomposition into several fragments - dissociative electron attachment (DEA). This phenomenon is discussed below, in section 1.2. In this thesis we study resonances in various systems.

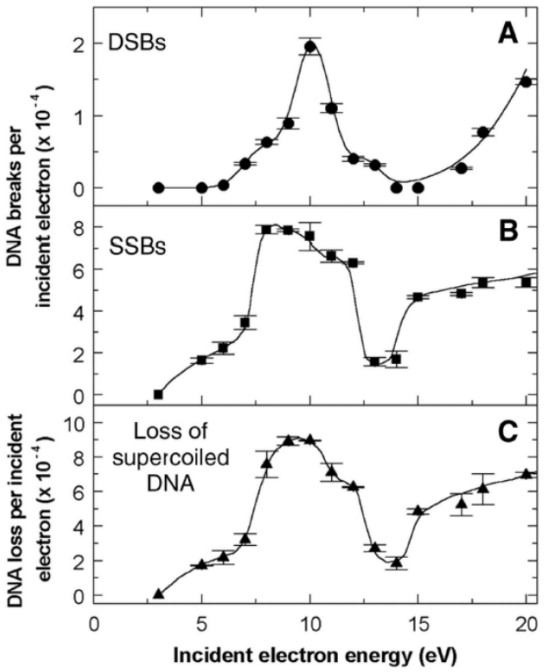

Figure 1.2: Experimental results of electron induced single and double strand breaks of DNA, from Boudaïffa *et al.* [9].

1.1 SYSTEMS STUDIED

Before we present the systems studied in this work, in order to motivate our choice, we first describe the structure of DNA and present some definitions important for this work.

DNA is a large molecule, a polymer, consisting of monomers called deoxynucleotides, with a double helix structure. The 'backbone' of each of the two strands consists of five-carbon sugar deoxyribose, shown in the left panel of figure 1.3 (in black) and phosphate groups (in red). Four nitrogenous bases (in blue) are attached to this backbone: adenine (A), guanine (G), cytosine (C), and thymine (T) (in RNA uracil replaces thymine), the sequence of which specifies the genetic code. A nucleobase linked to a sugar is called a nucleoside. The nucleoside together with a phosphate group (in other words, a backbone together with one of the nitrogenous bases) builds a nucleotide. Groups of nucleotides liked together in specific order create one strand of DNA. Deoxynucleotides usually exist as a double-stranded structure with the sugar-phosphate backbones of the two different strands

running in opposite directions [12] (the right panel of figure 1.3). The two DNA strands are held together by hydrogen bonds between two of the four the bases (adenine – thymine and guanine – cytosine).

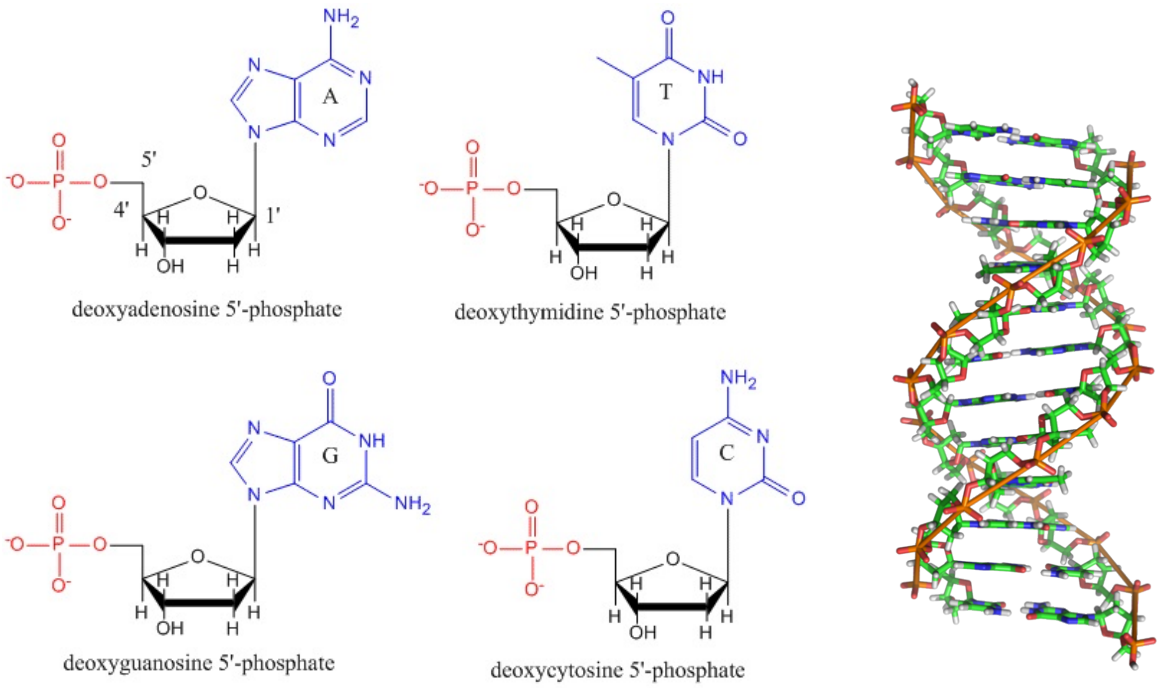

Figure 1.3: Structure of DNA. The pictures on the left and right are from [13, 14], respectively.

In living cells DNA always exists surrounded by water. Therefore, the main goal of this thesis is an investigation of how presence of water changes resonance formation in biological molecules. The theoretical investigation of a DNA strand surrounded by water is not currently feasible (the system is too huge to perform R-matrix calculations). Thus, we focus on much smaller targets: small clusters.

A *cluster* is an aggregate of a countable number of molecules (between 2 to 10^7). Its size is between a single molecule and a bulk solid [15]. Clusters are a type of material with different properties from those of a molecule and a bulk solid. Their chemical and physical properties, as well as their geometric and electronic structures are of fundamental interest since their structure is more complex than a single molecule but less complex than bulk solid. There are several intermolecular forces which can be responsible for binding molecules into clusters. However, in all clusters discussed in this work, molecules are bound by hydrogen bonding. A hydrogen bond can occur between atoms of different molecules or between atoms of the same molecule. The general form of hydrogen bonds can be written as: $X{-}H\cdots Y$, where X is an electronegative atom (the donor), covalently bound to a hydrogen atom. The hydrogen atom also interacts (more weakly than with X) with the second

atom, Y (the acceptor). Y is also an electronegative atom, it has a lone-pair of electrons, which causes atom Y to possess a slight negative charge. The donor atom effectively shares its hydrogen with the acceptor atom, forming a bond stronger than a van der Waals bond, weaker than a covalent one.

We have been investigating small clusters containing one of the DNA nucleobases, i.e. thymine-$(H_2O)_n$, n = 1, 2, 3, 5, to bridge the existing gap between the gas and solvation phase (we also performed calculations for isolated thymine, but only for comparison purposes, since this target has already been studied [16] using the same method as in this work). However, we started our investigations with less complex molecule: pyridine. To understand this choice, we first present a classification of DNA bases and discuss the past, present and future work undertaken at the OU.

Thymine, cytosine and the RNA nucleobase uracil are pyrimidinic nucleobases, derived from pyrimidine [17, 18, 19], whereas guanine and adenine are derived from purine [20], see figure 1.4. Pyrimidine belongs to a group of molecules called azabenzenes. *Azabenzene* molecules are benzene-

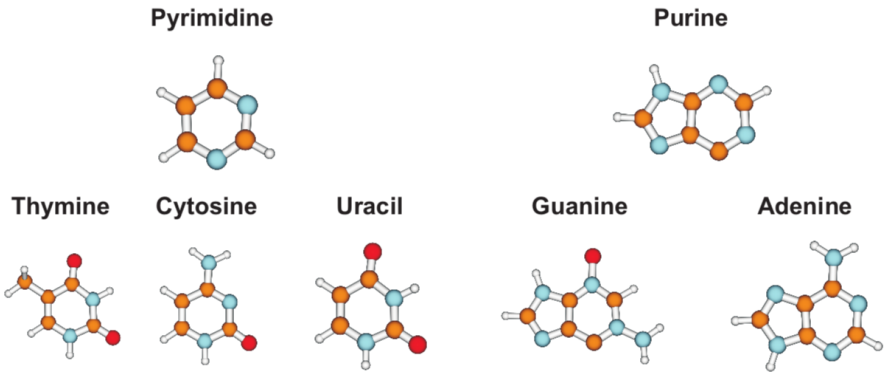

Figure 1.4: Classification of DNA bases depending on type of the molecule from which they are derived. Guanine and adenine have purine character and thymine, cytosine and uracil have pyrimidine character. In the figure the orange balls represent carbon, blue - nitrogen, white - hydrogen and red - oxygen (from reference [21]).

like molecules with one to six carbons replaced by nitrogen [22]. Due to the high symmetry of 6-membered rings of benzene there is only one possible combination of replacing a carbon atom with nitrogen to create a unique molecule, this molecule is called *pyridine*. Two nitrogen atoms in a benzene-like ring can form three unique molecules, which are called *diazines*, namely they are *pyridazine* (1,2-diazine), *pyrimidine* (1,3-diazine), *pyrazine* (1,4-diazine). Three nitrogen atoms in benzene-like ring can also form three unique molecules, called *triazine* (1,2,3-triazine, 1,2,4-triazine, and 1,3,5-triazine), and four nitrogen atoms form *tetrazine* (1,2,3,4-tetrazines, 1,2,3,5-tetrazines, and 1,2,4,5-tetrazines). *Pentazine* – 6-membered rings with five nitrogen atoms can form only one unique molecule. Both tetrazine and pentazine are unstable compounds, while *hexazine* (also known as hexaazabenzene) is a hypothetical allotrope of nitrogen composed of 6 nitrogen atoms arranged in a benzene-like ring.

A study of diazines, 2,4-oxo pyrimidine and uracil (see figure 1.5) by Z. Mašín preceded this work, see e.g.: [17, 23, 18, 24, 21]. The knowledge and experience gained by studying these molecules in our group was used as the starting point for some of the calculations presented in this thesis. In particular, the knowledge about the specific parameters most appropriate to perform R-matrix calculations for isolated molecules was very useful. It also allows us to compare in more detail results for pyridine with those for pyrimidine (see chapter 3).

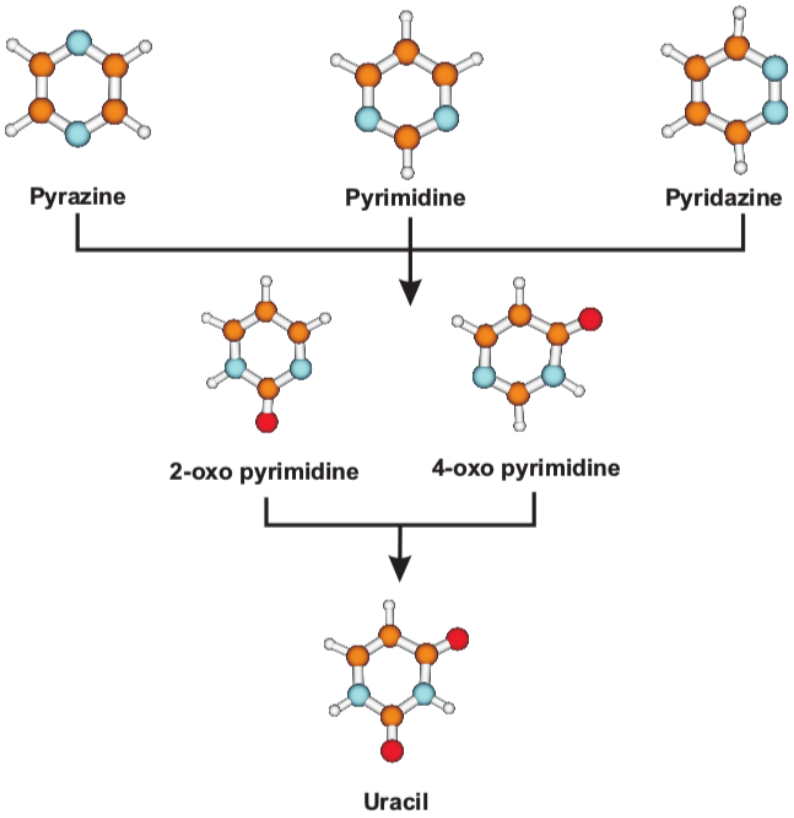

Figure 1.5: Structures of diazines: pyrazine, pyrimidine and pyridazine; 2-oxo pyrimidine, 4-oxo pyrimidine and uracil. The white balls represent hydrogens, orange - carbons, blue - nitrogens and red - oxygens. The picture comes from [21].

Although the knowledge and experience in studying diazines was an important factor to investigate pyridine, the main reason to chose this molecule for our studies was the possibility to compare our theoretical results with an experiment. The experiment was planned by the collaborating experimental group led by Sam Eden. The group is building an experiment to perform measurements of electron scattering by molecular clusters which is able to determine different fragmentation channels at The Open University. Experimental control over clustering conditions can be achieved by expanding the target gas through a small nozzle with variable backing pressure followed by a skimmer. This creates as stable supersonic gas jet with varying distributions of cluster sizes, depending on backing pressure and nozzle diameter. The experimental set-up additionally contains a Stark deflector [25] which allows the separation of clusters with different dipole moment/mass ratio (i.e. clusters with

different components/size). Afterwards, different clusters can be selected by an additional skimmer [26]. Next, the chosen clusters are dissociated by a low-energy electron beam. Then, a mass spectrometer is used to identify and quantify the anions produced. The conditions should be chosen to give a small cluster (one pyridine with a few water molecules), since it is easier to separate small clusters than large ones. This experiment will allow them to obtain yields for fragmentation channels. Pyridine was chosen by them because it possesses a quite big dipole moment and the fairly different dipole moment/mass ratio for each cluster will allow them to separate more easily clusters of different sizes. Due to many technical problems they do not have any measurements yet. We hope that it will be done in the future and the pyridine calculations will be compared with experimental results.

In this work both isolated pyridine as well pyridine clusters: pyridine-$(H_2O)_n$, n = 1, 2, 3, 5, have been investigated in detail. Additionally, we performed some calculations for formic acid clusters; calculations for the same clusters had been already performed using different method [27], therefore the calculations for only one of them are presented in this thesis, and only for comparison purposes.

1.2 LOW-ENERGY ELECTRON PROCESSES

The low-energy regime is defined as the region below the ionization threshold of the target. The electron-molecules interaction leads to several possible outcomes:

Elastic scattering	$AB + e^- \rightarrow AB + e^-$
Rotational excitation	$AB(j) + e^- \rightarrow AB(j') + e^-$
Vibrational excitation	$AB(\nu) + e^- \rightarrow AB(\nu') + e^-$
Electronic excitation	$AB + e^- \rightarrow AB^* + e^-$
Dissociative attachment	$AB + e^- \rightarrow (AB)^{*-} \rightarrow A^- + B$ $AB + e^- \rightarrow (AB)^{*-} \rightarrow A + B^-$
Impact dissociation	$AB + e^- \rightarrow (AB)^{*-} \rightarrow A + B + e^-$
Dissociative recombination	$AB^+ + e^- \rightarrow A + B.$

Elastic scattering is the simplest process and it does not change the energy of the scattering electron or the internal state of the target (no energy is exchanged). Inelastic processes cause changes in

the internal rotational, vibrational and/or electronic state of the target molecule. Dissociative electron attachment (DEA) is a multi-step process in which the electron is captured in a resonant state, $(AB)^{*-}$, or temporary negative ion (TNI) that may subsequently cleaves one or more of the molecular bonds. As a results of dissociation, at least one neutral and exactly one stable anionic fragment are produced (a simple model presenting this phenomenon is illustrated in figure 1.6). In the case

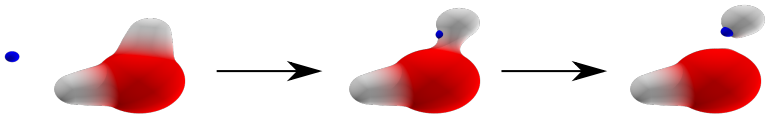

Figure 1.6: Illustration of the dissociative electron attachment phenomenon occurring in water molecule. An electron is represented by blue ball. Generated using POV-Ray.

when the electron is not attached to any of the dissociative fragments the process is called impact dissociation (illustrated in figure 1.7). The outcome of this process is: at least two neutral fragments and the electron. In case of dissociative recombination, the outcome is fragmentation in, at least, two neutral parts.

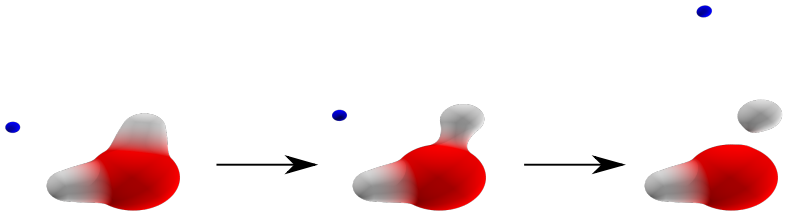

Figure 1.7: Illustration of the impact dissociative phenomenon occurring in water molecule. An electron is represented by blue ball. Generated using POV-Ray.

Dissociative electron attachment is one of the main processes responsible for the break-up of DNA. The process is well known from gas phase experiments [28] and with increased effort was observed in condensed phase systems [29]. Since DEA happens due to resonance, studying the properties of the resonances (energy and lifetime) is the first step to describe and understand DEA. Therefore, the main focus of this work is characterising of resonances. More details about resonances and DEA are given in the following sections.

1.2.1 RESONANCES

A *resonance* is the temporary trapping of a projectile (incoming electron) in a metastable state, leading to the formation of a transient negative ions (TNIs). The processes can be observed in atomic, nuclear and molecular physics. Resonances appear (in their simplest form) as sharp peaks in the integral cross section or time-delay as a function of energy [30]. An example can be seen in figure 3.12, in chapter 3. A resonance occurs only for a particular projectile energy (< 15 eV in most systems). Thus

the phenomenon is characterized by its energy E_r and width Γ. The last value is connected with the lifetime τ of the resonance by a simple relation: $\Gamma \approx \frac{\hbar}{\tau}$. For more details, see chapter 2, section 2.3.3. The re-emission of the electron is called autodetachment (AD).

Several types of resonances can be distinguished:

SHAPE RESONANCE

A shape resonance is characterized by the capture of the incoming electron in a potential barrier. The potential is a mixture of the short-range attractive forces of the target which is in the ground state and long-range repulsive forces caused by the angular-momentum barrier of the incoming electron. S-wave scattering, $\ell = 0$, does not lead to shape resonance, because no centrifugal barrier is present. The name of this resonance comes from the fact that the shape of the potential traps the incoming electron.

The projectile electron, with certain probability, can tunnel through the potential barrier and then it is trapped for some time (about 10^{-15}-10^{-10} s [31]) before it can tunnel back out. Autodetachment is the most probably channel leading to decay of TNIs.

The electron is attached to a molecule in its ground electronic state, usually at low incident electron energies: in the range from 0 eV, usually up to energy of the first excited threshold of the target (above this energy resonances have usually core-excited or mixed shape–core-excited character). The negative ion potential energy curve/surface lies usually above that of the neutral molecule. However when this resonance has energy close to ground state energy, the potential energy curve may be below the ground state energy for some geometries and the resonant state becomes a bound state.

CORE-EXCITED RESONANCES

A core-excited resonance is formed when the incoming electron excites the target molecule to an electronically excited state (parent state) and simultaneously it is temporarily trapped in one of the unoccupied spin-orbitals. It is built most often on a single excitation. These resonances usually happen for higher incident electron energies than shape resonance (since they need enough energy to excite the target). We can distinguish two type of core-excited resonances:

- *Feshbach* resonance (type I core-excited) – lying energetically below the parent state (usually 0 to ~ 0.5 eV below [32]). This resonance happens if the interaction potential between the excited molecule and the impinging electron is strong enough to support a bound state. It has much longer lifetimes than either shape resonance or the core-excited shape resonance described below. This is because the autodetachment channel is closed by parent state, the decay to the parent state is energetically forbidden. This resonance may decay into some nonparent states from which AD or DEA is possible, however that implies a change in configuration, leading to a long lifetime. The electron can also be released by absorbing again some energy from the

system.

- *Core-excited shape* resonance (type II core-excited) – lying above the trapping parent state into which they can decay. Its autodetachment lifetime is usually short. The name implies similarities to the shape resonance, as their mechanism of formation is the same except that the attractive part of effective potential arises between impinging electron and target molecule in its electronically excited state. The approaching electron has enough energy to electronically excite the molecule to which the electron is concurrently trapped.

VIBRATIONAL FESHBACH RESONANCES

Vibrational Feshbach resonances appear when the electron is trapped in a diffuse state, as a result of interacting with the long-range dipole moment of the electron-molecule system. This dipole-bound state is weakly bound, i.e it lies slightly below the ground state of the target. The incoming electron captured in the diffuse state can excite the near vibrational levels of the parent molecule causing a Vibrational Feshbach resonance.

DECAY OF RESONANCES

- *Autodetachment* (AD) is the most probable channel leading to decay of a TNI. The lifetime, τ, for AD processes is given by Heisenberg's uncertainty principle (the width of a resonance is linked to lifetime by the relation: $\Gamma \approx \frac{\hbar}{\tau}$). In the case of a shape resonance, the lifetime is a function of both the size of the barrier and the energy of the anion (i.e. the relative height and thickness of the barrier which the electron has to penetrate). The lifetime differs between molecules and between resonances in the same molecule, it is on the order of ten femtoseconds to milliseconds. For shape resonances, the autodetached electron has the same energy as the original, incoming electron. In the case of core-excited resonances some part of the initial kinetic energy of the electron is left within the molecule (i.e. in the rotational, vibrational, electronic degrees of freedom).

- *Dissociative electron attachment* (DEA) is one of the channels leading to decay of a TNI. It is the most likely decaying channel for long lifetime resonances. It appears for specific, narrow range of the incident electron energies, illustrated in figure 1.8. DEA is a bond selective process. Which bonds in the molecule can be broken depends on the incident electron energy. Multiple bond cleavages and new bonds formation are possible in DEA.

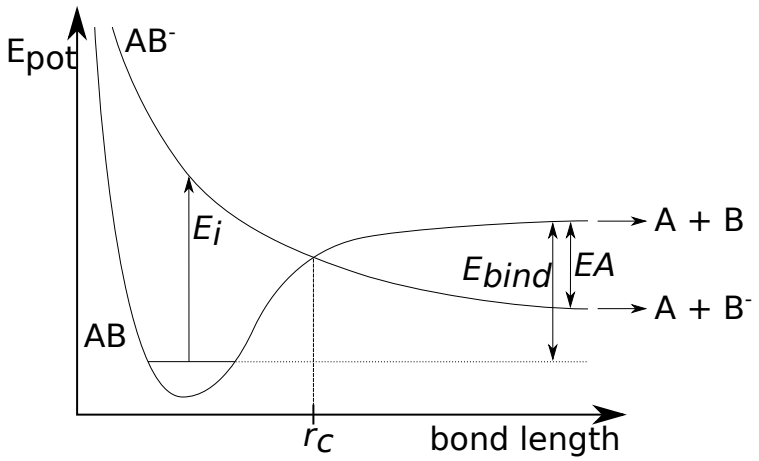

Figure 1.8: Illustration of DEA in a diatomic molecule AB. The AB curve is the potential energy curve of the neutral molecule, AB^- is a curve of its anion. E_i is incident electron energy; E_{bind} is energy needed to dissociate the bond; EA is electron affinity of fragment B. The picture comes from [33].

1.3 PRIOR RESEARCH

Since 2000, after the pioneering study by Boudaïffa *et al.* [9], mentioned at the beginning of this chapter, many experimental and theoretical studies have been performed, in order to understand the processes induced in DNA by low-energy electrons in more detail. DNA is a very complex system, moreover, in living cells it always exists in a water environment. Thus the experimental work for DNA fragmentation is difficult to interpret and theoretical electron scattering calculations are too computationally expensive to be performed for such huge systems as DNA fragments. Therefore, the research has been mostly centred on studying biological molecules and prototypes of biological molecules in the gas phase (isolated molecules). However, DNA subunits have also been treated, both experimentally and theoretically, in the solvation phase (a cluster containing only one molecule different from water) and experimentally in the condensed phase. A summary of prior research both theoretical and experimental are presented in figure 1.9. In the chart thymine and uracil have been distinguished amongst the nucleobases because thymine is one of the molecules studied in this work, and uracil has a similar structure and properties (the prior research for these two molecules is presented in more details in chapter 5).

In order to simplify the study and to gain a better insight into the processes, not only have DNA constituents been broadly studied but also the molecules from which they are derived as well as prototypes of biological molecules.

Various experimental and theoretical techniques have been appied to investigate complex biomolecules (DNA subunits and their prototypes) and a large number of papers have been published on the topic [3, 53, 55, 80, 81]. An extensive overview on the subject was given by I. Baccarelli [82]

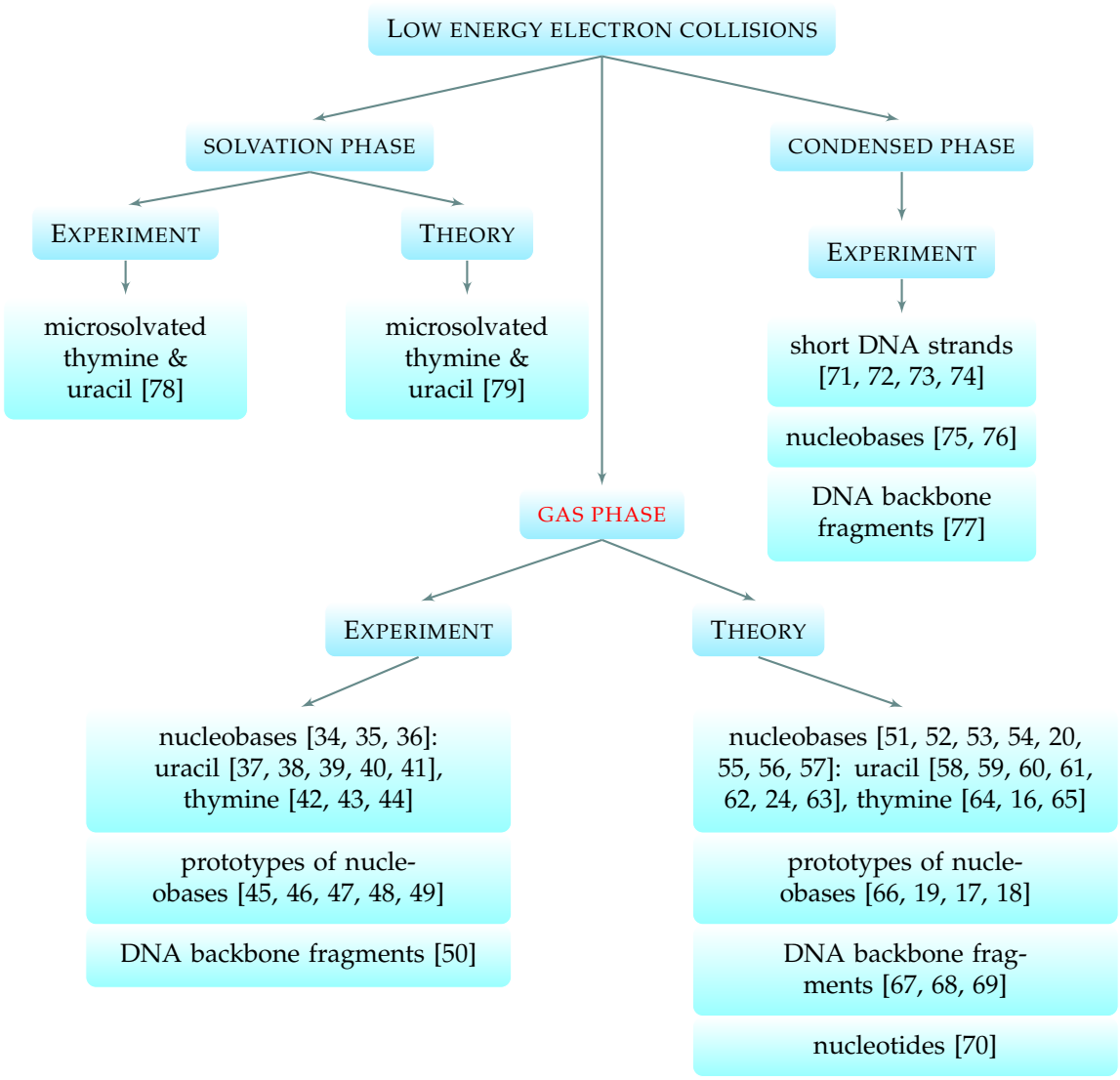

Figure 1.9: A chart illustrating prior research divided into experimental and theoretical study and phase states. Some examples of work in these areas are presented. Thymine and uracil are distinguished in the chart amongst the nucleobases due to their importance for this work.

in 2011. Since in this thesis we are interested in the formation of resonances in collisions with DNA bases and their prototypes in gas and solvation phases, we will focus mainly on the information available about them.

Although, the majority of the research took place after 2000, the attachment energies of electrons to the nucleic acid bases in their gas phases were measured in 1998 by Aflatooni *et al.* [34] (uracil even earlier by A. R. Johnston and P. D. Burrow; the results have been cited elsewhere [83, 84]), using an electron transmission spectroscopy (ETS) experiment. The experiment was performed for the electron energy range between 0-5 eV for the targets uracil and thymine, up to 4 eV for adenine and cytosine, and up to 3.5 eV for guanine. For all investigated systems they recorded three π^* resonances. All three pyrimidinic nucleobases give a similar resonance spectrum, while resonance energies for adenine and guanine are similar to each other but they differ form pyrimidinic

nucleobases. These π^* resonances are associated with the three double bonds in the aromatic structure of the benzene-like ring. Already in 1975, the pioneering research into electron collisions with azabenzene molecules (in ETS experiment) by Nenner and Schulz [85] showed that three electron resonances of π^* symmetry are observed in each of the studied azabenzene (pyridine, pyrimidine, pyrazine, pyridazine, s-triazine) and benzene (similar experiment for pyridine were performed by A. Modelli and P. D. Burrow [86]). The two resonances lowest in energy have been identified as pure shape π^* resonances, while the third one was suggested to have mixed shape–core-excited character. This was confirmed by Winstead and McKoy [55, 87] in their calculations using the Schwinger multichannel (SMC) method. The mentioned studies of Nenner and Schulz, Modelli and Burrow, and Aflatooni *et al.* will be used in this work as references to establish whether our theoretical results for isolated molecules are accurate.

Much work has been done to study the DEA fragmentation processes for nucleobases and their prototypes, e.g. [37, 39, 43, 38, 41, 44, 35]. Both long-life shape and core-excited resonances can lead to DEA, therefore the study of these resonances is important and allows one to link low-energy electron scattering results to the DEA processes described in the literature.

Although nucleobases and their prototypes have been broadly studied in the gas phase, there is not much knowledge about the resonance characteristic and fragmentation channels in the solvation phase. The only experimental work on DEA fragmentation process for solvated thymine and uracil has been caried out recently by J. Kočišek *et al.* [78]. Theoretical calculations of electron attachment energies and DEA cross sections of thymine/uracil system have been performed by Smyth *et al.* [79]. These investigations will be described in detail in chapter 5.

Since water attaches to DNA molecules by a hydrogen bond, the knowledge about the influence of this bond on DEA cross section [88] and resonance characteristic [27] for non-biological molecular can also be used. As reader will find out, we often refer to T. C. Freitas *et al.*'s work on formic acid-water clusters (HCOOH-$(H_2O)_n$, n = 1, 2) [27]. They were the first to deduce that water acting as a hydrogen (proton) donor stabilizes resonances – shift to lower energies, while water acting as hydrogen acceptor destabilizes resonances – shift to higher energies. The main goal of this work is to study the role of hydrogen bonds on the resonance characteristic, and to investigate whether the Freitas *et al.*'s conclusion for formic acid also holds for benzene-ring molecules, i.e. pyridine and thymine.

1.4 LAYOUT OF THE THESIS

In the next chapter, chapter 2, we describe the R-matrix method and a link between it and the more general S-matrix theory. We introduce the resonance phenomenon from a strictly theoretical point

of view. We also present computational tool which we use to perform our R-matrix calculations, i.e. UKRmol+ suite. In chapter 3 we present our results on electron collisions with isolated pyridine. In the following chapter 4 we use the information gained in chapter 3 for a detailed comparison and analysis of the results obtained for pyridine-water clusters: pyridine-$(H_2O)_n$, n = 1, 2, 3, 5. Results of electron collision calculations with another system, namely thymine clusters, are presented in chapter 5. In this chapter we introduce several clusters, with the main focus on the biggest one: thymine-$(H_2O)_5$. Finally, in chapter 6 we summarise our finding for all targets studied. We also discuss how our results help the understanding of the effect of hydrogen bonds on resonance characteristics. Suggestions for the future work can also be found in the final chapter.

2

THEORY

In this chapter, information about electronic structure theory, which is important for this work, is presented. It is followed by general information about scattering theory and a more detailed description of S-matrix and R-matrix theory. Scattering models, essential for this work, are presented in section 2.5. At the end, the software used to perform R-matrix calculations is discussed.

2.1 INTRODUCTION TO ELECTRONIC STRUCTURE THEORY

The electronic structure methodology is based on approximations needed to determine electronic wave functions. The main reason behind the need for approximations is the electron correlation and the non-separability of the Coulomb potential terms in the Hamiltonian.

The common way to solve the electronic part of the problem is to start with the Hartree-Fock (HF) approximation. The basic concept of the Hartree-Fock approximation is that each electron feels an average potential i.e. it moves in a so-called *mean field* generated by the remaining $N-1$ electrons. Therefore it is possible to express the many electron wave function as a product of N one-electron functions.

$$\mathcal{H} = \sum_{i=1}^{N} \left(-\frac{\nabla_i^2}{2} - \sum_{k=1}^{N_A} \frac{Z_k}{\rho_{ki}} \right) + \sum_{i>j}^{N} \frac{1}{r_{ij}}, \tag{2.1}$$

is replaced by the Hartree-Fock operator:

$$\mathcal{H}^{HF} = \sum_{i=1}^{N} \left(-\frac{\nabla_i^2}{2} - \sum_{k=1}^{N_A} \frac{Z_k}{\rho_{ki}} \right) + \sum_{i=1}^{N} v_i^{HF}, \tag{2.2}$$

N is the number of electron and N_A is the number of nuclei in the molecule, Z_k is the charge of nucleus k, ρ_{kj} is the distance between nucleus k and jth electron, v_i^{HF} is the average potential experienced by the ith electron due to the presence of the other electrons.

The eigenvector of the Hamiltonian (2.2) can be written as a product of one-electron functions since the non-separable Coulomb interaction has been replaced by a sum of effective one-electron potentials. The wave function is expressed as a Slater determinant since it needs to be antisymmetric according to the Pauli principle and it is given by:

$$|\Phi\rangle = |\phi_1 \bar{\phi}_1 \phi_2 \bar{\phi}_2 \dots \phi_{N/2} \bar{\phi}_{N/2}|, \tag{2.3}$$

where $\{\phi_i\}_{i=1}$ are molecular spin-orbitals with spin 'up' and $\{\bar{\phi}_i\}_{i=1}$ are molecular spin-orbitals with spin 'down'. The problem reduces to solving the following equation for each electron:

$$\left[\frac{1}{2}\nabla_i^2 - \sum_{k=1}^{N_A} \frac{Z_k}{\rho_{ki}} + v_i^{HF} \right] \phi_j(\mathbf{x}_i) = \varepsilon_j \phi_j(\mathbf{x}_i), \tag{2.4}$$

where ε_j is the energy of orbital $\phi_j(\mathbf{x}_i)$. However, since the potentials, v_i^{HF}, depend on all orbitals describing the electrons, the potentials (and therefore the orbitals) are determined simultaneously using a self-consistent field iterative procedure, known as SCF-HF.

The ϕ_i orbitals are usually expanded in a basis set of Gaussian-type orbitals (GTOs):

$$\phi_i(x_i, y_i, z_i) = \sum_{k=1}^{n_o} d_{ik} g_k(x_i, y_i, z_i), \;\; i = 1, \dots, n_o. \tag{2.5}$$

The coefficients d_{ik} are the molecular orbital coefficients. The $\{g_k\}_{k=1}^{n_o}$ are Gaussian functions and have been optimised for accelerating the convergence of quantum calculations and collected in the form of data base on a website [105].

To go beyond the Hartree-Fock approximation, the dynamical correlation between electrons must be taken into account. This accounts for the fact that electrons do not move independently but interact with each other via the Coulomb potential. The electron-electron repulsion can be taken into account by using a linear combination of Slater determinants. This can be done because the Hartree-Fock operator is Hermitian, so the set of all eigenfunctions of the operator forms a complete, orthonormal set [106].

A convenient way to express those other determinants is by taking the Hartree-Fock ground state

as a reference determinant and promoting each electron from a occupied orbital to an unoccupied orbital. If the occupied spin-orbital is indicated by the subscript *a, b, c...* and virtual spin-orbital by *r, s, t...*, and all possible ways of forming a Slater determinant of HF orbitals are considered, the exact wave function for any state of the system can be written as:

$$|\Psi\rangle = c_0|\psi_0\rangle + \sum_{ra} c_a^r|\psi_a^r\rangle + \sum_{\substack{a<b\\r<s}} c_{ab}^{rs}|\psi_{ab}^{rs}\rangle + \sum_{\substack{a<b<c\\r<s<t}} c_{abc}^{rst}|\psi_{abc}^{rst}\rangle + \dots \tag{2.6}$$

If K is the total number of Hartree-Fock orbitals, N is the total number of electrons then the number of possible combination of K objects taken N at a time is the binomial coefficient:

$$\binom{K}{N} = \frac{K!}{(K-N)!N!}. \tag{2.7}$$

When all possible Slater determinants are used the approximation is called *Full Configuration Interaction* (FCI).

Although the FCI procedure using HF orbitals can give accurate wave functions, it can be computationally prohibitive. Therefore, many methods have been developed to limit the size and computing time of the calculation of wave functions, e.g. *Multi Configuration Self Consistent Field* (MCSCF), *Complete Active Space Self Consistent Field* (CASSCF), etc. This last method will be used in this thesis to generate all multiconfiguration target wave functions.

In the CASSCF approach, the FCI coefficients in equation (2.6) and the GTOs coefficient in equation (2.5), are optimised concurrently. The method allows one to determine how much the excitations in FCI formula (2.6) contribute and, at the same time, the shape of the orbitals. In the first step of the CASSCF procedure, the HF orbitals are used as a starting guess. Next, the *frozen* orbitals are chosen; these orbitals are close to the nuclei and are not optimised. After that the *doubly occupied*, *active* (which together with frozen orbitals are occupied by the N target electrons) and *virtual* orbitals (which are unoccupied target orbitals) are selected. Both the doubly occupied and active orbitals are optimised but, unlike the first ones, the second ones, are always doubly occupied and no excitations out of them are permitted. The choice of active space is crucial to the success of the method, because electrons occupying the active orbitals contribute to the wave function. The choice of active orbitals depends on the electronic states being described, so there is no unique or best choice.

The CASSCF model is usually indicated by a pair of numbers: (n, m), where n indicates the number of electrons being distributed among the m active orbitals. The other $N - n$ electrons occupy the frozen and the doubly occupied orbitals.

Once the frozen, doubly occupied and active orbitals are chosen, the CASSCF optimisation can

proceed. The CASSCF energy of a target state is given by the equation:

$$E_{CASSCF} = \langle \Psi_{CASSCF} | H_N | \Psi_{CASSCF} \rangle. \tag{2.8}$$

Φ_{CASSCF}, the CASSCF wave function to be optimised, has a form:

$$|\Psi_{CASSCF}\rangle = exp(\gamma) exp(\delta) |\Psi_d\rangle \tag{2.9}$$

where $|\Psi_d\rangle$ is an initial guess wave function generated from the CASSCF configurations, while γ and δ are upper triangle matrices that determine the optimised parameters: d_{ik} – the orbital coefficients and c – the FCI coefficients.

2.2 INTRODUCTION TO SCATTERING THEORY

In classical mechanics, the outcome of a collision between two particles is fully determined by their velocity and impact parameter (the perpendicular distance between the path of a projectile and the axis passing through the center of a target). In quantum mechanics, since the concept of a path and a defined velocity is meaningless and so is the impact parameter, the purpose of the theory is to calculate the probability of the projectile interacting with and being scattered from a target, and the final state of the target. The kinematic information about the projectile is stored in a set of quantum numbers and a wavenumber $\vec{k}$, which may contain information about its momentum.

The region of interaction between an incoming electron and a target molecule is usually no larger than a few atomic diameters and, therefore, in practice it is not observable in classical mechanics. The strength of interactions between the projectile and the target depends on the range of the potential. If the potential is strongly attractive at close range, e.g. $V = -r^{-3}$, then the incoming particle is trapped by the potential and never emerges out of the attractive potential well [30] (figure 2.1). As $\vec{r} \to \infty$ the potential needs to fall off quicker than r^{-3} in order for a particle to behave like a free particle as it moves far away from a target (figure 2.2 and 2.3). Figure 2.2 illustrates a direct scattering event, where figure 2.3 depicts a case when particle is transiently trapped by the target.

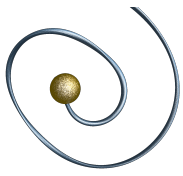

Figure 2.1: An incoming particle is permanently captured by an attractive potential.

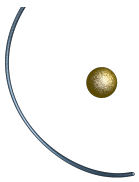

Figure 2.2: An incoming particle is directly scattered by an attractive potential.

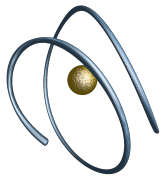

Figure 2.3: An incoming particle is temporarily trapped by an attractive potential.

In the most general way, scattering theory can be formalized as follow (figure 2.4):

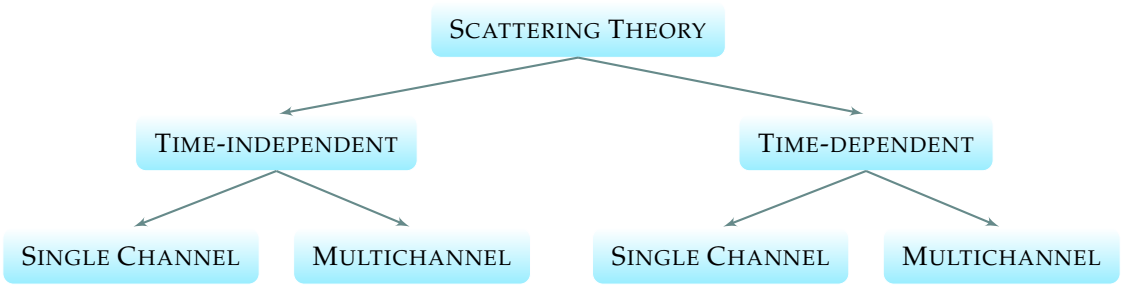

Figure 2.4: A flowchart illustrating the general formalism of scattering theory.

A collision between two particles can have different outcomes. Each of the final possible products of the collision for a specific state of the projectile and the target is called a *channel*. Therefore, a standard scattering process is called a *multichannel collision* when there are many different possible states in which the target and projectile can emerged after collision, (figure 2.5).

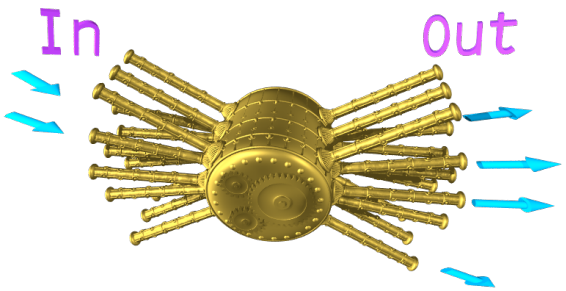

Figure 2.5: Illustration of a multichannel process. An outgoing projectile has many possible channels to leave the region of interaction.

Nevertheless, there are certain simple processes (e.g low-energy scattering of an electron off a proton) in which only one channel needs to be consider. This case is called a *single-channel* process, and it happens when all other channels are either closed (i.e. the other channels are energetically inaccessible) or can be neglected. The formalism of single-channel scattering is much simpler than the general case of the multichannel problem, but it includes almost all of the basic scattering concepts. Therefore, following the canonical way of introducing elementary scattering theory, in this chapter the scattering problem is first simplified to the single-channel case, in order to show in the simplest way the important facts which result from the solution of the problem. Subsequently, this approach will be developed into the multichannel case. These cases will be described in the time-independent approach, since the method used to obtained results in this work is also a time-independent method.

2.3 S-MATRIX THEORY

A standard approach to the scattering problem is to solve the stationary Schrödinger equation for the wave function $\Psi(\vec{x})$ representing the projectile:

$$\left[-\frac{\hbar^2}{2m}\nabla^2 + V(\vec{x})\right]\Psi(\vec{x}) = E\Psi(\vec{x}), \tag{2.10}$$

where m is the mass of the projectile, $\vec{x}$ represents the three dimensional Cartesian coordinates and $V(\vec{x})$ is the potential with which the projectile interacts.

The wave function $\Psi(\vec{x})$ is expressed as:

$$\Psi(\vec{x}) = \Psi_{\text{in}}(\vec{x}) + \Psi_s(\vec{x}) \tag{2.11}$$

where $\Psi_{\text{in}}(\vec{x})$ is the incoming plane wave and $\Psi_s(\vec{x})$ is the scattered wave, a perturbation of the incoming wave function.

2.3.1 SINGLE CHANNEL CASE

In the following, the partial-wave approach will be followed, in which a plane wave is expanded using *Legendre polynomials* $P_\ell(\cos\theta)$ (it is introduced below, see equation (2.24)), this is called a *partial-wave expansion*. The wave function of incoming electron can be expressed as:

$$\Psi = \sum_{\ell m} \frac{u_\ell(r)}{r} Y_\ell^m(\theta, \phi). \tag{2.12}$$

The asymptotic form of the scattered part $\Psi_s(\vec{x})$ should describe a free particle and should therefore be a solution to the free-particle Schrödinger equation.

To simplify the single-channel case even further, the next assumption is that the potential $V(\vec{x})$ in equation (2.10) as $r \to \infty$ is spherical and vanishes:

$$V(\vec{x}) = \begin{cases} V(r) & , \quad r << \infty, \\ 0 & , \quad r \to \infty. \end{cases} \tag{2.13}$$

From now on atomic units are used throughout. After rewriting equation (2.10) in polar coordinates and separation of variables: $\Psi(r, \theta, \varphi) = R(r)\Theta_\ell(\theta)\Phi_m(\varphi)$, the radial equation for the ℓth partial wave is:

$$\left[-\frac{d^2}{dr^2} + \bar{V}(r) + \frac{\ell(\ell+1)}{r^2} - k^2\right] u_\ell(k, r) = 0, \tag{2.14}$$

where $k^2 = \frac{2m}{\hbar^2}E$, $\bar{V}(r) = \frac{2m}{\hbar^2}V(r)$ and $u_\ell(k,r) = rR_\ell(r)$. The expressions for the products $\Theta_\ell(\theta)\Phi_m(\varphi)$ are the well-known spherical harmonics, defined as:

$$Y_\ell^m(\theta,\varphi) = (-1)^m \sqrt{\frac{(2\ell+1)}{4\pi}\frac{(\ell-m)!}{(\ell+m)!}}\, P_\ell^m(\cos\theta)\, e^{im\varphi}, \tag{2.15}$$

where m ranges over all possible values: $m = -\ell,\ -\ell{+}1\,,\ldots,\ \ell{-}1,\ \ell$, and $P_\ell^m(\cos\theta)$ are the *associated Legendre polynomials* (for the spherical potential $m = 0$, the notation $P_\ell^0(\cos\theta)$ is replaced by $P_\ell(\cos\theta)$ and the polynomials are called Legendre polynomials).

To solve this radial Schrödinger equation, the region in which the scattering phenomenon happens is divided into three parts (see figure 2.6):

region $\mathcal{A}$:

$$\left.\begin{array}{rcl} \bar{V}(r) & = & 0 \\ \frac{\ell(\ell+1)}{r^2} & = & 0 \end{array}\right\} r \to \infty, \tag{2.16}$$

region $\mathcal{B}$:

$$\left.\begin{array}{rcl} \bar{V}(r) & = & 0 \\ \frac{\ell(\ell+1)}{r^2} & \neq & 0 \end{array}\right\} a < r < \infty, \tag{2.17}$$

region $\mathcal{C}$:

$$\left.\begin{array}{rcl} \bar{V}(r) & \neq & 0 \\ \frac{\ell(\ell+1)}{r^2} & \neq & 0 \end{array}\right\} 0 \leq r \leq a, \tag{2.18}$$

where a is defined as the radius of the region beyond which the potential is negligible (that is, a defines the boundary between regions $\mathcal{C}$ and $\mathcal{B}$).

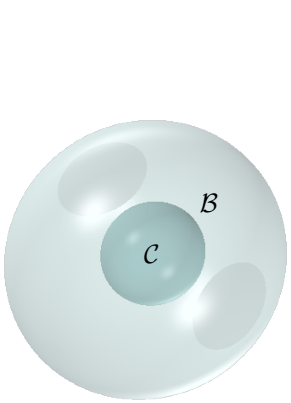

Figure 2.6: A division of region passed by projectile into three part: outer region $\mathcal{A}$, intermediate region $\mathcal{B}$ and inner region $\mathcal{C}$.

The solution of the radial Schrödinger equation for region $\mathcal{A}$ is the asymptotic form of the spherical Bessel function $j_\ell(kr)$:

$$\frac{u_\ell(k,r)}{r} = j_\ell(kr) \underset{r\to\infty}{\longrightarrow} \frac{1}{r}\left(\exp(ikr - \ell\pi/2) - \exp(-ikr - \ell\pi/2)\right). \tag{2.19}$$

This corresponds to an outgoing and an incoming spherical wave. Therefore, comparison with equation (2.11) shows that $\Psi_s(\vec{x}) \propto \frac{1}{r}\exp(ikr)$ is expected at large distances.

The asymptotic expression for the entire wave function for this region can be set to:

$$\Psi(r,\theta) \underset{r\to\infty}{\longrightarrow} e^{ikz} + f(\theta,k)\frac{\exp(ikr)}{r}, \tag{2.20}$$

where $f(\theta,k)$ is called the *scattering amplitude*, which is, in this case only, dependent on the polar (elevation) angle θ (see figure 2.7) and wave number k (the equation (2.20) does not depends on azimuth angle, ψ, because as it was mentioned before the potential $V(\vec{x})$ is spherical). The expression for it can be found by matching the scattering wave function $\Psi_s(\vec{r})$ for the three regions ($\mathcal{A}$, $\mathcal{B}$ and $\mathcal{C}$).

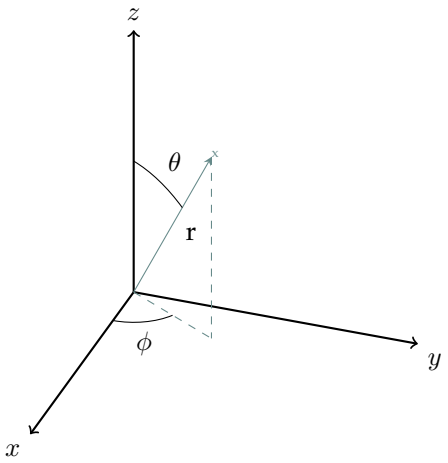

Figure 2.7: A spherical coordinates (r, θ, ϕ): radial distance r, polar angle θ, and azimuthal angle ϕ.

The solution for the inner region $\mathcal{B}$ is a spherical Hankel function of first order, $h_\ell^{(1)}(k,r)$. For $kr \gg 1$ (which is dimensionless), the function can be expressed:

$$\frac{u_\ell(k,r)}{r} = h_\ell^{(1)}(k,r) \approx \frac{(-i)^{\ell+1}}{k}\frac{\exp(ikr-\ell\pi/2)}{r}. \tag{2.21}$$

In this region the entire wave function can be expressed:

$$\Psi(r,\theta) = e^{ikz} + k\sum_{\ell=0}^{\infty}(2\ell+1)i^{\ell+1}a_\ell(k)h_\ell^{(1)}(kr)P_\ell(\cos\theta) \tag{2.22}$$

By matching regions $\mathcal{A}$ and $\mathcal{B}$ and knowing the expression for the spherical Hankel function for $kr \gg 1$, i.e. equation (2.21), the scattering amplitude can be rewritten as:

$$f(\theta,k) = \sum_{\ell=0}^{\infty}(2\ell+1)a_\ell(k)P_\ell(\cos\theta), \tag{2.23}$$

where the coefficients $a_\ell(k)$ are called *partial scattering amplitude* and can be found by matching the

scattering wave function for region $\mathcal{B}$ and $\mathcal{C}$.

The incoming wave from expression (2.22) can be decomposed into partial waves using the plane wave expansion in terms of spherical Bessel functions [89] and Legendre polynomials [90]:

$$\Psi_{\text{in}}(\vec{r}) = e^{ikz} = \sum_{\ell=0}^{\infty}(2\ell+1)i^{\ell}j_{\ell}(kr)P_{\ell}(\cos\theta). \tag{2.24}$$

The spherical Bessel function can be expressed as a sum of two spherical Hankel functions:

$$j_{\ell}(kr) = \frac{1}{2}\left(h_{\ell}^{(1)}(kr) + h_{\ell}^{(2)}(kr)\right). \tag{2.25}$$

This has physical significance: equation (2.21) shows that $h_{\ell}^{(1)}$ asymptotically behaves as an outgoing wave, whereas $h_{\ell}^{(2)}$ asymptotically behaves as $\frac{i^{\ell+1}}{k}\frac{\exp(-ikr)}{r}$ and is thus an incoming wave. Thus the incoming wave Ψ_{in} has features of both incoming and outgoing wave. By rewriting equation (2.24) using the spherical Hankel functions sum, (equation 2.25), the incoming wave is expressed:

$$\Psi_{\text{in}}(\vec{r}) = \sum_{\ell=0}^{\infty}\frac{(2\ell+1)i^{\ell}}{2}\left[h_{\ell}^{(1)}(kr) + h_{\ell}^{(2)}(kr)\right]P_{\ell}(\cos\theta) \tag{2.26}$$

Thus, transforming the formula (2.22) using (2.26) equation, the wave function can now be set to:

$$\Psi(r,\theta) = \sum_{\ell=0}^{\infty}\frac{(2\ell+1)i^{\ell}}{2}\left[h_{\ell}^{(1)}(kr)S_{\ell} + h_{\ell}^{(2)}(kr)\right]P_{\ell}(\cos\theta) \tag{2.27}$$

where

$$S_{\ell} = 1 + 2ika_{\ell}(k) \tag{2.28}$$

is defined as the *S-matrix element* for partial wave ℓ.

This wave function looks like an incoming wave (2.26) and differs only by the S_{ℓ} next to the spherical Hankel function expressing the outgoing wave. The full complexity of the scattering process is comprised in the S-matrix element.

2.3.2 SCATTERING AMPLITUDE

To understand the meaning of the S-matrix element S_{ℓ}, the current conservation law needs to be invoked. Since a potential cannot create or destroy particles, the total current density carried by a wave function, integrated over a large surface containing the target must be zero.

If the sphere of radius R is much bigger than the volume of the target and it is centred around it, the following formula is valid:

$$I = \int_{R}\mathbf{J}\cdot d\mathbf{R}, \tag{2.29}$$

where I is the integral over the whole sphere R and the flux $\mathbf{J}$ is defined as:

$$\mathbf{J} = \frac{\hbar}{m}\frac{1}{2i}\left(\Psi^*\nabla\Psi - \Psi\nabla\Psi^*\right) = \frac{\hbar}{m}\,\mathrm{Im}\left(\Psi^*\nabla\Psi\right). \tag{2.30}$$

The only possibility that integrating the equation (2.29) gives zero requires that $|S_\ell| = 1$ in equation (2.27), which implies that:

$$S_\ell = \exp(2i\delta_\ell), \tag{2.31}$$

where δ_ℓ is the phase shift of the scattering wave function gained on both directions of propagation (on the way in and the way out), thus the 2 in this definition; δ_ℓ is real.

The other approach is to look at the asymptotic form, for large values of r ($kr \gg 1$), of the incoming wave (2.26) for each ℓ term:

$$\psi_{\text{in}}^{(\ell)} = \frac{2\ell+1}{2ikr}\left[\exp(ikr) - (-1)^\ell\exp(-ikr)\right]P_\ell(\cos\theta). \tag{2.32}$$

In this approach the whole wave function (2.22) can be rewritten for each ℓ term as:

$$\psi^{(\ell)} = \psi_{\text{in}}^{(\ell)} + \frac{2\ell+1}{r}a_\ell(k)\exp(ikr)P_\ell(\cos\theta). \tag{2.33}$$

Since probability cannot be transferred from one angular momentum component to another, the only possibility of modifying the outgoing wave without changing probability is to change a phase. Thus the asymptotic expression for whole wave function is:

$$\psi^{(\ell)} = \frac{2\ell+1}{2ikr}\left[\exp(ikr)\exp(2i\delta) - (-1)^\ell\exp(-ikr)\right]P_\ell(\cos\theta). \tag{2.34}$$

This shows again that the only response to the potential is a change of phase.

Applying simple algebra to the new expression for the S-matrix element (2.31) and its definition (2.28), the partial scattering amplitude can be now written in the form:

$$a_\ell = \frac{S_\ell - 1}{2ik} = \frac{e^{2i\delta_\ell} - 1}{2ik} = \frac{e^{i\delta_\ell}\sin\delta_\ell}{k} = \frac{1}{k\cot\delta_\ell - ik}. \tag{2.35}$$

2.3.3 ANALYTIC PROPERTIES OF THE S-MATRIX: BOUND STATES AND RESONANCES

It was assumed that the variables k, E and ℓ in the expressions above are real. By allowing them to be complex, interesting properties of the complex partial amplitude, and thus S-matrix, can be obtained.

As a first case complex values of k and E (thus as well k^2) are considered, but the angular momentum ℓ is to remain real.

Expressing the asymptotic solution of equation (2.14) as:

$$u_\ell(k,r) \approx \frac{1}{2ik}\left(\exp(i(kr - l\pi/2 + \delta_\ell)) - \exp(-i(kr - l\pi/2 + \delta_\ell))\right), \tag{2.36}$$

and next presenting it in the form:

$$u_\ell(k,r) \underset{r\to\infty}{\longrightarrow} f_\ell^+(k^2)\exp(ikr) - f_\ell^-(k^2)\exp(-ikr). \tag{2.37}$$

where the functions $f_\ell^+(k^2)$ and $f_\ell^-(k^2)$, called Jost functions, are defined as [91]:

$$f_\ell^+(k^2) = \frac{1}{2ik}\exp(i(\delta_\ell - l\pi/2)), \tag{2.38}$$

$$f_\ell^-(k^2) = \frac{1}{2ik}\exp(-i(\delta_\ell - l\pi/2)), \tag{2.39}$$

and have the property

$$f_\ell^-(k^2) = (f_\ell^+(k^2))^*. \tag{2.40}$$

Dividing (2.38) by (2.39), the expression for S-matrix element is obtained:

$$S_\ell = \exp(2i\delta_\ell) = (-1)^{\ell+1}\frac{f_\ell^+(k^2)}{f_\ell^-(k^2)} \tag{2.41}$$

Considering the relation (2.35), the partial amplitude can be determined via the partial wave S-matrix element $S_\ell = e^{2i\delta_\ell}$ as:

$$a_\ell(k) = \frac{S_\ell - 1}{2ik} = \frac{e^{2i\delta_\ell} - 1}{2ik} = \frac{1}{2ik}\frac{(-1)^{\ell+1}f_\ell^+(k^2) - f_\ell^-(k^2)}{f_\ell^-(k^2)} \tag{2.42}$$

The solution of (2.14) is an analytic function of the parameter k^2 for the whole Riemann complex surface. Because in equation (2.36), a parameter k is present, the assumption will be taken that this parameter is this root of k^2 which has positive imaginary part.

The solution (2.36) of equation (2.14) was obtained by assuming that for large r, the $\bar{V}(r)u_\ell(k,r)$ and $\frac{\ell(\ell+1)}{r^2}u_\ell(k,r)$ vanishes or, in other words, that $\bar{V}(r)u_\ell(k,r)$ and $\frac{\ell(\ell+1)}{r^2}u_\ell(k,r)$ can be neglected compared to $k^2u_\ell(k,r)$. For those complex variables k^2 for which the assumption is not right, the function (2.36) is no longer a solution of the equation (2.14). Since, in the formula (2.36), the functions $\exp(ikr)$ and $\exp(-ikr)$ are present and are defined for all values of k, the mentioned values of k^2 need to be eliminated from the domain of the Jost function. The range of eliminated values k^2 is determined by the range of the potential and it is called left cut, e.g. $-\infty < k^2 < \nu$, where $1/\nu$ is the

range of the potential.

There is one more case when the ratio $\bar{V}(r)u_\ell(k,r)$ to k^2 and $\frac{\ell(\ell+1)}{r^2}u_\ell(k,r)$ to k^2 is not negligible, i.e, when $k^2 = 0$. These values also have to be cut from the domain of the Jost function. Mapping the k plane on the k^2 plane, two Riemann surfaces are obtained: the sheet for which $\operatorname{Im} k > 0$ is called the physical sheet and the sheet for which $\operatorname{Im} k < 0$ is called the unphysical sheet [91]. In figure (2.8) both sheets are presented simultaneously from different perspectives. In this figure the black dots on the real negative axis of $\operatorname{Im} k > 0$ correspond to bound states, the red dots on the positive real and negative imaginary quarter of $\operatorname{Im} k < 0$ plane correspond to resonances.

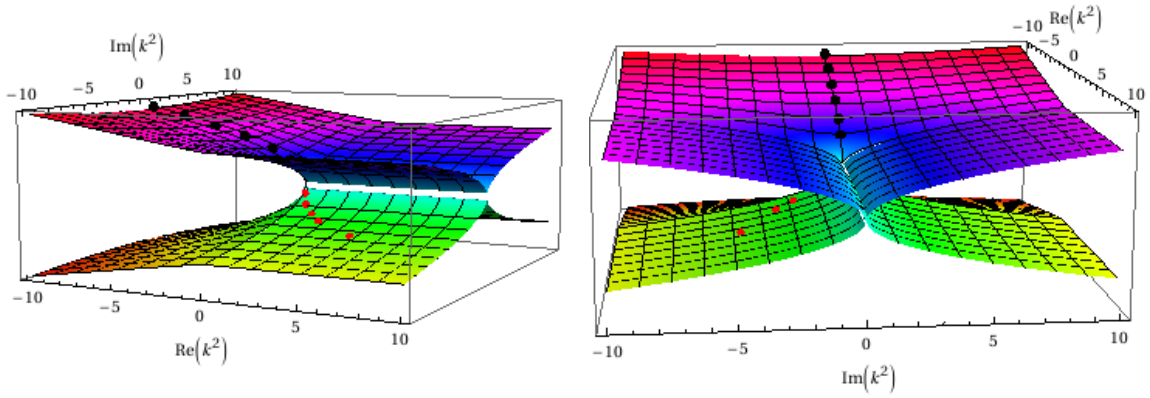

Figure 2.8: Riemann surfaces obtained by mapping the k plane on the k^2 plane. The black dots on the real negative axis of $\operatorname{Im} k > 0$ correspond to bound states, the red dots on the positive real and negative imaginary quarter of $\operatorname{Im} k < 0$ plane correspond to resonances. The graphs have been generated with *Mathematica*.

It can be easily seen that for every value of k^2 for which $f_\ell^-(k^2) = 0$ the equation (2.42) has poles. For these cases the radial wave function $u_\ell(k,r)$ (2.37) is reduced to:

$$u_\ell(k,r) \underset{r\to\infty}{\longrightarrow} f_\ell^+(k^2)\exp(ikr). \tag{2.43}$$

If the poles of a partial amplitude are in the physical sheet ($\operatorname{Im} k > 0$), then

$$u_\ell(k,r) \underset{r\to\infty}{\longrightarrow} f_\ell^+(k^2)\exp(i\operatorname{Re} kr)\exp(-|\operatorname{Im} k|r), \tag{2.44}$$

thus the function is normalized and it corresponds to bound states. However, then $k^2 = 2mE/\hbar^2$ has to be real and negative, so the poles may only lie on the physical sheet, on the negative $\operatorname{Re} k^2$ axes (from 0 to some value which depends on potential). If the poles are in the unphysical sheet ($\operatorname{Im} k < 0$), then

$$u_\ell(k,r) \underset{r\to\infty}{\longrightarrow} f_\ell^+(k^2)\exp(i\operatorname{Re} kr)\exp(|\operatorname{Im} k|r), \tag{2.45}$$

there is no physical limitation on the position of these poles, but the physical interpretation is possible only when they are lying close to the physical sheet, i.e. when:

$$k^2 = k_r^2 - \frac{ig}{2} \tag{2.46}$$

where k_r^2 and g are real. Considering the case when $k_r^2 > 0$ and $g > 0$ and using the relation that $k^2 = 2mE/\hbar^2$ and defining $\Gamma = g\hbar^2/m$, the following relation can be written:

$$E = E_r - \frac{i\Gamma}{2}. \tag{2.47}$$

This energy is called *resonance energy*, where E_r is resonance the position and Γ is resonance width. The last value is connected with the half-time τ of the resonance by the uncertainty principle:

$$\Gamma \approx \frac{\hbar}{\tau}. \tag{2.48}$$

The larger value of τ, the better energy is defined, which also implies that the width is smaller. This issue will be mentioned again when explaining methods for finding and analysing resonances.

From the unitary relation of the S-matrix [30]:

$$S_\ell S_\ell^* = 1 \tag{2.49}$$

it can be easily noticed that corresponding to the pole, defined by (2.47), there is a zero in the S-matrix for a complex energy in the upper half k-plane:

$$E = E_r + \frac{i\Gamma}{2}. \tag{2.50}$$

This energy corresponds to a *virtual state*.

If all other singularities of the S_ℓ matrix are far away and the real part of E lies close to pole, the S-matrix can be expressed in the form:

$$S_\ell = \exp(2i\delta_\ell^0)\frac{E - E_r - \frac{i\Gamma}{2}}{E - E_r + \frac{i\Gamma}{2}} \tag{2.51}$$

Using expressions (2.31) and (2.51) the following relation can be obtained:

$$\delta_\ell = \delta_\ell^0 + \delta_\ell^r, \tag{2.52}$$

wherein δ_ℓ^0 stands for *background* phase shift. The last term in the formula, δ_ℓ^r, is called the *resonance*

phase shift and it is expressed as:

$$\delta_\ell^r = \arctan \frac{\frac{1}{2}\Gamma}{E_r - E}. \tag{2.53}$$

Resonances are one of the most interesting phenomena of scattering theory and they are of high interest for this work. They are observed in atomic, nuclear, particle, molecular, and cluster physics. They manifest themselves in the total cross section, the eigenphase sum, and the time-delay (when these are investigated as a function of energy). A number of methods to identify and characterize resonances are available. Some of these methods will be briefly described below.

2.3.4 CROSS SECTION

The differential cross section is defined as the square of the modulus of scattering amplitude (see equations (2.23) and (2.35)):

$$\frac{d\sigma}{d\Omega} = |f(\theta,\phi)|^2 = \frac{1}{k^2}\left|\sum_{\ell=0}^{\infty}(2\ell+1)e^{i\delta_\ell}\sin\delta_\ell P_\ell(\cos\theta)\right|^2. \tag{2.54}$$

The total cross section is obtained by integration of the differential cross section over the solid angle giving

$$\sigma_{tot} = \int_0^{2\pi}\int_0^{\pi} |f(\theta,\phi)|^2 \sin\theta\, d\theta\, d\phi. \tag{2.55}$$

Substituting the expression for partial scattering amplitude $a_\ell = \frac{e^{2i\delta_\ell}-1}{2ik}$ into (2.23) and then into (2.54), the total cross section can be rewritten to form:

$$\sigma_{tot} = \sum_{\ell=0}^{\infty}\sigma_\ell = \frac{4\pi}{k^2}\sum_{\ell=0}^{\infty}(2\ell+1)\sin^2\delta_\ell. \tag{2.56}$$

For instance, the total elastic cross section is expressed in optical theorem by:

$$\sigma_{tot\_el} = 2\pi\int_0^{\pi}\frac{d\sigma}{d\Omega}\sin\theta\, d\theta = \frac{4\pi}{k}\,\mathrm{Im}\, f(0), \tag{2.57}$$

where $\mathrm{Im}\, f(0)$ is the imaginary part of scattering amplitude $f(\theta)$ for $\theta = 0$.

One way of identifying resonances is to look at cross sections. Resonances normally manifest themselves as peaks in the integral cross sections (though not always: see section 2.3.5). By making use of equations obtained in the previous section, the resonant cross section formula can be introduced. If the background phase shift δ_ℓ^0 from equation (2.52) is zero then from (2.56) and (2.53) the

expression for the partial wave cross section has the form

$$\sigma_\ell = \frac{4\pi}{k^2}(2\ell+1)\frac{\frac{1}{4}\Gamma^2}{(E-E_r)^2+\frac{1}{4}\Gamma^2}. \tag{2.58}$$

At the resonance energy, i.e when $E = E_r$ the partial wave cross section has its maximum value $4\pi(2\ell+1)/k^2$ and it decreases to zero when the energy is significantly below or above resonance energy.

In the case when the background phase shift δ_ℓ^0 from equation (2.52) cannot be neglected, the partial wave cross section is given by [92]:

$$\sigma_\ell = \frac{4\pi}{k^2}(2\ell+1)\sin^2\delta_\ell = \frac{4\pi}{k^2}(2\ell+1)\frac{(\frac{E-E_r}{\frac{1}{2}\Gamma}-\cot\delta_\ell^0)^2}{1+(\frac{E-E_r}{\frac{1}{2}\Gamma})^2}\sin^2\delta_\ell^0. \tag{2.59}$$

This equation implies that when the energy is $E = \frac{1}{2}\Gamma\cot\delta_\ell^0 + E_r$ the partial wave cross section σ_ℓ is zero and it achieves its upper limit when $E = -\frac{1}{2}\Gamma\cot^{-1}\delta_\ell^0 + E_r$. Fitting these expressions to the cross section could, in principle, allow us to determine E_r and Γ.

2.3.5 PHASE SHIFT

Another method to identify the presence of resonances is by investigating the phase shift (2.52). A resonance is characterised by a π radians jump in the eigenphase sum. The shape of the eigenphase sum when a resonance is present is described by the Breit-Wigner formula [93, 94] which is obtained by substituting (2.53) into (2.52):

$$\delta_\ell = \delta_\ell^0 + \delta_\ell^r = \delta_\ell^0 - \arctan\frac{\Gamma/2}{E-E_r}, \tag{2.60}$$

The resonant part of the phase shift δ_ℓ^r increases from 0 to π in the energy range of the resonance. The nearer the zero of the Jost function on the unphysical sheet ($\mathrm{Im}\,k < 0$) is to the real axis, the more suddenly δ_ℓ increases (with respect to the cross section, the smaller the imaginary part of equation (2.47), i.e. Γ, is the sharpest peak in the cross section).

Figure 2.9 illustrates how the change of the value of the constant background phase shift δ_ℓ^0 influences the shape of the partial cross section (2.59) near the resonance. These curves correspond to ideal cases. In practice, the picture is often more complicated (e.g. the background phase shift can change rapidly with energy and can completely mask the presence of resonance). Therefore, analysing resonances using the eigenphase method or looking at a cross section may not always yield accurate results.

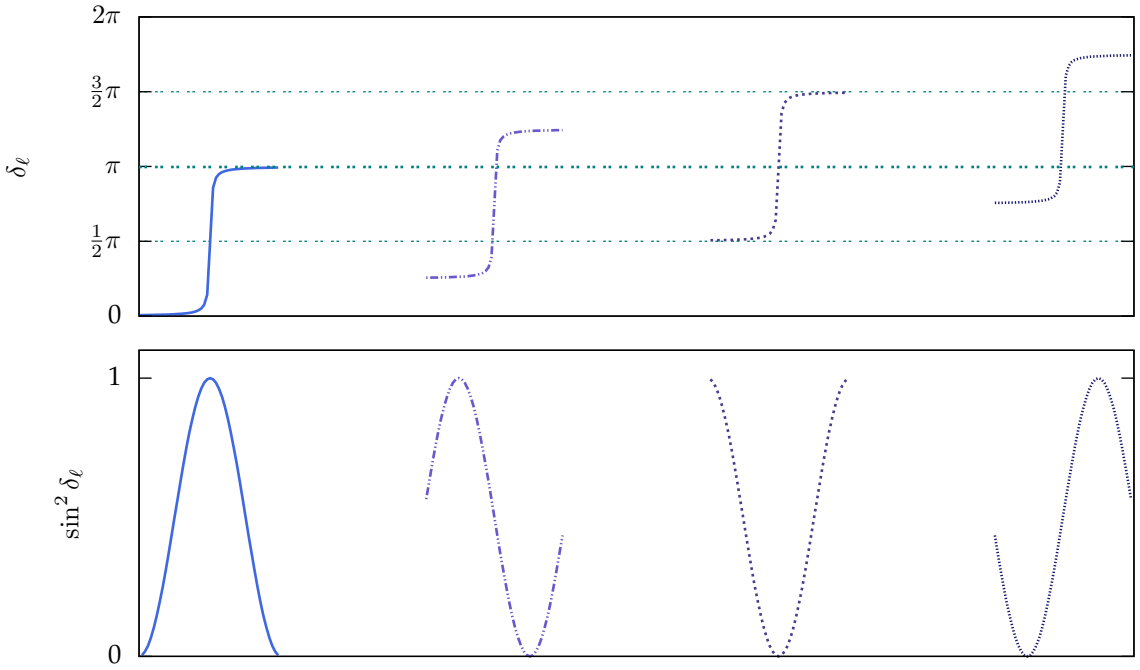

Figure 2.9: The total phase shift δ_ℓ (top panel) and the partial wave cross section σ_ℓ (bottom panel) plotted for four different values of the background phase shift δ_ℓ^0. The δ_ℓ plots show the resonant phase shifts for $\delta_\ell^0 = 0,\ \frac{1}{4}\pi,\ \frac{1}{2}\pi$ and $\frac{3}{4}\pi$. The plots in the bottom panel show the corresponding behaviour of the partial wave cross section. Picture adapted form [30].

2.3.6 MULTICHANNEL CASE

In the multichannel process a wave function, $\Psi^{\gamma^\Gamma_{j,\ell_j,m_j}}_{\gamma^\Gamma_{i,\ell_i,m_i}}$, which expresses the radial behaviour of the scattering projectile, is described by more indices than for single-channel case, since there are more possibilities in which state the projectile is before and after collision. The upper indices indicate the state of the system before collision and the lower subscripts the state after collision. The indices i and j correspond to the initial and final channels, respectively. The asymptotic form of the wave function is:

$$\Psi^{\gamma^\Gamma_{j,\ell_j,m_j}}_{\gamma^\Gamma_{i,\ell_i,m_i}}(r) \underset{r\to\infty}{=} \delta_{i,j}\delta_{\ell,\ell'}\delta_{m,m'}\Psi^{in}_{i,\ell_i}(r) + S^\Gamma_{i,\ell_i,m_i;j,\ell_j,m_j}\Psi^{s}_{j,\ell_j}(r) \tag{2.61}$$

where

$$\Psi^{\text{in}}_{i,\ell_i}(r) = \sqrt{\frac{2}{\pi k_i}}\exp(-i(k_i r - \ell_i\pi/2)), \tag{2.62}$$

$$\Psi^{\text{s}}_{j,\ell_j}(r) = \sqrt{\frac{2}{\pi k_j}}\exp(i(k_j r - \ell_j\pi/2)). \tag{2.63}$$

The S-matrix element is now generalized to a full matrix with elements $S^\Gamma_{i,l_i,m_i;j,l_j,m_j}$(E). It contains all information about the collision. It can be transformed to the T-matrix by the relation:

$$\mathbf{T}^{\Gamma} = \mathbf{S}^{\Gamma} - \mathbf{1}, \tag{2.64}$$

to obtain a cross-section for transition from state i to state j:

$$\sigma_{i\to j}(E) = \frac{\pi}{k_i^2} \sum_{\Gamma} \sum_{S} \sum_{l_i,l_j} \sum_{m_i,m_j} \frac{2S+1}{2(2s_i+1)} |T^{\Gamma}_{i,l_i,m_i;j,l_j,m_j}(E)|^2, \tag{2.65}$$

where S is the total spin of the system, s_i is the spin of the target state i and Γ indicates the irreducible representation of the point group of the molecule.

2.3.7 TIME-DELAY

The investigation of cross section and the eigenphase sum does not always lead to the identification of all resonances and/or their characterization. This is particularly true in the multichannel case. They are unreliably close to electronic thresholds; they fail when resonances are too wide and may not detect all resonances when these overlap. The method which deals well with these problems is time-delay analysis [95] which allows for a more effective identification, because, in this method, the background is completely separated from the resonance and resonances are separated from each other. Most of the results presented throughout this work are obtained using this method. The advantages of time-delay analysis over the standard methods have been discussed in many works, e.g.: Baccarelli *et al.* [96], Shimamura *et al.* [97].

The time-delay is defined as the difference of interacting and free sojourn time spent by a projectile within a distance a of a target in the limit of $a \to \infty$. The time-delay can also be understood as the excess of the particle density present in the region around the target compared to the situation when there would not have been any interaction, and then by dividing the excess by the total incoming flux through a closed surface at a distance far away from the target centre. The time-delay is calculated from the time-delay matrix Q-matrix and it is given by [95]:

$$t_D = Tr[\mathbf{Q}], \tag{2.66}$$

where:

$$\mathbf{Q}(E) = i\hbar \mathbf{S}^* \frac{d\mathbf{S}}{dE}. \tag{2.67}$$

is obtained from the S-matrix.

The most important information about the resonances is obtained from the analysis of the positive eigenvalues (this is why the time-delay is also called the positive eigenvalues of the Q-matrix) and related eigenvectors of the Q-matrix as a function of scattering energy. In many cases it is sufficient

only to consider the largest eigenvalues of the Q-matrix, c_{max}, which represents the time-delay deriving from channels with the largest time-delay. Considering only the largest eigenvalues (the longest time-delay) has an important advantage because this means that strongly varying but non-resonant contributions do not need to be taken into consideration. This is crucial for targets for which many channels are open.

At resonance energies, the dependence of c_{max} with E has a Lorentzian form given by:

$$c_{max}(E) = \frac{\Gamma}{(E - E_r)^2 + (\Gamma/2)^2}, \tag{2.68}$$

The eigenvectors of the Q-matrix corresponding to these largest eigenvalues also contain important information. The square of their coefficients – $|c_j|^2$ is equal to probability of decay of the metastable state into the jth channel. This is why they can be used to establish the parent state (the state of the target just before capture of scattering electron) of the resonance (excluding Feshbach resonances, because their parent states correspond to a closed channels for decay).

We can also distinguish, the opposite to the time-delay occurrence, a time-advance – the negative eigenvalues of the Q-matrix. In this situation the incoming electron can be accelerated by passing through a strongly attractive interaction region, or can be reflected by a strongly repulsive interaction. The time-advance can also be observed if the initial channel corresponds to an excited state of the target molecule. In this instance, the projectile can obtain additional energy by deexciting the target.

2.4 R-MATRIX THEORY

The R-matrix method is one of several methods used to solve scattering problems and it is the one used in this work. It was first introduced 1947 by E. P. Wigner and L. Eisenbud [98] to solve scattering problems in nuclear physics. The fundamental idea of this method is that the configuration space describing the projectile and target is divided into two regions: inner and outer region. The boundary between these regions is defined by an R-matrix sphere of radius a. In the internal region the problem is a many-body one and the interaction is strong. In the case of an electron scattering from atoms or molecules this region must contain all the electronic densities of the target states included in the calculation (must encompass the radial extent of the most diffuse orbital). In this region the scattering electron becomes indistinguishable from the electrons of the target and both exchange and correlation effects must be included. This makes the inner region calculation complex and only solvable numerically. In the outer region the interaction is weak and, in many cases, it is exactly solvable. In this region the scattering electron is distinguishable from the target electrons and exchange and correlation effects can be neglected. The inner region data is used as boundary conditions to solve

the outer region problem. From the known solution in the outer region, the K-matrix and thus the S-matrix and cross sections, can be calculated. In turn, from the S-matrix the time-delay can be obtained, which allows one to determine resonance parameters (these can also be obtain directly from the K-matrix).

The R-matrix method was developed and extended by many scientists. Comprehensive reviews of the theory and their applications in molecular physics have been written by P. G. Burke [92], P. G. Burke and K. A. Berrington [99], P. G. Burke and W. D. Robb [100] and J. Tennyson [101]. In order to explain the basics of the R-matrix method the approach in this work we proceed as in [21]. First the theory is presented for potential scattering followed by the case of electron-molecule scattering.

2.4.1 POTENTIAL SCATTERING

Here, as in section 2.3, the simplest scattering case is used: the scattering of a structureless particle by a short-range spherically symmetric central field, described by the time-independent Schrödinger equation (2.10) in the single channel case. The potential satisfies the same conditions defined by (2.16-2.18), i.e. it is negligible in the region $r \geq a$. As it was before, a is the radius where the short-range potential vanishes, but here, additionally, it also means the R-matrix radius, i.e. the radius which defines the boundary between inter and outer regions. It will be shown that the division between the two regions is crucial in order to solve the scattering problem using the R-matrix method.

The radial equation (2.14) from the section 2.3.1 is here rewritten in the form:

$$[\mathcal{H} - E]\, u_\ell(k, r) = 0, \tag{2.69}$$

where $E = k^2$ and $\mathcal{H}$ is:

$$\mathcal{H} = -\frac{d^2}{dr^2} + \bar{V}(r) + \frac{\ell(\ell+1)}{r^2}. \tag{2.70}$$

In section 2.3.1 the solution of the time-independent Schrödinger equation (2.27) was written in terms of the S-matrix element and Hankel functions. In the R-matrix approach the radial function is described using Bessel (j_ℓ) and Neumann (n_ℓ) functions and the K-matrix instead of the S-matrix,

$$\frac{u_\ell(k, r)}{r} = j_\ell(kr) + K_\ell n_\ell(kr), \tag{2.71}$$

where the K-matrix is related to S-matrix, in single channel case, as follow:

$$S_\ell = (1 + \mathrm{i}K_\ell)(1 - \mathrm{i}K_\ell)^{-1}. \tag{2.72}$$

It has been already shown that $S_\ell = \exp(2i\delta_\ell)$ (2.31). By imposing this relationship and operating

on (2.72), the K-matrix is simply given by:

$$K_\ell = \tan \delta_\ell. \tag{2.73}$$

The K-matrix element is an energy-dependent constant and can be determined by imposing continuity of the logarithmic derivatives of the solution at $r = a$:

$$\left.\frac{du_\ell(k,r)/dr}{u_\ell(k,r)}\right|_{r=a} = \left.\frac{d(j_\ell(kr) + K_\ell n_\ell(kr))/dr}{j_\ell(kr) + K_\ell n_\ell(kr)}\right|_{r=a}. \tag{2.74}$$

By finding the solution $u_\ell(k,r)$ for $r \leq a$ and solving equation (2.74) the value of K_ℓ can be determined and that gives a complete solution of equation (2.69) for whole range of r. Also, by determining K_ℓ, relevant observables can easily be obtained (e.g. partial wave cross sections).

The $u_\ell(k,r)$ in the region $r \leq a$ is calculated numerically and has to satisfy the boundary condition:

$$u_\ell(k,0) = 0. \tag{2.75}$$

In the region $r \to \infty$, $u_\ell(k,r)$ (2.71) has form of asymptotic Bessel and Neumann functions:

$$\begin{aligned} u_\ell(k,r) \quad &\underset{r\to\infty}{\sim} \quad \sin\left(kr - \frac{\ell\pi}{2}\right) + K_\ell \cos\left(kr - \frac{\ell\pi}{2}\right) \\ &= \quad \sin\left(kr - \frac{\ell\pi}{2}\right) + \frac{\sin\delta_\ell}{\cos\delta_\ell}\cos\left(kr - \frac{\ell\pi}{2}\right) \\ &\propto \quad \sin\left(kr - \frac{\ell\pi}{2} + \delta_\ell\right). \end{aligned} \tag{2.76}$$

In order to determine K_ℓ advantage is taken of the fact that the general solution of equation (2.69) for the external region, i.e. $r \geq a$, is known and the fact that at the boundary $r = a$ the solution of equation (2.69) in the outer region has to be equal to the solution for inner region, i.e. it has to fulfil condition (2.74). In general, in the region where the potential is non-zero, an analytical solution does not exist. To obtain the solution for this region, the R-matrix method will be used, in which the radial wave function $u_\ell(k,r)$ is expanded in an energy-independent basis, the so-called *R-matrix basis functions*, $U_i(r)$:

$$u_\ell(k,r) = \sum_{i=1}^{\infty} A_i(E) U_i(r), \qquad r \in \langle 0, a\rangle. \tag{2.77}$$

In practice the summation above is over some finite number n big enough to obtain an accurate description of $u_\ell(k,r)$. Due to the fact that the method to obtain the basis sets is known, the problem of determining the radial functions $u_\ell(k,r)$ (2.77) reduces to finding the coefficients $A_i(E)$ for each energy*.

*It will be later shown that even less than that is needed to solve the scattering problem.

The fact that the radial functions are expanded in terms of the basis set implies the need to determine the matrix elements of the Hamiltonian in this basis set. Since the basis set is defined only in the inner region, the Hamiltonian (2.70) is nonhermitian [100, 101, 21]. The nonhermicity can be removed by adding an extra operator to the Hamiltonian. This operator derived by Bloch [102] is called the *Bloch operator* and is defined as:

$$\mathcal{L} = \frac{1}{2}\delta(r-a)(\frac{d}{dr} - \frac{b}{r}), \tag{2.78}$$

where $\delta(r-a)$ stands for the Delta function, a is the radius of R-matrix sphere and b is an arbitrary constant which is often taken as zero. The Hamiltonian containing the Bloch operator is hermitian and it is expressed as:

$$\widetilde{\mathcal{H}} = \mathcal{H} + \mathcal{L}. \tag{2.79}$$

The basis functions in expression (2.77) are eigenvectors of this new operator,

$$\widetilde{\mathcal{H}} u_i(r) = E_i U_i(r), \tag{2.80}$$

and can be expand in the arbitrary basis, $\{v_j(r)\}_{i=1}^{n}$ (it is essential for the R-matrix method that the functions $v_j(r)$ do not vanish at $r = a$):

$$U_i(r) = \sum_{j=1}^{n} c_{ij} v_j(r), \tag{2.81}$$

with the c_{ij} coefficients obtained by diagonalizing the matrix of elements, $\langle v_i(r)|\widetilde{\mathcal{H}}|v_j(r)\rangle$.

By substituting the new Hamiltonian (2.79) into (2.69), the radial function is given by:

$$u_\ell(k,r) = (\mathcal{H} + \mathcal{L} - E)^{-1}\mathcal{L} u_\ell(k,r). \tag{2.82}$$

But the radial function for the internal region is expand in terms of R-matrix basis functions (2.77), thus:

$$\sum_{i=1}^{\infty} A_i(E) U_i(r) = (\mathcal{H} + \mathcal{L} - E)^{-1}\mathcal{L} u_\ell(k,r). \tag{2.83}$$

By multiplying the equation from the left by the basis function $U_k(r)$, integrating over the inner region and inserting the explicit form of the Bloch operator, the formula for the coefficients $A_i(E)$ is determined:

$$A_i(E) = \frac{1}{2}\frac{U_i(a)}{E_i - E}\left(\frac{d}{dr}u_\ell(k,r)\bigg|_{r=a} - \frac{b}{a}u_\ell(k,a)\right), \tag{2.84}$$

where b is the arbitrary constant that comes from the Bloch operator. The expression (2.77) at the

boundary $r = a$ can be now rewritten in terms of the coefficients (2.84):

$$u_\ell(k,a) = \frac{1}{2a}\sum_{i=1}^{\infty}\frac{U_i(a)U_i(a)}{E_i - E}\left(a\frac{d}{dr}u_\ell(k,r)\Big|_{r=a} - bu_\ell(k,a)\right). \tag{2.85}$$

The term before the brackets defines the R-matrix:

$$R(E) = \frac{1}{2a}\sum_{i=1}^{\infty}\frac{U_i(a)U_i(a)}{E_i - E}. \tag{2.86}$$

The equation (2.85) can be rewritten using the R-matrix definition:

$$u_\ell(k,a) = R(E)\left(a\frac{d}{dr}u_\ell(k,r)\Big|_{a} - bu_\ell(k,a)\right). \tag{2.87}$$

Performing simple manipulations of this equation, e.g. taking $b = 0$, dividing both sides by $u_\ell(k,a)$ and matching the solutions of outer and inner region, i.e. for $r = a$ by substituting equation (2.74), the coefficient $K_\ell(E)$ is obtained:

$$K_\ell = \frac{j_\ell(ka) - aR(E)\frac{dj_\ell(kr)}{dr}\big|_{r=a}}{aR(E)\frac{dn_\ell(kr)}{dr}\big|_{r=a} - n_\ell(ka)}. \tag{2.88}$$

2.4.2 ELECTRON-MOLECULE SCATTERING

In this subsection the R-matrix method, described in the previous section, is applied to electron-molecule scattering. The aim of the previous subsection was to introduce the main definitions and become familiar with the procedure. However, replacing a potential with a many-electron molecular target vastly complicates the problem. Many processes may take place during a collision and the multiplicity of channels has to be taken into account. In order to illustrate these electronic processes, the R-matrix basis functions are chosen to reflect them as accurately as possible. That selection is not trivial, and influences the quality of the scattering calculations.

INNER REGION

In this region, we describe the full scattering wave function $\Psi_E^\Gamma(\mathbf{x}_1,\ldots,\mathbf{x}_{N+1})$ in terms of basis functions (similarly to (2.77)) $\Psi_k^\Gamma(\mathbf{x}_1,\ldots,\mathbf{x}_{N+1})$:

$$\Psi_E^\Gamma(\mathbf{x}_1,\ldots,\mathbf{x}_{N+1}) = \sum_k A_k(E)\Psi_k^\Gamma(\mathbf{x}_1,\ldots,\mathbf{x}_{N+1}), \tag{2.89}$$

where $\mathbf{x}_i$ denotes the three spatial and spin coordinates of i-th electron; N is the number of target electrons. The spatial part of $\mathbf{x}_i$ coordinate can be indicated by $[x_i, y_i, z_i]$ and linked with spherical coordinates by the relation: $[r_i, \theta_i, \varphi_i] = [\sqrt{x_i^2 + y_i^2 + z_i^2}, \arccos\left(z_i/\sqrt{x_i^2 + y_i^2 + z_i^2}\right), \arctan\left(y_i/x_i\right)]$.

The R-matrix basis functions Ψ_k^Γ are energy-independent and the energy dependence of the total wave function, Ψ_E^Γ, is contained in the coefficients $A_k(E)$. The index Γ runs over all irreducible representation of the point-group of the molecule and includes the appropriate total spin. The basis functions can be expanded using the *Close-Coupling approximation*:

$$\Psi_k^\Gamma(\mathbf{x}_1,\ldots,\mathbf{x}_{N+1}) = \mathcal{A}\sum_{i=1}^{n_b}\sum_{j=1}^{n_{c,i}}\Phi_i(\mathbf{x}_1,\ldots,\mathbf{x}_N)\gamma_{ij}(x_{N+1})a_{ijk} + \sum_{i=1}^{m}\chi_i^\Gamma(\mathbf{x}_1,\ldots,\mathbf{x}_{N+1})b_{ik}, \tag{2.90}$$

where $\mathcal{A}$ guarantees the antisymmetrization of the whole wave function. The functions $\Phi_i(\mathbf{x}_1,\ldots,\mathbf{x}_N)$ describe bound electronic states of the molecular target; the number of states included is indicated by n_b. The functions $\gamma_{ij}(\mathbf{x}_{N+1})$ describe the unbound (scattering) electron and are the only single-particle functions which do not vanish on the surface of R-matrix sphere. The last functions in the expression (2.90), $\chi_i^\Gamma(\mathbf{x}_1,\ldots,\mathbf{x}_{N+1})$, are L^2 integrable functions that describe the short-range correlation polarization effects. The radial extent of these functions, as well as Φ_i, must be contained inside the R-matrix sphere. A good description of polarization is essential to obtain accurate resonance parameters as well as accurate cross sections at low energy. The coefficients a_{ijk} and b_{ik} are analogous to the coefficients c_{ij} in the formula (2.81). The choice functions describing target, $\Phi_i(\mathbf{x}_1,\ldots,\mathbf{x}_N)$ (type and number of states, n_b) and L^2 functions of (2.90) establish a *scattering model*. These scattering models are described in more detail in section 2.5.

The functions $\gamma_{ij}(\mathbf{x}_{N+1})$ are called *continuum function*, and inside the R-matrix sphere are expressed as:

$$\gamma_{ij}(\mathbf{x}_{N+1}) = \frac{u_{\ell_{ij},m_{ij}}(r_{N+1})}{r_{N+1}}Y_{\ell_{ij},m_{ij}}(\Omega_{\mathbf{r}_{N+1}}). \tag{2.91}$$

where $\mathcal{Y}_{\ell_{ij},m_{ij}}(\Omega_{\mathbf{r}_{N+1}})$ are real solid spherical harmonics [103]. Inside the R-matrix sphere the continuum is described using a combination of GTOs sitting on the centre of mass and on the atoms. The index i enforce that only those spherical harmonic which couple with the target state i are considered.

On the grounds of the fixed-nuclei approximation (in which nuclei neither rotate nor vibrate) , the kinetic energy terms for the nuclei can be ignored and the Hamiltonian for the system, denoted as H_{N+1}, has the form:

$$H_{N+1} = \sum_{i=1}^{N+1}\left(-\frac{\nabla_i^2}{2} - \sum_{k=1}^{N_A}\frac{Z_k}{\rho_{kj}}\right) + \sum_{i>j}^{N+1}\frac{1}{r_{ij}} + \sum_{k>l}^{N_A}\frac{Z_kZ_l}{R_{kj}}, \tag{2.92}$$

where Z_k denotes the charge of the nucleus k and R_{kl} is the distance between the nuclei k and l. The distance between the electron j and the nucleus k is denoted by ρ_{kj} and r_{ij} is the distance between the electrons i and j.

The Bloch operator for this system is expressed:

$$L = \frac{1}{2}\sum_{i=1}^{N+1}\sum_{j=1}^{n_{ch}} |\Phi_j Y_{l_j,m_j}(\hat{\mathbf{x}}_i))\delta(r_i - a)\left(\frac{d}{dr_i} - \frac{b-1}{r_i}\right)(\Phi_j Y_{l_j,m_j}(\hat{\mathbf{x}}_i)| \tag{2.93}$$

where j runs over all n_{ch} scattering channels, which are defined as: $\langle\Phi_j Y_{l_j,m_j}(\hat{\mathbf{x}}_i)|$; a is the R-matrix radius; b is the arbitrary constant mentioned in previous subsection (see equation 2.78), and Y_{l_j,m_j} are spherical harmonics. The angled brackets are replaced by round brackets to indicate that the integration implied by the brackets is performed over the inner region only.

The steps to obtain the R-matrix are similar to those described in the previous subsection (equations 2.78-2.85). Therefore the final form is presented here:

$$R_{ij}(E) = \frac{1}{2a}\sum_k \frac{w_{ik}(a)w_{jk}(a)}{E_k - E}, \tag{2.94}$$

where E_k is a R-matrix pole, while $w_{ik}(a)$ is a surface amplitude defined as:

$$w_{ik}(a) = \left(\Phi_i Y_{l_i,m_i}\frac{1}{r_{N+1}}\middle|\Psi_k\right)_{r=a}, \tag{2.95}$$

where again the brackets indicate that the integration is performed only over the inner region angular coordinates of the $N+1$ electron. The radial integration is not performed, and the resulting radial wave function is evaluated at $r = a$.

OUTER REGION

The outer region wave function, i.e. for $r_{N+1} \geq a$, is expressed as:

$$\Psi(\mathbf{x}_1,\ldots,\mathbf{x}_{N+1}) = \sum_{j=1}^{n_{ch}} \Phi_j(\mathbf{x}_1,\ldots,\mathbf{x}_N)\frac{u_j(r_{N+1})}{r_{N+1}}Y_{l_j,m_j}(\Omega_{\mathbf{r}_{N+1}}). \tag{2.96}$$

The function u_j satisfies the equation:

$$\left(\frac{d^2}{dr^2} - \frac{l_i(l_i+1)}{r^2} + k_i^2\right)u_i(r) = 2\sum_{j=1}^{n_{ch}}\sum_{\lambda=0} a_{ij\lambda}r^{-\lambda-1}u_j(r), \tag{2.97}$$

where $k_i = \sqrt{2(E-E_i)}$, and E_i is a channel energy, and the coefficients $a_{ij\lambda}$ are related to the multipole moments of the molecule target.

As in the previous subsection, the K-matrix can be obtained by matching the solutions $u_i(r)$ in the asymptotic region $r \to \infty$ to the scattering boundary conditions in each channel (equation 2.88). After that we can link the S-matrix and T-matrix with the K-matrix:

$$\mathbf{T} = 2\mathrm{i}\mathbf{K}(\mathbf{1} - \mathrm{i}\mathbf{K})^{-1}, \tag{2.98}$$

$$\mathbf{S} = (\mathbf{1} + \mathrm{i}\mathbf{K})(\mathbf{1} - \mathrm{i}\mathbf{K})^{-1}. \tag{2.99}$$

2.5 SCATTERING MODELS

In this work, results will be presented for calculations based on three standard scattering models. The quality of calculations depends on the chosen model and this choice depends on their purpose; it will be shown that for comparison of the scattering calculation between two different targets more control is given by the simplest model (for this purpose it is important to ensure that comparison is "like-with-like"). The simplest method may be sufficiently good for that, but to obtain calculations which may predict or recreate experimental measurements, more sophisticated methods are required.

STATIC EXCHANGE MODEL

The most basic scattering model among those described here is the *Static Exchange* (SE) approximation. In this model the target is described at the Hartree-Fock level and only the ground state of the target is included in expansion (2.90). Polarization effects are not included, that is the target is not allowed to be polarized in the presence of the incoming electron. The expression for the L^2 function in equation (2.90) can be written as:

$$\chi_i^{SE} : (\text{ground state})^N(\text{virtual})^1, \tag{2.100}$$

where the 'ground state' label means the Hartree-Fock ground state configuration. The orbitals which are indicated by the 'virtual' label, specify a subset of those HF orbitals (see section 2.1) that are unoccupied in the ground state configuration (in other words the 'virtual orbitals' indicate orbitals which are unoccupied in the ground state description of the target, 'N' system, and can be occupied in the 'N+1' system). Since polarization effect are not considered, the only possible configurations are with the incoming electron in one of the virtual orbitals.

STATIC EXCHANGE PLUS POLARIZATION MODEL

In the *Static Exchange plus Polarization* (SEP) model only the ground state, described at HF level, is taken into account in equation (2.90). At this level of approximation the molecule is allowed to be polarized by the incoming electron. Because of that the molecule is permitted to polarize, one electron from the valence space can be promoted to one of the virtual orbitals. This effect is described by the L^2 functions, χ_i:

$$\chi_i^{SEP} : (\text{core})^{N_d}(\text{valence})^{N-N_d-1}(\text{virtual})^{1+1}, \tag{2.101}$$

where N_d is the number of frozen electrons. The core orbitals of the molecule are always doubly occupied by the N_d electrons (see section 2.1). The valence orbitals are those occupied in the ground

state from which single excitation are allowed. There is no simple way to choose the optimal number of the virtual orbitals. If too few of them are used the quality of the calculations can be poor. On the other hand, if too many are used the calculations can be 'overcorrelated' (i.e. the effect of giving a better description of the scattering wave functions than those of the target). To find this optimal number, the calculations are performed with a various number of the virtual orbitals (chosen with an increasing energy order).

CLOSE-COUPLING MODEL

In the *Close-Coupling* (CC) model the eigenfunctions Ψ_k^Γ, expressed by (2.90) also include target electronic excited states (but only those which are energetically closely-coupled). The main problem using this method is taking care of quality in the description of the N-electron target wave functions, Φ_i, and the $(N+1)$-electron scattering wave function, Ψ_k^Γ. This requires good balance between the choice of the target configuration interaction (see section below) model and the L^2 functions contained in (2.90). For these calculations the complete active space (CAS) configuration interaction representation of the target wave function was chosen. With this choice, it has been shown [104] that the L^2 function for the CC model for molecules with large polarizabilities should be as follows:

$$\chi_i^{CC} : \begin{cases} (\text{core})^{N_d}(\text{CAS})^{N-N_d+1}, \\ (\text{core})^{N_d}(\text{CAS})^{N-N_d}(\text{virtual})^1, \end{cases} \tag{2.102}$$

where CAS expresses the orbitals of the active space, that together with the 'core' orbitals are chosen in accordance to the physical problem they suppose to describe. In the first set of configurations in (2.102) the scattering electron occupies an orbital describing the target. In the second set, the scattering electron occupies a virtual orbital.

2.6 UKRMOL+ SUITE AND COMPLEMENTARY TOOLS

In this section the software used to carry out the R-matrix calculations is described. The software, called the UKRmol+ suite, is a re-engineered version of UKRmol suite (see flowcharts in appendix A) with many new features. The UKRmol suite was developed for a couple of decades; a description of it can be found in [107]. The new software, like its predecessor, is divided into two subsets of programs: UKRmol+in (previously UKRmol-in) and UKRmol-out (which remains the same). The subsets perform, respectively, the calculations linked to the inner and outer region in the R-matrix method. Additionally, some of the UKRmol+in programs are also used to perform target calculations, as it was the case in the UKRmol-in suite.

The main new feature of this suite is that all the programs dealing with integrals and orbitals in the UKRmol suite have been replaced with one program called SCATCI-INTEGRALS implemented by Z. Mašín. The fundamental advantage of this program for the calculations described in this work is that it allows one to use more partial waves in the calculations than UKRmol, which is limited in practice to partial waves with $\ell_{max} \leq 5$. The other advantages are more practical: the UKRmol+ suite is more compact (SWEDEN-based programs: SWMOL3, SWORD, SWEDMOS and SWTRMO as well as GAUSPROP and GAUSTAIL[†] are replaced by SCATCI-INTEGRALS), it requires fewer input variables and the code can be complied using either double or quadruple precision. Moreover, the code is implemented both for serial and parallel execution of the programs. It is also more flexible in use, i.e. calculation can be performed either in spherical or Cartesian coordinates. The disadvantage of the new suite is that it requires a MOLDEN file (which provides orbitals of a calculated system) as an input for the SCATCI-INTEGRALS program, which can be only obtain using external software, for instance, MOLPRO which is commercial software (UKRmol can also use MOLPRO output or generate its own HF orbitals or pseudo-natural orbitals). Additionally the UKRmol+ suite is still being developed in order to replace the GTOs describing the continuum by a mixed GTO and B-spline basis set [108].

The programs used to carry out the target calculations are indicated in figure 2.10 and those used to perform inner region calculations are shown in figure 2.11. The target calculations are performed first. To perform calculations using UKRmol+ first MOLPRO is invoked. It needs, as input, the geometry of the investigated molecule and the GTO target basis set which can be given explicitly and

[†]These programs are only the parts of UKRmol suite and are not explained in this work. Their description can be found in [107]. The names are given only as an indication of the changes made between UKRmol and UKRmol+ suites.

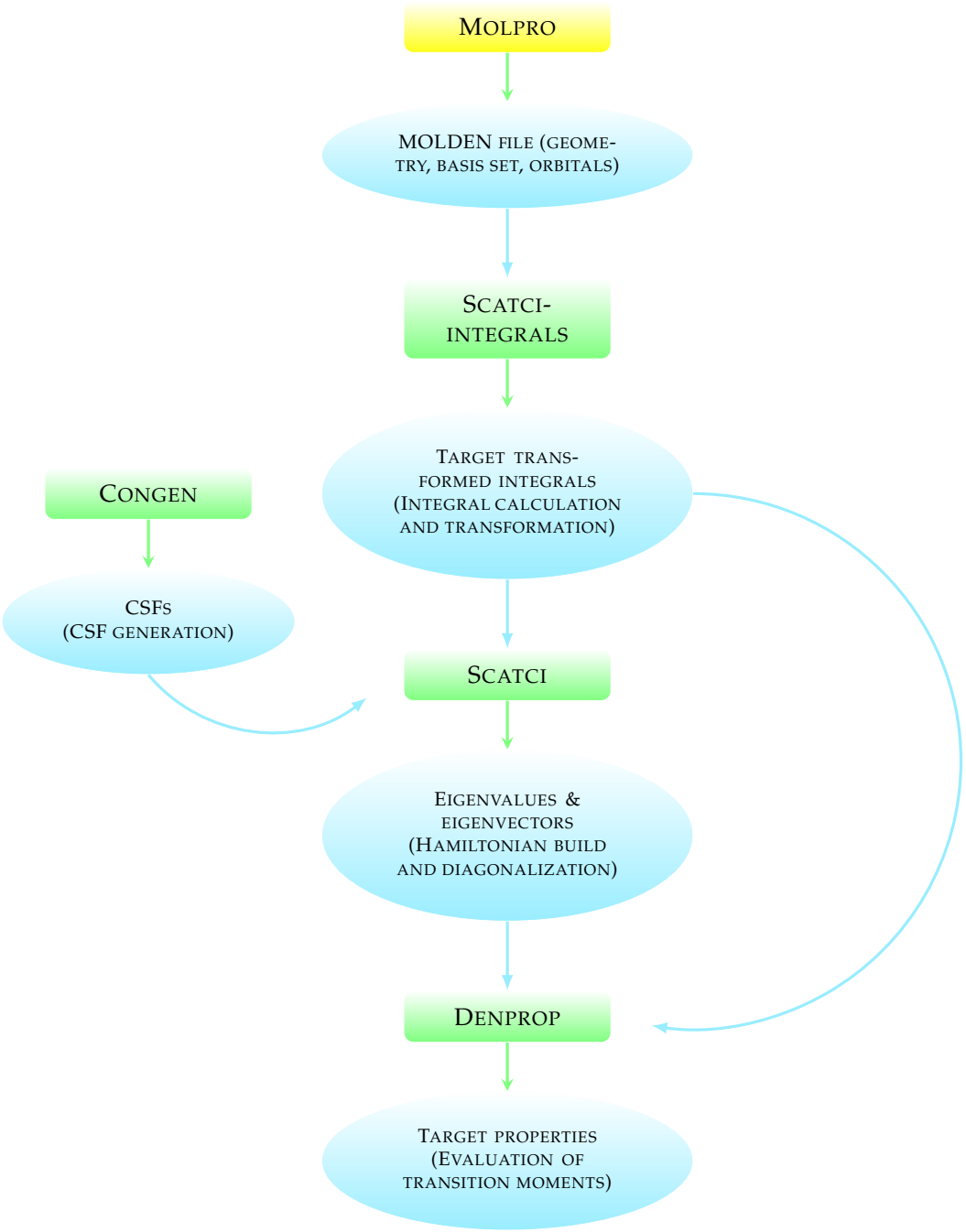

Figure 2.10: A flowchart of the UKRmol+ programs called in target calculations. The green boxes indicate programs in the suite; the yellow boxes indicate programs which are not part of the UKRmol+ suit. The blue boxes indicate the main output/input of the different programs. See main text for more details.

can be found in the literature (for example on the website [105]) or simply by specifying the name of the basis set in the input file. MOLPRO is a quantum chemistry software suite that can determine, among other things, molecular orbitals. This program is very versatile, it is capable of generating not only HF orbitals but also CASSCF (and other types) of orbitals. SCATCI-INTEGRALS performs the orthogonalization of the orbitals and calculates and transforms the integrals over the elementary

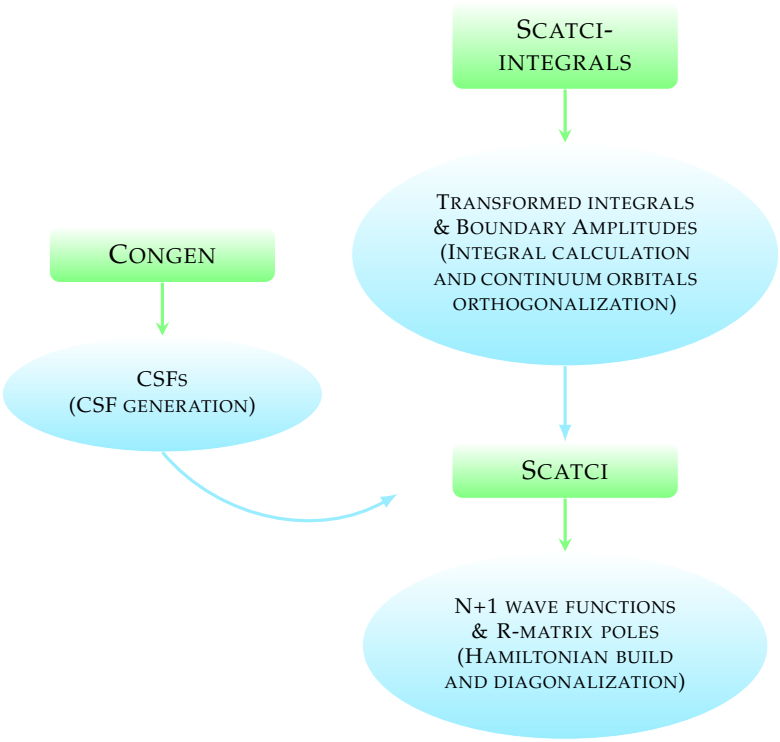

Figure 2.11: The sequence of programs called in the inner region calculations (the meaning of the boxes is the same as in figure 2.10). See main text for more details.

atomic GTOs into integrals over the target molecular orbitals (previously done by SWORD, SWEDMOS, SWTRMO). It also computes the property integrals (previously done by GAUSPROP) required by DENPROP. CONGEN generates the configuration state functions (CSFs), which are used in the CI description of the target. The next program is SCATCI that builds and diagonalizes the Hamiltonian matrix for the system using output from CONGEN and SCATCI-INTEGRALS. The property integrals calculated by SCATCI-INTEGRALS, along with SCATCI output, are needed to run DENPROP, the last program in target part of calculation, which gives as an output the target properties i.e. dipole and quadruple permanent and transition moments, which are necessary to perform the outer region calculations.

The inner region calculations use the same (but not all) programs as the target calculations. In this case the SCATCI-INTEGRALS input is increased by a continuum GTO basis set describing the scattering electron [109]. This program calculates the 'tail' integrals (between the boundary of R-matrix sphere and infinity) in order to obtain the inner region integrals (previously done by GAUSTAIL). In an inner region calculation, SCATCI-INTEGRALS (previously done by SWEDMOS) performs two orthogonalizations, first, the continuum basis set to the target orbitals, second, the continuum orbitals among themselves. CONGEN generates the CSFs for the R-matrix basis functions (2.90). The coefficients a_{ijk}, b_{ik} and the poles, E_k of the R-matrix basis functions (2.90) are obtained by the diagonalizing Hamiltonian, in SCATCI. SCATCI-INTEGRALS also allows one to calculate all necessary integrals at once. Using the MOLDEN file from MOLPRO, all target and inner region integrals can

be obtained in a single step.

The flowchart for outer region calculations is illustrated in figure 2.12. The first program in this

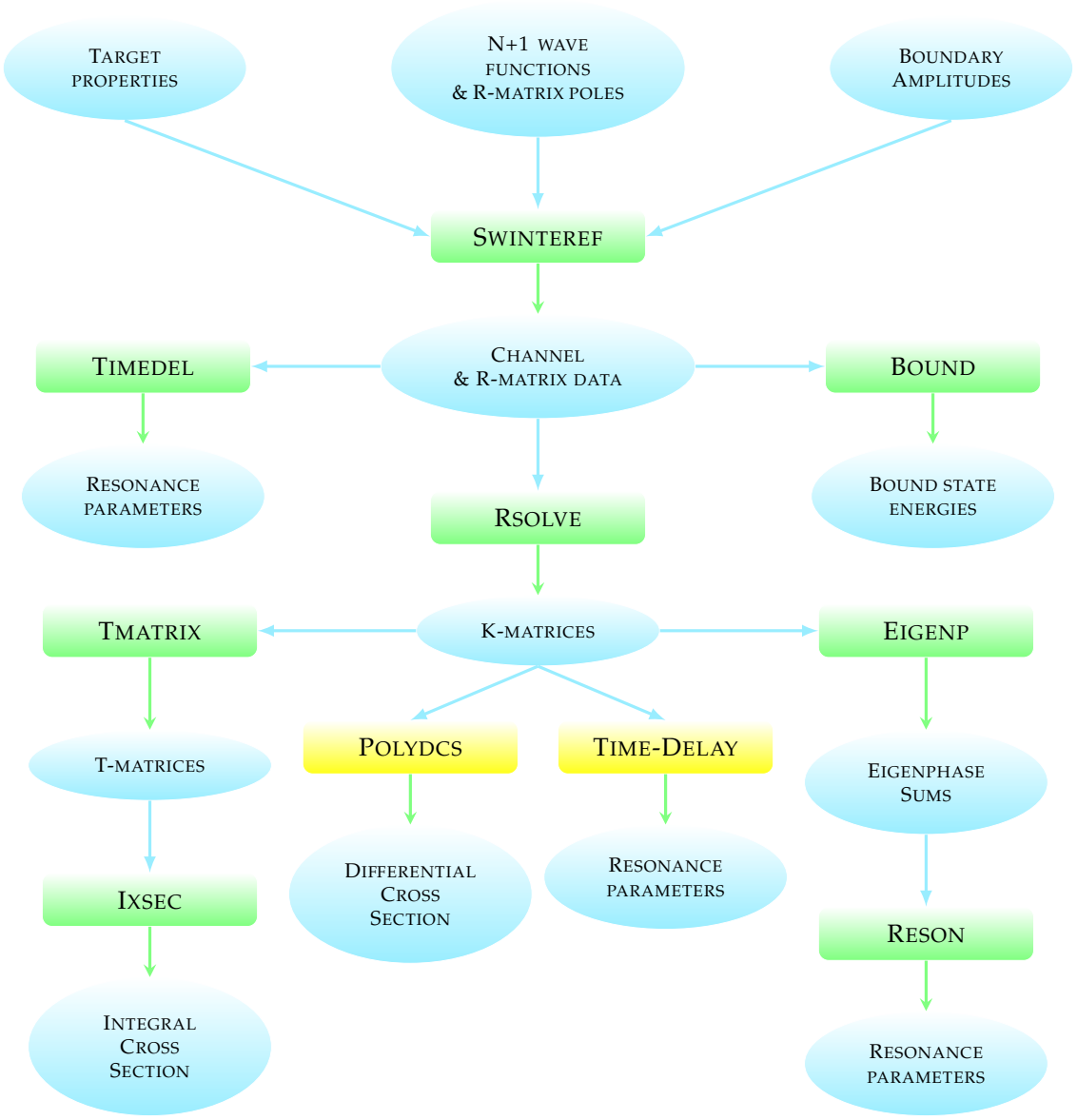

Figure 2.12: The sequence of programs called in the outer region calculations (the meaning of the boxes is the same as in figure 2.10). The flowchart is adapted from [107]. See main text for more details.

suite is SWINTERF. This program requires data from the target and inner region calculations (i.e. the target properties, raw boundary amplitudes, eigenvectors and R-matrix poles) and generates data about channels and that is needed to build the R-matrix (i.e. the boundary amplitudes). BOUND calculates the energies of bound states of the $N+1$ electron system. RSOLVE generates the K-matrices, EIGENP calculates eigenphases sums by diagonalizing the K-matrix, TMATRX builds T-matrices and IXSEC produces the integral elastic and inelastic cross section. Both RESON and TIMEDEL use the K-matrices data to determine accurate resonance parameters, i.e. the position and the width, by two different methods. Unlike inner region calculations, not all programs have to be invoked to perform

outer regions ones. In this case the user specifies which program to run depending on what one is interested in. Both inner and outer region programs can be found in the CCPForge repository [110].

To perform the calculations included in this work other programs were used, which are not part of UKRmol/UKRmol+ suite, or like RADDEN are tools which may be run additionally. To carry out any scattering calculation an appropriate value of the R-matrix radius must be chosen. This choice is not trivial and it is crucial for the quality of the calculation. In order to choose the value of the R-matrix radius a complementary program, RADDEN, was created by Z. Mašín, which calculates the radial charge densities of the target orbitals. That allows the user to select a radius for which the charge density is negligible small. HAMDIAG performs the parallel diagonalization of Hamiltonian. It is invoked after SCATCI, which, in this case, only builds the Hamiltonian without diagonalizing it. TIME-DELAY was also created by Z. Mašín on the basis of TIMEDEL. TIME-DELAY is not as functional as its predecessor but it is easier to run and its performance is much quicker than that of TIMEDEL.

The K-matrices data can be input into POLYDCS [111] (developed by N. Sanna and F. Gianturco and external to UKRmol suite of codes) to obtain elastic differential cross section (DCS) for a chosen range of energies. Additionally, the program calculates a Born correction for the elastic DCS and integral cross section to account for the partial waves not included in the *ab initio* calculation. Moreover, rotationally elastic and state-to-state rotationally inelastic cross section can be calculated. The last program on the flowchart is BORNCROS, which can be used to obtain the Born correction for the electronically inelastic cross section.

In order to perform calculations using UKRmol software more efficiently a perl script was written by K. Houfek and developed and adapted for the UKRmol+ suite by the author of this thesis. The main future of the script are presented in appendix A.2.

3

ELECTRON COLLISIONS WITH PYRIDINE

Pyridine has been chosen as a molecule to study because it is similar to diazines which have been theoretically investigated in the R-matrix group at The Open University. Therefore the knowledge collected during the study of diazines was used to perform the calculation for pyridine. Also, comparison of pyridine and the diazines would allow us to investigate how the presence of only one nitrogen in the benzene ring influences the characteristics of resonances. Moreover, the Molecular Clusters experimental group at The Open University led by S. Eden indicated an interest in performing measurements of electron attachment to small pyridine-water clusters. Their experimental set up will enable them to Stark select clusters (in terms of their dipole/mass ratio) and will therefore allow them to investigate in detail the effect of hydrogen bonding on (dissociative) electron attachment (see section 1.1). Our plan was to determine complementary theoretical data (resonance positions and widths) that would hopefully provide further insight into the DEA process. In addition, due to the approximate description of polarization effects in our models (see section 2.5), the comparison with experiment would provide us with a tool to 'tune' our calculations. Unfortunately, these experiments are yet to be carried out.

Last but not the least, pyridine is similar to DNA pyrimidinic bases because of its 6 member ring structure (in the case of the shape resonances, the incoming electron is trapped into the π^* orbitals, which are ring orbitals), but it is far less computationally demanding; pyridine possesses higher symmetry and fewer electrons than any of DNA bases (e.g. thymine possesses 66 electrons, that is

36% more than pyridine). Therefore pyridine is interesting to investigate as a biological prototype of DNA basis.

3.1 PYRIDINE CHARACTERISTICS

Pyridine is a basic heterocyclic organic compound*, its chemical formula is C_5H_5N and the structure of this molecule is shown in the figure 3.1. A CH group in benzene is replaced by nitrogen which has a non-bonding pair of electrons. Pyridine has 42 electrons; the orbitals in the ring do not differ significantly from those of benzene (see, table B.1, in appendix B) and there are still the six π-electrons from the three double bonds in the aromatic structure.

At room temperature pyridine is liquid, with density close to that of water, i.e. 0.9819 g/cm^3; pyridine is colourless and possesses a specific odour. Its vertical ionization energy is around 9.51 eV [112], the first electronic excitation threshold is around 4 eV [113], its dipole moment is 2.19 Debye [114] and its spherical polarizability is 64 a_0^3 [115]. This molecule is an asymmetric top but with only 5% difference between two of its rotational constants it can be approximated as a symmetric top; it belongs to the C_{2v} point group.

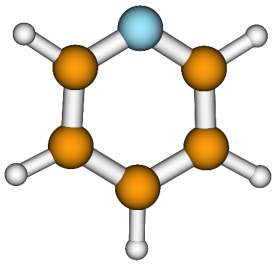

Figure 3.1: Geometrical structure of the pyridine molecule. In the figure the orange balls represent carbon, blue - nitrogen and white - hydrogen. Generated using MOLDEN.

The structures of benzene, pyridine and pyrimidine are similar (a comparison between the three molecules is given in appendix B, in order to show how a presence of nitrogen changes the resonance characteristic). In appendix B, in figure B.1 the sixty lowest energy HF orbitals with are listed (all the orbitals included in the scattering calculations – 21 orbitals describe the HF ground state of the target and 39 are virtual orbitals – are listed in that table). Here, as an example, the LUMO (*lowest unoccupied molecular orbital*) and LUMO+1 of these molecules are tabulated in figure 3.2, to show how additional nitrogen replacing one of the carbons from the ring, changes the orbitals. The changes in shape between the orbitals of three molecules are not significant (the pyrimidine orbitals are slightly more compact than those of the other molecules; pyrimidine bond-lengths changed not more than

*Heterocyclic compounds are organic compounds (those containing carbon atoms in ring formation), with at least one atom other than carbon, in the ring system.

0.5% from those of pyridine), but it should be noticed that the shape of pyridine LUMO corresponds to LUMO+1 for benzene and pyrimidine, i.e. the order of the orbitals is not the same.

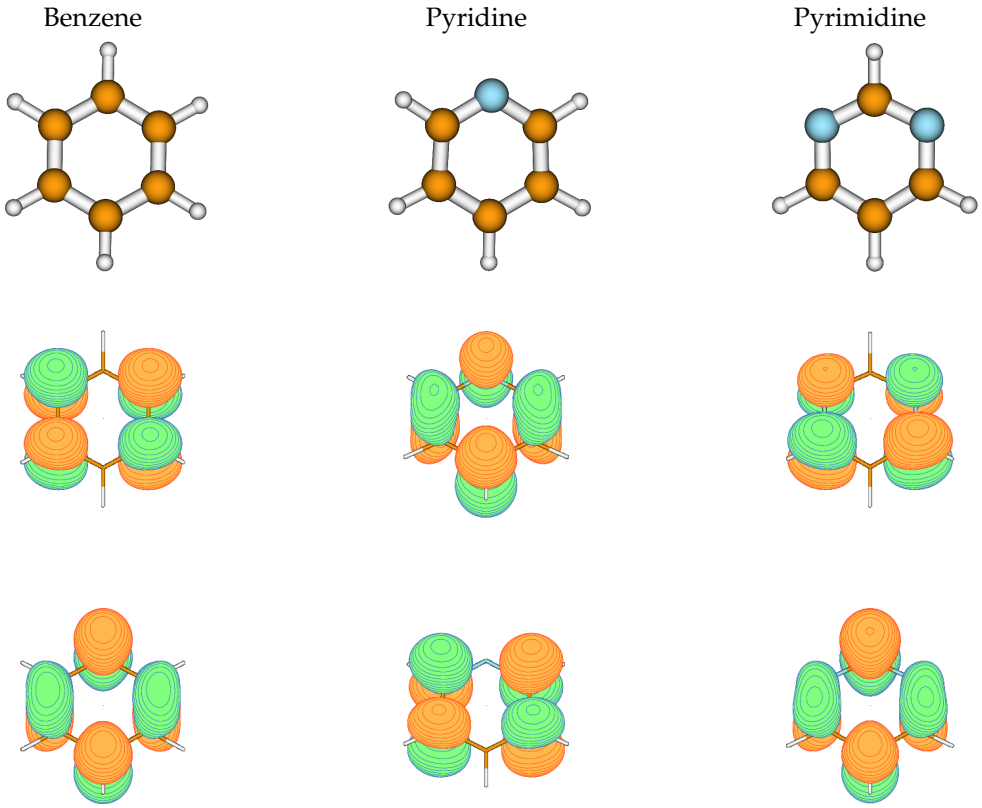

Figure 3.2: In the first row, geometrical structures of the benzene, pyridine and pyrimidine molecule are presented. In the second and third row, the LUMO, and LUMO+1 of benzene, pyridine and pyrimidine molecule, respectively. The LUMO of benzene is of e_{2u} symmetry, the pyrimidine LUMO and the pyridine LUMO+1 orbitals are of a_2 symmetry; the LUMO+1 of benzene is of b_{2u} symmetry while the pyrimidine LUMO+1 and the pyridine LUMO are of b_1 symmetry. Generated using MOLDEN.

3.2 CALCULATION DETAILS

3.2.1 TARGET

In order to perform R-matrix calculations, a set of parameters describing target and scattering models has to be specified. Most of the parameters describing the target, e.g. the ground state equilibrium geometry and basis set, remain the same for all scattering models used for pyridine calculations. If the parameters are not defined at the beginning of a section describing a scattering model, it means that they remain the same as are defined here.

Two ground state equilibrium geometries have been tested: there were no differences in the scattering results between the equilibrium geometries optimised at the QCISD and MP2 level [112] so the first one was chosen. Due to the similarities in the structure and properties between diazines and pyridine, the characteristics of the calculations for diazines were adopted to perform our calculations. The basis sets were chosen in accordance with earlier work undertaken by Z. Mašín as the most appropriate to study diazines [23]. Namely, the selected basis sets are: a compact one, cc-pVDZ, and a diffuse one, 6-311+G**.

	level	cc-pVDZ	6-311+G**	Acc. value
E	HF	-246.71	-246.75	-248.37
	CASSCF	-246.78	-246.82	
μ	HF	2.22	2.43	2.19
	CASSCF	2.90	3.07	

Table 3.1: Energy (in Hartree) and dipole moment (in Debye) of the ground state of pyridine calculated at the HF and CASSCF level, using the basis sets indicated in the table. These values are compared with the theoretical value of the ground state energy calculated at the B3LYP level using 6-311+G(3df,2p) basis set [112] and the experimental magnitude of dipole moment [114].

CASSCF target orbitals are generated using the State-Averaged Complete Active Space Self Consistent Field (SA-CASSCF) method, available in MOLPRO, (the method is described in [116]). In this approach the target electronic states are expressed as a combination of Configuration State Functions (CSFs), where HF orbitals are represented by single CSF (2.3). In order to get the states with vertical excitation energies lying below ~ 10 eV, in reasonable agreement with more accurate *ab initio* calculations (these values are labelled 'Best est.' in tables 3.2 and 3.3, and correspond to best estimates based on calculations obtained by Schreiber *et al.* and their survey of literature data [113]), a few tests have been performed. In the tests different number of states (always those with lowest energies were chosen) and active space were tested. In table 3.2 are tabulated the vertical excitation thresholds for some tested State-Averaged and Active Space (much more tests with different combinations of State-Averaged and Active Space have been performed, here are shown only a few of them).

The main properties (i.e. ground state energy and dipole moment) of pyridine obtained from our calculations are listed in table 3.1. It can be seen that the ground state energies obtained in our calculations for both models with both basis sets are not very good, comparing with the accurate energy (the energies obtained at HF and CASSCF level differ from the accurate value by $\sim 0.6 - 0.7\%$ both for compact and diffuse basis set). The calculated values of dipole moment are not very good either[†]. The best agreement with experimental value of dipole moment was obtained using HF orbitals with compact basis set (it differs by $\sim 1.4\%$ compare to experimental value; for diffuse basis set at HF level it differs by $\sim 11\%$; the dipole moment calculated at CASSCF level is $\sim 32\%$

[†]Improving these properties increases the size of scattering calculation and therefore unable us to perform them. Fortunately in the past calculations with poor description of the target were performed and still gave a reliable information about scattering problems.

and $\sim 40\%$ higher compared with the experimental value, for the compact and diffuse basis sets, respectively). The dipole moment is important in the scattering description, because it influences the long-range electron-molecule interaction.

To perform the SA-CASSCF calculations 17 of the 33 electronic excited states (including the ground state) included in the Close-Coupling calculation, were optimised. That is, the set of states: S[3,2,2,2], T[2,2,2,2] (the notation is explained in the caption of table 3.2) have been chosen. In the active space 10 electrons are allowed to occupy 8 orbitals (that can be denote as: CAS(10,8)), the set of orbitals are indicated as A[1,4,1,2] in table 3.2.

Basis set			compact						diffuse		
State-Averaged			S[2,2,2,2], T[1,1,1,1]			S[3,2,2,2], T[2,2,2,2]			S[3,2,2,2], T[2,2,2,2]		
Active Space			A[1,4,1,2]	A[1,3,1,2]	A[1,4,0,2]	A[1,4,1,2]	A[1,3,1,2]	A[1,4,0,2]	A[1,4,1,2]	A[1,3,1,2]	A[1,4,0,2]
state	Best est.	exp.									
$1\,^3A_1$	4.06	3.8[a]	5.02	4.53	3.85	3.86	4.54	3.85	3.82	4.52	3.81
$1\,^3B_1$	4.25	4.1[a]	4.80	4.37	4.69	4.85	4.49	4.72	4.82	4.77	4.69
$1\,^1B_1$	4.59	4.59[b]	5.36	5.02	5.26	5.41	5.14	5.29	5.37	5.45	5.24
$1\,^3B_2$	4.64		5.00	5.24	4.99	4.99	5.23	4.99	4.93	5.22	4.93
$1\,^1B_2$	4.85	4.99[c]	4.96	5.92	4.98	4.96	5.90	4.95	4.90	5.85	4.90
$2\,^3A_1$	4.91		3.85	5.68	5.02	5.01	5.62	5.01	4.97	5.70	4.96
$1\,^1A_2$	5.11		6.35	6.37	6.23	6.42	6.54	6.25	6.42	6.13	6.23
$1\,^3A_2$	5.28		6.28	6.20	6.17	6.34	6.37	6.18	6.34	6.14	6.16
$2\,^3B_2$	6.08		7.27	7.12	7.27	7.25	7.06	7.25	7.19	7.26	7.19
$2\,^1A_1$	6.26	6.38[c]	8.20	7.94	8.21	8.18	7.89	8.19	8.09	8.03	7.16
$3\,^1A_1$	7.18		8.59	9.58	8.55	8.56	9.55	8.53	8.48	9.54	8.10
$2\,^1B_2$	7.27	7.22[c]	8.24	9.04	8.24	8.23	9.05	8.22	8.17	9.18	8.16
μ		2.19[d]	3.02	3.53	3.26	2.90	3.34	3.29	3.07	3.15	3.44
$E_{g.s.}$	-248.37[e]		-246.78	-246.75	-246.78	-246.78	-246.75	-246.78	-246.82	-246.79	-246.82

Table 3.2: Vertical excitation energies, in eV, obtained using different sets of states in the State-Averaged procedure and different orbitals in the Active Space; also given best estimate based on calculations obtained by Schreiber *et al.* and their survey of literature data [113] (Best est.), together with experimental (exp.) results, in eV. In the last two rows a dipole moment (μ), in Debye, and ground state energy ($E_{g.s.}$), in Hartree, are presented, respectively. The notation 'S[2,2,2,2]' and 'T[1,1,1,1]' means that, in respective, two singlet (S) states and one triplet (T) state of each irreducible representation have been optimised in the State-Averaged procedure (the numbers in the squired brackets indicate number of states per irreducible representation — for C_{2v} point group, the numbers correspond to a_1, b_1, b_2, a_2 irreducible representation, respectively). In the next column Active Space (A) are presented, the numbers in squared brackets stand for number of orbitals per symmetry which are used in Active Space. The listed vertical excitation energies have been performed for two sets of states used in State-Averaged procedure for compact basis set and one set for diffuse basis set; and for three different sets of Active Space.
The superscripts indicated the source of these values: [a]reference [117], [b]reference [118], [c]reference [119], [d]reference [114], [e]B3LYP/6-311+G(3df,2p) [112]

The vertical excitation thresholds for all states included in the CC expansion are listed in table 3.3. All our calculated vertical excitation thresholds, except the first one, are higher than the best estimate values ('Best est.' listed in table 3.3). The values of vertical excitation thresholds calculated with the diffuse basis set give slightly better agreement with the best estimate values. The values for the compact basis set are higher than (or equal to) those for the diffuse one but the differences are small, i.e. smaller than 0.14 eV. The thresholds for the five lowest excited states for both compact and diffuse basis sets are in fairly good agreement with the best estimate values; the differences are not higher than ± 0.6 eV. The agreement gets worse as the vertical excitation threshold increases. This agreement is similar to that obtained for the diazines [18].

No.	Symmetry	cc-pVDZ	6-311+G**	Best est.
2	$1\,^3A_1$	3.86	3.82	4.06
3	$1\,^3B_1$	4.85	4.83	4.25
4	$1\,^1B_2$	4.96	4.90	4.85
5	$1\,^3B_2$	4.98	4.93	4.64
6	$2\,^3A_1$	5.01	4.97	4.91
7	$1\,^1B_1$	5.41	5.37	4.59
8	$1\,^3A_2$	6.34	6.34	5.28
9	$1\,^1A_2$	6.42	6.42	5.11
10	$3\,^3A_1$	7.24	7.18	
11	$2\,^3B_2$	7.25	7.19	6.08
12	$3\,^3B_2$	7.79	7.73	
13	$2\,^1A_1$	8.18	8.09	6.26
14	$2\,^1B_2$	8.23	8.17	7.27
15	$3\,^1A_1$	8.56	8.48	7.18
16	$2\,^3B_1$	9.26	9.23	
17	$2\,^1B_1$	9.46	9.42	
18	$3\,^3B_1$	9.56	9.50	
19	$3\,^1B_2$	9.79	9.70	
20	$2\,^3A_2$	9.83	9.78	
21	$4\,^1A_1$	9.98	9.86	
22	$2\,^1A_2$	10.17	10.11	
23	$4\,^3B_1$	10.36	10.33	
24	$3\,^1B_1$	10.63	10.60	
25	$3\,^3A_2$	10.85	10.79	
26	$4\,^3A_1$	11.01	10.93	
27	$4\,^3A_2$	11.05	10.96	
28	$4\,^3B_2$	11.10	10.99	
29	$3\,^1A_2$	11.25	11.15	
30	$5\,^1A_1$	11.94	11.83	
31	$4\,^1B_1$	12.03	11.97	
32	$4\,^1A_2$	12.10	12.03	
33	$4\,^1B_2$	12.95	12.81	

Table 3.3: Vertical excitation thresholds in eV, for all states included in the CC calculation, calculated at CASSCF level using a CAS(10, 8) active space for the basis sets indicated in the table. The values labelled 'Best est.' are the same as in table 3.2.

3.2.2 SCATTERING

Among other parameters which enter the specification of an R-matrix scattering calculation are the R-matrix radius a and the maximum value of the angular momentum of the continuum partial waves. For calculations with the compact basis set, an R-matrix radius $a = 13a_0$ was used and in this case the effect of including an extra partial wave ($\ell_{max} = 5$) was tested. In the case of the diffuse basis set, the radius $a = 18a_0$ was chosen as the most appropriate; the continuum basis sets included $\ell_{max} = 4$ partial wave. These values of the radius were chosen by analysing the radial charge densities of the target obtained by RADDEN (see section 2.6), above the chosen radius the charge density was negligible; the same values were also the optimal ones for diazines [21].

The calculations were carried out for three different scattering models, the *Static Exchange* approximation, the *Static Exchange plus Polarization* approximation and for *Close-Coupling* approximation. Table 3.4 lists all parameters used to carry out the calculations for SE, SEP and CC models.

Scattering model	SE	SEP		CC	
Basis set	cc-pVDZ	cc-pVDZ	6-331+G**	cc-pVDZ	6-331+G**
R-matrix radius	$13a_0$	$13a_0$	$18a_0$	$13a_0$	$18a_0$
No. of target states	1	1	1	33	33
Target description	HF	HF	HF	CAS(10,8)	CAS(10,8)
No. of virtual orbitals	20	35	50	60	80
Deletion threshold	10^{-7}	10^{-7}	$(1; 1.8; 8; 1.5)\times10^{-7}$	10^{-7}	10^{-7}
Equilibrium geometry	QCISD	QCISD	QCISD	QCISD	QCISD

Table 3.4: The calculation details used in our work for the SE, SEP and CC scattering models. The number of virtual orbitals were chosen as the values for which the positions of resonances best agreed with experimental results; the equilibrium geometry was taken from [112]. Deletion threshold refers to a value of eigenvalues of continuum orbitals below which they are deleted from the calculation (in order to avoid linear dependence problems). If only one value is specified for the deletion threshold, it means that the same value was used for each irreducible representation, if there are four values it means that different deletion threshold for each irreducible representation are used (i.e. respectively, A_1, B_1, B_2, A_2).

3.3 CROSS SECTIONS

3.3.1 SE MODEL

SE results tend to be qualitative rather than quantitative, the resonances appear at much higher energies than experimentally, due to the lack of polarization (see section 2.5). The method does not give reliable resonances features, i.e. positions, widths (on the grounds that polarization always stabilises the position of resonance, one can know that in reality the position of resonances are lower than those obtained by this method). In the SE approximation, the target is in its ground state and relaxation,

in the presence of the scattering electron, is not allowed, i.e. the incoming electron may only occupy one of the empty virtual orbital while the target remains in the ground state. However, as it will be explained later, it is (at the moment) the best model to compare resonance characteristics of isolated molecule and clusters. The method is likely to be sufficient to see how resonance is affected when the target is bound with water, at least for small clusters (T. C. Freitas *et al.* show that calculations at SE level gives similar results as at SEP level [27]). Calculations for SE level have therefore been performed for this reason and these results are presented in Chapter 4. In this subsection only some results are introduced to present the main feature of this model and for the sake of comparison with other models.

Figure 3.3 shows the integral elastic cross sections (IECS) for electron scattering from pyridine calculated for 20, 30, 35 and 40 virtual orbitals (v.o.) with the compact basis set and partial waves up to $\ell_{max} = 6$. The inclusion of some virtual orbitals is essential for the description of resonances (see equation 2.100) but increasing the number of v.o. does not change significantly the IECS nor resonance energies, as can be seen in figure 3.3; only at higher energies there is a very slight change in the calculated cross section.

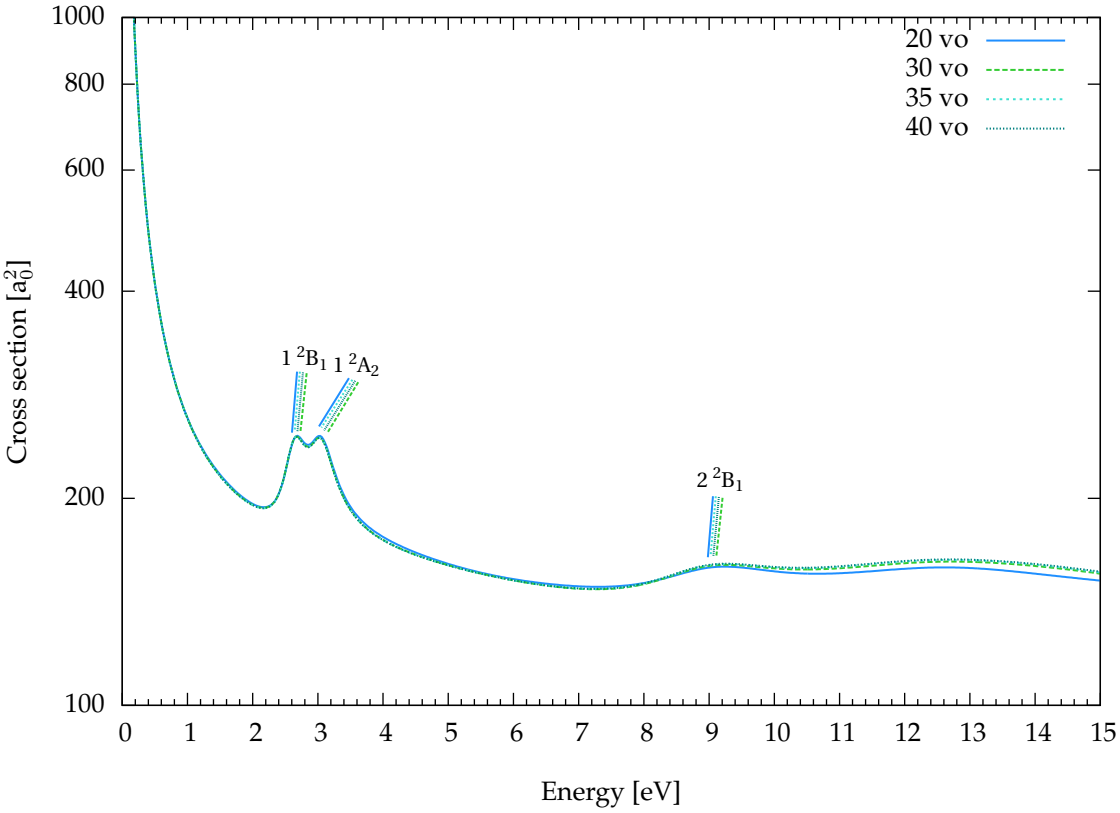

Figure 3.3: Integral elastic cross sections for electron scattering from pyridine calculated for 20, 30, 35 and 40 virtual orbitals as indicated in the figure with the compact basis set.

3.3.2 SEP MODEL

The theoretical results of low-energy electron collision with isolated pyridine at the SEP level presented in this subsection have already been published [120]. The same lines of argumentation are presented here. Taking advantage of the fact that calculations for the same target at the same level of approximation have been performed by Barbosa *et al.* [121] using the Schwinger multichannel method, both results are compared.

In order to describe short-range correlation-polarization effects, the type of L^2 configurations (χ_i) presented by equation (2.101) is used. In this case, $N = 42$ is total number of electrons in pyridine and $N_d = 12$ is the number of frozen electrons. To find the optimal number of virtual orbitals, the calculations were first performed with a small number of the lowest energy virtual orbitals. The number was augmented by adding more orbitals in increasing energy order until good agreement with the experimental positions (Nenner and Schulz [85]) of the π^* resonances was achieved. The optimal number of virtual orbitals for the compact basis set was — 35 and for diffuse basis set — 50; for diazines it is respectively, 35 and 40 virtual orbitals. The fact that in the case of pyridine a larger number of virtual orbitals is required for the diffuse basis set, than in case of pyrimidine, can be attributed to pyridine orbitals being some what more diffuse than those of the diazines (because pyridine has one fewer nitrogen than the diazines). Nevertheless, the different number of virtual orbitals does not change the cross section significantly and these changes are smaller than the differences in the cross sections between compact and diffuse basis sets.

Pyridine is a dipolar molecule, therefore the IECSs were calculated with use of the Born approximation, in order to include partial waves which are excluded from the *ab initio* calculations to reduce the computational expense. Figure 3.4 presents:

- The integral elastic cross sections (IECSs), both Born corrected (rotationally summed) and uncorrected (i.e. determined exclusively with the UKRmol suite); each calculated with compact and diffuse basis sets. The calculations have been performed for $\ell_{max} \leq 4$.
- For the compact basis set, there are results with $\ell_{max} = 5$.
- The integral elastic cross sections for energies up to about 12 eV calculated with the Schwinger multichannel method, both *ab initio* and Born corrected, obtained by Barbosa *et al.* [121].

Besides the three resonances, appearing very clearly as peaks for all the models plotted in the figure, there is one more feature, characteristic of R-matrix SEP calculations. Namely, above the first excitation threshold very narrow spikes are present in the R-matrix cross section. They are called pseudo-resonances, because they have no physical meaning (i.e. they do not correspond to physical resonances). They appear due to the fact that the L^2 correlation functions χ_i^Γ (second expansion

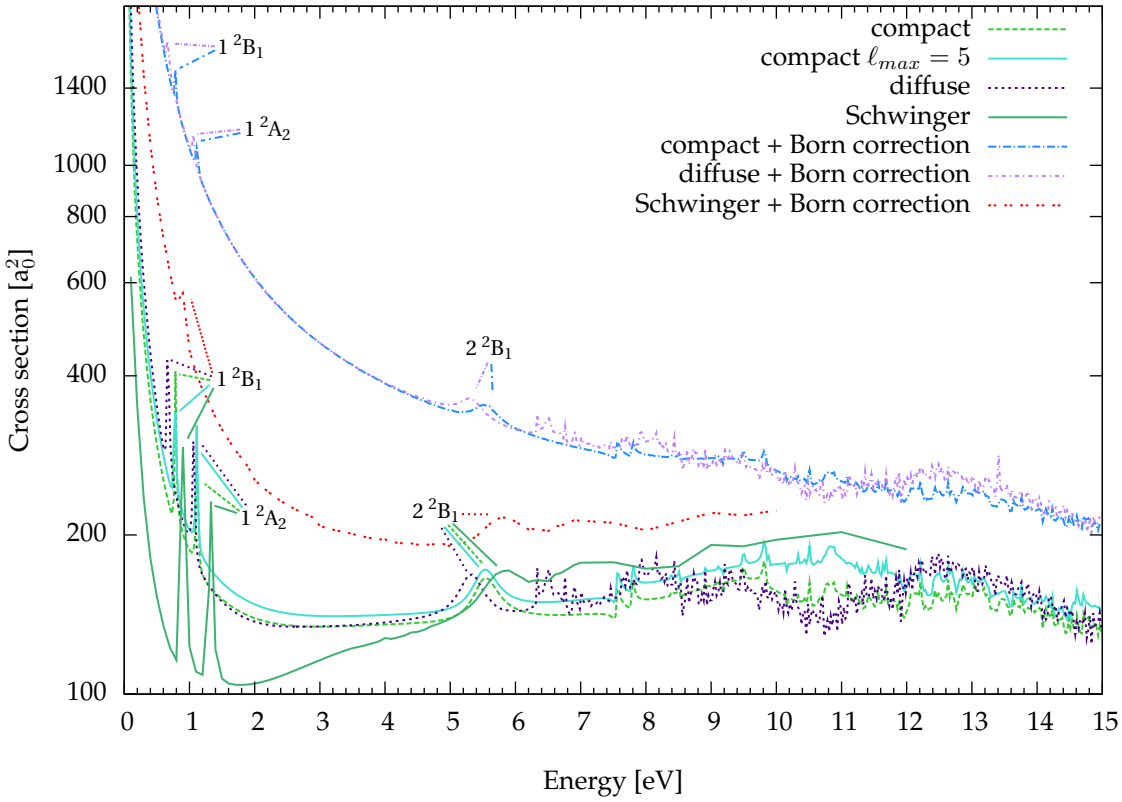

Figure 3.4: Integral elastic cross sections for electron scattering from pyridine calculated using: the R-matrix method with the compact and diffuse basis sets, and the Schwinger multichannel method obtained by Barbosa *et al.* [121]. The cross sections labelled 'Born correction' incorporate a Born-based correction; the one labelled $\ell_{max} = 5$ contains the extra partial wave.

in 2.90) allow for additional correlation effects not included in the target description (first expansion in 2.90). (In other words, the square integrable function includes target eigenstates which are not present in the target representation.)

Inspecting figure 3.4, the conclusion is that the cross sections obtained using the R-matrix method, both for compact and diffuse basis sets, have very similar shape. The main difference is that for the diffuse basis set the resonance positions are slightly shifted toward lower energy and in the 2-3 eV range the uncorrected cross section for the diffuse basis set displays a small decrease. The Born-closure procedure does not change the positions of resonance, it only increases the magnitude of the cross section. Furthermore, including an extra partial wave in the R-matrix calculation, this also increases cross section but does not change the positions of resonance, either.

The main differences, easily visible in figure 3.4, are between the R-matrix and Schwinger results. The uncorrected Schwinger cross section is significantly different in shape (even ignoring the differences caused by the pseudo-resonances) and displays resonances in slightly higher positions to the R-matrix calculation. Below 5 eV, the uncorrected Schwinger cross section is smaller than the R-matrix one. The differences between the R-matrix and Schwinger cross sections could be due to the

use of different basis sets, different number of partial waves, different configurations for the expression of the short-range polarization or caused by fact that R-matrix calculations do not include the polarization potential in the outer region. Similar differences have been observed in the shape of the cross sections for the nondipolar pyrazine obtained with both of these methods and were explained by the differences in the description of the polarization [21]. Therefore it is the most likely cause too.

The corrected Schwinger cross section is much smaller than the R-matrix one in the whole energy range. The difference is explained by fact that the Schwinger integral cross section is obtained in a different way from the R-matrix one. Namely, the Schwinger integral cross section is determined by integrating the corresponding EDCS between 1° and 180°, whereas the R-matrix cross sections correspond to the integration over the whole angular range (but they are obtained using an analytic formula: $\sigma = \sigma^B + 4\pi(A_0 - A_0^B)$, where the subscript B denotes that the relevant quantity is calculated using the Born Series approximation and the A_0 coefficients are described in [122]). The 'slightly' different integration ranges may cause such big differences, because the EDCS is extremely big between the 0° and 1°. To confirm the fact that these differences come from the integration regions, the following test has been performed for 6 eV: R-matrix EDCS in the range 1° to 180° were integrated, resulting in a cross section around 187 a_0^2 (for 0° to 180° is around 319 a_0^2). For the same energy the value of the corrected Schwinger cross section is 211 a_0^2. The difference between these two values for the uncorrected R-matrix and the Schwinger methods is the same. This indicates that the difference in the corrected cross sections is mainly due to the different integration ranges. The fact that EDCS is huge for the small angle can be emphasized by fact that to get the integral cross section (see, equation 2.57), the expression $\frac{d\sigma}{d\Omega}\sin(\theta)$ was integrated and in spite being very big even where $\sin(\theta) \approx 0$ for small θ (0° and 1°). It is also worth noting that to converge the numerical integration, an extremely fine angle resolution is necessary. This means that the corrected cross sections differ mainly because of the integration ranges. Nevertheless, very recently, the problem of the elastic cross section behaviour at small angles has been discussed [123]: the conclusion reached was that corrected R-matrix results for angles close to 0° may be overestimated. Since there is no experiment which can provide data for such small angles, there is no easy method to confirm that.

Differences between the corrected and uncorrected R-matrix and Schwinger multichannel cross sections are also visible at higher energies. The trend of R-matrix cross section above 1 eV is decreasing while the Schwinger cross sections tend to increase. In order to investigate the behaviour at higher energies, the cross sections obtained by the methods discussed above together with cross section obtained using *IAM-SCAR* method (independent atom representation – screening corrected additivity rule) [124, 125, 126] and *IAM+Rotations* method (independent atom representation complemented with inclusions of rotation) [127, 128, 129, 130, 131] are plotted in figure 3.5.

The IAM-SCAR and IAM+Rotations methods can be applied to electron-scattering over a broad

energy range, ∼10-1000 eV. However, they are inaccurate for energies much lower than 30 eV, so it is not surprising that the IAM-SCAR cross section is significantly different from both other ones for low energies. The IAM+Rotations cross section gives fairly similar results to corrected the R-matrix method in the energy range around 1-15 eV. Since the IAM methods are not designed for low-energy electron collisions and do not include quantum effects, the peaks that correspond to resonances are absent in the IAM-SCAR and IAM+Rotations cross sections. Starting from around 6 eV, the corrected and uncorrected R-matrix cross section have a fairly similar trend to the IAM+Rotations and IAM-SCAR cross section, respectively. This indicates that an extrapolation of the R-matrix cross section is possible for the higher energy range. Similar agreement has been obtained for pyrimidine [132]. The cross section for pyrimidine and pyridine are similar since their dipole moment is fairly similar as well (that of pyrimidine is 2.334 D [133]).

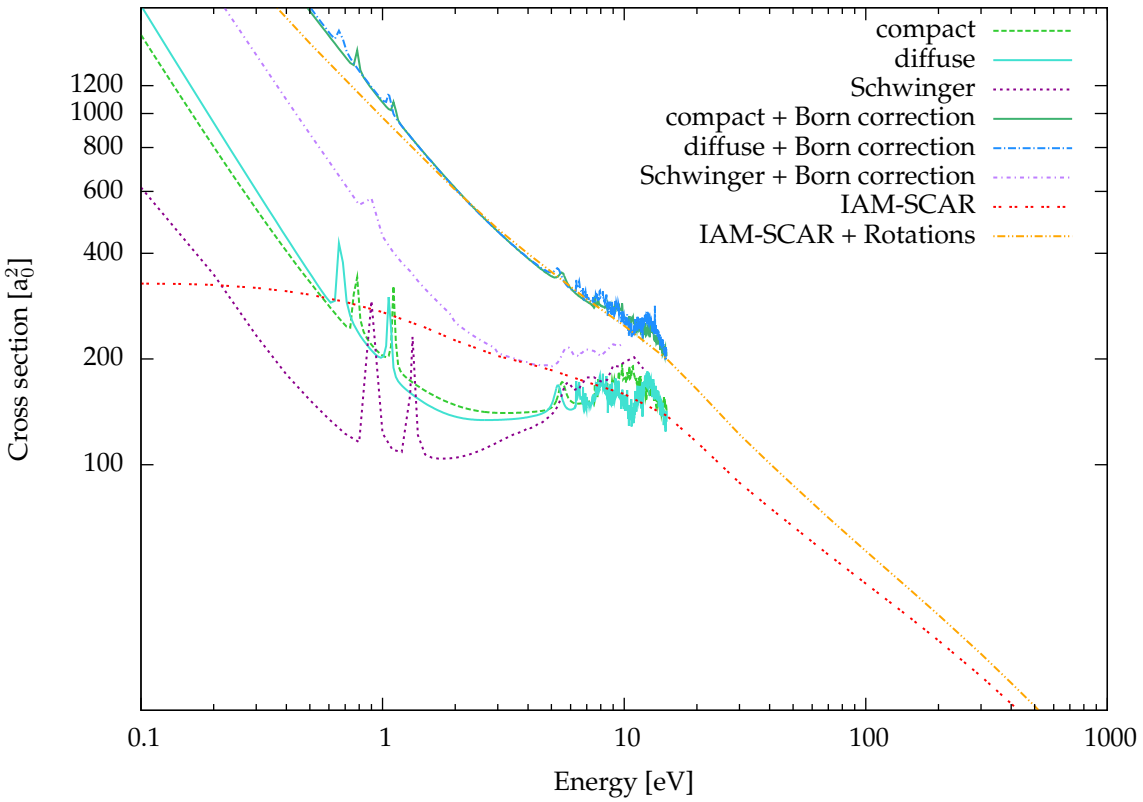

Figure 3.5: Integral elastic cross section for electron scattering from pyridine for the basis sets indicated in the figure. Also plotted are the multichannel Schwinger results of Barbosa *et al.* and IAM-SCAR results of Blanco *et al.* [120]. The cross sections labelled 'Born correction' incorporate a Born-based correction.

It should be noted that the IAM+Rotations and the Born-corrected R-matrix cross sections are not comparable in a straightforward way. The IAM+Rotations cross section is determined considering a 300 K population for the initial rotational states. The corrected R-matrix cross section is obtained on the grounds that the molecule is initially in its rotational ground state and summed over all possible

final states with $J < 9$. J. Franz and F. A. Gianturco argued in their work on positron scattering from pyrimidine [134] that, for a rigid rotor with parameters similar to those of pyridine, the temperature will have a small effect on the cross section below 20 eV. However, this may not be the case [123]; the effect is difficult to quantify.

DIFFERENTIAL CROSS SECTION

Figure 3.6 shows EDCS for several energies, calculated with the R-matrix, Schwinger (lower energies) and IAM-SCAR methods [120]. The differences between the R-matrix EDCS calculated with different basis sets are not very significant. Looking at the figure 3.6 for low energy, it can be easily seen that for all plots, both R-matrix EDCS with compact basis set and diffuse one as well as the Schwinger EDCS have similar shape. They become less similar when the energy increases. It is not surprising that the differences are smaller between R-matrix EDCS calculated with the compact and diffuse basis set than between these and the EDCS obtained using Schwinger method, since the two methods describe polarization on different levels. The R-matrix and Schwinger EDCS shapes and size are similar in most of the angular range; only for small angles ($< 10°$) is the size different, probably because of the different way of implementing of Born correction into these methods. Due to the logarithmic scale of the figure these differences are almost impossible to see in the graph.

In figure 3.6 the IAM-SCAR+Rotations results are also shown for E > 10 eV. For 10 eV the IAM-SCAR EDCS are plotted with other data. Although at 10 eV IAM-SCAR does not give trustworthy results, it is the highest energy for which it can be compare with R-matrix results. It is not surprising that the shape of the EDCS differs significantly between the *ab initio* and IAM-SCAR results. For energies < 50 eV the IAM-SCAR+Rotations EDCS are similar in their shape and size to those of pyrimidine (the IAM-SCAR+Rotations EDCS for pyrimidine is not illustrated in the figure), however above those energies the EDCS for pyridine is significantly bigger [120].

By comparing the R-matrix for pyridine with pyrimidine [21, 17], it can be easily seen that their sizes are similar, but the changes become more significant with higher energies. It can be noticed from figure 3.6, that the differences at 3 eV start to be noticeable from $120°$, at 6 eV from $60°$ and at 10 eV from $50°$. The reason of these differences can be found in the additional lone pair of pyrimidine due to the second nitrogen. This additional lone pair may gently boost the exchange effect and bring about the EDCS changes. Nevertheless, the EDCS shapes do not change significantly, so the conclusion can be extracted that the additional nitrogen replacing a carbon does not affect meaningfully the scattering data.

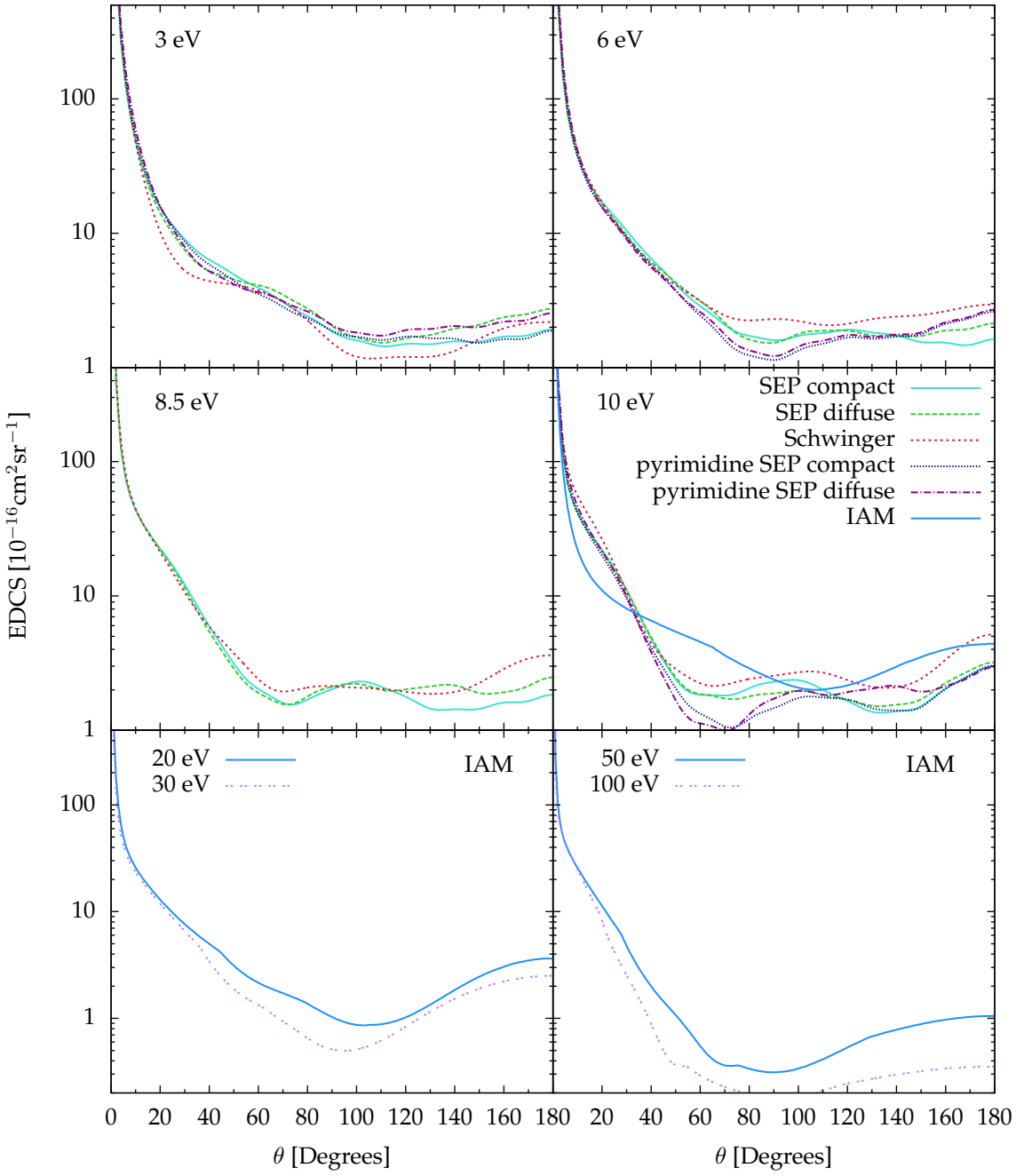

Figure 3.6: Elastic differential cross section for electron scattering from pyridine for the energies indicated in the panels, calculated using the R-matrix, multichannel Schwinger method [121] and IAM-SCAR+Rotations method [120]. Also plotted are R-matrix EDCS for pyrimidine. The R-matrix results are Born-corrected. The label 'IAM' stands for 'IAM-SCAR+Rotations'; the two bottom panes show IAM-SCAR+Rotations cross sections for several energies.

3.3.3 CC MODEL

In this section the Close-Coupling (CC) cross sections for pyridine are described and compared to the SEP ones; therefore some SEP data are repeated here.

In the target model used for CC calculations 32 of the 42 electrons of pyridine were allocated to

16 core orbitals (frozen electrons) and the remaining 10 electrons were distributed among 8 valence orbitals (six orbitals of the π type and two of the σ type). Virtual (unoccupied) orbitals (v.o.) were used in order to describe better the scattering process: 60 v.o. in the case of the compact basis set and 80 v.o. in the case of the diffuse basis set. The crucial step was to choose the appropriate active space. Since the size of scattering calculations rises rapidly with the size of the active space, the smallest suitable active space was used. In more detail, the electrons were distributed among: frozen core orbitals $1-10a_1$, $1-6b_2$; active orbitals $11a_1$, $1-4b_1$, $7b_2$, $1-2a_2$; virtual orbitals for compact basis set: $12-35a_1$, $5-14b_1$, $8-26b_2$, $3-9a_2$ and for diffuse basis set: $12-42a_1$, $5-17b_1$, $8-33b_2$, $3-12a_2$.

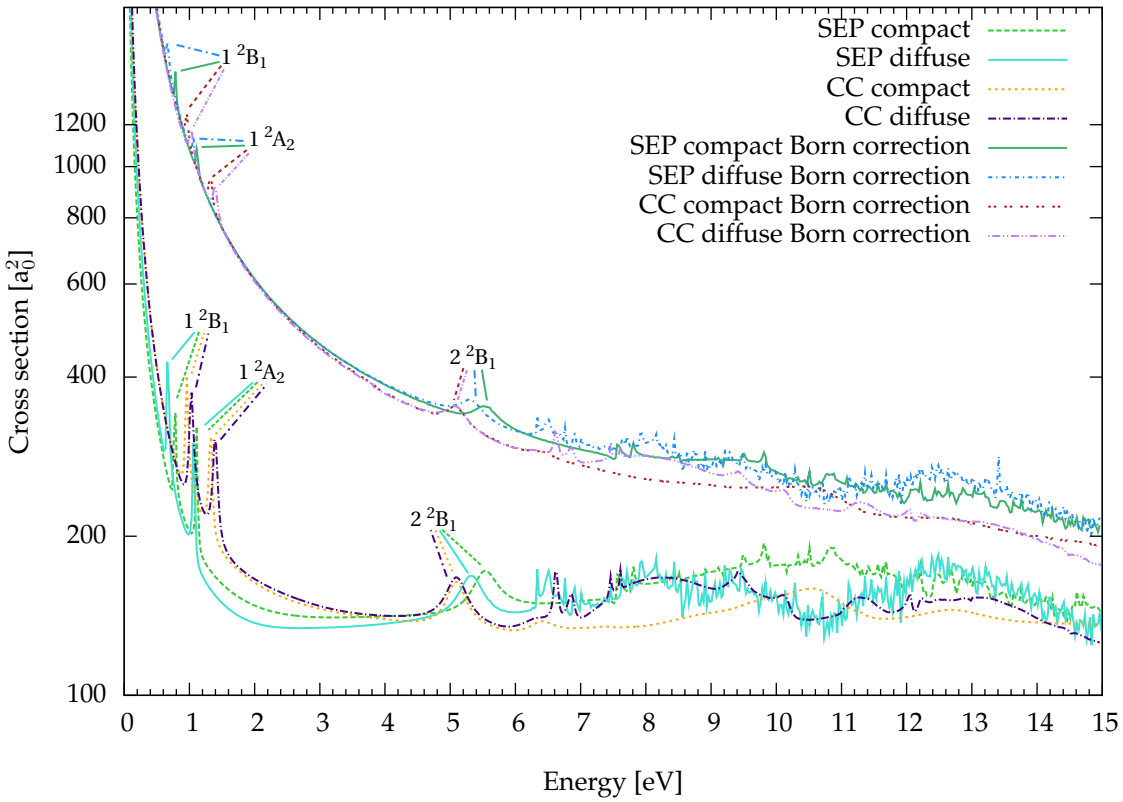

Figure 3.7: Integral elastic cross section for electron scattering from pyridine calculated with the R-matrix method using the approximation levels and the basis sets indicated. The cross sections labelled 'Born correction' incorporate a Born-based correction.

Figure 3.7 shows that the shape and size of all uncorrected R-matrix IECSs are very similar. The main difference between the SEP and CC IECSs is the presence of pseudo-resonances characteristic of the SEP model. Another difference is the somewhat different positions of the resonant peaks. Moreover, the CC results can give good characteristic of the core-excited resonances. A wide peak appears around 11 eV for the compact basis set, and a much broader one around 12-13 eV for the diffuse basis set. Resonances at these energies may be non-physical and caused by the inclusion of insufficient partial wave in the continuum expansion (the core-excited resonances are discussed in detail in the next section).

DIFFERENTIAL CROSS SECTION

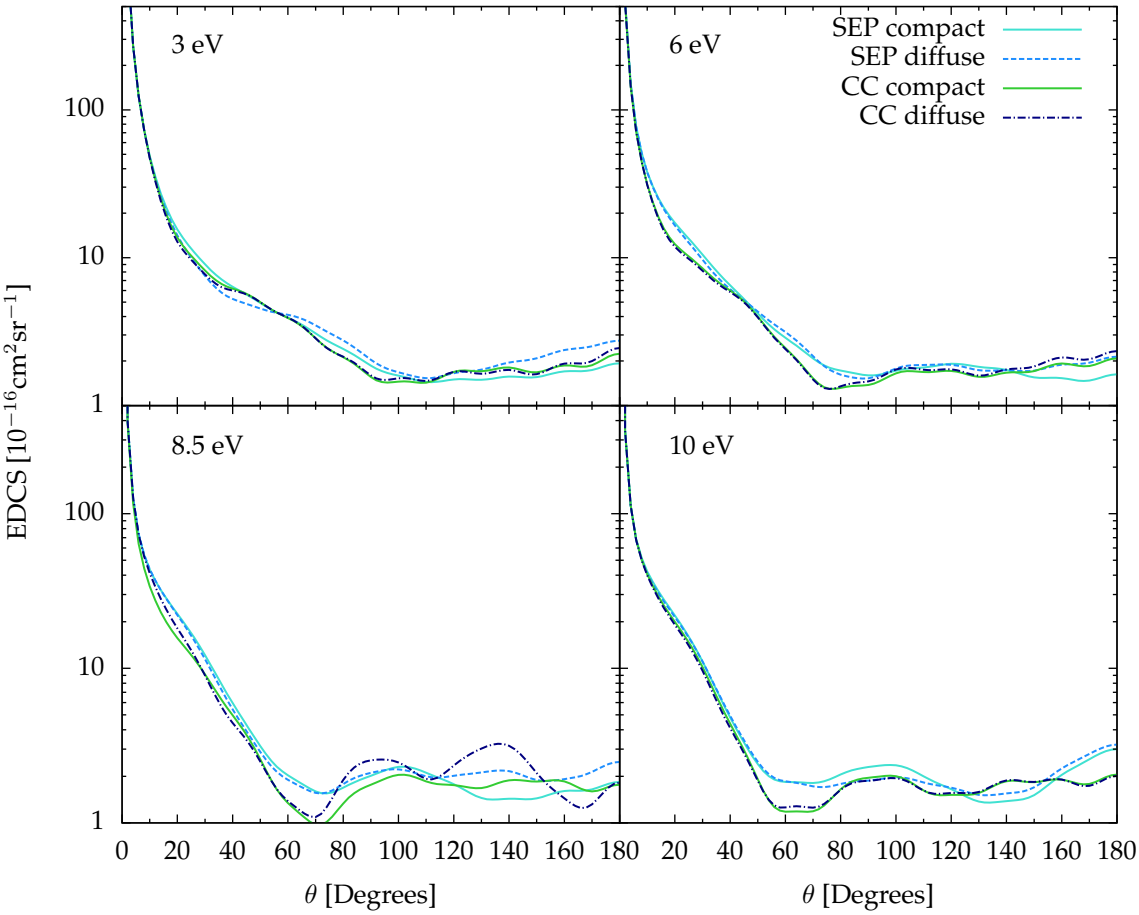

Figure 3.8: Elastic differential cross sections for electron scattering from pyridine for the energies, basis sets and models indicated in the panels.

The EDCSs, plotted in figure 3.8 for the SEP and CC models, are very similar in size and fairly similar in shape. Only the EDCS at 8.5 eV for the CC model with the diffuse basis set has a different shape above 110° (this baffling shape is observed in all the EDCS for energies between 7.5 eV and 9.5 eV; it can be due to the fact that different basis set may give different target and virtual orbitals; but it also might be due to inclusion not enough partial waves in the continuum expansion or a problem with quality of representation of the continuum).

TOTAL INELASTIC CROSS SECTIONS

Figure 3.9 shows the total inelastic cross sections (TICSs) for the CC model with both basis sets. Their size is very similar, although, their shape differs slightly above about 7 eV. The cross section obtained using the compact basis set is smoother. At least two peaks are visible for both basis sets. Also plotted in figure 3.9 is the TICSs obtained with the IAM-SCAR method. This cross section is zero slightly below 10 eV, when in fact, the first electronic excitation threshold is around 4 eV. This is due

to the implementation of this model. The IAM-SCAR TICSs for pyrimidine [132] is noticeably smaller than for pyridine [120]. The same behaviour is visible for the R-matrix TICSs for pyrimidine [21, 17] and pyridine. Although the pyrimidine TICS is smaller than that of pyridine the shape has some similarities. They both have irregular structure with a few peaks above 5 eV. The pyrimidine TICS, however, has one clear peak around 4.5 eV, when in the case of pyridine TICS it is much harder to identify a peak around 4-5 eV. There is no experimental data for inelastic cross sections of pyridine.

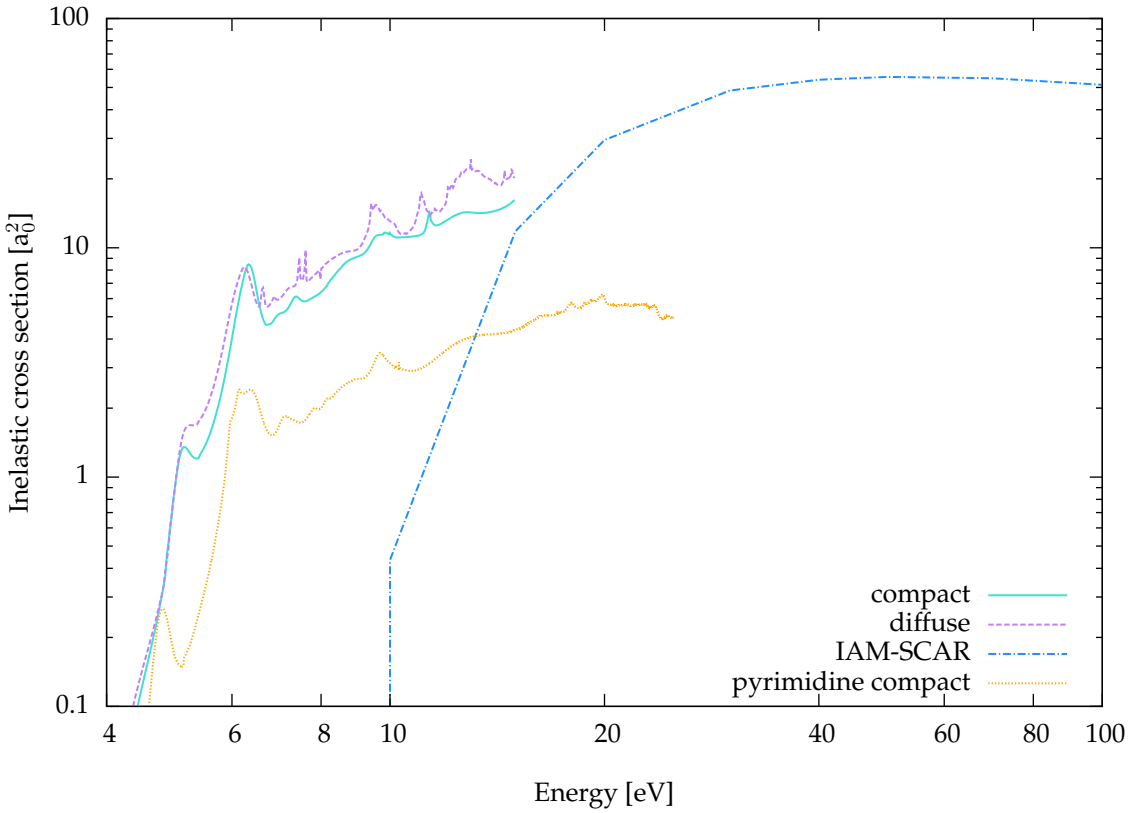

Figure 3.9: The R-matrix total inelastic cross section for the compact and diffuse basis sets and IAM-SCAR inelastic cross section for pyridine; the R-matrix TICSs for pyrimidine [21, 17] is also plotted.

In order to gain further insight how the TICS change between different basis sets and how they differ between pyridine and pyrimidine, figure 3.10 presents the contribution to the TICS from each of irreducible representation. It is clear that TICSs with diffuse basis set has more peaks but the trend and size of the TICS is very similar. The pyrimidine TICSs for all symmetries is smaller but has a similar shape. Especially for the $^2B_1$ and $^2A_2$ symmetries it can be noticed that all TICSs (except for the diffuse basis set above 10 eV) have more or less the same number of peaks but these pyrimidine ones are shifted in lower energies. Due to the fact that all TICSs presented in the figure 3.10 have complicated structure it is not easy (and sometimes not possible) to identify resonances on the TICSs, a better tool to characterise them is time-delay analysis, therefore in the next section the results will be presented using it.

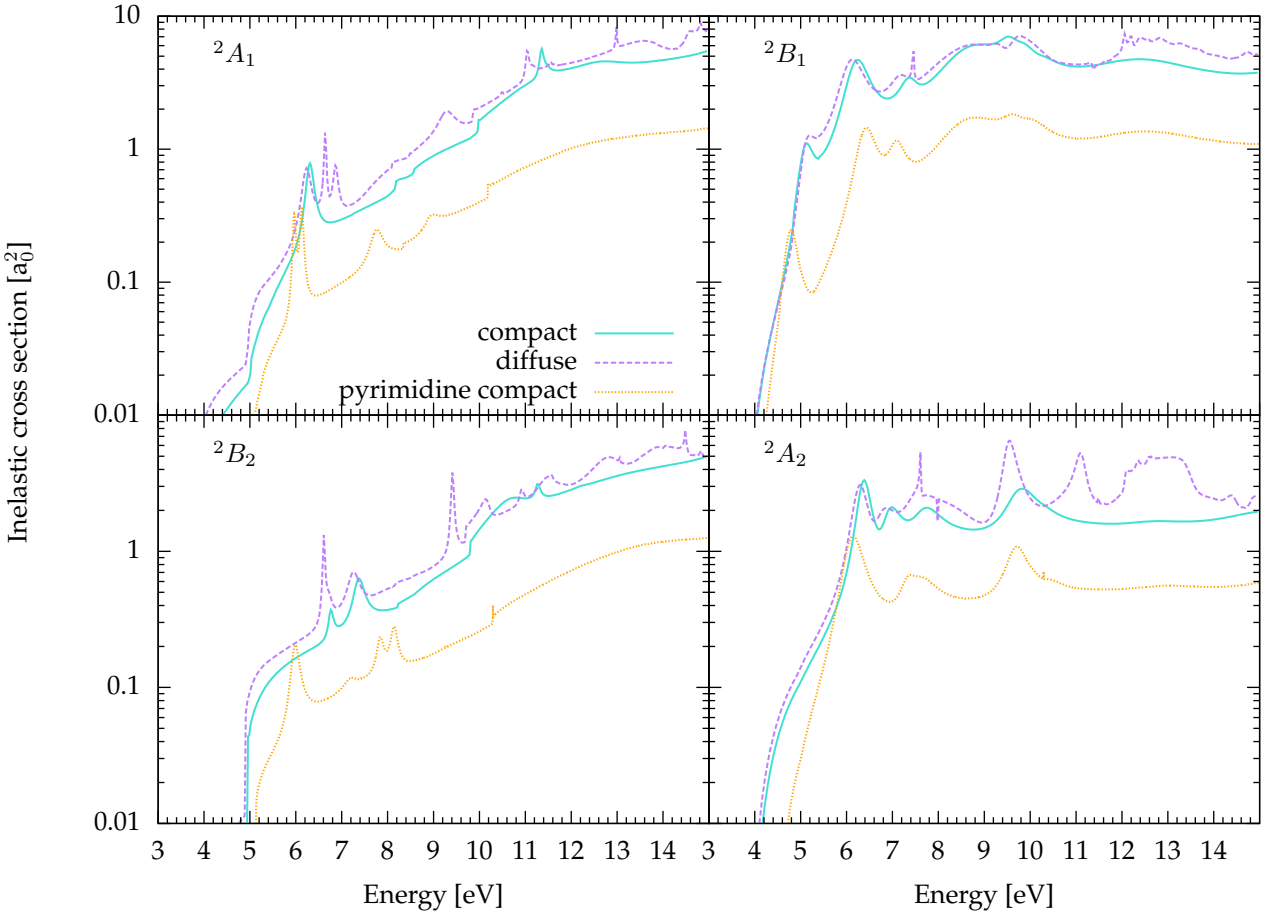

Figure 3.10: Combination of each irreducible representation to the total inelastic cross section for pyridine and pyrimidine for the basis sets indicated in the figure.

3.4 RESONANCES

In the sections 2.3.4, 2.3.5 and 2.3.7 we have described some of the methods available to analyse resonances. In the previous section one could see resonances manifest themselves in the cross sections as a Gaussian peaks. Nevertheless, not all resonances appear on the cross section. There are two more useful methods to analyse resonances, namely: the time-delay analysis and the investigation of the cross section for the excited states (the last one can be used only to identify core-excited resonances).

The analysis of the eigenphase sum is not presented in this work, because in the case of large molecules like azabenzene, the resonances are manifested by very small, and in some cases, invisible steps, which makes it difficult to use [21].

The time-delay analysis can be used not only to find all resonances and determine their position and width, but also to characterise them in terms of their parent state(s). In order to determine the parent states, it is necessary to look for signatures of the resonances in particular scattering channels, using to this aim the analysis of the branching ratios (probability of decay of the metastable state into an open channel).

First, in the next subsection the shape resonances are characterised in more details both at SEP and CC level, using the cross sections and time-delay analysis. Next, in subsection 3.4.2 the core-excited resonances are characterised using both the time-delay analysis and the cross section for the excited states.

3.4.1 SHAPE RESONANCES

Low-energy electron collisions with pyridine (and other azabenzene molecules) were first studied by Nenner and Schultz [85] in 1975 using electron transmission spectroscopy (ETS). In 1983, Modelli and Burrow [86] also used this method to study the temporary anion states of pyridine and substituted pyridines. The two energetically lowest resonances (in azabenzene – up to triazine) were interpreted as π^* shape resonances by Nenner and Schultz [85] (however it is possible that in some diazines the lowest resonances are bound states), with the trapping of the scattering electron into the lowest-lying unfilled π^* orbitals. The first resonance in pyridine is associated with the first empty orbital – b_1 and the second with electron capture into the second empty orbital – a_1. Since the energy of the third resonance is higher than the first electronic excitation threshold (for pyridine and all diazines it is around 4 eV) the third resonance was interpreted as a shape resonance (trapping an electron into the next, b_1, empty orbital, in the case of pyridine) mixed with a core-excited resonance associated with low-lying excited states of the molecule. Their interpretation was confirmed by Winstead and McKoy [135, 136] in calculations of electron collisions with pyrazine and by Mašín [21] studying all diazines. As already mentioned, low-energy collisions with pyridine have also been studied computationally by Barbosa *et al.* [121] using the Schwinger multichannel method.

The presence of the first three resonances (shape resonances), is clearly visible in the integral elastic cross section in figures 3.4 and 3.7, as well as the time-delay, plotted in figures 3.11 and 3.12. In the cross sections all these resonances appear below 6 eV both in R-matrix and the Schwinger results. Above this energy, at SEP level, many pseudo-resonances are present in the R-matrix cross section that make it impossible to determine whether there are any physical resonances in this energy range. The time-delay analysis in figure 3.11 displays Lorentzian peaks. Unfortunately, due to many pseudo-resonances, analysis of resonances above 6 eV is not straightforward. It is worth noting that for the compact basis set the time-delay does not display many pseudo-resonances, almost all peaks are distinguishable (below 10 eV). On the other hand, the diffuse basis set has much more structure, there are a few more peaks which do not correspond to any of peaks for the compact basis set and shows many more pseudo-resonances.

Despite the fact that the SEP time-delay (as well as the SEP cross sections) is not very easy to interpret above 6 eV it is possible to notice a resonance at about 7.6 eV for the compact basis set,

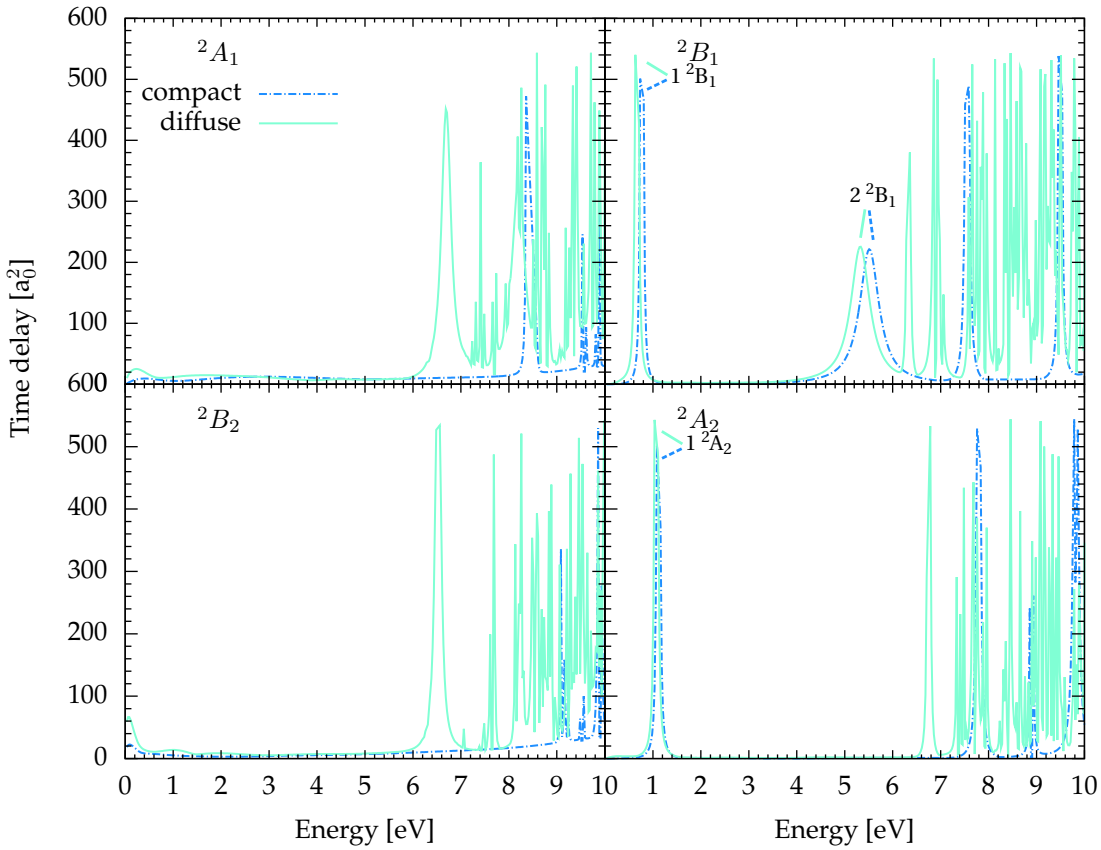

Figure 3.11: The time-delay (the largest eigenvalue of the **Q**-matrix) for each symmetry, as a function of electron energy. The calculations were performed at SEP level for the basis sets indicated.

for $^2B_1$ symmetry (the time-delay plot for the diffuse basis set displays many pseudo-resonances above 6 eV but Lorenzian-like peaks contaminated with spikes can be distinguished at 7 eV and at 7.8 eV; one of them may correspond to the resonances at 7.6 eV for the the compact basis set). This resonance may correspond to 3 $^2B_1$ at 6.21 eV illustrated in figure 3.12, obtained at CC level[‡] (it is also visible in the TICS, in figure 3.10 – the second peak for B_1 symmetry at 6.21 eV). It will be shown in section 3.4.2.1 (see, table 3.6) that one of the parent states of this resonance is the ground state, therefore this resonance may be a forth π^* with mixed shape–core-excited character. The existence of a fourth π^* resonance has been identified in the diazines and is discussed in the literature (e.g. [137]).

The resonance positions and widths (with their symmetries) obtained from SEP and CC calculations together with results from ETS experiments [85, 86] are collected in table 3.5. These parameters have been obtained using RESON [138], a Breit-Wigner profile fitting program (see, section 2.6). As mentioned before, for the SEP calculations with the compact basis set, the use of 35 virtual orbitals gives the best agreement with the results of Nenner and Schulz. To show that this number is optimal, the resonance parameters for other numbers of virtual orbitals are also listed at the beginning of table 3.5. Note that the two lowest resonances for the compact basis set with 40 v.o. are over-correlated,

[‡]It is expected that mixed shape–core-excited resonances appear in CC calculations at lower energy than in SE or SEP calculations.

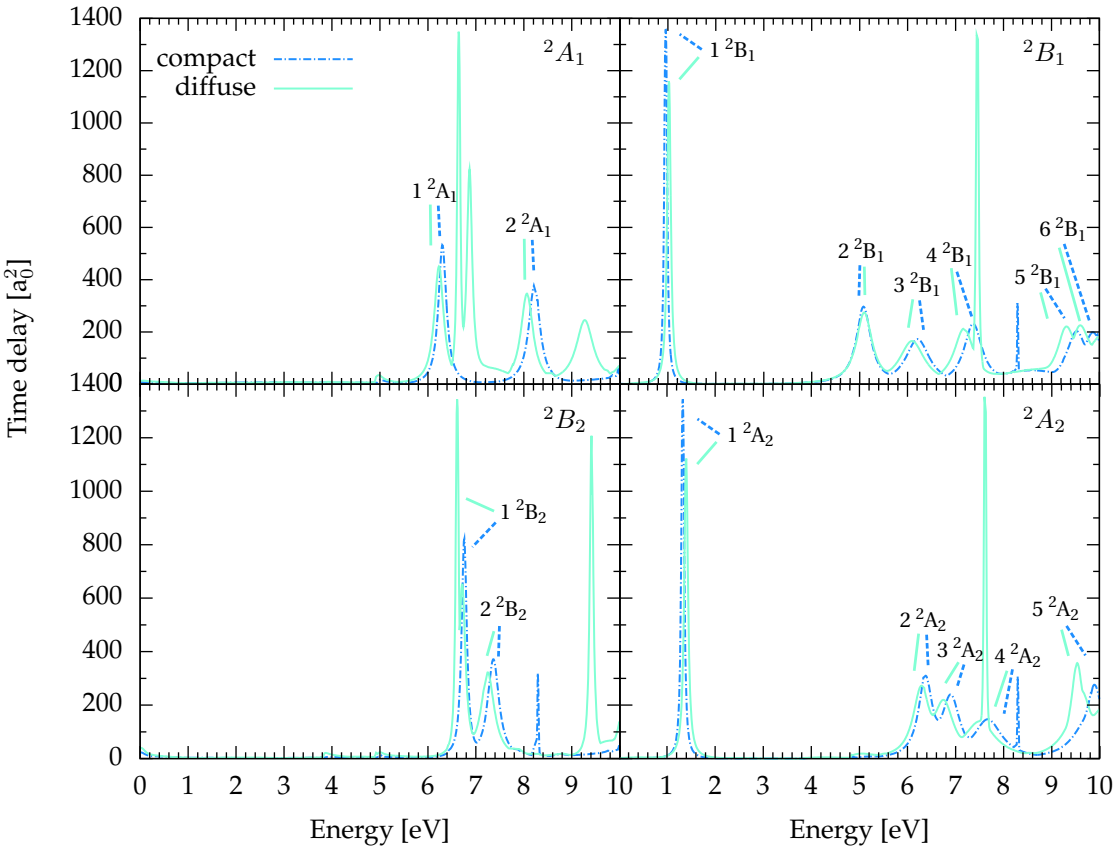

Figure 3.12: The time-delay (the largest eigenvalue of the Q-matrix) for each symmetry, as a function of electron energy. The calculations were performed at CC level for the basis sets indicated.

i.e. their energy is much lower than their experimental values.

Level	Basis set	Nr. vo	$^2B_1$		$^2A_2$		$^2B_1$	
SEP	cc-pVDZ	25	1.15	(0.057)	1.46	(0.058)	5.8	(0.60)
	cc-pVDZ	40	0.48	(0.01)	0.9	(0.016)	5.32	(0.48)
SEP	cc-pVDZ	35	0.77	(0.022)	1.11	(0.025)	5.51	(0.48)
	6-311+G**	50	0.67	(0.027)	1.07	(0.030)	5.33	(0.47)
CC	cc-pVDZ	60	0.95	(0.049)	1.33	(0.053)	5.09	(0.49)
	6-311+G**	80	1.02	(0.076)	1.39	(0.080)	5.05	(0.51)
Barbosa *et al.* [121]			0.90		1.33		5.80	
Nenner and Schulz [85]			0.62		1.20		4.58	
Modelli and Burrow [86]			0.72		1.18		4.48	

Table 3.5: Positions (and widths), in eV, of the π^* resonances in pyridine; the number of virtual orbitals (Nr. vo) used in the calculations is indicated. The positions of the resonances calculated by Barbosa *et al.* [121] are listed as well; the Schwinger multichannel results were calculated at the SEP level considering only singlet-coupled excitations. Also listed are the experimental results of Nenner and Schulz [85] and Modelli and Burrow [86].

The best agreement with the experimental data for the first two resonances (i.e. the first $^2B_1$ and the $^2A_2$ shape resonances) among all R-matrix calculations is for the SEP calculations with the diffuse basis set; these are lower in energy than in the CC model. Nevertheless, all SEP calculations provide a third resonance that is too high in energy. This is because the third resonance has a mixed shape and

core-excited character [137, 135] and to describe it accurately configurations describing electronically excited states of the target must be included in the calculation. The CC results confirms this; the third resonance ($^2B_1$) lies in lower energy than for the SEP model (this resonance also manifests itself in the total inelastic cross section, illustrated in figure 3.10 – the first peak at energy $\sim$ 5.1 eV for $^2B_1$ symmetry).

3.4.2 CORE-EXCITED RESONANCES

3.4.2.1 TIME-DELAY ANALYSIS

Pyridine has an ionization threshold of ~ 10 eV, but in our calculations the ionization process is not considered (pseudostates would be required to describe ionization). Since the probability of capture of an electron in a resonant state is almost equal to zero above the ionization threshold, no resonance should appear above 10 eV. Nevertheless, because some excited states (parent states of resonances) appear at too high an energy (above the ionization threshold), a few resonances appear above 10 eV; they will not be characterized in this work.

Figure 3.12 shows the time-delay for all symmetries and basis sets: the resonances appear as Lorentzian peaks (section 2.3.7); table 3.6 collects the positions and widths of the shape, core-excited and mixed shape–core-excited resonances as well as their most likely parent states[§]. The parameters have been determined using GRACE plotting program. This program enables one to enter a formula to which a curve is fitted and gives two parameters: a width and a resonant energy — energy of a Lorentzian peak (the resonance positions are very similar to those listed in table 3.5, but the widths differ significantly; the more reliable parameters are these obtained by GRACE, the differences may be due to a numerical artefact in RESON). The most likely parent states have been found using the analysis of branching ratios. Many of the resonances that were found using this method possess more than one parent state; in table 3.6 only the most dominant are reported in decreasing order of dominance. The resonances which appear for both basis sets are more reliable than those which appear only for one basis set. All resonances which appear for the compact basis set also are present in the calculations with the diffuse basis set. Therefore, in the next section, the resonances for the compact basis set will be considered. The same approach was used for diazines in Z. Mašín's thesis [21]. In table 3.6 those that appear for the diffuse basis set only are not numbered.

Very narrow peaks are also visible in figure 3.12 which appears at 8.29 eV for the compact basis set for $^2B_1$, $^2B_2$ and $^2A_2$ symmetries (not for $^2A_1$ symmetry but this can be due to the fact that at 8.22 eV a Lorentzian peak is already present which can mask that very narrow peak). This narrow peak has no Lorentzian shape, therefore it cannot be confirmed as a resonance. It is also very unlikely

[§]In table 3.6, for comparison purposes, are also listed (in increasing energy order per symmetry) pyrimidine resonance energies and widths with the compact basis set and their parent states [21].

that three different resonances would appear at the same energy. It would seem to have threshold character: it is narrow and appears in all symmetries exactly at the same energy, however, there is no threshold for pyridine at this energy (see table 3.3). Calculations with much smaller grid have been performed around 8.29 eV to check if they are a numerical artefact; the presence of these peaks did not change with increasing precision. Therefore they are presented in figure 3.12 and in table 3.6 (the values with question marks in the last column) but they will not be characterised or discussed further.

sym.	Pyridine			Pyrimidine	
	E_r (Γ)		main parent states	E_r (Γ)	main parent states
	compact	diffuse		compact	
$1\,^2A_1$	6.30 (0.20)	6.23 (0.24)	$1\,^3B_1$, $1\,^1B_1$	5.96 (0.18)	$1\,^3B_1$, $1\,^1B_1$
$^2A_1$		6.64 (0.08)	g.s., $1\,^3A_1$	6.15 (0.18)	$1\,^3A_2$, $1\,^1B_1$, $1\,^3B_1$
$^2A_1$		6.86 (0.13)	g.s., $1\,^1B_2$	7.75 (0.35)	$2\,^3A_2$, $2\,^3B_1$, $1\,^3A_2$
$2\,^2A_1$	8.22 (0.28)	8.06 (0.31)	$1\,^3A_2$, $1\,^1A_2$, $1\,^3B_1$	8.34 (10^{-4})	$2\,^1A_1$
$^2A_1$		9.27 (0.44)	g.s., $2\,^1A_1$	8.94 (0.42)	$2\,^3B_1$, $2\,^1B_1$, $2\,^3A_2$
$1\,^2B_1$	0.96 (0.07)	1.02 (0.09)	shape resonance (g.s.)	0.96 (0.14)	g.s.
$2\,^2B_1$	5.08 (0.37)	5.10 (0.40)	g.s., $1\,^3A_1$, $1\,^3B_1$, $2\,^3A_1$	4.78 (0.38)	g.s., $1\,^3A_1$, $1\,^3B_1$
$3\,^2B_1$	6.21 (0.63)	6.09 (0.66)	g.s., $1\,^3A_1$, $2\,^3A_1$	6.37 (0.58)	g.s., $1\,^3A_1$
$4\,^2B_1$	7.37 (0.47)	7.18 (0.51)	$1\,^1B_2$, $1\,^3B_2$, $2\,^3A_1$	7.11 (0.48)	$1\,^3A_1$, $1\,^3B_2$, $1\,^1B_2$
$^2B_1$		7.45 (0.07)	g.s., $1\,^3B_2$, $1\,^1B_1$	8.47 (1.69)	g.s., $1\,^3A_1$, $2\,^3A_1$, $1\,^3B_2$
	8.29		??		
$5\,^2B_1$	9.53 (0.53)	9.32 (0.49)	$3\,^3A_1$, $2\,^3A_1$, g.s		
$6\,^2B_1$	9.86 (0.54)		$2\,^3B_2$, $2\,^1B_2$, g.s.		
$^2B_1$		9.62 (0.47)	$2\,^3B_2$, $1\,^1B_1$, g.s.		
$^2B_2$		6.61 (0.08)	g.s., $1\,^1B_1$	5.98 (0.24)	$1\,^3B_1$, $1\,^1B_1$
$1\,^2B_2$	6.76 (0.13)	6.71 (0.16)	$1\,^3B_1$, $1\,^1B_1$, $1\,^1A_2$	7.19 (0.35)	$1\,^3A_2$, $1\,^1A_2$
$2\,^2B_2$	7.37 (0.29)		$1\,^3B_1$, $1\,^1B_1$, $1\,^3A_2$	7.83 (0.22)	$2\,^3A_2$, $1\,^1A_2$, $2\,^1A_2$
$^2B_2$		7.24 (0.34)	$3\,^3A_1$, $2\,^3B_2$	8.16 (0.22)	$1\,^3A_2$, $2\,^3A_2$, $2\,^3B_1$
	8.29		??		
$^2B_2$		9.41 (0.09)	g.s., $2\,^1B_1$		
$1\,^2A_2$	1.32 (0.08)	1.40 (0.09)	shape resonance (g.s.)	0.53 (0.17)	g.s.
$2\,^2A_2$	6.38 (0.35)	6.30 (0.39)	g.s., $1\,^3A_1$, $1\,^3B_2$	6.11 (0.51)	g.s., $1\,^3A_1$, $1\,^3B_2$
$3\,^2A_2$	6.88 (0.45)	6.74 (0.49)	$1\,^3A_1$, $1\,^3B_2$, $2\,^3A_1$	7.33 (0.43)	$2\,^3A_1$, $1\,^1B_2$, $1\,^3A_1$
$4\,^2A_2$	7.66 (0.75)	7.51 (0.75)	$1\,^1B_2$, $2\,^3A_1$, $1\,^3B_2$, g.s.	7.60 (0.67)	$1\,^3B_2$, $1\,^1B_2$, $2\,^3A_1$
$^2A_2$		7.61 (0.03)	g.s., $1\,^3A_1$, $1\,^1B_2$		
	8.29		??		
$5\,^2A_2$	9.88 (0.40)		$3\,^3A_1$, $2\,^1A_1$, $2\,^1B_2$		
$^2A_2$		9.53 (0.30)	g.s., $1\,^1B_1$, $1\,^1A_2$		

Table 3.6: Positions, E_r (and widths, Γ), in eV, of all resonances in pyridine for the energy range from 0.01 eV up to 10 eV. The resonances which appear for the diffuse basis set only are not numbered. The main parents states are listed in the decreasing order of importance. The abbreviation 'sym.' stands for symmetry and 'g.s.' stands for ground state, that is $1\,^1A_1$ parent state. The two question marks ('??') are for peaks which we are not able to be identified as a resonance (for more details, look for corresponding text). Also listed pyrimidine resonance energies and widths obtained using the compact basis set [21].

All resonances appearing in the time-delay analysis, except the two shape π^* resonance described earlier, are mixed shape–core-excited or core-excited resonances. Only the $^2B_2$ resonance at 9.41 eV

for the diffuse basis set could be a Feshbach resonance connected with state $2\,^1B_1$ with energy 9.42 eV. The previous study of diazines by Z. Mašín [21] shows however, that below 10 eV in the case of pyrimidine there is one Feshbach resonance for the compact basis set (at 8.34 eV with parent state of A_1 symmetry) and four for pyridazine (at 7.27 eV and 7.93 eV, 8.89 eV, 9.87 eV connected with states of symmetries A_1 and B_2, respectively). The time-delay for the diffuse basis set displays more Lorentzian peaks than for the compact basis set. A similar situation occurs in the time-delay analysis for pyrazine, described in [23]. It is not surprising that the resonance spectrum looks different for these two basis sets since the orbitals, particularly the v.o., generated with them are different. The additional peaks (appearing only for the diffuse basis set) are in general narrower than the others and all of them have the ground state as one of their parent states. In the case of three pairs of resonances: $^2B_1$ at energy 9.86 eV with compact and 9.62 eV with diffuse basis set, $^2B_2$ at energy 7.37 eV with compact and 7.24 eV with diffuse basis set, $^2A_2$ at energy 9.88 eV with compact and 9.53 eV with diffuse basis set, despite the Lorentzian peaks having similar positions in the two basis sets, the parent states of these resonances are different for each basis set. This means that the resonances cannot be identified as the same resonance for both basis sets.

Although the structure of pyridine and pyrimidine are similar and give fairly similar cross sections the identification of resonances between these two systems is not straightforward. The number of resonances (with energy below 10 eV) per symmetry is not always the same. E.g. for A_1 and B_2 symmetries only 2 pyridine resonances are characterised for compact basis set while pyrimidine manifests 4 resonances per each of these symmetries. A few resonances for the two systems correspond to the same parent states (e.g. pyridine resonance at 6.30 eV and pyrimidine one at 5.96 eV correspond to the parent states of the same symmetry: $1\,^3B_1$, $1\,^1B_1$). The energy of pyrimidine resonances which may correspond to pyridine resonances, in most cases, is smaller than the pyridine ones. A few resonances for both systems are linked to the parent states of the same symmetry but the order of importance of these states is not the same for these two molecules (e.g. the order of parent states of $4\,^2A_2$ resonance for pyridine at 7.66 eV is: $1\,^1B_2$, $2\,^3A_1$, $1\,^3B_2$, g.s. and for pyrimidine at 7.60 eV is: $1\,^3B_2$, $1\,^1B_2$, $2\,^3A_1$).

3.4.2.2 CROSS SECTIONS FOR THE EXCITED STATES

The excited state cross sections (ESCS) correspond to the process in which the target is initially in an excited state. If a molecule is in the same excited state before and after the collision the process is elastic and corresponds to the elastic cross section for excited state (ESECS). If after the collision the molecule is in a higher or lower state than the initial one, then the process is inelastic. The transfer from higher to lower state involves de-excitation of the molecule (and therefore super-elastic scattering: the electron has more energy after the collision than before) and it also contributes to the

excited state total cross section (ESTCS) (i.e. ESTCS is the sum of elastic and inelastic processes for the excited state cross section).

The analysis of the ESECS cross section and ESTSC can provide additional information about resonances lying at energies above the first vertical excitation energy. The ESECS and ESTCS were calculated, for all excited states included in our calculation, with the compact basis set. The ESECS are presented in figures 3.13, 3.14 and 3.15.

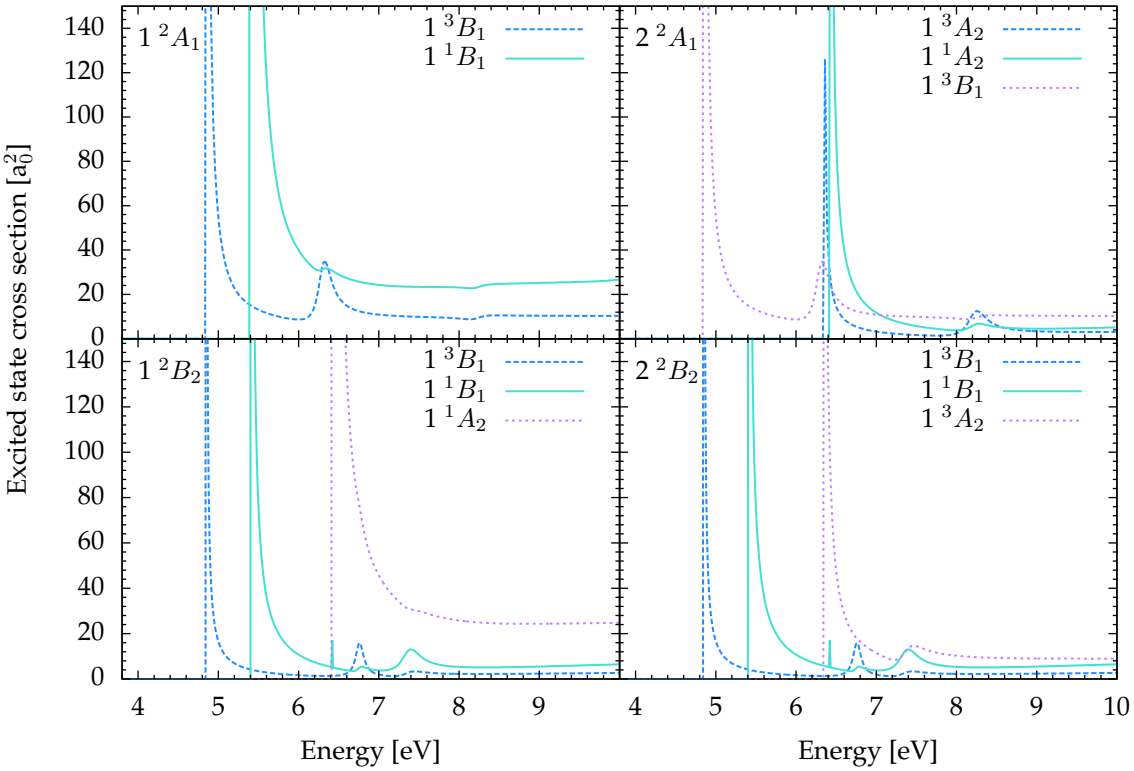

Figure 3.13: Cross sections for electron scattering from pyridine initially in the electronic state indicated in the legend. Each panel shows the cross sections for those states identified as the main parent state of a specific resonance, which is indicated in the panel (here for resonances: $1\ ^2A_1$, $2\ ^2A_1$ and $1\ ^2B_2$, $2\ ^2B_2$).

The plots of the ESECS show some peaks, which are present at energies corresponding to the positions of core-excited resonances. This confirms that the state whose cross section displays a peak is a parent state of those resonances. As it can be seen from the figures, not all parent states identified using the time-delay analyses show this behaviour for their ESECS. For example, despite the branching ratios analysis showing clearly that the $2\ ^3A_1$ excited state is likely to be a parent state of the $5\ ^2B_1$ resonance, the ESCS is flat in the energy range where the resonance appears, i.e. at 9.53 eV. The same situation occurs for the $1\ ^3B_1$ parents state of the $2\ ^2A_1$ resonance at energy 8.22 eV, $2\ ^3A_1$ parents state of the $3\ ^2A_2$ resonance at energy 6.88 eV and $1\ ^1A_1$ parents state of the $4\ ^2A_2$ resonance at energy 7.66 eV. This means that analysing the ESCSs is a complementary method to the time-delay analysis (using the branching ratios); if the state is identified as a parent state both by

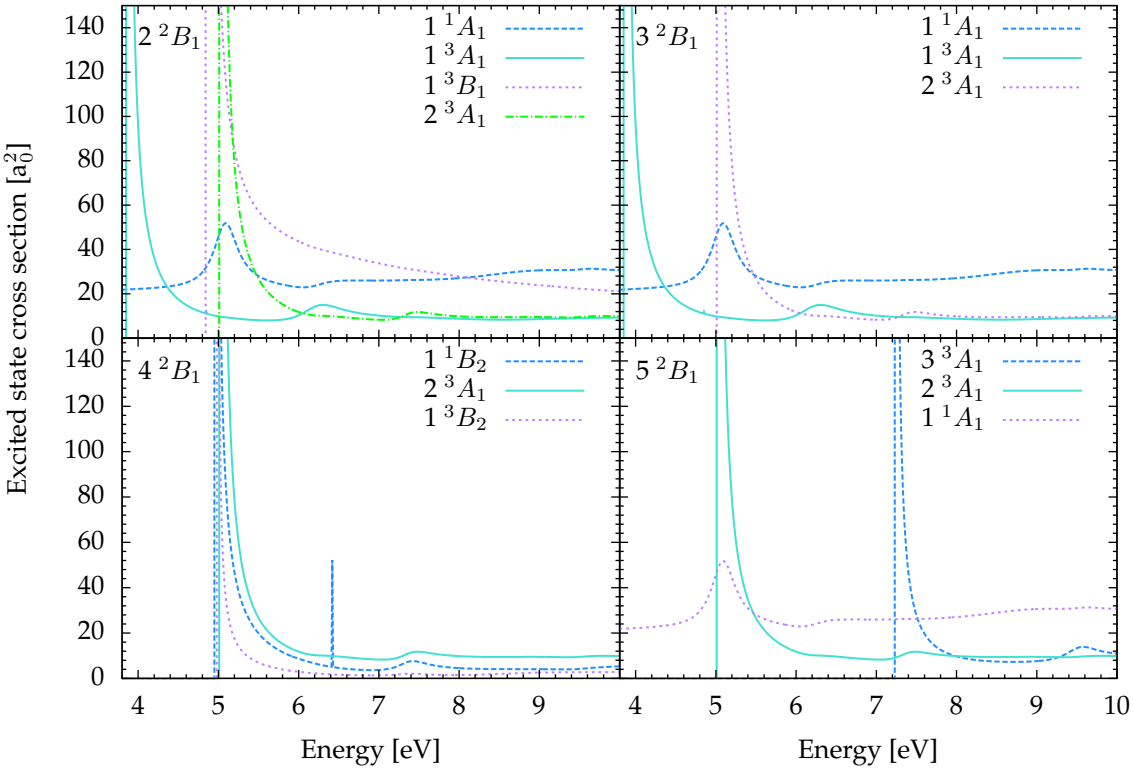

Figure 3.14: Cross sections for electron scattering from pyridine initially in the electronic state indicated in the legend. Each panel shows the cross sections for those states identified as the main parent state of a specific resonance, which is indicated in the panel (here for resonances: 2 $^2B_1$ – 5 $^2B_1$).

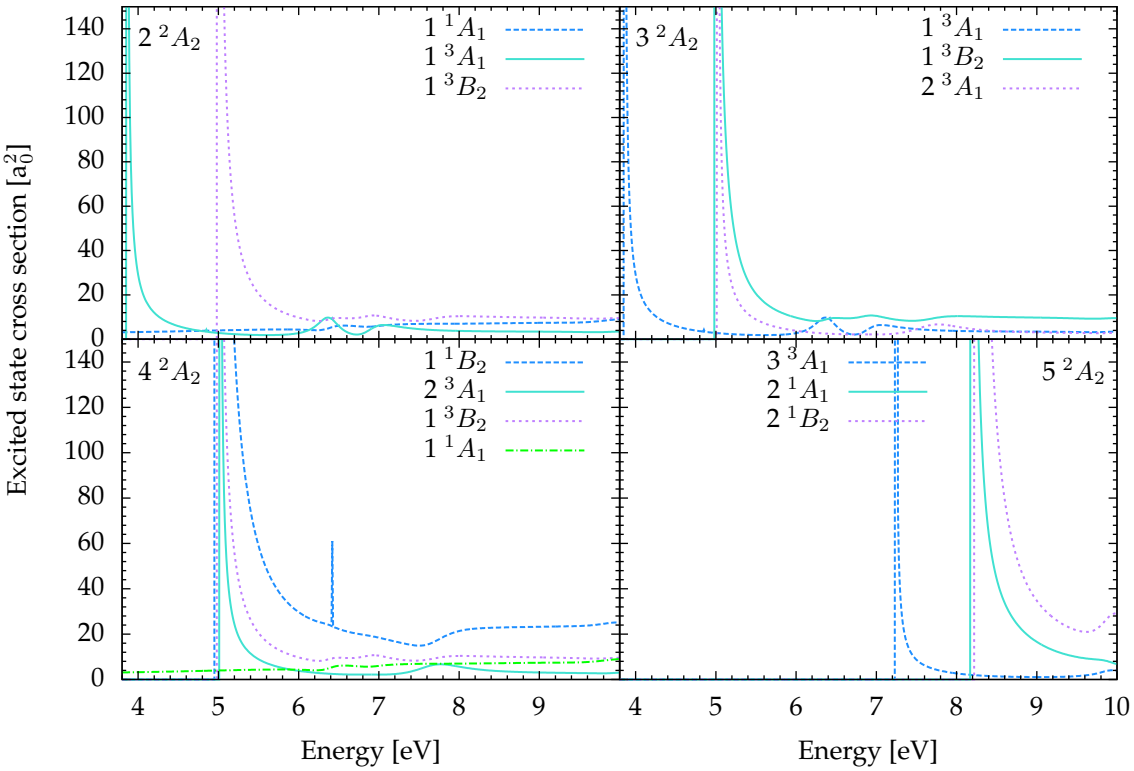

Figure 3.15: Cross sections for electron scattering from pyridine initially in the electronic state indicated in the legend. Each panel shows the cross sections for those states identified as the main parent state of a specific resonance, which is indicated in the panel (here for resonances: 2 $^2A_2$ – 5 $^2A_2$).

time-delay and ESCS analysis, it gives us confidence that it is a parent state.

Figures 3.13, 3.14 and 3.15 also show very narrow peaks for the $1\ ^1B_1$ excited state at energy ~ 6.4 eV, $1\ ^3A_1$ excited state at energy ~ 4.8 eV and $1\ ^1B_2$ excited state at energy ~ 6.4 eV. These are threshold peaks.

3.5 SUMMARY

In order to examine resonances in small molecular clusters it is important to have a good picture of processes happening in an isolated molecule. Examining the low-energy electron scattering for pyridine in more details and comparing with the Schwinger method calculations at the SEP level and with experiment (Nenner and Schulz [85]) confirms that our method gives good descriptions of shape resonances. Unfortunately, the are no experimental data, at the moment, to confirm the positions of core-excited resonances obtained in this work. The only experimental results we are aware of, are DEA measurements in pyridine, obtained by M. Weyland *et al.* [33], using the velocity slice imaging method. Although a core-excited resonance is the initial step of DEA, and the two processes are linked, the interpretation of the experimental data in terms of results presented in this work is not trivial.

Another experiment, which can be used to confirm the theoretical results is the electron energy loss measurement of cross section for electronic excitation. This method was used to confirm core-excited resonances in pyrimidine [139]; the agreement between theory and experiment was very good (the calculated resonance positions are shifted into higher energies compared to the experimental one, but this is expected, since the polarization effect is not fully described in the theoretical model). Unfortunately, there is no reported measurement of cross section for electronic excitation for pyridine.

4

ELECTRON COLLISIONS WITH PYRIDINE-WATER

The main purpose of the work presented in this chapter is to investigate the influence of water on the characteristics of resonances in pyridine (abbreviated to Pyr). Water is bound to pyridine by hydrogen bonding. The influence of hydrogen bonding on resonance behaviour has already been studied in formic acid (HCOOH, abbreviated to FA) clusters by T. C. Freitas *et al.* [27] who performed calculations with 1 and 2 added water molecules (for various geometries) at SE and SEP levels. The main conclusion of their work was that when water acts as the hydrogen (proton) acceptor in the hydrogen bond the shape resonance of HCOOH is destabilized and when water plays the role of the hydrogen (proton) donor, the resonance is stabilized. This can be understood by a qualitative, simplified electrostatic picture: water as a proton donor creates a positive charge near to the pyridine ring. The positive charge represents a more attractive electrostatic static potential seen by the incoming electron, which leads to the stabilization of the π^* shape resonance. Water acting as a proton acceptor creates negative charge near to the ring, which is repelling for the incoming electron and leads to the destabilization of the π^* shape resonance.

For clusters with two water molecules the resonance shift also depends on hydrogen bonds, i.e. if the two water molecules acts as a hydrogen donor, the resonance of HCOOH is stabilized more than for a cluster of formic acid with one water. In the case when one water molecule is a hydrogen acceptor and the second is a hydrogen donor the resonance is still destabilized but by a smaller amount than for HCOOH-H_2O with water acting as a hydrogen acceptor. These conclusions are

valid both for the SE and SEP method. The later calculation for phenol clusters performed by E. M. de Oliveira *et al.* [140] support the conclusions obtained from studies of formic acid clusters.

Our targets have significantly different structure and geometry from formic acid clusters. Pyridine clusters have more similarities to phenol but, although both pyridine and phenol are 6-membered rings, the water in the phenol cluster is not bound directly to the ring as it is in pyridine-water (abbreviated to Pyr-H_2O). In all three systems, however, the pure shape resonances are π^*. Therefore this chapter investigates whether the conclusions made by T. C. Freitas *et al.* also apply for pyridine clusters.

In this chapter calculations at SE, SEP and CC level are presented for low-energy electron collisions with the Pyr-H_2O and compared with isolated Pyr. Additionally, at SE level, results for larger clusters are presented, i.e. for pyridine-$(H_2O)_n$, n $= 2,\ 3,\ 5$. We mainly focused on pyridine with one water molecule, because the calculations are very computationally expensive for targets with many electrons. The structure of this system is presented in figure 4.1.

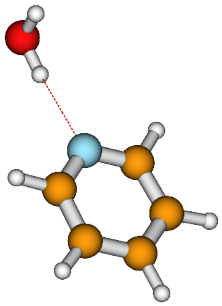

Figure 4.1: Geometrical structure of the pyridine-water clusters. The dotted red line indicates the hydrogen bond. In the figure the orange balls represent carbon, blue - nitrogen, white - hydrogen and red - oxygen. Generated using MOLDEN. The geometry of the system comes from [141].

Additionally, R-matrix calculations have been performed for isolated HCOOH and HCOOH-$(H_2O)_n$, n = 1, 2, for the same geometries as those presented in [27]. The results are consistent with those obtained with the Schwinger multichannel method. Therefore, the calculations are not presented in a separate chapter but only calculations for isolated FA and HCOOH-H_2O (for one chosen geometry) are used for comparison purposes in section 4.3.1.

4.1 CALCULATION DETAILS

4.1.1 TARGETS

The geometry of isolated pyridine used in the calculations presented in this chapter remains the same as in the previous chapter. The geometry of the systems: Pyr-H_2O, Pyr-$(H_2O)_2$, Pyr-$(H_2O)_3$ was taken from [141]; the geometry of the Pyr-$(H_2O)_5$ system comes from [142]. Pyridine clusters with more than one water molecule have not been broadly studied so far. No data were found to compare with our calculated target properties for the larger systems.

	H_2O	Pyr	Pyr-H_2O	Pyr-$(H_2O)_2$	Pyr-$(H_2O)_3$	Pyr-$(H_2O)_5$
P.G.	C_{2v}	C_{2v}	C_s	C_1	C_s	C_1
n^{e^-}	10	42	52	62	72	92
E	**-76.027**[a] -76.233[b]	**-246.714**[a] -247.537[b]	**-322.752**[a] -323.783[b]	**-398.795**[a]	**-474.833**[a]	**-626.905**[a]
μ	**2.01**[a] 2.28[b] 1.85[d]	**2.22**[a] 2.46[b] 2.19[e]	**4.68**[a] 4.27[c]	**3.46**[a]	**2.70**[a]	**6.57**[a]
α	9.67[f] 10.13[h] 9.78[i]	60.00[g] 64.06[h] 64.10[j]	68.16[g]			

Table 4.1: Structural and electrostatics properties of water, pyridine and their clusters: pyridine-$(H_2O)_n$, n = 1, 2, 3, 5. Listed are: point group (P.G.), number of electrons (n^{e^-}), ground state energy (E) in Hartree, dipole moment (μ) in Debye and spherical polarizability (α) in atomic units (a_0^3) of the ground state. [a] Calculated with the cc-pVDZ basis set at HF level in the current work. [b] Calculated at MP2/6-31++G** level [143]. [c] Calculated at MP2/cc-pVDZ level [142]. [d] Experimental value [144]. [e] Experimental value [114]. [f] Calculated at MP2/aug-cc-pVQZ [112]. [g] Calculated at MP2/6-31+G(d) [145]. [h] Experimental value [112]. [i] Experimental value [146]. [j] Experimental value [147, 148].

The properties of the pyridine clusters, isolated pyridine and water, obtained in this work with the cc-pVDZ basis set at HF level, are collected in table 4.1, together with experimental and other calculated values. The Pyr-H_2O dipole moment is over twice as large as that of pyridine. Water also increases polarizability of the system (if the interaction between molecules is neglected, in the first approximation the mean polarizability is additive). Table C.1, in appendix C collects the HF orbitals (determined using the cc-pVDZ basis set) of pyridine-water, pyridine and water listed in a way to show the correspondence between orbitals of the isolated systems to those of the cluster. For the occupied orbitals the correspondence is straightforward: the pyridine-water orbitals correspond to either pyridine or water orbitals, with the difference that the cluster orbitals have slightly lower energy than the corresponding pyridine orbitals and higher energy than the corresponding water orbitals. In the case of the unoccupied orbitals, some orbitals are a mixture of those of the two isolated systems. However, the majority of unoccupied pyridine-water orbitals have most of their

density located around to pyridine and the shape of those orbitals is virtually the same as for isolated pyridine. But there are also orbitals with density located around the water and corresponding to orbitals of isolated water. A few pyridine-water orbitals describe density spread all over the cluster and their correlation to isolated molecule ones is not straightforward (this is the case for the 31th and 32th pyridine-water orbital, see table C.1, in appendix C). In some cases, for instance, the 40th cluster orbital, in spite of the fact that most of its density is located around pyridine, does not correspond to any of the pyridine ones.

Since the main goal of this work is to obtain an insight into the water influence on resonances, it is crucial to compare systems which are described on the same level of approximation, to ensure that the differences between the systems come only from the presence of water, i.e. to compare 'like-for-like'. That is not trivial and it is the biggest challenge of this work: to ensure that the properties, e.g. polarizability, of the targets necessary to perform sophisticated calculations are described at the same level. Therefore it is important to correlate the orbitals of Pyr and Pyr-H_2O, since the polarization effect is described by promoting a target electron into a virtual orbital.

Apart from HF orbitals (used in SE and SEP calculations) CASSCF orbitals have also been generated (and used in CC scattering calculations); both HF and CASSCF orbitals were generated using MOLPRO. In the Pyr-H_2O active space 12 electrons are allowed to occupy 9 orbitals (CAS(12,9)). Various active spaces have been tested but this is the largest one for which calculations could be performed (calculations for larger active spaces are too computational demanding). This active space gives the first 9 target states (the ground state and 8 excited states) which correspond to the first 9 pyridine states calculated using CAS(10,8). We decided to restrict our calculation to 9 states to include only excited states linked to pyridine. For Pyr-H_2O and isolated pyridine in the State-Averaged procedure all 9 states have been used (in the State-Averaged procedure for pyridine calculations, presented in chapter 3, 33 states have been used).

4.1.2 SCATTERING

The R-matrix calculations were carried out with an R-matrix radius $a = 15a_0$ for Pyr-H_2O, Pyr-$(H_2O)_2$ and Pyr-$(H_2O)_3$ and $a = 18a_0$ for Pyr-$(H_2O)_5$. These values of the radius were chosen by analysing the radial charge densities of the target obtained using RADDEN (see section 2.6): above the chosen radius the charge density was negligible. The continuum basis sets included $\ell_{max} = 6$ partial wave ('Continuum ℓ_{max}' in table 4.2).

The calculations were carried out for three different scattering models (SE, SEP and CC) for Pyr-H_2O, and one scattering model (SE) for Pyr-$(H_2O)_2$, Pyr-$(H_2O)_3$ and Pyr-$(H_2O)_5$. Table 4.2 lists all parameters used to carry out the calculations for these systems. The SEP calculations were performed

System	Pyr-H_2O			Pyr-$(H_2O)_2$	Pyr-$(H_2O)_3$	Pyr-$(H_2O)_5$
Scattering model	SE	SEP	CC	SE	SE	SE
Basis set	cc-pVDZ	cc-pVDZ	cc-pVDZ	cc-pVDZ	cc-pVDZ	cc-pVDZ
R-matrix radius	$15a_0$	$15a_0$	$15a_0$	$15a_0$	$15a_0$	$18a_0$
No. of target states	1	1	9	1	1	1
Target description	HF	HF	CAS(12,9)	HF	HF	HF
No. of virtual orbitals	20	4-50	0-60	20	20	20
Deletion threshold	10^{-7}	10^{-7}	10^{-7}	10^{-7}	10^{-7}	10^{-7}
Continuum ℓ_{max}	6	6	6	6	6	6

Table 4.2: Details of the calculation for Pyr-H_2O (the SE, SEP and CC scattering models) Pyr-$(H_2O)_2$, Pyr-$(H_2O)_3$ and Pyr-$(H_2O)_5$ (SE model). The numbers of 'Continuum ℓ_{max}' are the maximum values of the angular momentum of the continuum partial waves. The meaning of the other labels is the same as in figure 3.4.

with 7 frozen (1-5a',1-2a'') orbitals and 19 active (6-17a',3-9a'') ones for Pyr-H_2O and compared with Pyr calculations with 6 frozen (1-4a_1,1-2b_2) and 15 active (5-11a_1,1-2b_1,3-7b_2,1a_2) orbitals.

4.1.3 POLARIZABILITY

In order to compare results of scattering calculations at the SEP level between pyridine and pyridine-water we need to have the same amount of polarization included in each calculation. If the polarization of two systems is not described at the same level, comparing the relative positions of a resonance in these two systems cannot give reliable information on the resonance shifts. For instance, if for one system the polarization is described much better than the other one, the resonance position may be stabilized* even if, in reality, the position of this resonance is destabilized. Therefore we performed additional calculations to find out how well the polarizability is described in our SEP calculations. The aim of this section is to introduce the procedure used to estimate the polarizability described in the calculations.

The polarizability describes the tendency of an atom or a molecule to distort the electron cloud in the presence of an external charge or electric field. In general usage the term refers to the *mean polarizability*, i.e., the average over the three main axes of the molecule (average of the diagonal components of polarizability tensor):

$$\alpha = (\alpha_{xx} + \alpha_{yy} + \alpha_{zz})/3. \tag{4.1}$$

Experimentally the polarizability can be measured as the ratio of induced dipole moment (μ_{ind}) to the external field (E):

$$\alpha = \mu_{\text{ind}}/E. \tag{4.2}$$

The UKRmol suite, specifically DENPROP (see section 2.6) can calculate the polarizability of the

*In this work *stabilization* means that a resonance energy decreases; resonance width, however, may decrease, increase or stay unchanged. Moreover, the term *destabilization* is used when the resonance energy increases.

target. This property is not used explicitly in the calculations, but as it has been mentioned, it can be used to give an insight in the quality of the polarization description in SEP calculations. In this program the components of the polarizability tensor, α_{ij}, for state k, are calculated using a sum-over-states perturbation method [149, 150]:

$$\alpha_{ij} = 2\sum_{n\neq 0}^{M} \frac{\langle\Phi_k|\mu_i|\Phi_n\rangle\langle\Phi_n|\mu_j|\Phi_k\rangle}{E_n - E_k}, \tag{4.3}$$

where the indexes i and j represent the Cartesian components x, y and z; E_n and $|\Phi_n\rangle$ are eigenvalue and eigenvector of the n^{th} excited state. The state for which the polarizability is calculated is labelled as: k with energy E_k. When $k = 0$, this state is the ground state ($|\Phi_0\rangle$ with ground state energy E_0). M indicates the number of states included in the sum; in principle the sum runs over all states, in practice only the states with the same spin symmetry as $|\Phi_k\rangle$ need to be included, due to the selection rule governing the dipole operator μ. The elements $\langle\Phi_k|\mu_i|\Phi_n\rangle$ and $\langle\Phi_n|\mu_j|\Phi_k\rangle$ form equation (4.3) are called the transition dipole moments, from state Φ_k to Φ_n and from state Φ_n to Φ_k, respectively.

The i-component of the polarizability of the ground state is expressed by:

$$\alpha_{ii} = 2\sum_{n\neq 0}^{M} \frac{|\langle\Phi_0|\mu_i|\Phi_n\rangle|^2}{E_n - E_0}. \tag{4.4}$$

In our calculations at the SEP level only the ground state of the target is described, but in the scattering calculations, the L^2 functions which are expressed by equations (2.100) and (2.101) (and are responsible for describing polarization effects) contain single excitations of the target:

$$\chi_i : \ (\text{core})^{N_d}(\text{valence})^{N-N_d-1}(\text{virtual})^1.$$

These single excitations are marked as Φ_n in equation (4.4) and they appear only for the scattering ('N+1') part of calculations.

Figures 4.2 and 4.3 show the convergence of the mean polarizability and its components for Pyr and FA for an increasing number of virtual orbitals (number of states) included in the SEP calculations. The pyridine mean polarizability, presented in figure 4.2, converges to 73.25 a_o^3, whereas its experimental value is 64.1 a_o^3 [147, 148]. Our polarizability calculated using 20 v.o. is already slightly over the experimental value.

A different picture is obtained for formic acid, presented in figure 4.3. In this case our mean polarizability converges to 18.73 a_o^3, while its experimental value is 22.4 a_o^3 [112] (this behaviour is expected by [150]). At this stage we are not able to answer why for pyridine our calculations give a much higher value of mean polarizability than the experimental value while our mean polarizability

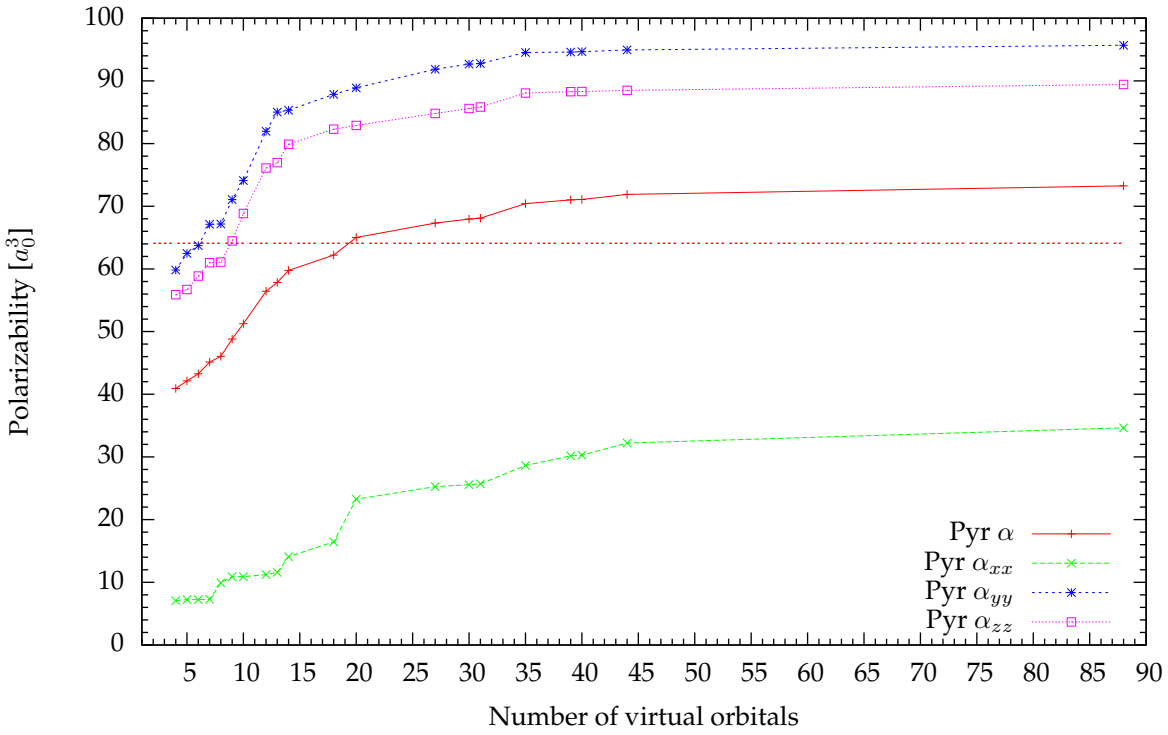

Figure 4.2: Convergence of the sum-over states mean polarizability of pyridine calculated using the HF model with number of virtual orbitals indicated in the x-axis. The red dotted line indicates the experimental value of the polarizability.

for formic acid is much below experimental value.

The attempt to establish how much polarizability is included in the calculations which give resonance energies close to experimental values for Pyr and FA systems (and to extrapolate the Pyr results for Pyr-H_2O) is presented in appendix C.2. However, the inconsistency of the estimated polarizability for Pyr and FA (in Pyr polarizability is overestimated, in FA underestimated) suggest that either there might be an error in calculating polarizability or our understanding of how to link the mean polarizability to our scattering results is not quite accurate. Therefore, this attempt of finding a way to establish how many v.o. we need to include in our calculations to obtain accurate resonance positions is not successful.

4.2 DIFFERENTIAL CROSS SECTION

In this section we present our results of elastic differential cross sections (EDCS) for Pyr-H_2O. We will analyse these results by comparing them together with results obtained for isolated pyridine and water. We do not present integral cross sections for Pyr-H_2O, since as a tool to analyse resonances we use time-delay, which is presented in the next section.

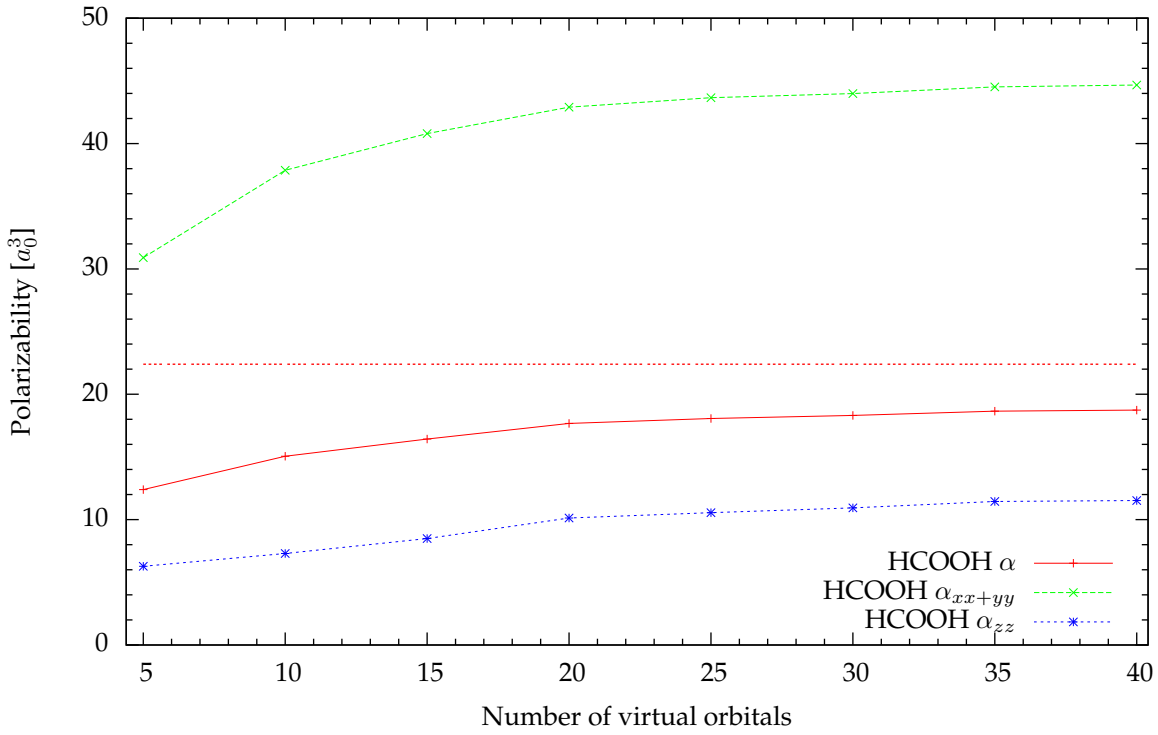

Figure 4.3: Convergence of the sum-over states mean polarizability of formic acid calculated using the HF model with number of virtual orbitals indicated in the x-axis. The red dotted line indicates the experimental value of the polarizability. Note that for symmetry reasons we are unable to separate the xx and yy components.

The calculations of EDCS for Pyr-H_2O have been performed at SE and SEP level. We present Pyr-H_2O EDCSs for the same energies as for the ones discussed in section 3.3.2 (in figure 3.6) of chapter 3. The Pyr-H_2O EDCS is compared with EDCS for isolated pyridine and isolated water, in figures 4.4 and 4.5.

We performed a test: calculations for pyridine have been carried out in C_{2v} and C_s point group. This showed that the program used to generate EDCS, i.e. POLYDCS (see section 2.6), produces slightly different results at high angles (160°-180°) depending on the point group used to carry out the calculations. Therefore, we are aware that the EDCS presented here cannot give reliable results at high angles.

Since Pyr-H_2O belongs to the C_s point group, the EDCSs for isolated pyridine and water have also been calculated for this point group (due to the numerical artefact at high angles, mentioned above; therefore the pyridine EDCS slightly differs from the one presented in section 3.3.2, at higher angles).

The SE EDCSs for the specific energies of all presented here systems are similar to the SEP EDCSs. In figures 4.4 and 4.5 we have plotted curves which are the sum of the isolated water and pyridine EDCSs. Clearly, the water EDCS has a small contribution and does not significantly change the

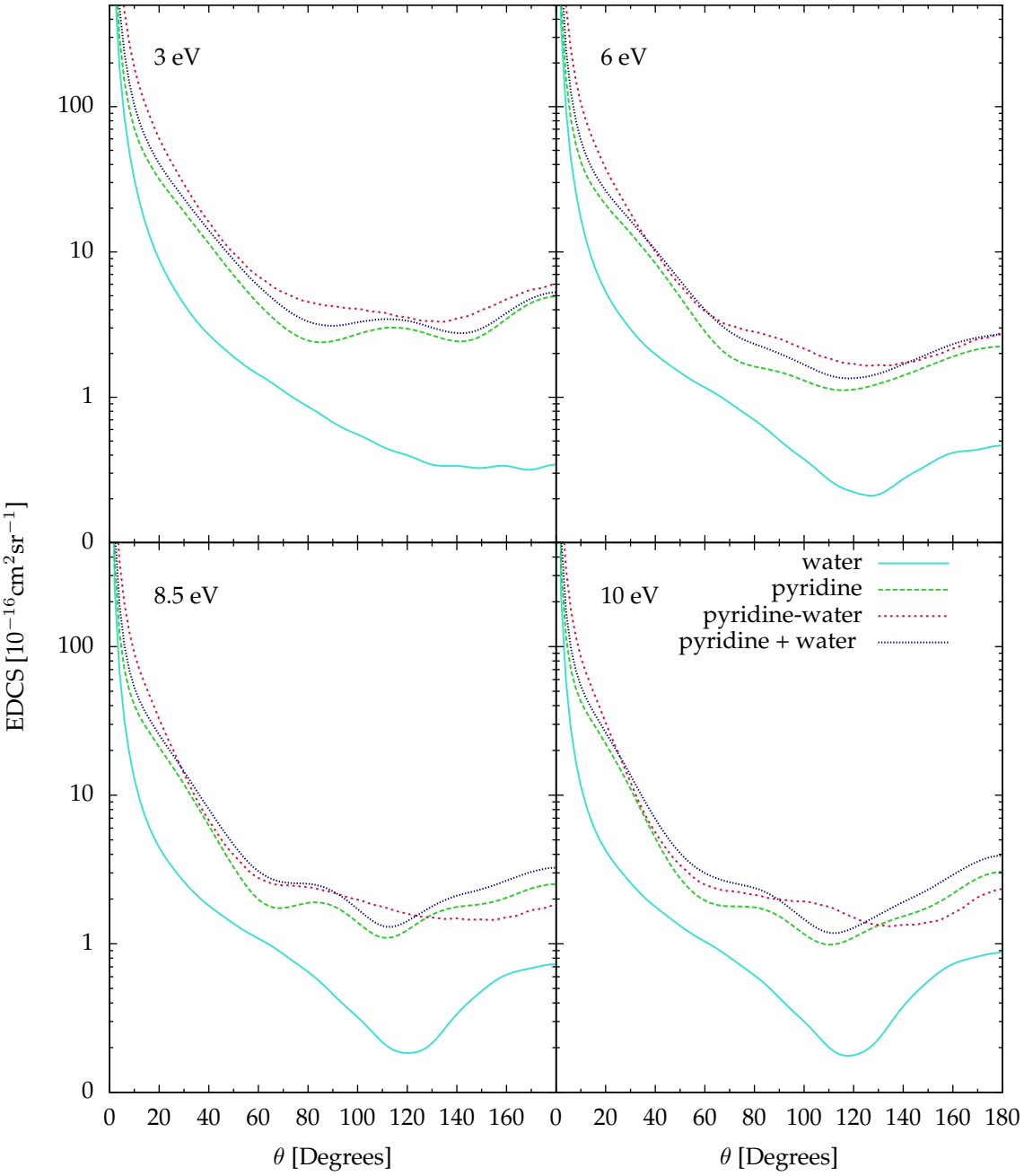

Figure 4.4: Elastic differential cross sections for electron scattering from systems indicated in the legend and energies marked in the panels, obtained using the compact basis set at SE level.

shape of pyridine EDCS (the 'pyridine + water' EDCS has similar shape to the pyridine EDCS) for all presented energies for both methods. Although Pyr and Pyr-H_2O EDCSs have similar sizes and quite similar shapes, we can see that the Pyr-H_2O EDCS is not simply the sum of water and pyridine EDCS. For instance, in all graphs, except the one for 3 eV at SEP level, the pyridine/'pyridine + water' EDCS has two local minima in the medium angle range (for the one for 3 eV at SEP level, has one minimum). Whereas Pyr-H_2O EDCS in this range is flatter. Only one local minimum is visible in the presented Pyr-H_2O graphs.

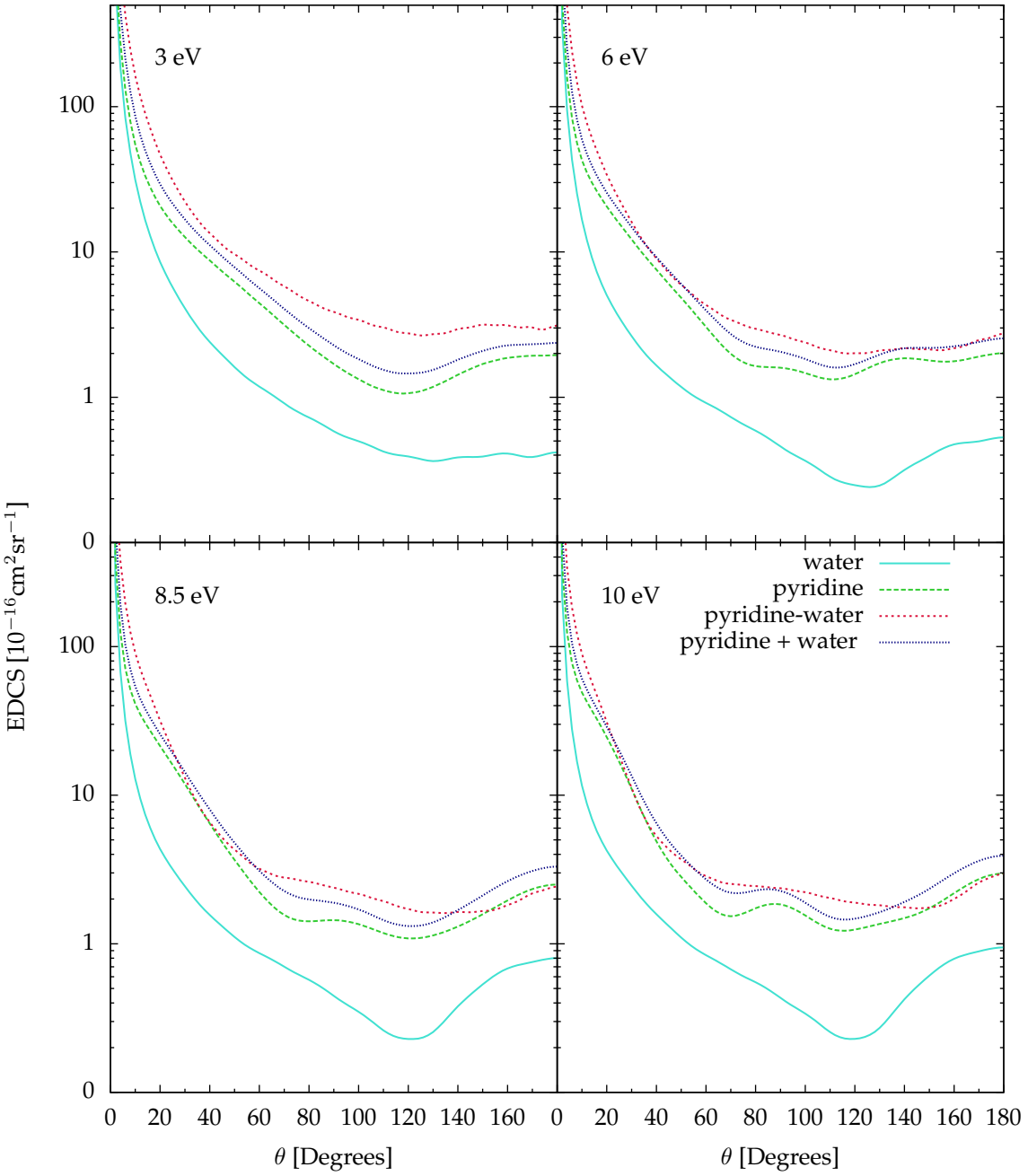

Figure 4.5: Elastic differential cross sections for electron scattering from systems indicated in the legend and energies marked in the panels, obtained using the compact basis set at SEP level, with 30 v.o. for Pyr and Pyr-H_2O and 10 v.o. for water calculations.

For all energies discussed here, except 6 eV, there are resonance peaks at SE level (see figure 4.12, in sections 4.3.1), which are slightly shifted towards lower energies for pyridine-water with respect to pyridine. The SEP EDCS have been calculated using 30 v.o. For this number of v.o. there is no resonance at 3 eV and 6 eV for Pyr and Pyr-H_2O. Above 8 eV pseudo-resonances are present in both systems. Analysing the the graphs, we can see that the differences between Pyr ('pyridine + water') and Pyr-H_2O are not significant regardless whether the energy of EDCS is resonant or non-resonant.

Therefore, it seems that the shifts of resonances positions caused by presence of water do not have significant effects on EDCS, and the dissimilarities are caused only by different properties (rotational constants, dipole moments) of these two systems.

4.3 RESONANCES IN PYRIDINE-WATER

The approach undertaken here is to start from the simplest scattering method, SE, which does not include correlation-polarization effects. The approximation is crude, since polarization has a significant effect on the characteristic of resonances. However, this method gives good insight into the water influence on resonance characteristics as the only differences between the calculations come from the presence of water. Next, SEP and CC calculations are presented, which give more reliable scattering results but are more difficult to interpret in terms of the comparison of the two systems. The resonance characteristics are analysed using the time-delay.

Investigating molecules bound with water in detail, we realised that the effect of the water on the resonance characteristics can be better analysed if it is separated into two contributions that can be studied separately. We distinguish direct and indirect effects (defined below). A study of these effects together with the total effect (also defined below) gives a better insight into the influence of water on our results. However, we use this approach only to analyse our SE results; to analyse our SEP and CC results we investigate only total effects. Nevertheless in the next chapter, we use this approach to analyse both SE and SEP results. The effects are as follows:

- Indirect effect: comprises of the changes to the molecular (here Pyr) geometry after binding with water. With few exceptions, the geometry of molecules in the clusters investigated by us differs from the equilibrium geometry. If the geometry of the molecule in a cluster is sufficiently different[†] from its equilibrium one, the resonance positions are shifted. This effect can be investigated without including water in the calculations (see figure 4.6).

- Direct effect: includes the changes in resonance characteristics caused by the presence of water, excluding the changes caused by differences in geometries, i.e. we compare resonance characteristics of the isolated molecule and the cluster (here Pyr and Pyr-$(H_2O)_n$), where the geometry of the molecule (Pyr) is the same as in cluster (see figure 4.6).

- Total effect: includes both direct and indirect effects, i.e. we compare resonance characteristics of molecule and cluster (Pyr and Pyr-$(H_2O)_n$) in their equilibrium geometries (see figure 4.6).

[†]The changes in resonance positions are observable if at least a few bond-lengths differ at least ~ 0.01 Å between the two geometries.

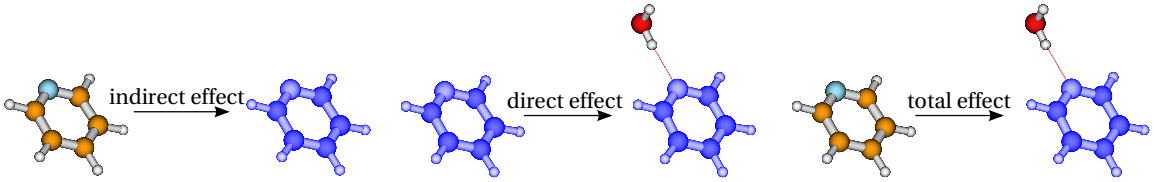

Figure 4.6: Schematic illustration of which systems are compared to investigate indirect, direct and total effects of water on clusters. The picture of pyridine in 'natural' colours indicates that pyridine is in its equilibrium geometry, the blue colour indicates the geometry of pyridine in the cluster. In the case of indirect effects, results of isolated pyridine in its equilibrium geometry are compared with isolated pyridine in the geometry which it has in the cluster. In the case of direct effects, results of pyridine in the geometry which it has in the cluster are compared with results for the cluster. In the case of total effects, results of isolated pyridine in its equilibrium geometry are compared with those for the cluster.

4.3.1 SE MODEL

In this section we investigate indirect, direct and total effects of water on the resonance characteristics. In the case of direct effects, we will also present and analyse our results for isolated HCOOH and HCOOH-H_2O and compare them to the results of T. C. Freitas *et al.* [27] who performed calculations for a number of clusters (HCOOH-H_2O and HCOOH-$(H_2O)_2$ with water binding to different sites). The geometries of those clusters have been provided to us by one of the authors. We performed R-matrix calculations for those systems. Our results for FA clusters are qualitatively in agreement with those obtained by T. C. Freitas *et al.* using the Schwinger multichannel method. Here, we present results only for one cluster which is depicted in figure 4.7. We chose this geometry because water acts as a proton donor as in the Pyr-H_2O system (among the clusters studied by T. C. Freitas *et al.* are some in which water plays either the proton donor or proton acceptor role). Our goal is to confirm that the conclusions of T. C. Freitas *et al.* for HCOOH-H_2O systems also hold for the direct effect in Pyr bound to water.

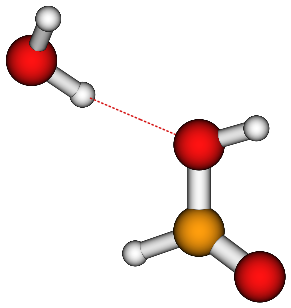

Figure 4.7: Geometrical structure of the HCOOH-H_2O for which results are presented in this chapter. The geometry comes from [27]. Generated using MOLDEN.

The investigation of the direct effect for FA differs from that for Pyr. Namely, in our definition of direct effect we compare results for the cluster in its equilibrium geometry with those for the molecule in the same geometry as in the cluster, which usually, is not the equilibrium geometry of the molecule. However, the direct effect could be defined in more general way: without specifying that cluster is in its equilibrium geometry. The geometry of formic acid in T. C. Freitas *et al.* work is kept the same in all of studied by them clusters and it is the geometry of isolated FA in its equilibrium geometry. Therefore, in the work of T. C. Freitas *et al.* only the explicit effect of water is considered,

(changes in geometry are not included), so the investigation of FA also counts as a looking at the direct effect.

The last step will be studying the systems in terms of total effects. In this case our conclusions on Pyr-H_2O can be compared to those of E. M. de Oliveira *et al.* [140] who performed calculations for isolated phenol and phenol-H_2O clusters in their equilibrium geometries. Comparison of these systems gives total effects of water on isolated system.

Since only the pure shape resonances ($1\ ^2B_1$ and $1\ ^2A_2$ for pyridine, $1\ ^2A''$ for formic acid and $1\ ^2A'$, $1\ ^2A''$ for phenol) can be fully described at SE level, we will mainly focus on comparison of these resonances and attempts to compare the Pyr resonance of mixed shape–core-excited character (the $2\ ^2B_1$) are left until section 4.3.3.

4.3.1.1 INDIRECT EFFECTS

In order to have a better insight into changes caused by water binding to pyridine, we investigated the changes in its geometry. Figure 4.8 illustrates the bond-lengths of pyridine in its equilibrium geometry, Pyr Eq, (figure 4.8a) and the geometry in the cluster with one water, Pyr 1w, (figure 4.8b). The changes in bond-lengths are smaller than $\sim 1.4\%$. The bond-lengths between all atoms are shorter for pyridine in the cluster.

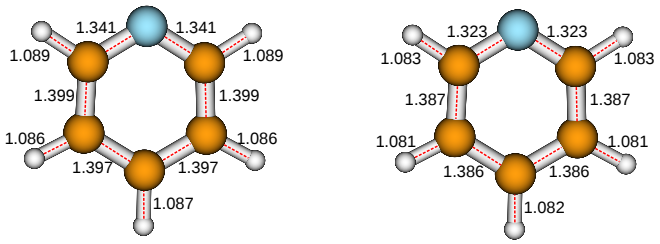

(a) Eq (b) 1w

Figure 4.8: Bond-lengths, in Å, of isolated pyridine in equilibrium geometry (Eq) and in cluster with one water (1w).

Figure 4.9 presents the time-delay plots for isolated pyridine in both geometries. All three resonances visible in the figure are slightly destabilized for Pyr 1w. Comparing the time-delays for Pyr Eq with Pyr 1w, a correlation between the bond-lengths (in general: volume of the molecule) and resonance positions can be noticed: a resonance position is lower in energy for the system with longer bond-lengths (bigger volume).

The resonance shifts are collected in table 4.3. The shifts are not significant, however it is important to notice the direction of the shift. A single water molecule binding to pyridine changes the

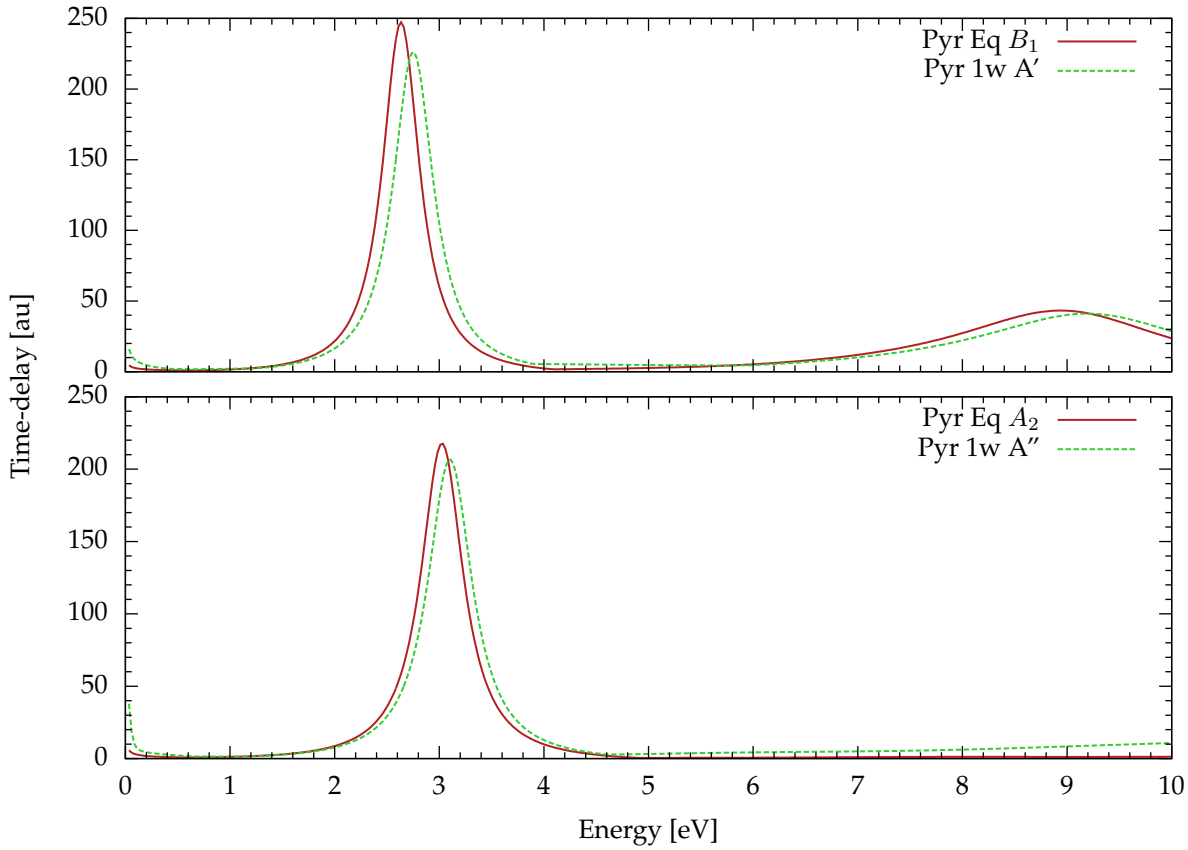

Figure 4.9: Time-delay for isolated pyridine in two different geometries: equilibrium (Eq) and its geometry in the cluster Pyr-H_2O (Pyr 1w). The calculations were performed at SE level with the cc-pVDZ basis set and 20 virtual orbitals. The time-delay is plotted for the symmetries indicated in the panels.

system	Δ^{E_r}	1 π^*	2 π^*
Pyr	E_r^{1w}-E_r^{Eq}	0.12	0.08

Table 4.3: Shifts in the resonance positions of isolated pyridine in the geometry corresponding to the clusters with respect to isolated pyridine in their equilibrium geometry. The calculations were performed at SE level with 20 v.o.

geometry (decreases its bond-lengths/volume) which destabilises the resonances[‡].

4.3.1.2 DIRECT EFFECTS

PYRIDINE, PYR-H_2O

Figure 4.10 presents the time-delay for isolated pyridine in its Pyr-H_2O geometry (Pyr 1w) and Pyr-H_2O in its equilibrium geometry. Therefore, it illustrates the direct effect of water on Pyr (we do not include the changes in geometry). In this case water stabilizes all resonances visible in the figure.

FORMIC ACID, FA-H_2O

The same situation can be observed in figure 4.11 for isolated formic acid in its geometry in the cluster

[‡]In the next chapter, we will find out that the opposite behaviour is observed for thymine-$(H_2O)_5$.

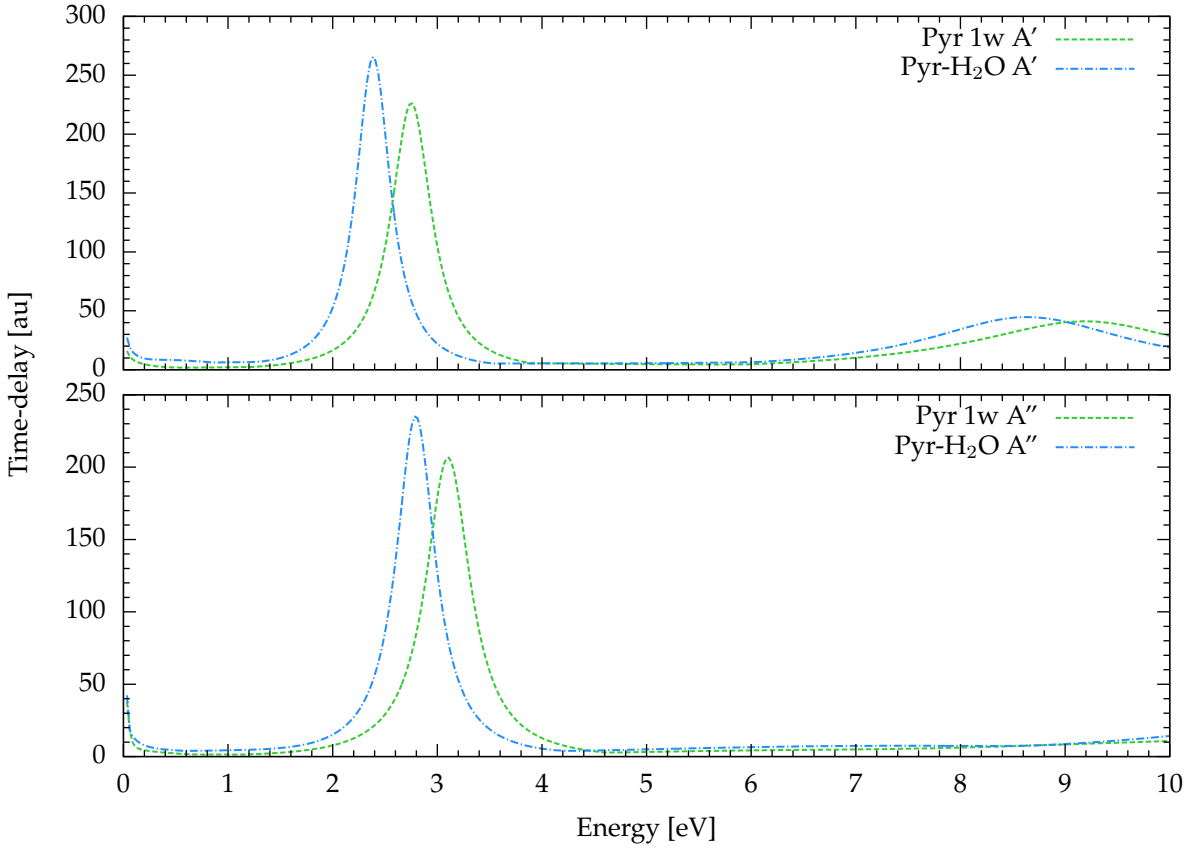

Figure 4.10: Time-delay for isolated pyridine in its geometry in the cluster Pyr-H_2O (Pyr 1w) and for Pyr-H_2O in its equilibrium geometry. The calculations were performed at SE level with the cc-pVDZ basis set and 20 virtual orbitals. The time-delay is plotted for the symmetries indicated in the panel.

FA-H_2O (FA 1w) and the FA-H_2O cluster in its equilibrium geometry.

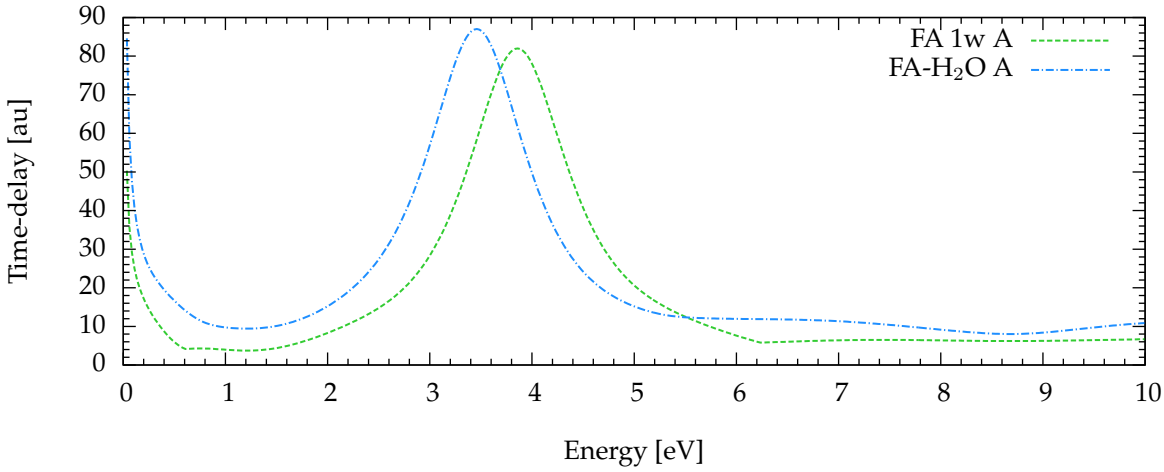

Figure 4.11: Time-delay for isolated formic acid in its geometry in the cluster FA-H_2O (FA 1w) and for FA-H_2O in its equilibrium geometry. The calculations were performed at SE level with the cc-pVDZ basis set and 20 virtual orbitals. The time-delay is plotted for the symmetries indicated in the panel.

Table 4.4 collects resonance shifts for Pyr and FA. The shift in the FA cluster is similar in size with the one presented by T. C. Freitas *et al.* [27], they reported shift of 0.5 eV. The changes between our

and their results may be due to different basis set used in calculations (they used aug-cc-pVDZ, while we used cc-pVDZ basis set). The direction of the shifts (stabilization of resonances) of the studied systems confirms the conclusion by T. C. Freitas *et al.* [27], that water acting as proton donor (as in these cases) stabilizes resonances[§].

system	Δ^{E_r}	1 π^*	2 π^*
Pyr	E_r^{1w}-E_r^{Eq}	-0.36	-0.31
FA	E_r^{1w}-E_r^{Eq}	-0.40	–

Table 4.4: Shifts in the resonance positions of pyridine and formic acid for the case where geometry does not change in the cluster. The calculations were performed at SE level with 20 v.o. See text for details.

4.3.1.3 TOTAL EFFECTS

Figure 4.12 illustrates the time-delay for isolated pyridine (Eq) and Pyr-H_2O in their equilibrium geometries. We see that the presence of water stabilizes the resonances but the changes are not significant. The first shape resonance ($1\ ^2B_1$ or $1\ \pi^*$ resonance) is shifted to lower energy by about 0.24 eV compared to that of isolated pyridine. The second shape resonance ($1\ ^2A_2$ or $2\ \pi^*$ resonance) is shifted to lower energy by about 0.21 eV.

The total effect of water is by definition the sum of indirect and direct effects. Indeed, summing the resonance shifts for indirect (see table 4.3) and direct effect (see table 4.4) gives the shifts due to the total effects (see table 4.5).

system	Δ^{E_r}	1 π^*	2 π^*
Pyr	E_r^{1w}-E_r^{Eq}	-0.24	-0.21

Table 4.5: Shifts in the resonance positions of isolated pyridine in its equilibrium geometries with respect to Pyr-H_2O in its equilibrium geometries. The calculations were performed at SE level with 20 v.o.

The change in geometry induced by water has an opposite effect on the resonance shift than the explicit presence of water. The resonance positions for pyridine in equilibrium geometry are lower in energy than those for pyridine in geometry of the cluster but higher in energy than those for Pyr-H_2O. The direct effects are stronger than indirect ones, therefore as a result of the total effects, all resonances are stabilized. In terms of direct effects, the stabilization of the resonances is caused by the fact that water is a proton donor (as the introduction to this chapter explains that was shown by T. C. Freitas *et al.* [27]). However, in case of the indirect effect there is no qualitative picture to explain the water effect on destabilization of the resonances.

[§]In the next chapter, we will find out that the analysis of thymine clusters also confirm this conclusion.

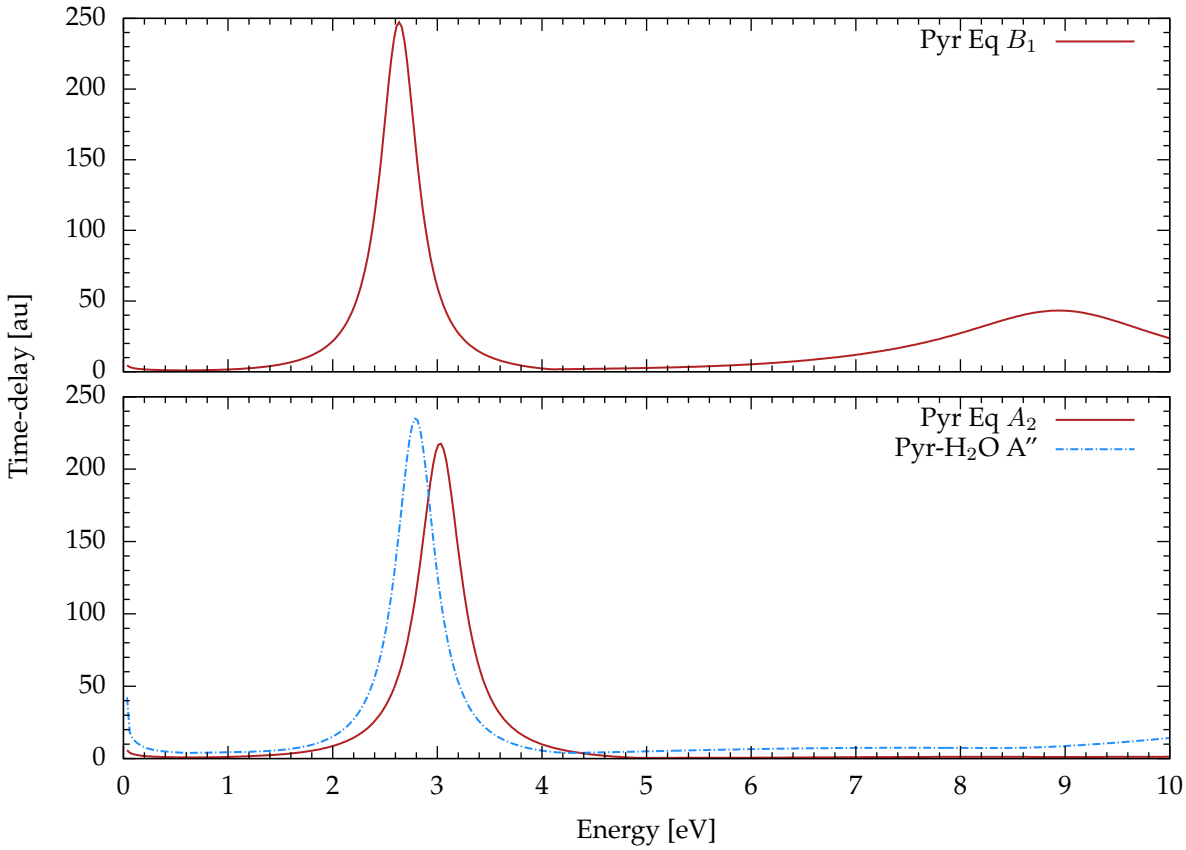

Figure 4.12: Time-delay for isolated pyridine (Eq) and Pyr-H_2O in their equilibrium geometries. The calculations were performed at SE level with the cc-pVDZ basis set and 20 virtual orbitals. The time-delay is plotted for symmetries indicated in the panel.

The resonance shift in the phenol-water system is -0.07 eV for the first π^*resonance and -0.13 eV for the second one. E. M. de Oliveira *et al.* [140] studied total effects and we cannot look at direct and indirect effects separately. However, it is reasonable to assume that as in pyridine, the direct effect are stabilizing and the indirect are either destabilizing or very mildly stabilizing.

Qualitatively the conclusions for our SE result for the resonance characterisitics are in agreement with those of T. C. Freitas *et al.* [27] for formic acid (direct effects) and E. M. de Oliveira *et al.* [140] for phenol (total effects) with 1 and 2 water molecules (for various geometries) at SE level.

4.3.2 SEP MODEL

It has already been shown in the chapter 3 that the inclusion of more virtual orbitals in the scattering calculations, i.e. increasing polarization by promotion of a target electron to one of many virtual orbitals, stabilizes resonances. Therefore, it is key to describe the same amount of polarizability in the systems in order to compare their resonance positions. The method we hoped to use (described in 4.1.3) is not viable thus we cannot estimate how much of the polarizaibility of the systems is being described (nevertheless, we attempted to describe the dependence between resonance energies and polarizability for Pyr, Pyr-H_2O and FA; the results are presented in appendix C.2).

The only option was to look at how the resonance positions changed as we added virtual orbitals one by one. First, in the set of virtual orbitals for both targets were included only orbitals that have the same or similar electron charge distributions. Since the orbitals of pyridine-water have different energy to those of isolated pyridine, and since the cluster possesses additional orbitals with charge density connected to water, inclusion in both scattering calculations of the same number of virtual orbitals, does not guarantee that one of the electrons which is allowed to occupy one of the virtual orbitals will occupy the same orbitals in both systems. Nevertheless, most of pyridine-water orbitals are similar to those of pyridine and/or water orbitals.

In our calculations virtual orbitals are chosen in order of increasing energy (it is not possible to exclude an orbital with energy between the lowest and highest energy of selected orbitals). Unfortunately, only 4 virtual orbitals of the lowest energies of pyridine-water have the same or similar shape to those of pyridine. The 5$^{\text{th}}$ and 6$^{\text{th}}$ v.o. of pyridine-water (20$^{\text{th}}$ a' and 21$^{\text{th}}$ a' orbitals of pyridine-water in the table C.1, in appendix C)¶ are a mixture of pyridine and water orbitals and the two orbitals (both of a' symmetry) correspond only to one of pyridine (13$^{\text{th}}$ a_1 orbital of pyridine, in the table C.1). Table 4.6 presents the position of the two lowest shape resonances for the two systems and their shifts for various numbers of virtual orbitals. Inclusion of 4 v.o. gives the resonance shifts: 0.23 eV for the $1\ ^2B_1$ resonance and 0.22 eV for the $1\ ^2A_2$ resonance (at SE level the resonance shifts are: 0.24 eV and 0.21 eV for the first and second pure π^* resonance, respectively). Including an additional v.o. in the calculations for both systems decreases the shift (but the change is not significant, as observed in table 4.6, for 'v.o.' = 5). Nevertheless, comparing the relative positions of the resonances, when 6 v.o. of pyridine-water and 5 v.o. of pyridine are included (the 20$^{\text{th}}$ a' and 21$^{\text{th}}$ a' orbitals of pyridine-water correspond to 13$^{\text{th}}$ a_1 pyridine orbital), the shift for both resonances increases. However, including more v.o. decreases the shift again, and for calculations with 9 v.o. for Pyr-H_2O and 8 v.o. for pyridine, the shift is the same as for calculations with 4 v.o. It can be seen in table C.1, that pyridine-water orbitals with charge distribution around water and pyridine have much lower energy than the corresponding ones for the isolated systems, for instance, 10$^{\text{th}}$ v.o. and 12$^{\text{th}}$ v.o. (24$^{\text{th}}$ a' and 25$^{\text{th}}$ a') Pyr-H_2O orbitals. Inclusion of these orbitals, i.e. 10 v.o. and 13 v.o. for Pyr-H_2O and 9 v.o. and 12 v.o. for pyridine, increases the shift for the first shape resonances (the shift for the second resonances is unchanged). The 14$^{\text{th}}$ Pyr-H_2O v.o. (the 26$^{\text{th}}$ a' Pyr-H_2O orbital in table C.1), even if it has a charge distribution mostly around the pyridine, does not seem to correspond to any pyridine orbital. Including this orbital in the calculations, i.e. 14 v.o. for Pyr-H_2O and 12 v.o. for pyridine, changes the relative position of the first resonance even more. It can be seen from the table C.1 that

¶Throughout this section, the numbers in brackets are given for readers who are interested in the shape of orbitals illustrated in table C.1, in appendix C. In this table all (frozen, active, virtual) orbitals are numbered whereas in table 4.6 the number of virtual orbitals (for all symmetries: v.o. and amount of virtual orbitals per symmetry: v.o./sym) are given. Therefore the reader should be aware that the numbers in brackets are linked only to the table in appendix and are not connected to the amount of virtual orbitals counted in table 4.6.

among the 39 lowest virtual orbitals of pyridine-water (18^{th} a'– 42^{th} a', $10^{\text{th}}a''$– 23^{th} a'' orbital) there are 35 which correspond to isolated pyridine orbitals. The position of the shape resonances for isolated pyridine with 35 v.o. are in the best agreement with experiment (see chapter 3). By including 35 v.o. in Pyr-H_2O we include different orbitals than in the isolated systems. Unfortunately, since the orbitals with the lowest energies of the specific symmetry are selected, any orbital with energy lower than the energy of the last orbital of the specific symmetry cannot be eliminated. Therefore, in table 4.6 we compare the results for 39 v.o. and 35 v.o. for pyridine-water and pyridine, respectively (see figure 4.13). The highest number of v.o. for which the resonance positions are collected in table 4.6 are 50 v.o. for Pyr-H_2O and 44 v.o. for Pyr.

Pyr-H_2O				Pyridine				$E_r^{\text{Pyr-}H_2O}$-E_r^{Pyr}	
v.o.	v.o./sym	$E_r^{A'}$	$E_r^{A''}$	v.o.	v.o./sym	$E_r^{B_1}$	$E_r^{A_2}$	$\Delta_1^{E_r}$	$\Delta_2^{E_r}$
4	$2a'\ 2a''$	2.19	2.59	4	$1a_1\ 1b_1\ 1b_2\ 1a_2$	2.42	2.81	-0.23	-0.22
5	$3a'\ 2a''$	2.12	2.54	5	$2a_1\ 1b_1\ 1b_2\ 1a_2$	2.34	2.74	-0.22	-0.20
6	$4a'\ 2a''$	2.06	2.50	5	$2a_1\ 1b_1\ 1b_2\ 1a_2$	2.34	2.74	-0.28	-0.24
7	$4a'\ 3a''$	2.01	2.43	6	$2a_1\ 1b_1\ 2b_2\ 1a_2$	2.28	2.66	-0.27	-0.23
8	$5a'\ 3a''$	1.95	2.37	7	$3a_1\ 1b_1\ 2b_2\ 1a_2$	2.21	2.60	-0.26	-0.23
9	$6a'\ 3a''$	1.54	1.98	8	$3a_1\ 2b_1\ 2b_2\ 1a_2$	1.77	2.20	-0.23	-0.22
10	$7a'\ 3a''$	1.48	1.95	9	$4a_1\ 2b_1\ 2b_2\ 1a_2$	1.72	2.17	-0.24	-0.22
13	$8a'\ 5a''$	1.34	1.86	12	$5a_1\ 2b_1\ 4b_2\ 1a_2$	1.62	2.08	-0.28	-0.22
14	$9a'\ 5a''$	1.32	1.85	12	$5a_1\ 2b_1\ 4b_2\ 1a_2$	1.62	2.08	-0.30	-0.23
20	$12a'\ 8a''$	1.13	1.60	18	$7a_1\ 3b_1\ 6b_2\ 2a_2$	1.42	1.83	-0.29	-0.23
30	$19a'\ 11a''$	0.69	1.11	27	$11a_1\ 5b_1\ 8b_2\ 3a_2$	0.99	1.35	-0.30	-0.24
35	$22a'\ 13a''$	0.60	0.99	31	$13a_1\ 5b_1\ 10b_2\ 3a_2$	0.90	1.23	-0.30	-0.24
39	$25a'\ 14a''$	0.37	0.85	35	$15a_1\ 6b_1\ 11b_2\ 3a_2$	0.75	1.09	-0.38	-0.24
50	$30a'\ 20a''$	0.11	0.59	44	$28a_1\ 10b_1\ 21b_2\ 6a_2$	0.35	0.83	-0.24	-0.24

Table 4.6: Position of the first and second shape resonances of pyridine and Pyr-H_2O. Also given are the resonance shifts ($\Delta_1^{E_r}$ and $\Delta_2^{E_r}$). The numbers of virtual orbitals used in the calculations are indicated in the column 'v.o.'; in the column 'v.o./sym' the number of virtual orbitals per symmetry is listed.

It can be seen that the shift for the second shape resonance is hardly influenced by the number of v.o. The shift for the first shape resonances is more significantly affected (from 0.23 eV for 4 v.o. to 0.38 eV for 39 v.o.). The reason for the bigger effect on the first resonance is not clear at the moment.

As was the case for the SE calculations, the conclusions for SEP results are also in agreement with those of T. C. Freitas *et al.*'s formic acid-water calculations at SEP level [27]. They observed that inclusion of polarization stabilizes resonance even more than at SE level. In their case the inclusion of polarization changed the shift by about 20% (from $\sim$ 0.5 eV at SE level to $\sim$ 0.6 eV at SEP level). That is also the case for the pyridine-water $1\ ^2B_1$ shape resonance: the shift also changes by about 20% (from $\sim$ 0.24 eV at SE level to $\sim$ 0.30 eV at SEP level with 35 v.o.). Nevertheless, this is not the case for the $1\ ^2A_2$ shape resonance, for which the shift stays almost the same after including polarization.

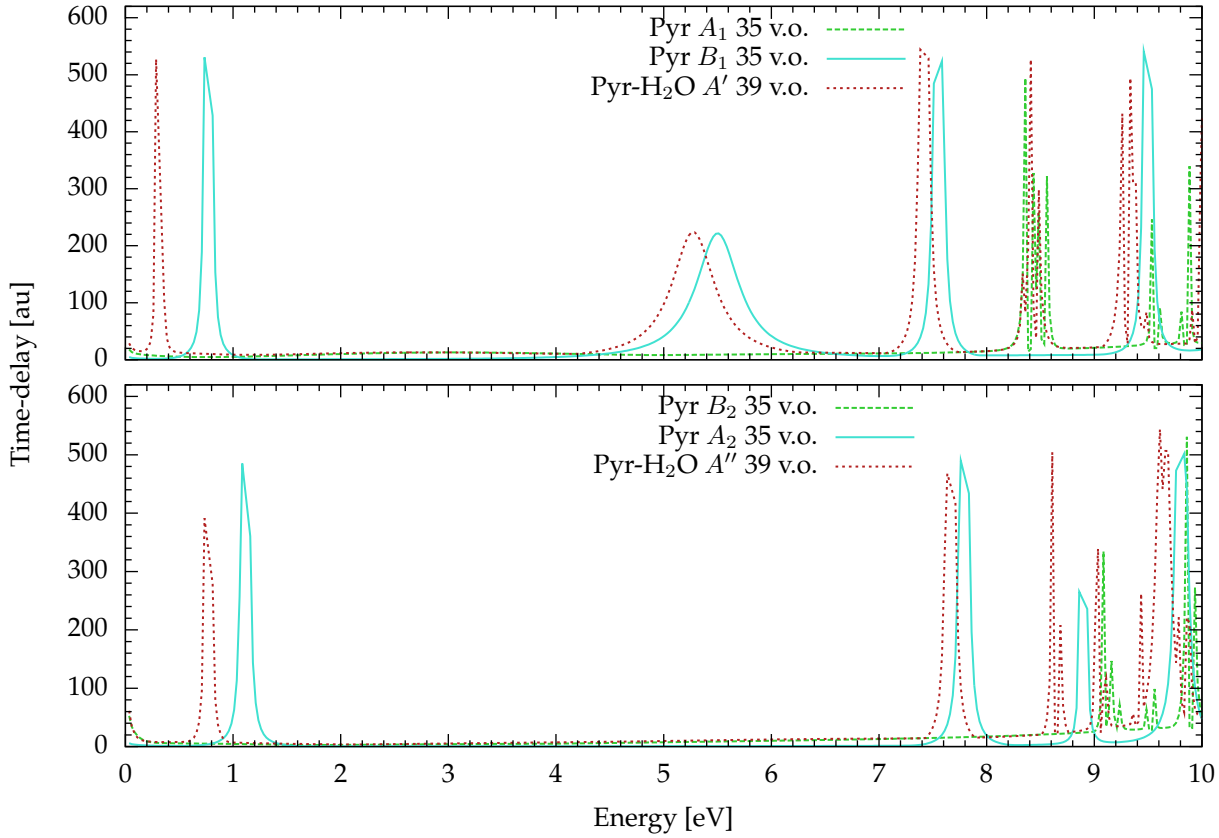

Figure 4.13: The time-delay of pyridine and Pyr-H_2O for the symmetries indicated in the panels, as a function of electron energy. The calculations were performed at SEP level using the cc-pVDZ basis set and the number of virtual orbitals (v.o.) indicated in the figure. The spikes appearing above 7 eV are pseudo-resonances.

This means that the second π^*resonance is less sensitive to polarization.

4.3.3 CC MODEL

The approach undertaken in this section is similar to the previous ones. First, results for 0 v.o. are presented (figure 4.14). Next results with inclusion of additional polarization are discussed. The numbers of virtual orbitals included in calculation has been chosen as in the previous section. The energies and energy order of CASSCF orbitals differ from HF orbitals but the changes are not very significant; hence the orbitals are not presented in the appendix.

Figure 4.14 shows that results for pyridine and pyridine-water, with 0 v.o., do not differ much. Similarly to SE and SEP calculations, the pure shape resonances are slightly shifted to lower energy in the presence of water. This is also the case for some of the core-excited (and mixed shape–core-excited) resonances but not for all. The $1\ ^2A_1$ and $2\ ^2A_1$ resonances (respectively, at ∼7.6 eV and ∼9.5 eV in A' symmetry for Pyr-H_2O) and $1\ ^2B_2$ and $2\ ^2B_2$ resonances (respectively, at ∼8.2 eV and ∼8.6 eV in A'' symmetry for Pyr-H_2O) of pyridine-water are slightly shifted to higher energy compared to isolated pyridine. It can also be noted that pyridine has an extra peak at ∼7.5 eV ($3\ ^2B_1$

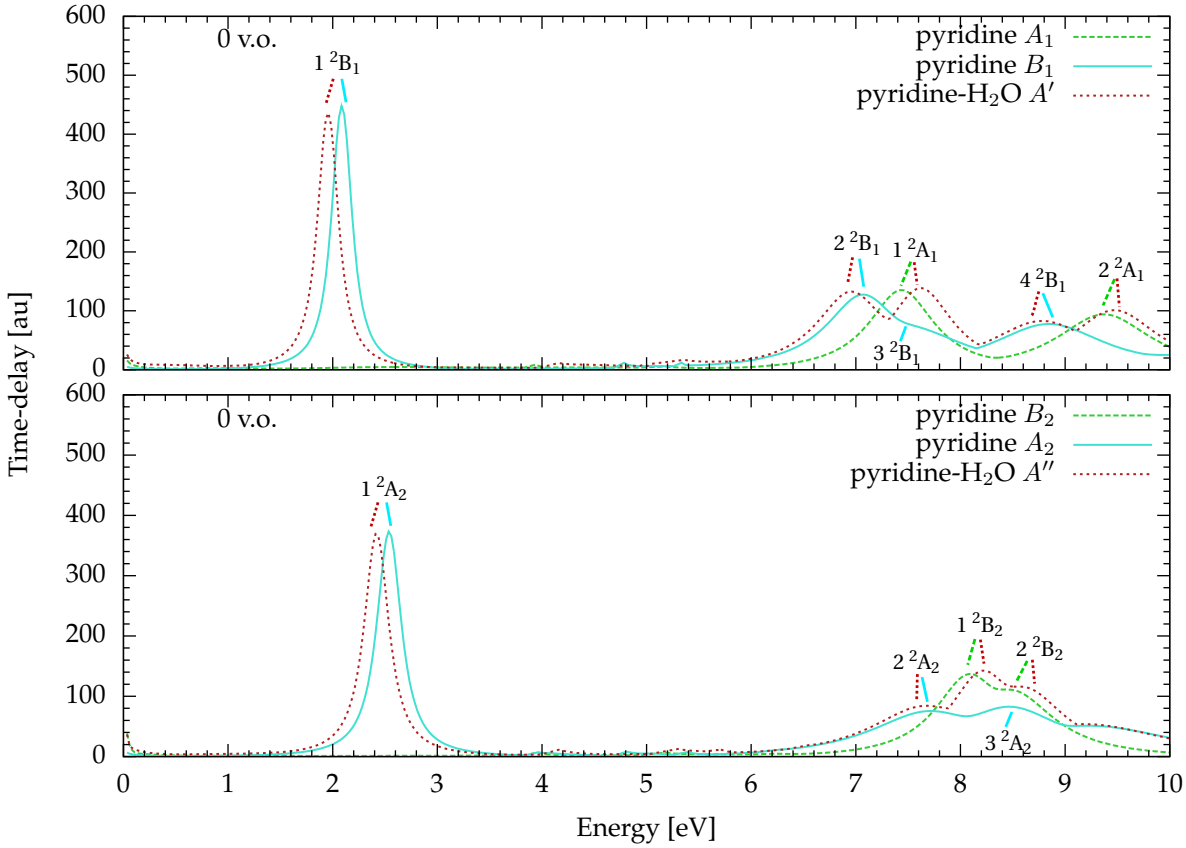

Figure 4.14: The time-delay of pyridine and Pyr-H_2O for corresponding symmetries indicated in the panels, as a function of electron energy. The calculations were performed at CC level using the cc-pVDZ basis set for 0 virtual orbitals. The ground state and 8 excited states are included in both calculations.

resonance) very close to another one at ∼7.1 eV (2 $^2B_1$ resonance). This extra peak cannot be seen in the pyridine-water plot due to the lower symmetry of the system (i.e. it is hidden by another peak).

Inclusion of polarization (virtual orbitals) into calculations lowers all of the resonances visible in figure 4.14. The dependence of time-delay on the number of virtual orbitals for pyridine and pyridine-water is shown in figure 4.15 and 4.16, respectively. In figure 4.15, we also plotted the time-delay for our best calculations presented in chapter 3. It can easily be seen that inclusion of 6 virtual orbitals into pyridine calculation and 7 v.o. into Pyr-H_2O one do not change the resonance positions much, but inclusion of 18 v.o. and 20 v.o. for Pyr and Pyr-H_2O, respectively, changes the position of resonances significantly and new resonances appear. The 2 $^2B_1$ and 3 $^2B_1$ resonances of pyridine (at ∼7.1 eV and ∼7.5 eV) which are not completely distinguished for calculations with 0 v.o. and 6 v.o. are now more separated. Also, one new structure appears at the time-delay for pyridine-water of A' symmetry at 6.66 eV (see figure 4.16 or table 4.7, 20 v.o.). Inclusion of additional polarization stabilizes all of the Pyr-H_2O resonances presented here (there are no destabilized resonances any longer). The resonance spectra of Pyr and Pyr-H_2O for the calculations with the highest number of v.o. presented in this work (80 v.o. for Pyr and 94 v.o. for Pyr-H_2O) are illustrated in figure 4.17. The

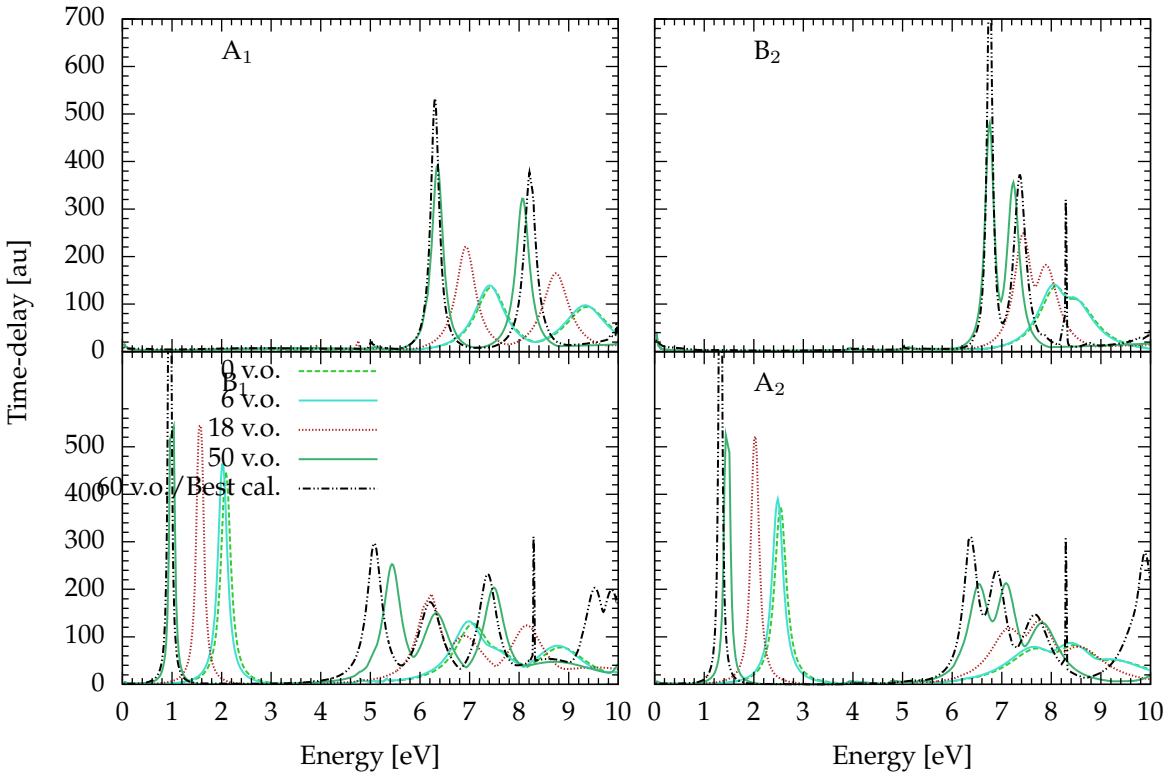

Figure 4.15: CC time-delay for pyridine calculated with cc-pVDZ basis set; symmetries and number of virtual orbitals (v.o.) are indicated in the figure. 'Best cal.' refers to out best calculations at CC level for isolated pyridine described in chapter 3.

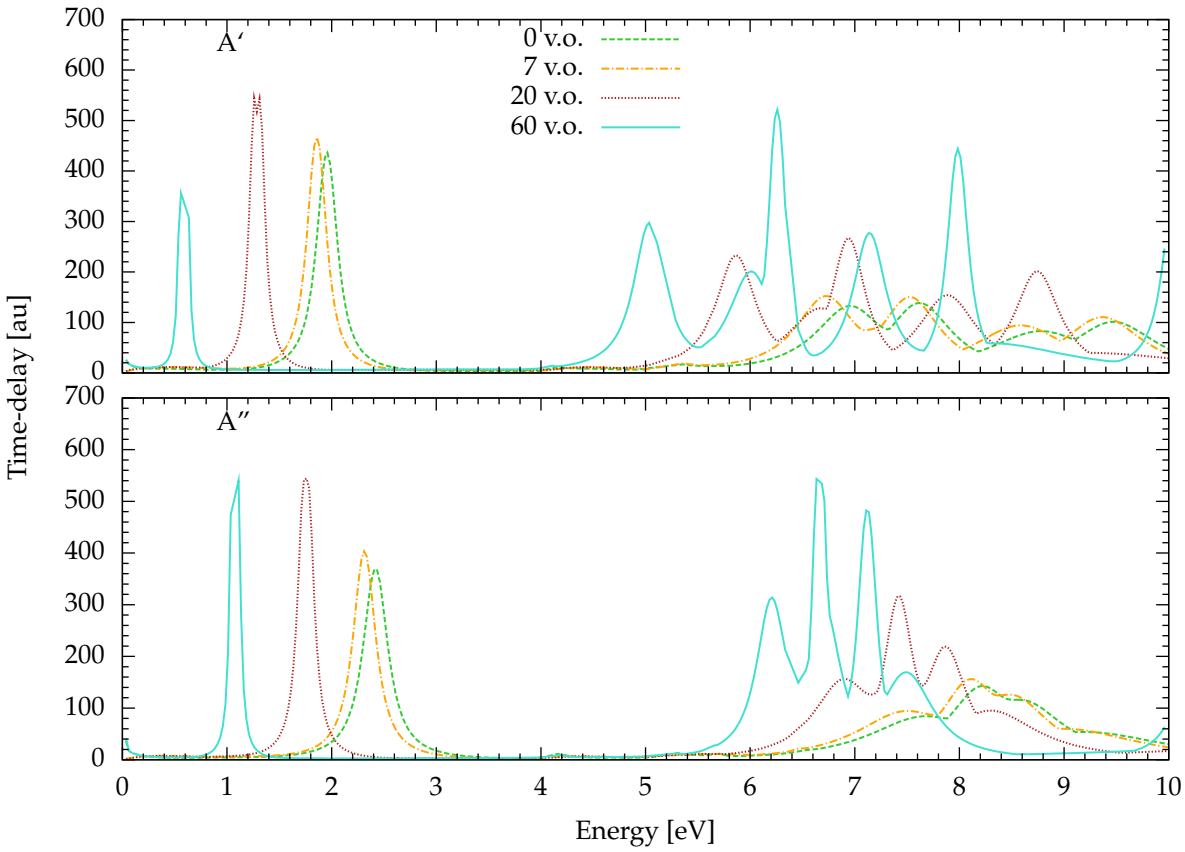

Figure 4.16: CC time-delay for Pyr-H_2O calculated with cc-pVDZ basis set; symmetries and number of virtual orbitals (v.o.) are indicated in the figure.

Res	Pyr-H_2O	Pyridine		$E_r^{\text{Pyr-}H_2O}$-E_r^{Pyr}	Res	Pyr-H_2O	Pyridine		$E_r^{\text{Pyr-}H_2O}$-E_r^{Pyr}
	$E_r^{A'}$	$E_r^{A_1}$	$E_r^{B_1}$	Δ^{E_r}		$E_r^{A''}$	$E_r^{B_2}$	$E_r^{A_2}$	Δ^{E_r}
	0 v.o.	0 v.o.				0 v.o.	0 v.o.		
$1\,^2B_1$	1.95		2.09	-0.14	$1\,^2A_2$	2.42		2.53	-0.11
$2\,^2B_1$	6.96		7.07	-0.11	$2\,^2A_2$	7.65		7.71	-0.06
$3\,^2B_1$	7.62		7.44	0.18	$1\,^2B_2$	8.22	8.09		0.13
$1\,^2A_1$	7.62	7.44		0.18	$3\,^2A_2$	8.22		8.46	-0.24
$4\,^2B_1$	8.78		8.85	-0.07	$2\,^2B_2$	8.61	8.46		0.15
$2\,^2A_1$	9.47	9.37		0.10	$4\,^2A_2$	9.20		9.20	0.00
	7 v.o.	6 v.o.				7 v.o.	6 v.o.		
$1\,^2B_1$	1.85		2.03	-0.18	$1\,^2A_2$	2.31		2.48	-0.17
$2\,^2B_1$	6.73		6.98	-0.25	$2\,^2A_2$	7.49		7.65	-0.16
$3\,^2B_1$	7.52		7.04	0.48	$1\,^2B_2$	8.11	8.05		0.06
$1\,^2A_1$	7.52	7.04		0.48	$3\,^2A_2$	8.11		8.40	-0.29
$4\,^2B_1$	8.59		8.77	-0.18	$2\,^2B_2$	8.49	8.40		0.09
$2\,^2A_1$	9.37	9.34		0.03	$4\,^2A_2$	9.05		9.16	-0.11
	20 v.o.	18 v.o.				20 v.o.	18 v.o.		
$1\,^2B_1$	1.29		1.56	-0.27	$1\,^2A_2$	1.75		2.02	-0.27
$2\,^2B_1$	5.87		6.19	-0.32	$2\,^2A_2$	6.90		7.15	-0.25
$3\,^2B_1$	6.66		6.90	-0.24	$1\,^2B_2$	7.42	7.44		-0.02
$1\,^2A_1$	6.94	6.93		0.01	$3\,^2A_2$	7.42		7.75	-0.33
$4\,^2B_1$	7.89		8.15	-0.26	$2\,^2B_2$	7.87	7.89		-0.02
$2\,^2A_1$	8.74	8.74		0.00	$4\,^2A_2$	8.30		8.53	-0.23
	60 v.o.	50 v.o.				60 v.o.	50 v.o.		
$1\,^2B_1$	0.58		1.00	-0.42	$1\,^2A_2$	1.08		1.46	-0.38
$2\,^2B_1$	5.08		5.44	-0.36	$2\,^2A_2$	6.21		6.56	-0.35
$3\,^2B_1$	6.02		6.34	-0.32	$1\,^2B_2$	6.67	6.74		-0.07
$1\,^2A_1$	6.27	6.34		-0.07	$3\,^2A_2$	6.76		7.08	-0.32
$4\,^2B_1$	7.15		7.49	-0.34	$2\,^2B_2$	7.13	7.23		-0.10
$2\,^2A_1$	7.99	8.06		-0.07	$4\,^2A_2$	7.49		7.81	-0.32
	94 v.o.	80 v.o.				94 v.o.	80 v.o.		
$1\,^2B_1$	0.47		0.91	-0.44	$1\,^2A_2$	0.96		1.37	-0.41
$2\,^2B_1$	4.90		5.33	-0.43	$2\,^2A_2$	6.09		6.46	-0.37
$3\,^2B_1$	5.90	6.22		-0.32	$1\,^2B_2$	6.53	6.61		-0.08
$1\,^2A_1$	6.12		6.24	-0.12	$3\,^2A_2$	6.60		6.99	-0.39
$4\,^2B_1$	7.02		7.40	-0.38	$2\,^2B_2$	6.98	7.11		-0.13
$2\,^2A_1$	7.83	7.93		-0.10	$4\,^2A_2$	7.37		7.71	-0.34

Table 4.7: Positions of the shape and core-excited resonances of pyridine and Pyr-H_2O at CC level. Also given are the energy shifts of the resonances in the cluster (Δ^{E_r}). The energy of the resonances is given for various numbers of virtual orbitals indicated in the table.

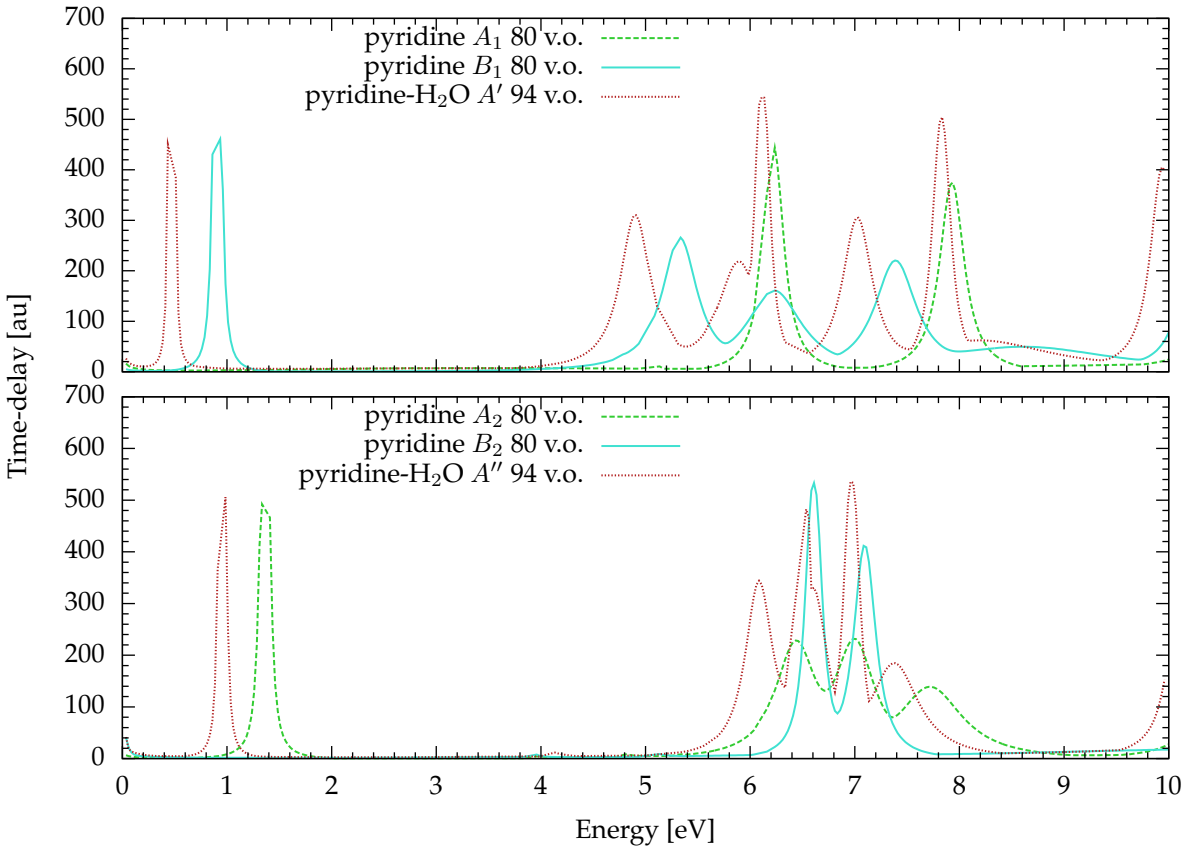

Figure 4.17: The time-delay for Pyr and Pyr-H_2O calculated at CC level with cc-pVDZ basis set; symmetries and number of virtual orbitals are indicated in the figure.

positions of the resonances and their shifts for different numbers of v.o. are collected in table 4.7.

The CC calculations show that water stabilizes all resonances presented in this section (the shape and core-excited resonances as well as the resonances with mixed shape–core-excited character) for calculations with higher number of v.o. than 20. However the resonance shifts are not the same for all resonances. The majority of the resonance shifts in calculations with 60 (and 94) v.o. for Pyr-H_2O compared with 50 (and 80) v.o. for Pyr are approximately between -0.3 eV and -0.4 eV. For resonances $1\,^2A_1$, $2\,^2A_1$, $1\,^2B_2$ and $2\,^2B_2$ the shifts are not higher than -0.13 eV.

4.4 Resonances in Pyr-$(H_2O)_N$, n = 2, 3, 5

The structure of the systems presented in this section is illustrated in figure 4.18. All calculations presented here are at SE level. Pyr-$(H_2O)_2$ and Pyr-$(H_2O)_5$ belong to C_1 point group, whereas Pyr-$(H_2O)_3$ belongs to C_s (note that Pyr-H_2O also belongs to C_s point group and isolated Pyr to C_{2v}). Table 4.8 illustrates the correlation of irreducible representations between these point groups.

In this section we present indirect and total effects of water on pyridine. Direct effects are not presented in this section as they can be derived from the the total and indirect effects (as a difference between them).

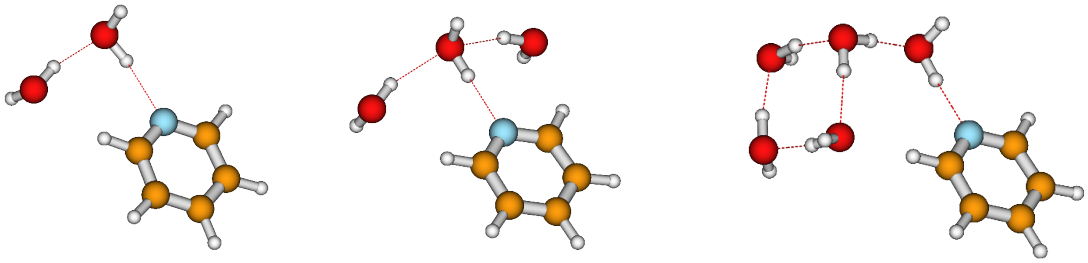

Figure 4.18: Geometrical structure of the pyridine-water clusters studied in this work. Generated using MOLDEN. The geometry of Pyr-$(H_2O)_n$, n = 2, 3 comes from [141] and the geometry of Pyr-$(H_2O)_5$ comes from [142].

n	n = 0	n = 1, 3	n = 2, 5
P.G.	C_{2v}	C_s	C_1
	A_1,B_1	A'	A
	B_2,A_2	A''	

Table 4.8: Correlation table for point groups of Pyr-$(H_2O)_n$, n = 1, 2, 3, 5.

INDIRECT EFFECTS

The investigation of changing the geometry of pyridine induced by water is presented for clusters Pyr-$(H_2O)_n$, n = 2, 3, 5. Figure 4.19 illustrates the bond-lengths for the equilibrium geometry of pyridine, Pyr Eq, (figure 4.19a) and for the geometry of pyridine in the cluster with five water molecules, Pyr 5w, (figure 4.19b). The changes in bond-lengths between these systems are smaller than $\sim 1.4\%$. The changes in bond-lengths between pyridine in cluster Pyr-$(H_2O)_5$ (Pyr 5w) and pyridine in clusters with fewer water molecules: Pyr-H_2O (Pyr 1w), Pyr-$(H_2O)_2$ (Pyr 2w), Pyr-$(H_2O)_3$ (Pyr 3w), are no larger than $\sim 0.2\%$. Therefore, the comparison of time-delay between Pyr Eq and Pyr 2w, Pyr 3w, Pyr 5w does not differ from that presented in section 4.3.1.1. Indeed, the changes in time-delay for Pyr 1w, Pyr 2w, Pyr 3w and Pyr 5w (presented in figure 4.20) are not noticeable. This is not surprising, since in each cluster only one water molecule attaches to the ring (to the nitrogen); the other water molecules bind to water. Thus the geometry of pyridine in the clusters is similar.

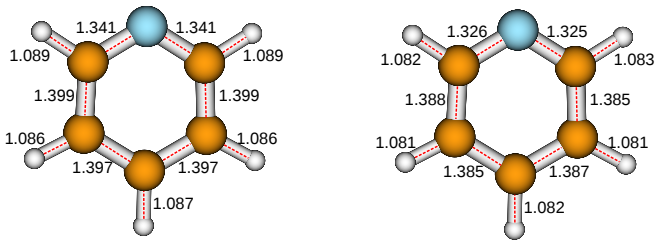

(a) Pyr Eq (b) Pyr 5w

Figure 4.19: Bond-lengths, in Å, of pyridine in equilibrium geometry (Pyr Eq) and in clusters with 5 water molecules (Pyr 5w).

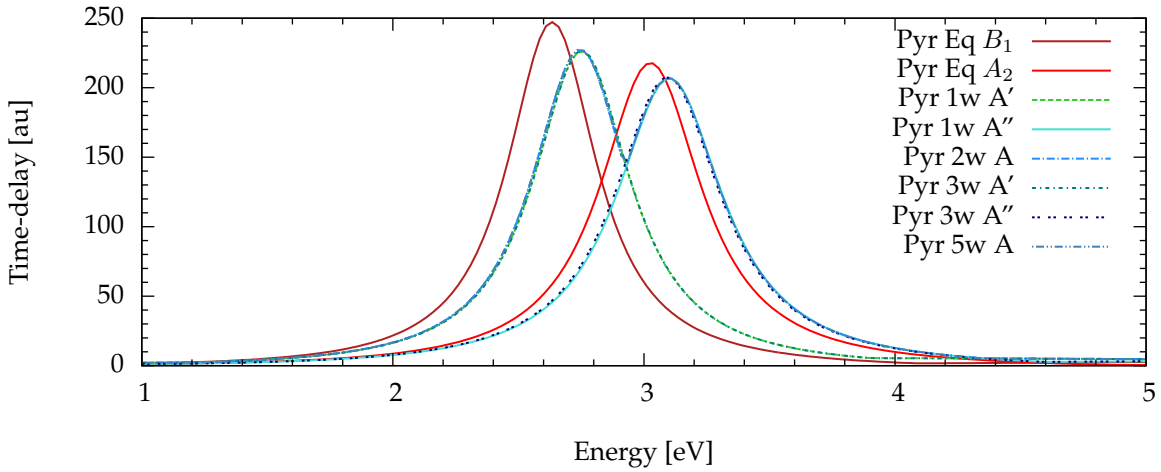

Figure 4.20: Time-delay for isolated pyridine in various geometries: its equilibrium geometry (Pyr Eq) and its geometry in the cluster Pyr-H_2O (Pyr 1w), Pyr-$(H_2O)_2$ (Pyr 2w), Pyr-$(H_2O)_3$ (Pyr 3w) and Pyr-$(H_2O)_5$ (Pyr 5w). The calculations were performed at SE level with the cc-pVDZ basis set and 20 virtual orbitals. The time-delay is plotted for the symmetries indicated in the panel.

TOTAL EFFECTS

Figure 4.21 illustrates the resonances for isolated pyridine and Pyr-$(H_2O)_n$, n = 1, 2, 3, 5. Due to the fact that the isolated pyridine belongs to C_{2v} point group and Pyr-$(H_2O)_n$, n = 1, 3 to C_s the time-delay for A_1 and B_1 irreducible representations are summed. Since Pyr-$(H_2O)_2$ and Pyr-$(H_2O)_5$ belong to the C_1 point group, the time-delay for these systems is plotted twice in the panel for the A_1 + B_1/A' symmetry and the one for A_2 + B_2/A'' (see table 4.8). For all these systems water stabilizes the resonances but the shifts are not significant, especially for pyridine-$(H_2O)_2$ and pyridine-$(H_2O)_3$. The biggest change in resonance position can be noticed for pyridine-$(H_2O)_5$. Table 4.9 lists the resonance shifts for these systems.

Res	Pyr-H_2O	Pyr-$(H_2O)_2$	Pyr-$(H_2O)_3$	Pyr-$(H_2O)_5$
$1\,^2B_1$	-0.25	-0.13	-0.12	-0.36
$1\,^2A_2$	-0.21	-0.08	-0.05	-0.26

Table 4.9: Energy shifts of the two lowest, pure π^*shape resonances in pyridine-H_2O, pyridine-$(H_2O)_2$, pyridine-$(H_2O)_3$ and pyridine-$(H_2O)_5$ with respect to those in isolated pyridine.

We observe that the trend of resonance shift for the clusters is connected with the energy of π^*orbitals of the systems, see table 4.10. The energy differences between orbitals of pyridine-water clusters and isolated pyridine are close to the resonance shifts. The shifts are also correlated with the dipole moments of the clusters (table 4.1). That can be understood if for simplicity we assume that dipole moment of pyridine in the cluster is approximately equal to the dipole moment of isolated pyridine. The total dipole moment of the cluster is a vector sum of the dipole moment of isolated pyridine and water. With this assumption if the total dipole moment is larger than that of isolated

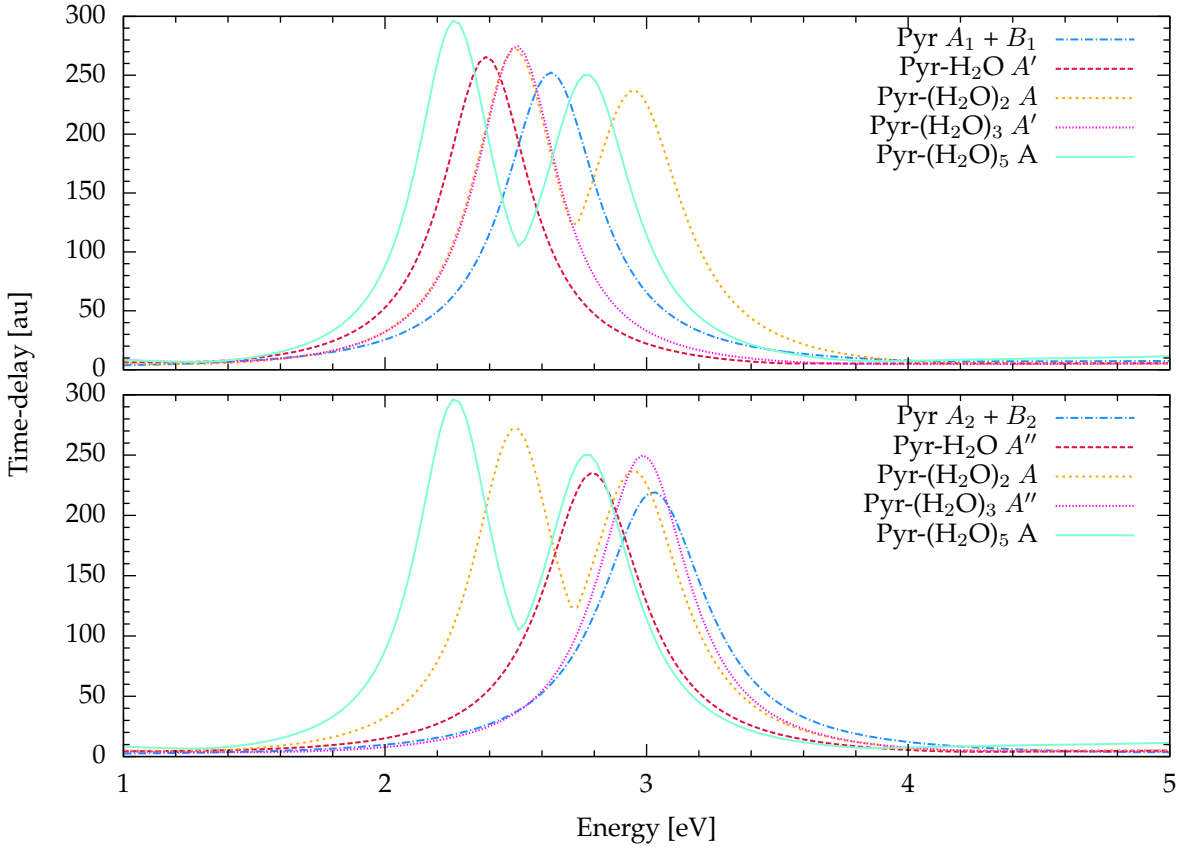

Figure 4.21: The time-delay for pyridine and Pyr-$(H_2O)_n$, n $= 1,\ 2,\ 3,\ 5$ for the corresponding symmetries, as a function of electron energy. The calculations were performed at SE level using the cc-pVDZ basis set. The time-delay for pyridine-$(H_2O)_n$, n $= 2,\ 5$ is plotted twice (the reason for it is explained in the main text).

pyridine it means that the water dipole moment has increasing contribution to the total dipole moment. Thus, more positive charge is next to the ring. In this situation the scattering electron is more attracted to the cluster than to isolated pyridine — the resonance is stabilized. The opposite situations takes place when total dipole moment of the cluster is smaller than that of isolated pyridine. In this case water dipole moment has decreasing contribution to the total dipole moment. Therefore more negative charge is next to the ring, which is less attractive for incoming electron.

The fact that the 1 π^* resonance is more affected by presence of water than the 2 π^* resonance for each cluster presented in this section, can be explained by higher density around the nitrogen which is bound to water. The shape of first and second π^* orbitals are presented in table 4.10.

Although T. C. Freitas *et al.* also studied formic acid bound to two water molecules [27], the comparison with Pyr-$(H_2O)_2$ is not straightforward since in the case of formic acid the 2 water molecules are directly bound to this molecule, whereas in case of pyridine one water binds to nitrogen and the second water molecule binds to the oxygen in the other water molecule (see, figure 4.18).

The results presented here show that water molecules stabilize the two lowest shape resonances. However, increasing the number of water molecules does not always increase the resonance shifts.

Res.	Pyr	Pyr-H_2O	Pyr-$(H_2O)_2$	Pyr-$(H_2O)_3$	Pyr-$(H_2O)_5$
1 π^*	3.14 eV 	2.88 eV 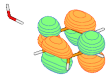	2.98 eV 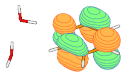	2.98 eV 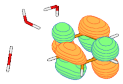	2.67 eV 
2 π^*	3.53 eV 	3.29 eV 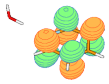	3.43 eV 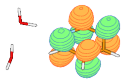	3.45 eV 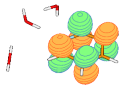	3.20 eV 

Table 4.10: The lowest π^*orbitals of pyridine and the pyridine clusters indicated. The nitrogen is located at the position facing the water molecules.

We noticed a correlation between dipole moments of the clusters and resonance shifts. Additionally, we noticed that water affects the first shape resonance more strongly than the second one.

4.5 SUMMARY

In this chapter we compared resonances positions of isolated pyridine with those affected by presence of water. We compared Pyr-H_2O to pyridine in SE, SEP and CC level. The shape and core-excited resonances and those of mixed shape–core-excited character are stabilized in presence of water. However, water does not affect all resonances equally strong. The differences between the resonance shifts can be linked to shape of the orbitals into which incoming electron is trapped: water affects more the orbitals with density around nitrogen (those with density close to water).

The SE calculations for clusters with more than one water molecule also show stabilization of the resonances. In all the clusters presented in this chapter only one water molecule is bound to the pyridine ring and in all clusters the water molecule acts as a hydrogen donor. Our observations are consistent with the T. C. Freitas *et al.* hypothesis that resonance are stabilized when water acts as a hydrogen donor. The results of pyridine cluster calculations, however, do not allow us to verify the resonance behaviour in the case when water acts as a hydrogen acceptor and in the case when more than one water is bound to the ring. These cases can be verified for thymine clusters calculations presented in the next chapter.

5

ELECTRON COLLISIONS WITH THYMINE-$(H_2O)_5$

Thymine, as one of the four nucleobases in DNA (see chapter 1), has been of interest to electron-molecule interaction researchers for a long time. This molecule, as well as its equivalent in RNA - uracil, has been widely studied both experimentally and theoretically, due to their similarities, number of studies compare the two molecules. The attachment energies of electrons to the nucleic acid bases in their gas phases were measured for the first time (except for uracil) in 1998 by Aflatooni *et al.* [34] in an ETS experiment. After 2000, several experimental groups have measured ion yield of anionic fragments of thymine and uracil produced through dissociative electron attachment: Hanel *et al.* [37], Denifl *et al.* [43, 38], Ptasińska *et al.* [44], Scheer *et al.* [39, 40], Abouaf *et al.* [35], Aflatooni *et al.* [41], Burrow *et al.* [36]. Theoretically, gas-phase collisions between slow electrons and thymine or uracil molecules have been studied by: C. Winstead and V. McKoy [59, 20, 19, 55], and F. Kossoski *et al.* [63] (they carried out scattering calculations employing the Schwinger multichannel (SMC) method); Y. Wang *et al.* [57] and F. A. Gianturco *et al.* [58, 60], (they used the single-center expansion (SCE) potentials); S. Tonzani and C. Greene [54] (they used the R-matrix method together with model potentials); A. Dora *et al.* [64, 16], and Z. Mašín and J. D. Gorfinkiel [24] (they used the R-matrix method); In this chapter, simpler calculation for isolated thymine are presented, for the purpose of comparison and as a basis for calculations of clusters of thymine surrounded by water molecules.

Only a handful of studies on microsolvated nucleobases are available. S. Kim *et al.* studied theoretical vertical detachment energies of thymine, uracil and adenine-uracil base pair [151, 152, 153]. In 2014, M. Smyth *et al.*'s study of thymine surrounded by 5 water molecules was published [79]. They calculated vertical electron attachment (VEA) energies for the first π^* resonance and found it decreases with respect to the isolated molecule. They assumed this is the case for all resonances (also for the σ^* resonance which leads to DEA). With this assumption, using nonlocal complex potential theory and the multiple scattering theory [51, 154, 155] they calculated DEA cross section for hydrogen detachment for isolated thymine and uracil* (more details about their work is given in section 5.4.4). Very recently, in 2016, J. Kočišek *et al.* [78] published an experimental study of electron attachment to microhydrated uracil and thymine (more details is given in section 5.4.4). Their results seem to be in contradiction with M. Smyth *et al.*'s theoretical outcome, which predicted that solvation of thymine and uracil strongly enhances the cross section for the N_2-H fragmentation process. The experimental results show that the fragmentation process (both for N_1-H and N_2-H) does not occur when thymine and uracil are surrounded by a few water molecules.

The main goal of this chapter is similar to that of the previous one, i.e. to investigate the effect of water on the resonance characteristics. The discrepancy between theoretical and experimental results mentioned above is not satisfactory. Therefore, we hope to gain a better understanding of the influence of water on resonance position by performing R-matrix scattering calculations that support either the Smyth *et al.*'s or Kočišek *et al.*'s results. Our calculations have been performed for exactly the same geometry as in [79] (the geometry was provided by one of the authors of that work).

Unlike chapter 4 (pyridine-water clusters), in this chapter we discuss results for several different geometries of the Thy-$(H_2O)_5$ clusters. Calculations for thymine bound to 1, 2, 3 water molecules for a number of geometries that will be discussed later (also provided by M. Smyth *et al.*) have also been performed. That helped us to investigate hydrogen bonding effects in more detail, and allowed us to determine whether T. C. Freitas *et al.*'s conclusion of the role of water on resonances in HCOOH holds for systems with more than 2 water molecules (T. C. Freitas *et al.* studied clusters of formic acid with one and two water molecules for various geometries).

The main challenge of performing R-matrix calculations for the systems presented in this chapter was their size, especially for thymine-$(H_2O)_5$ (116 electrons and no symmetry). Calculations with such big computational requirements had never been performed before, due to limitation of the UKRmol suite. These calculations were also challenging because the new UKRmol+ suite, used to perform these calculations, needed to be debugged; computer restrictions and allocating and sorting a huge amount of data were also issues.

Although the calculations were completed, we investigated a different solution — a way to reduce

*M. Smyth *et al.* state that there is no difference between their theoretical model of uracil and thymine [79]. Therefore they performed calculations using mixed data for both molecules. They assume that the results hold both for uracil and thymine.

the computational demands. Therefore, we tested a model in which the water molecules were not explicitly included in the calculations. The effects of their presence on thymine orbitals was included by using modified orbitals to describe thymine. We studied a system of thymine with its orbitals modified by the presence of water. In one case water is described using the polarized continuum model [156] and in the second it is represented as point charges [156]. The new thymine orbitals, polarized orbitals and orbitals modified by water described as point charges, were provided to us by S. Caprasecca.

5.1 THYMINE CHARACTERISTICS

Thymine (abbreviated to Thy) is pyrimidinic nucleobase, a heterocyclic aromatic compound, its chemical formula is $C_5H_6N_2O_2$. The structure of thymine is illustrated in figure 5.1

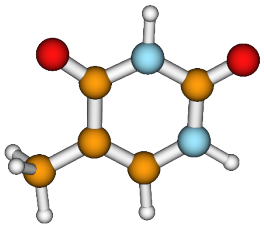

Figure 5.1: Geometrical structure of the thymine molecule. Blue colour represents nitrogen, orange – carbon, red – oxygen and white (grey) – hydrogen atoms. Generated using MOLDEN.

The alternative names for thymine are 2,4-Dihydroxy-5-methylpyrimidine or 5-methyluracil. As the name implies, the only difference in the structure between thymine and uracil is a methyl group replacing a hydrogen in uracil. In DNA, thymine binds to adenine by two hydrogen bonds. In RNA, thymine is replaced with uracil in most cases.

Thymine possesses 66 electrons; the orbitals in the ring are similar to those of pyrimidine (the thymine orbitals can be found in appendix D, table D.1) and there are still the six π-electrons from the three double bonds in the aromatic structure.

At room temperature thymine has the appearance of a white to off white crystalline powder, with a melting point of 316-317°C and a boiling point of 335°C; it is odourless. Its vertical ionization energy is close to that of other benzene ring molecules and it is around 9.1-9.2 eV [157, 158], the first electronic excitation threshold is around 3.6-3.9 eV [42, 159] and its dipole moment is 4.13 Debye [160]. It belongs to the C_1 point group.

5.2 CALCULATION DETAILS

The indirect, direct and total effects of water on isolated system were introduced in chapter 4. However, we remind the reader of the definitions:

- Direct effect of water includes the changes in resonance characteristics that the presence of water causes, excluding changes in the thymine geometry, i.e. we compare Thy and Thy-$(H_2O)_n$ results, where the Thy geometry is preserved in all systems.
- Indirect effect of water includes the changes of Thy geometry which can be investigated without including water in the calculations.
- Total effect of water includes both direct and indirect effects, i.e. we compare Thy and Thy-$(H_2O)_n$ in their equilibrium geometries.

The targets studied in this chapter were chosen so as to study these effects in some detail.

5.2.1 TARGET GEOMETRIES

In this chapter we are investigating a number of targets: isolated thymine and several thymine clusters with various numbers of water molecules; moreover, we also examine clusters with a specific number of waters for various binding sites of H_2O to thymine. For the sake of investigating indirect effects we also compare different geometries of thymine. The large number of targets, their names and the differences between them may be, at the beginning, confusing for reader. Therefore, we first present all of them here, and then we repeat the structure of the discussed targets at the beginning of each section. The targets are not presented here in the same order in which they appear throughout this chapter, but in a way, we hope that, is easy to follow. The studied targets are:

1. Thy-$(H_2O)_5$

   Investigations of clusters with 5 water molecules are the main goal of this chapter. They are presented in section 5.4. We are presenting 2 clusters of this type:

   - Thy-$(H_2O)_5$ in its equilibrium geometry. The structure of this cluster is presented in figure 5.2a, and we refer to it as *ABCDE cluster* (in abbreviation: *ABCDE*) or by using expression: *cluster in ABCDE geometry*.
   - Thy-$(H_2O)_5$ cluster in a non-equilibrium geometry. This cluster is investigated for complementary purposes. The structure of this cluster is presented in figure 5.2b, and we refer to it as *ACDEF cluster* (in abbreviation: *ACDEF*) or by using expression: *cluster in ACDEF geometry*.

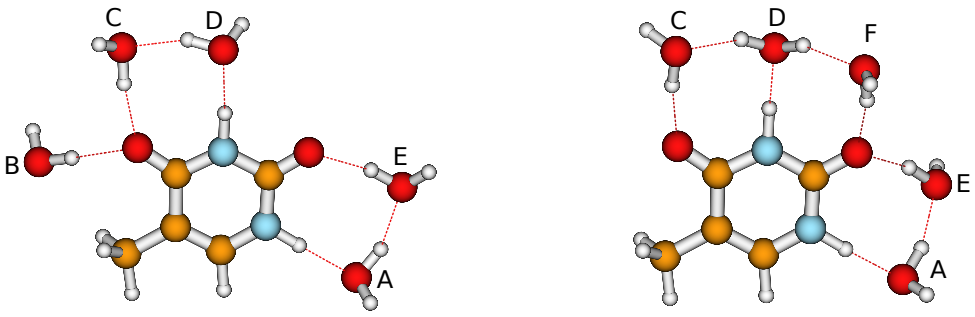

(a) ABCDE (b) ACDEF

Figure 5.2: Structure of Thy-$(H_2O)_5$ for the two different geometries studied in this work. The labels of each water molecule in the geometry ABCDE are used throughout the text.

2. Thy-H_2O

   In order to gain better insight into electron scattering from the ABCDE cluster, we investigated thymine bound to only one water from this cluster at a time. In this case we investigate ten systems:

   - Five Thy-H_2O for each of the waters in the cluster ABCDE. In this cases the Thy-H_2O clusters are not optimised. They are created by removing 4 water molecules from the ABCDE cluster. These clusters are presented in section 5.3.3. Each cluster is labelled by a capital letter in accordance to the position of the water molecule in cluster ABCDE (see figure 5.2a). Therefore, we refer to each of them as *A (B, C, D or E) cluster*. The structure of each of the clusters is presented in figure 5.3a.

   - Five Thy-H_2O with optimised geometry for each of the waters in the cluster ABCDE. In this case, 4 waters are removed from the ABCDE cluster and then a (local) optimisation is performed for the thymine-water cluster. These clusters are presented in section 5.3.2. These clusters are also labelled by the capital letter corresponding to position of the water molecule in the cluster ABCDE, but to distinguish them from the cluster above 'eq' is added to the name. Therefore, we refer to each of them as *Aeq (Beq, Ceq, Deq or Eeq) cluster*. The structure of each of the clusters is presented in figure 5.3b. It turned out that geometries of the clusters Aeq and Eeq are very similar; this is also the case for clusters Beq and Ceq. The results and conclusions for Aeq and Beq clusters hold also for Eeq and Ceq clusters, respectively. Therefore we will only include clusters Aeq, Beq and Deq in the future discussion.

3. Thy-$(H_2O)_2$

   Thy-$(H_2O)_2$ has been investigated for similar reasons as Thy-H_2O. Unlike the single water case above, we do not consider clusters with optimised geometries.

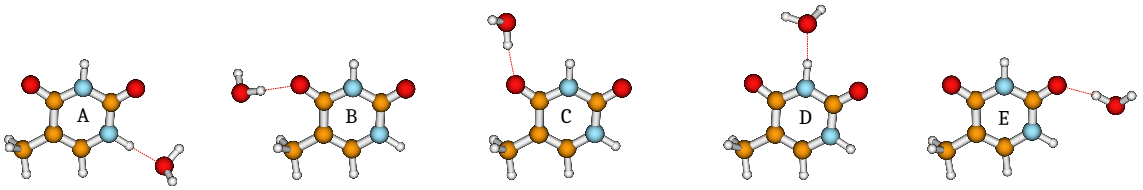

(a) Thy-H_2O

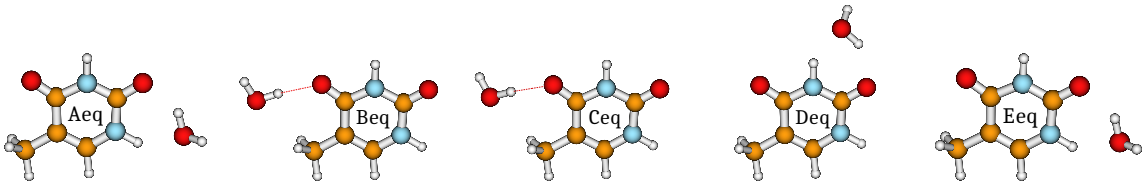

(b) Thy-H_2O eq

Figure 5.3: Structure of Thy-H_2O clusters studied in this work. (a): Thy-H_2O extracted from cluster ABCDE. (b): optimised geometry of Thy-H_2O. See text for more details. Generated using MOLDEN.

- Four Thy-$(H_2O)_2$ clusters. Each of them is created by removing 3 water molecules from the ABCDE cluster. These clusters are presented in section 5.3.3. Each cluster is labelled by a capital letter in accordance to position of the water molecule in the cluster ABCDE. Therefore, we refer to each of them as *AD (AE, BC or BD) cluster*. The structure of each of the cluster is presented in figure 5.3a.

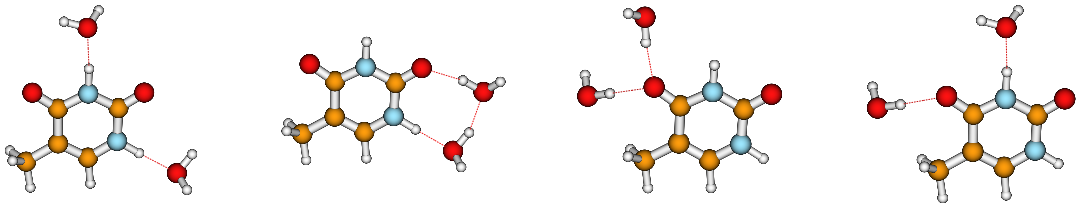

(a) AD (b) AE (c) BC (d) BD

Figure 5.4: Structure of Thy-$(H_2O)_2$ for four different geometries. Generated using MOLDEN.

4. Thy-$(H_2O)_3$

   The geometries of these clusters as those above are not optimised.

- Two Thy-$(H_2O)_3$ clusters. We refer to each of them as *BCD cluster* and *BCE cluster*. The structure of each of the cluster is presented in figure 5.5.

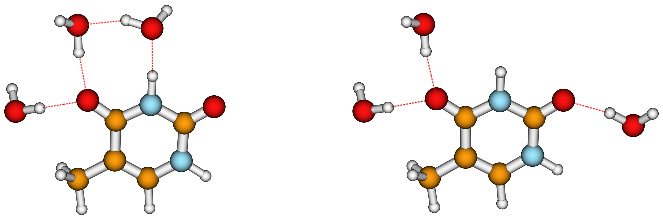

(a) BCD (b) BCE

Figure 5.5: Structure of Thy-$(H_2O)_3$ for two different geometries. Generated using MOLDEN.

5. Thy

   Calculations for isolated thymine in three different geometries have been performed:

   - Thy in equilibrium geometry - in order to compare with the clusters above and investigate total effects of water on thymine. We refer to this system as: *Thy eq* or *Thy in the geometry G1* (in abbreviation: *Thy G1*). This system is discussed in section 5.3.1. The structure and its bond-lengths are presented in figure 5.6a.
   - Thy in non-equilibrium geometry, the geometry of thymine is the same as in the ABCDE cluster - in order to compare with the ABCDE clusters and investigate direct effects of water on thymine; and to compare to Thy in geometry G1 to investigate indirect effects. We refer to this system as: *Thy in geometry G2* (in abbreviation: *Thy G2*) or *Thy in the geometry of the ABCDE cluster*. The structure and its bond-lengths are presented in figure 5.6b.
   - Thy in its geometry in the ACDEF cluster (non-equilibrium geometry) - in order to compare with the ACDEF clusters and investigate direct effects of water on thymine; and to compare to Thy in geometry G1 to investigate indirect effects. We refer to this system as: *Thy in geometry G3* (in abbreviation: *Thy G3*) or *Thy in the geometry of the ACDEF cluster*. The structure and its bond-lengths are presented in figure 5.6c.
   - Thy in geometry of Aeq, Beq, Ceq, Deq, Eeq cluster (non-equilibrium geometry) - in order to compare with Aeq, Beq, Ceq, Deq, Eeq clusters and investigate direct effects of water on thymine. Nevertheless, the reader will find out in section 5.3.2 that, in this case, the thymine geometries in these clusters are very similar to each other and to Thy G1, therefore we do not present an additional image with bond-lengths for these geometries.

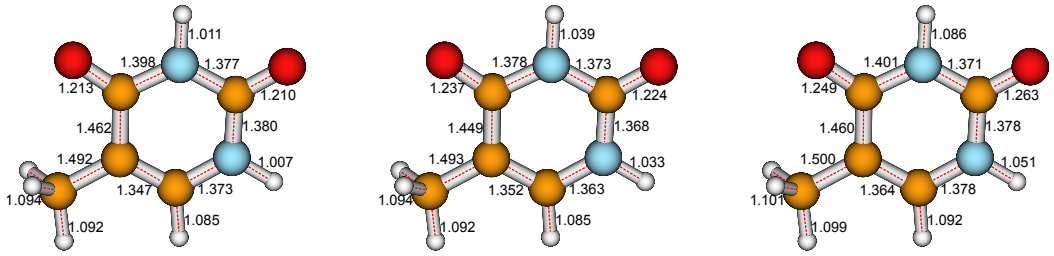

(a) G1 (b) G2 (c) G3

Figure 5.6: Bond-lengths, in Å, of thymine in equilibrium geometry (G1) and in clusters: ACDEF (G2) and ABCDE (G3).

6. Thy-pol

   Thymine with modified (polarized) orbitals for two geometries is presented in section 5.4.5:

   - *Thy-pol ABCDE* is a thymine molecule with orbitals modified by the presence of water molecules which have the position and orientation as in ABCDE cluster. Water in this

case is described using the polarized continuum model. The thymine geometry is that of thymine G2, in figure 5.6b.

- *Thy-pol ACDEF* is as above but using the locations of water from the ACDEF cluster. The thymine geometry is the same as that of isolated thymine G3, in figure 5.6c.

7. Thy-char

   Thymine described by polarized orbitals obtained using point charges is presented in section 5.4.5:

   - *Thy-char ACDEF* is a thymine molecule with orbitals modified by the presence of water molecules which have the position and orientation as in the ACDEF cluster. Water in this case is described by point charges. The thymine geometry is the same as that of isolated thymine G3, in figure 5.6c.

The geometry of all targets presented in this chapter was provided by Prof. J. Kohanoff: M. Smyth *et al.* [79] performed geometry optimisations at the density functional level of theory (DFT), using the hybrid functional PBE0 [161].

5.2.2 TARGET DETAILS

For all of calculations presented here we used the compact basis set: cc-pVDZ. The reasons for this are:

- the basis set has been shown to be appropriate for the desciption of resonances in a pyrimidine (thymine is pyrimidinic nucleobase) [123, 139],
- A. Dora *et al.* [16] performed R-matrix calculations for thymine using this basis set, and we intend to compare our results with theirs. Therefore we have kept as many parameters unchanged as possible.
- this compact basis set is less computationally demanding than a diffuse one as it requires a smaller R-matrix radius.

The calculations presented in this chapter have been performed at SE and SEP level, therefore only in the ground electronic state of the targets needs to be described. These was done at HF level; some of the HF orbitals are presented in appendix D, table D.1.

The calculated ground state energies and dipole moments for all systems studied are collected in table 5.1. We can see that Thy G1, as expected, has the lowest ground state energy of the thymine geometries; Thy in cluster ABCDE (G2) has lower ground state energy than Thy in cluster ACDEF (G3). Consequently, the energy of Thy-pol ABCDE is smaller than that one of Thy-pol ACDEF. The ground

state energies of the Thy-H_2O extracted from the ABCDE cluster are very similar to each others, the differences are not larger than 0.004 Hartrees. The differences between the ground state energies for optimised geometries of cluster Thy-H_2O: Aeq, Beq, Deq are not larger than 0.007 Hartrees. As expected the energies of optimised Thy-H_2O are lower than those of non-optimised Thy-H_2O. The differences between the ground state energies of Thy-$(H_2O)_2$ and Thy-$(H_2O)_3$ clusters are not larger than 0.018 Hartrees and 0.016 Hartrees, respectively. It is not surprising that the dipole moment depends very significantly on the geometry of the systems: cluster C possesses the largest dipole moment and D the smallest one.

System		E	μ
Thy	G1	-451.548	4.64
	G2	-451.542	4.92
	G3	-451.528	4.94
Thy-H_2O	A	-527.581	6.45
	B	-527.579	4.47
	C	-527.577	7.19
	D	-527.579	2.54
	E	-527.578	3.41
	Aeq	-527.591	3.93
	Beq	-527.584	3.67
	Deq	-527.588	4.95
Thy-$(H_2O)_2$	AD	-603.618	4.04
	AE	-603.630	4.47
	BC	-603.612	6.21
	BD	-603.616	2.72
Thy-$(H_2O)_3$	BCD	-679.663	3.35
	BCE	-679.647	4.63
Thy-$(H_2O)_5$	ABCDE	-831.752	4.65
	ACDEF	-831.740	4.26
Thy-pol	ABCDE	-451.532	5.97
	ACDEF	-451.521	6.48

Table 5.1: Calculated ground state energy (E) in Hartree and dipole moment (μ) in Debye of isolated Thy and Thy clusters with water presented in this work.

5.2.3 SCATTERING

Calculations have been performed at SE and SEP level using an R-matrix radius of 18 a_0 (the complete charge distribution of Thy-$(H_2O)_5$ is contained in this radius). Although, the radius of 13 a_0 is sufficient for isolated thymine, we wanted to keep as many calculation parameters as possible the same for all targets. We have confirmed that the change of R-matrix radius between 13 a_0, 15 a_0 and 18 a_0 does not have a significant effect on the resonance characteristic for isolated thymine. This is

illustrated in figure 5.7 (top panel).

Convergence tests have been carried out for the maximum angular momenta of the continuum, for these systems: thymine, thymine with polarized orbitals, thymine-$(H_2O)_5$. Inclusion of partial waves up to $\ell_{max} = 4$ is not enough: it is clearly visible in figure 5.7 (bottom panel) that at higher energies (above 7 eV) lack of partial waves manifests itself as additional peaks in the time-delay which disappear as ℓ_{max} increases. Differences between calculations with $\ell_{max} = 5$ and $\ell_{max} = 6$ are still significant above 9 eV, therefore $\ell_{max} = 5$ is still not sufficient. Results for thymine, thymine-$(H_2O)_5$ and thymine with polarized orbitals converge with ℓ_{max} = 6; this number is used in the calculations presented in next section.

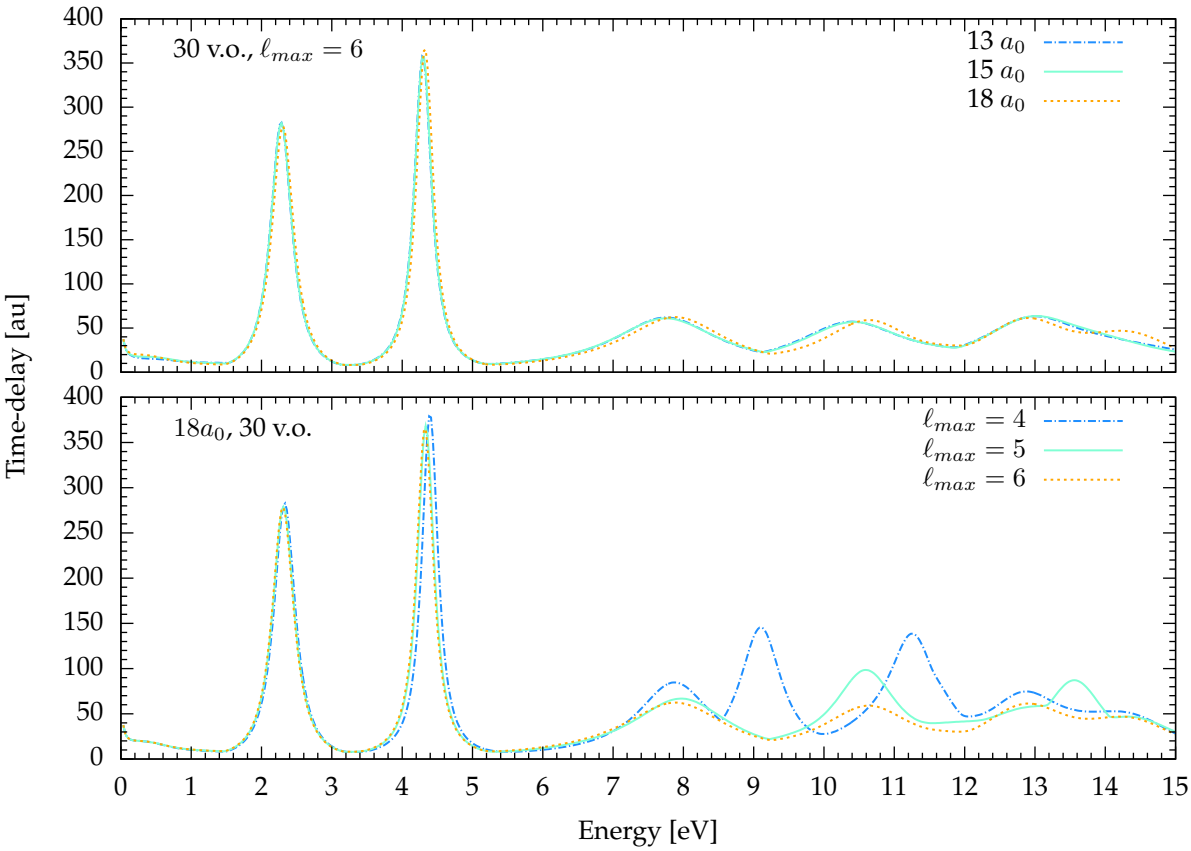

Figure 5.7: Convergence tests for isolated thymine at SE level presented using the time-delay. The top panel illustrates results for different R-matrix radii; the bottom panel shows convergence with partial waves. The R-matrix radius, number of virtual orbitals (v.o.), and maximum value of partial waves (ℓ_{max}) used in the calculations are indicated in the panels.

The SEP calculations have been carried with 15 frozen and 18 active thymine orbitals. 10 virtual orbitals have been included in the calculations for all systems, excluding: isolated thymine, for which calculations have been carried out with inclusion of up to 50 v.o.; and Thy-$(H_2O)_5$ up to 30 v.o. Both target and scattering parameters used to perform our calculations are collected in table 5.2.

System	Thy	Thy-H_2O	Thy-$(H_2O)_2$	Thy-$(H_2O)_3$	Thy-$(H_2O)_5$	Thy-pol
Scattering model	SE/SEP	SE/SEP	SE/SEP	SE/SEP	SE/SEP	SE/SEP
Basis set	cc-pVDZ	cc-pVDZ	cc-pVDZ	cc-pVDZ	cc-pVDZ	cc-pVDZ
R-matrix radius	$18a_0$	$18a_0$	$18a_0$	$18a_0$	$18a_0$	$18a_0$
Target description	HF	HF	HF	HF	HF	HF
No. of virtual orbitals	10-50/20	10/10	10/10	10/10	10/30	10/10
Deletion threshold	10^{-7}	10^{-7}	10^{-7}	10^{-7}	10^{-7}	10^{-7}
Geometry of thymine	G1,G2,G3	G1,G2	G2	G2	G2,G3	G2,G3
Continuum ℓ_{max}	6	6	6	6	6	6

Table 5.2: The calculation details used for the targets and scattering models studied in this chapter. The numbers of 'Continuum ℓ_{max}' are the maximum values of the angular momentum of the continuum partial waves. 'G1' stands for equilibrium geometry, 'G2'– geometry of the components in the cluster ABCDE, 'G3' – geometry of the components in the cluster ACDEF (see text). The meaning of the other labels is the same as in figure 3.4 and 4.2.

5.3 RESONANCES

In this section we present and analyse the resonances in Thy-$(H_2O)_n$, n = 1, 2, 3, 5. We focused on the two pure shape and the mixed shape–core-excited π^* resonances with the lowest energies. Initially, the results for isolated thymine are presented and compare with prior studies. Next the results for isolated thymine are compared with the resonances in thymine-water clusters.

The calculations for Thy-$(H_2O)_n$, n = 1, 2, 3, 5 have been performed in order to investigate the correlation between our results and the previously studied molecules in clusters with water, i.e. to investigate how the resonance shifts depending on whether water plays the role of hydrogen donor or acceptor in the cluster. These studies are closer to those of T. C. Freitas *et al.* [27] than the one presented in the previous chapter, since in case of the thymine and formic acid, water may act as a hydrogen acceptor or donor, whereas in pyridine clusters water acts only as a hydrogen donor (first water molecule binds to the pyridine nitrogen, the second and the next water molecules bind to the first water molecule, leading to a high water concentration on one side of pyridine – close to nitrogen). Therefore, the studies of thymine clusters give more information about role of water depending on the donor/acceptor character and its binding site, than pyridine systems.

In the last section of this chapter the results for Thy-$(H_2O)_5$ are analysed in more detail, by analysing indirect, direct and total effects and comparing the results to available data in the literature.

5.3.1 THYMINE

In this section we compare the resonance characteristic obtained in this work with other results. We also examine the change in resonance characteristics as a function of the number of virtual orbitals

used in the calculations. In the case of calculations at SE level, 10 v.o. is sufficient to describe 3 the π^* resonances. Calculation with 30 (and more) v.o. describe more structure in the time-delay than calculations for 10 v.o., but we will not analyse the resonances at higher energies in detail (except for the 4th resonance, for which resonance parameters are listed in table 5.3). It can be seen in figure 5.8 that including more v.o. in the calculations hardly change the time-delay below 9 eV. At the SEP level we performed calculation for 30, 40, and 50 v.o. These results together with SE ones are presented in figure 5.8.

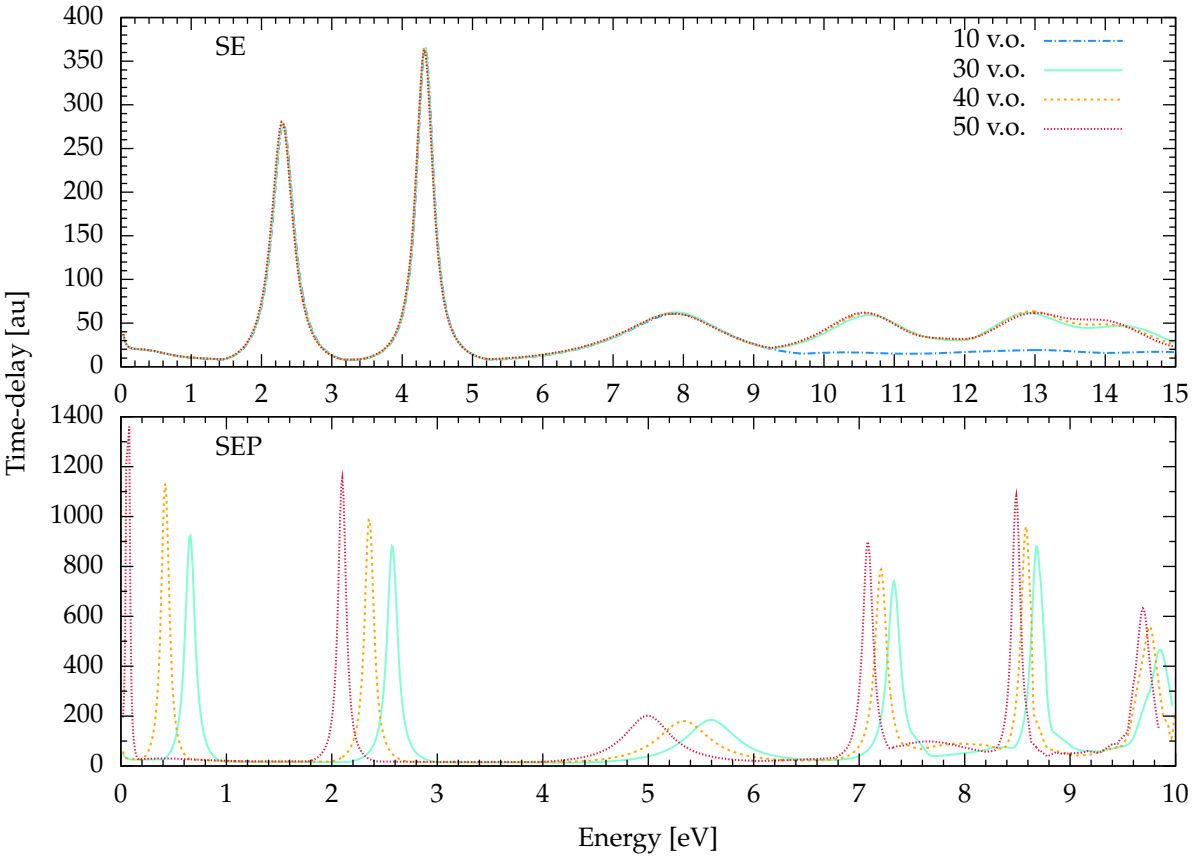

Figure 5.8: SE and SEP time-delay calculations for isolated thymine with the numbers of virtual orbitals indicated in the figure, performed with the cc-pVDZ basis-set and $\ell_{max} = 6$, for the non-equilibrium geometry G3 (these calculations have been performed for G3 geometry as it was the first geometry which was available to us).

Table 5.3 lists the energies and widths of resonances calculated at SE and SEP level with 40 v.o. for thymine in its equilibrium geometry and compares our results to other calculations and observed values.

The resonance energies obtained in this work at SE and SEP levels are higher than those obtained by Dora *et al.* Since the SE calculations for low energies are not significantly dependent on the number of v.o. and our SEP calculations have been performed with 10 v.o. more than Dora *et al.*'s calculations, the different resonance positions are probably caused by the different geometry used in these calculations. Dora *et al.*'s calculations have been performed for a thymine geometry optimised

Reference	model	1 π^*	2 π^*	3 π^*	4 π^*
This work	SE	2.56 (0.41)	4.68 (0.31)	8.24 (1.88)	10.79 (1.62)
Dora *et al.*[a]		2.45 (0.36)	4.60 (0.27)	7.98 (1.55)	11.41 (1.06)
Tonzani & Greene[b]		2.40 (0.20)	5.50 (0.60)	7.90 (1.00)	
This work	SEP	0.72 (0.12)	2.74 (0.12)	5.73 (0.72)	7.63 (0.14)
Dora *et al.*[a]		0.60 (0.11)	2.73 (0.11)	5.52 (0.57)	7.41(0.12)
Winstead & McKoy[c]		0.30	1.90	5.70	
Aflatooni *et al.*[d]	Exp.	0.29	1.71	4.05	

Table 5.3: Position (widths), in eV, of the π^* resonances for isolated thymine. In this work both SE and SEP calculations have been performed with 40 v.o., $\ell_{max} = 6$, $a = 18a_0$. [a] Dora *et al.* [16]; [b] Tonzani and Greene [54]; [c] Winstead and McKoy [19]; [d] Observed (ETS) vertical attachment energies, Aflatooni *et al.* [34].

using density functional theory with the B3LYP functional and the 6-31+G* basis set. It was optimised imposing C_s symmetry, whereas the equilibrium geometry actually belongs to the C_1 point group.

We note that we do not present SEP results with higher number of v.o. here, since our main purpose is to compare our results to Thy-(H_2O)$_5$. The SEP calculations for Thy-(H_2O)$_5$ are computationally expensive and we have performed SEP calculations for this cluster with up to 30 v.o. which corresponds to 20 v.o. of the isolated Thy (see section 5.4.2). Comparison of SEP results for Thy-(H_2O)$_5$ with our best results for Thy would require us to perform calculations with very high number of v.o. for Thy-(H_2O)$_5$, which at this stage cannot be done. The SEP results, presented here have only qualitatively character: to investigate whether they give the same, similar or different picture as SE results. They do not give reliable resonance position, as we have not included enough v.o. in these calculations.

5.3.2 THYMINE-H_2O

In order to investigate the direct and indirect influence of water on the characteristics of the resonances, we performed calculations for Thy-H_2O cluster in three different geometries (presented in figure 5.9) and for isolated thymine in its geometry in these three Thy-H_2O clusters (Aeq, Beq, Deq).

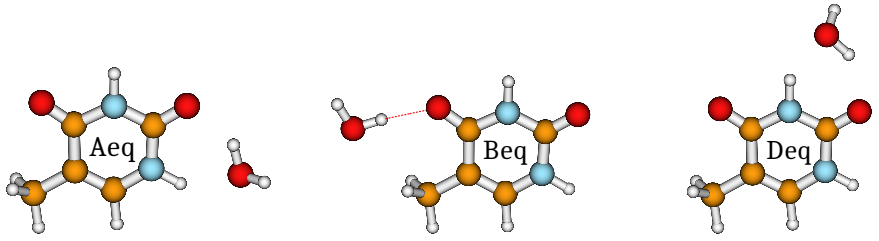

Figure 5.9: Structure of Thy-H_2O for the three different optimised geometries. Generated using MOLDEN.

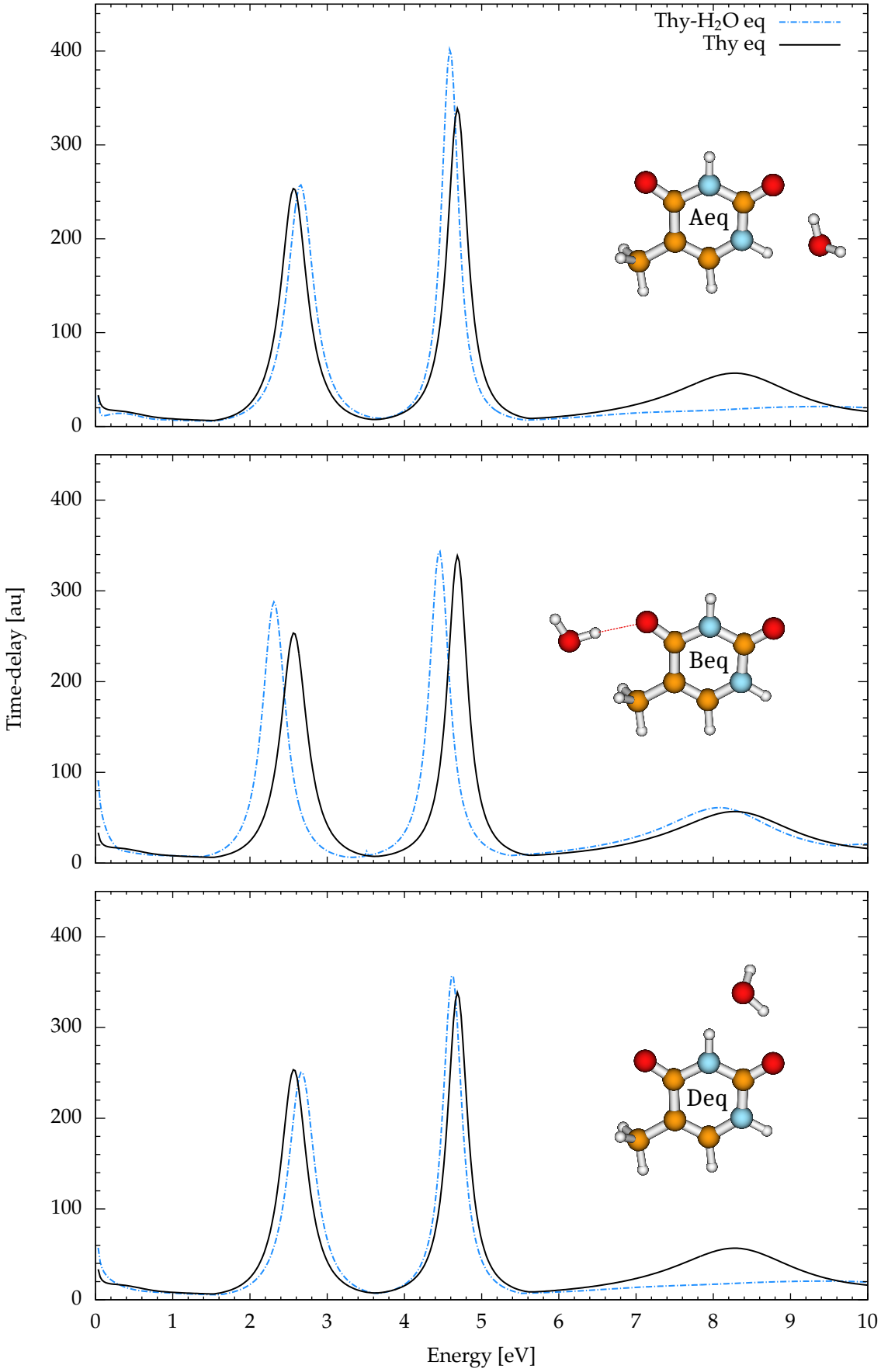

Figure 5.10: SE time-delay for three geometries of the Thy-H_2O clusters, Thy-H_2O eq, compared to the SE time-delay for isolated thymine (G1), Thy eq.

To investigate the direct effect of water, the Thy-H_2O clusters in their optimised geometry ought to be compared with isolated Thy in the geometry of the specific Thy-H_2O system. Unlike the case of pyridine-H_2O and (as will be shown in section 5.4) thymine-$(H_2O)_5$, the equilibrium geometry of isolated thymine does not differ significantly from those of thymine in the Thy-H_2O clusters investigated. For this reason the results for thymine in the specific geometry of the cluster can be replaced by results for thymine in its equilibrium geometry. The indirect effects on the resonance characteristics are negligible and the total effects are approximately equal to the direct effects. These (total) effects can be seen in the SE time-delay plotted in figure 5.10.

The structures of the discussed clusters, presented in figure 5.9, are plotted using MOLDEN, which draws red dashed lines when it determines that a hydrogen bond is present in the system (and it does this by looking at geometrical parameters). Our plots indicate the presence of a hydrogen bond for cluster Beq but not for clusters Aeq and Deq. In the original paper [79], water is hydrogen bonded to thymine for all these clusters. In that paper, water in cluster Aeq is bound both by hydrogen and oxygen to thymine, while water in cluster Deq is only bound by hydrogen. We note that the authors of this paper used density function theory (DFT) to determine the wave function for theses system, while we use HF wave functions. The fewer number of hydrogen bonds identified in our calculations suggest that the hydrogen bonds calculated using the HF approximation are weaker than using DFT. Nevertheless, we believe the effect on the resonances will be similar.

The assumption that the water molecules in clusters Aeq and Deq acts both as proton donor and proton acceptor, may explain why their resonances (presented in figures 5.10) do not behave in the same way: at the SE level the first π^* resonance is slightly destabilized while the second π^* resonance is slightly stabilized. This can be understood by analysing the orbitals into which the electron is trapped. The first π^* orbital has low density close to the water, however it has slightly more density nearer to water oxygen than hydrogen. Also the bond-length between water oxygen and thymine hydrogen is slightly shorter than between water hydrogen and thymine oxygen. Therefore water acts stronger as a proton acceptor than proton donor; that can explain the destabilization of the first π^* resonance. The second π^* orbital has much more density close to hydrogen than oxygen, therefore in this case water acts stronger as a proton donor than proton acceptor; this stabilize the second π^* resonance.

For geometries Aeq and Deq, the third resonance (of mixed shape–core-excited character) is not present as the third π^* orbital is not present amongst the 10 v.o.included in the calculations. At the SEP level both resonances are destabilized, however the shift of the first resonance is larger then the second one (see figure 5.11). In the case of cluster Beq where water acts as a hydrogen donor, the three resonances visible in the time-delay are stabilized both at SE and SEP levels.

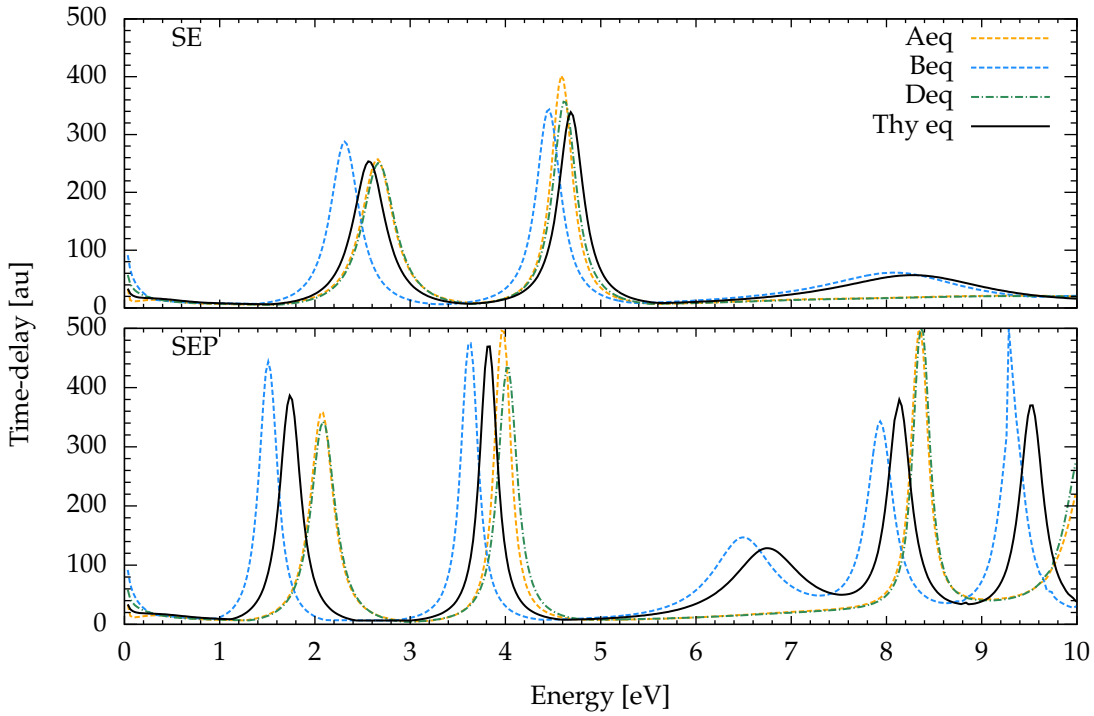

Figure 5.11: Time-delay calculations for thymine in G1 geometry and Thy-H_2O in all geometries studied at SE and SEP levels using 10 v.o.

The positions and widths of the resonances for Thy-H_2O are collected in table 5.4 and the time-delay for all geometries at SE and SEP level is summarized in figure 5.11. The SEP calculations have been performed only for 10 v.o. to reduce computational cost, therefore the resonances appear higher than expected. They are presented here for the purpose of comparing them to SEP calculation with 10 v.o. for isolated thymine. However, for the reasons explained in the previous chapter, section 4.3.2, comparing results for different targets at SEP level is not straightforward (the number of virtual orbitals for each system should be chosen to describe polarization at the same level), therefore the comparison of resonance positions for isolated thymine and Thy-H_2O, both calculated using 10 v.o., may not be reliable[†]. Therefore, we trust more the SE results than SEP ones. The SEP results are presented here to check whether inclusion of polarization qualitatively changes the picture of water effect on resonance shifts.

Geom	SE			SEP			
	$1\,\pi^*$	$2\,\pi^*$	$3\,\pi^*$	$1\,\pi^*$	$2\,\pi^*$	$3\,\pi^*$	$4\,\pi^*$
Thy eq	2.56 (0.41)	4.68 (0.31)	8.24 (1.88)	1.74 (0.27)	3.82 (0.22)	6.76 (0.94)	8.13 (0.29)
Aeq	2.65 (0.41)	4.59 (0.26)		2.07 (0.26)	3.97 (0.19)		8.34 (0.22)
Beq	2.31 (0.36)	4.45 (0.30)	8.05 (2.37)	1.51 (0.22)	3.62 (0.21)	6.49 (0.85)	7.94 (0.34)
Deq	2.67 (0.41)	4.62 (0.30)		2.08 (0.27)	4.02 (0.22)		8.37 (0.22)

Table 5.4: Positions (widths), in eV, of the π^* resonances at SE and SEP levels with 10 v.o. for thymine-H_2O clusters in their optimised geometries (see text and figure 5.11).

[†]The approach described in the section 4.3.2 is to include in the SEP calculation for the cluster all virtual orbitals which appear for isolated system. In this and the next section we did not apply this approach due to lack of time to perform the proper calculations.

The four SEP resonances presented in table 5.4 have the same trend: for geometries Aeq and Deq all four resonance go up in energy, compared to the resonances in isolated thymine; for geometry Beq they all go down in energy. The second resonance in clusters Aeq and Deq moves in a different direction for SEP calculations to the SE one. The more likely explanation of this inconsistency is that the SEP results for isolated thymine contain more polarization than the SEP results of Aeq and Deq clusters. Therefore the resonance positions of isolated thymine may be shifted too much towards lower energies.

5.3.3 THYMINE-$(H_2O)_n$, n = 1, 2, 3

In order to have a better insight into the effect of water on thymine, i.e. to investigate whether water has an additive effect on the resonance positions, calculations for Thy-$(H_2O)_n$, $n = 2,\ 3$ have been performed. These calculations together with calculations for clusters with one water molecule have been also performed to investigate the direct effect of water on the resonances positions. The results presented in this section are for non-optimised geometries of these clusters. These geometries have been obtained by removing specific water molecules from the Thy-$(H_2O)_5$ cluster presented in section 5.4. Therefore, the results for Thy-H_2O, which are presented in this section are not the same as in the previous section (in the section 5.3.2, the geometries of each investigated cluster have been optimised). The structure of Thy-H_2O for the non-optimised geometries studied in this section are illustrated in figure 5.12. First, we start by comparing the optimised and non-optimised cases

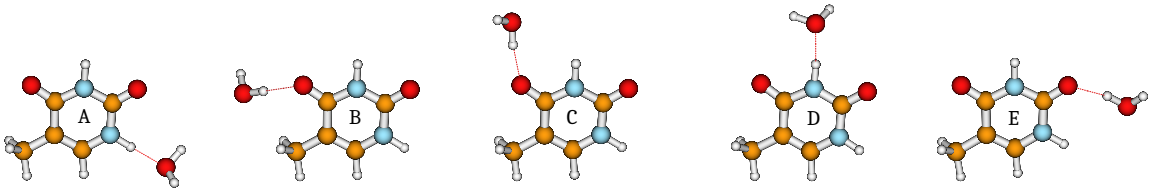

Figure 5.12: Structure of Thy-H_2O for the five different non-optimised geometries (same as figure 5.3a). Generated using MOLDEN.

for a single H_2O. The main observed difference between optimised and non-optimised Thy-H_2O clusters (apart from different bond-lengths between their atoms) is that whereas, the geometry (see picture 5.3b) of clusters Beq and Ceq are almost identical, this is not the case for clusters B and C. Their geometries (see picture 5.12), therefore, energies and dipole moments (see table 5.1) and time-delay (see figure 5.13) are fairly different. A similar situation appears for the Aeq and Eeq clusters (which are almost identical) and fairly different A and E clusters. The water is bound to different thymine atoms in the A and E systems: thymine acts as a hydrogen donor for A and as a hydrogen acceptor for E).

The differences in the time-delay between optimised and non-optimised Thy-H_2O clusters are:

- In clusters A and D Thy acts as a hydrogen donor; for these Thy-H_2O clusters resonances shift towards higher energies than for clusters Aeq and Deq.
- In clusters B, C and E, Thy acts as a hydrogen acceptor, and the resonances move to lower energies than for clusters Beq and Eeq.

The observed similarities between optimised and non-optimised Thy-H_2O cluster are:

- When Thy acts as a hydrogen acceptor, the resonances of clusters B, C and Beq are stabilized both at SE and SEP level compared to Thy G1 and Thy G2, respectively.
- The resonances of clusters A, D and Aeq, Deq are destabilized compare to isolated Thy (Thy G1 and Thy G2, respectively) at SEP (but not at SE) level (however in the case of Aeq and Deq it is not entirely clear whether Thy acts as a hydrogen donor).
- For clusters A and Aeq the third resonance is not present (this is also the case for cluster Deq) due to the fact that the third π^* orbital is not amongst the 10 v.o.

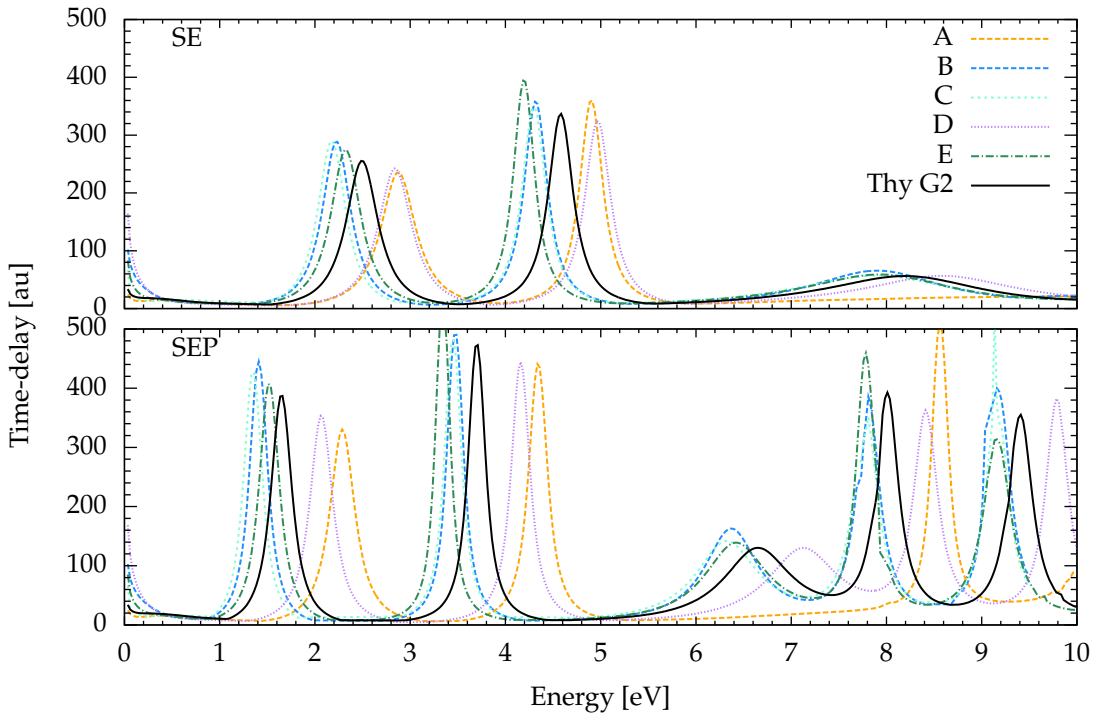

Figure 5.13: Time-delay calculations for thymine in G2 geometry and Thy-H_2O in all non-optimised geometries (indicated in the panel) at SE and SEP levels with 10 v.o.

Figure 5.13 illustrates the direct effect of water on the resonance positions for Thy-H_2O clusters. These results confirm once more time T. C. Freitas *et al.*'s conclusion of the role of hydrogen bonds on resonance shifts. The SEP results are consistent with SE ones: the resonances are stabilized for clusters where water act as hydrogen donor and destabilize for clusters where water acts as hydrogen acceptor. Both SE and SEP results give the same qualitative picture for all resonances presented (even

the SEP resonances visible in figure 5.13 which are not present at the SE level have the same trend as the pure π^* shape resonances). However, for the same reason explained in the previous section, comparison of relative resonance positions of isolated thymine and Thy-H_2O at SEP level, may not give reliable results.

The time-delay presented in figure 5.13 shows as well that the resonance shift also depends (however, less prominently) on the bonding location of water in the clusters (in other words, it depends on which thymine atom binds to the water molecule). For instance, we can see in figure 5.13 both at SE and SEP level, that the first π^* resonance of Thy-H_2O E is less stabilized than for clusters B and C, however the second π^* resonance for cluster E is the strongest stabilized. At the SE level, A and D clusters are almost equally destabilized, whereas at SEP level the resonance position is more strongly destabilized in cluster A than in cluster D. However the differences in resonance shifts for different clusters may also be caused by inclusion of different v.o.

In order to investigate how the direct effects vary depending on the number of water molecules in the clusters, calculations have been performed for clusters presented in figures 5.14 and 5.15. The time-delay graphs comparing results for Thy-H_2O, Thy-$(H_2O)_2$ and Thy-$(H_2O)_3$ are presented in figures 5.16 and 5.17. The isolated Thy results are for the geometry G2. The calculations have also been performed at SEP level, but they give the same qualitative picture, therefore they are not presented here.

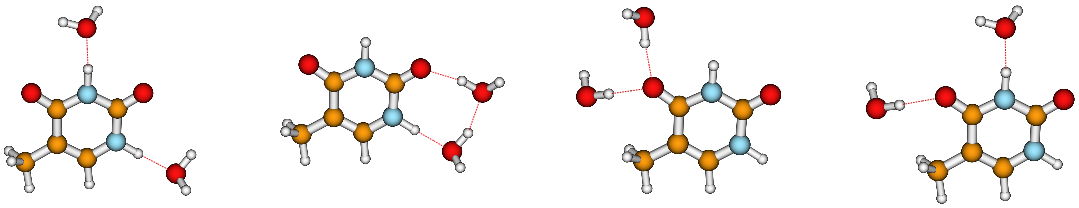

(a) AD (b) AE (c) BC (d) BD

Figure 5.14: Structure of Thy-$(H_2O)_2$ for the four different non-optimised geometries studied in this chapter (same as in figure 5.4). Generated using MOLDEN.

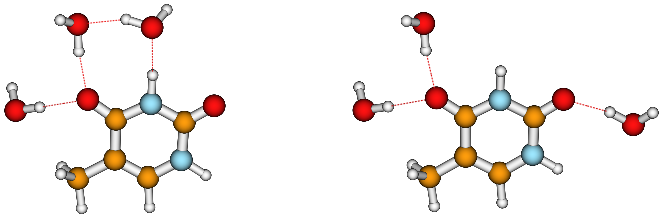

(a) BCD (b) BCE

Figure 5.15: Structure of Thy-$(H_2O)_3$ for the two different non-optimised geometries studied in this chapter (same as in figure 5.5). Generated using MOLDEN.

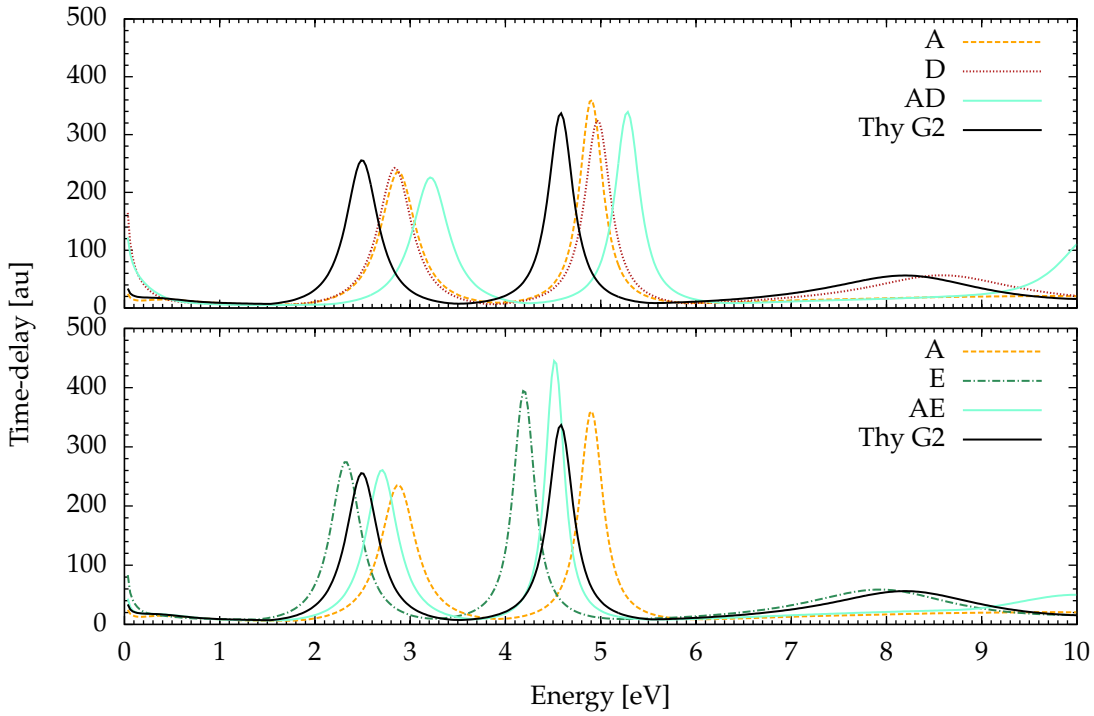

Figure 5.16: Time-delay calculations at SE level with 10 v.o. for isolated Thy and Thy-$(H_2O)_n$, n $= 1,\ 2$ for the geometries indicated in the panels.

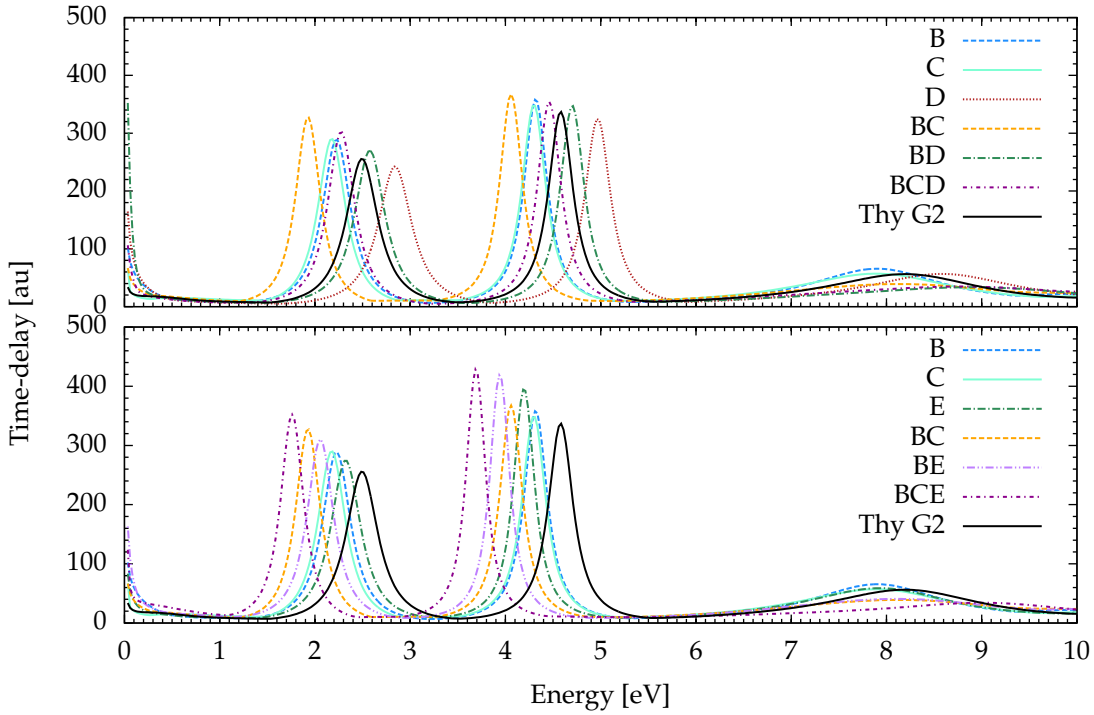

Figure 5.17: Time-delay calculations at SE level with 10 v.o. for isolated Thy and Thy-$(H_2O)_n$, n $= 1,\ 2,\ 3$ for the geometries indicated in the panels.

We can see that the effect of water on the Thy resonances is approximately additive (the shift does not always add quantitatively) for these systems. If in Thy-$(H_2O)_2$, the thymine acts as a hydrogen donor for both water molecules (cluster AD in figure 5.16) the destabilization effect is bigger than for Thy-H_2O clusters A and D. On the contrary, if thymine acts as a hydrogen acceptor for both water molecules, the stabilization effects are bigger. The stabilization or destabilization effect can be

reduced or even cancelled out if one water is a donor and another an acceptor. An example where these effects almost cancel, is the second resonance for the AE cluster in figure 5.16, bottom panel, or the first resonance for the BD cluster in figure 5.17, top panel. The same conclusions apply for Thy-$(H_2O)_3$ (see figure 5.17).

This investigation shows that whether a single water molecule attaching to Thy stabilizes or destabilizes the resonance depends on whether it is the donor or acceptor in the hydrogen bonding. In addition, it also shows that which one of the thymine atoms the water molecule binds to has also an effect on how much the resonances is stabilized/destabilized. The effect of water on the Thy resonances is approximately additive for the Thy-$(H_2O)_n$, n $= 2,\ 3$. Both pure shape resonances are not de-/stabilized of the same amount due to difference in the orbital density of the first and second π^* orbitals.

5.4 THYMINE-$(H_2O)_5$

In this section scattering results are presented for two different clusters containing five water molecules, their structure is presented in figure 5.18. The main difference between these two systems is the water (labelled as a 'B') bound to the oxygen close to the methyl group is not present in the second cluster and it is replaced by a water (labelled as a 'F') bound to the second oxygen. The orientation and distance of the other water molecules are slightly different. Another difference, much less prominent but as important, is that the thymine geometry in these two clusters is different.

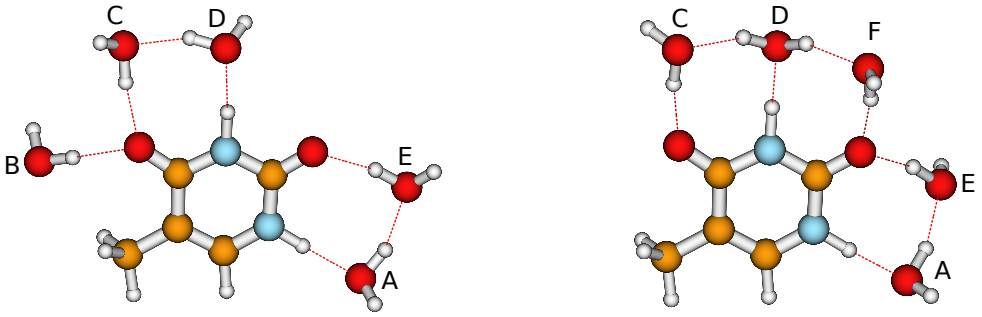

(a) ABCDE (b) ACDEF

Figure 5.18: Structure of Thy-$(H_2O)_5$ for the two different geometries discussed in this section (same as figure 5.2). Generated using MOLDEN.

We will discuss the indirect, direct and total effects of water in both clusters. Next, we will compare our results for the ABCDE cluster with the results of M. Smyth *et al.* [79] for the same cluster, and analyse these results in terms of their agreement with J. Kočišek *et al.*'s experiment [78]. Finally, we will analyse results for polarized thymine and compare them with our *ab initio* calculations for both clusters.

5.4.1 INDIRECT EFFECTS

In order to investigate the influence of changes to the Thy geometry due to the presence of water, we analyse indirect effects. Figure 5.19 illustrates which systems are compared in order to investigate indirect effects.

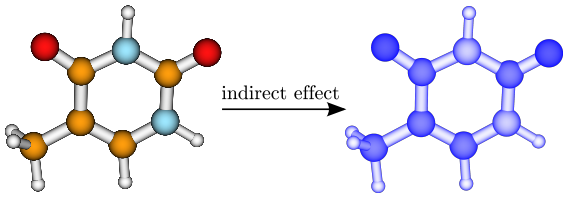

Figure 5.19: In the investigation for indirect effects results of isolated thymine in its equilibrium geometry are compared with those for isolated thymine in the geometry changed by presence of water. The picture of thymine in 'natural' colours indicates that thymine is in its equilibrium geometry, the blue colour indicates that the geometry of thymine in the cluster changed.

The thymine geometries are detailed in figure 5.20. On the left-hand-side we present thymine in its equilibrium geometry (G1), in the middle thymine with the geometry it has in the cluster ABCDE (G2) and on the right-hand-side thymine with the geometry it has in the cluster ACDEF (G3). The bond-lengths for the equilibrium geometry of the isolated thymine (G1) ring are longer than thymine in the cluster ABCDE, except for the that between the carbon bound to methyl group (C_4) and the carbon bound with hydrogen (C_3); the non-ring bonds are either the same or shorter for Thy G1 than in case of the ABCDE cluster (Thy G2). The comparison of the thymine bond-lengths for the equilibrium geometry with the one for the ACDEF cluster shows that almost all (both ring and non-ring) bond-lengths of Thy G1 are shorter than Thy G3 ones, except for these between N_1 and C_2, C_2 and N_2, and C_4 and C_1. On the whole, looking at the volume of these systems, we have found that thymine in the clusters is bigger than in its equilibrium geometry: on average the thymine atoms in the cluster ACDEF are slightly further from the center of mass than in the cluster ABCDE and even further than in its equilibrium geometry.

To investigate indirect effects, calculations have been performed for thymine in the geometries shown in figure 5.20. Table 5.5 shows that changes in bond-lengths have an effect on the energy of the π^* orbitals. The conclusion which arises here is that larger distances between atoms lower the energies of the three π^* orbitals and therefore the SE resonance energies (see figure 5.21) due to a decrease of the energy of orbitals into which the electron is trapped.

The changes in position of the resonances are presented in table 5.6. Note that in this table the resonance shifts obtained at SE level are calculated with 10 v.o. and at SEP level are calculated with 20 v.o. and 30 v.o., whereas the time-delay seen in figure 5.21 is calculated using 30 v.o. both at SE and SEP level. We can already see that the indirect effect on the resonance positions is not negligible.

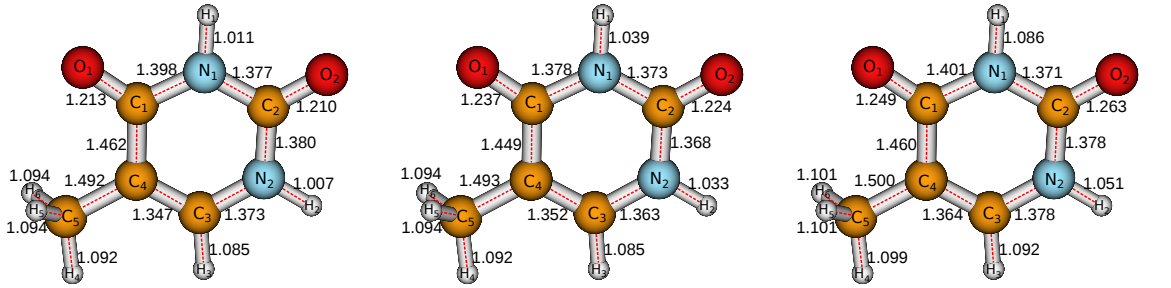

$\updownarrow O_1H_2$ = 4.997	$\measuredangle H_5C_5C_4$ = 110.739	
$\updownarrow H_1H_3$ = 4.768	$\measuredangle H_4C_5C_4$ = 111.148	
$\updownarrow O_2C_5$ = 5.571	$\measuredangle H_4C_5H_5$ = 108.734	
$\measuredangle O_1C_1N_1$ = 120.383	$\measuredangle H_5C_5H_6$ = 106.595	
$\measuredangle H_1N_1C_2$ = 115.599	$\measuredangle H_6C_5H_4$ = 108.732	
$\measuredangle O_2C_2N_2$ = 123.252	$\measuredangle C_1N_1C_2$ = 128.205	
$\measuredangle H_2N_2C_3$ = 121.033	$\measuredangle N_1C_2N_2$ = 112.642	
$\measuredangle H_3C_3C_4$ = 122.070	$\measuredangle C_2N_2C_3$ = 123.779	
$\measuredangle C_5C_4C_1$ = 118.009	$\measuredangle N_2C_3C_4$ = 122.803	
$\measuredangle H_6C_5C_4$ = 110.753	$\measuredangle C_3C_4C_1$ = 117.949	
	$\measuredangle C_4C_1N_1$ = 114.623	

(a) G1

$\updownarrow O_1H_2$ = 5.029	$\measuredangle H_5C_5C_4$ = 110.963	
$\updownarrow H_1H_3$ = 4.792	$\measuredangle H_4C_5C_4$ = 110.666	
$\updownarrow O_2C_5$ = 5.558	$\measuredangle H_4C_5H_5$ = 108.342	
$\measuredangle O_1C_1N_1$ = 120.186	$\measuredangle H_5C_5H_6$ = 106.473	
$\measuredangle H_1N_1C_2$ = 115.505	$\measuredangle H_6C_5H_4$ = 108.563	
$\measuredangle O_2C_2N_2$ = 123.508	$\measuredangle C_1N_1C_2$ = 126.342	
$\measuredangle H_2N_2C_3$ = 119.663	$\measuredangle N_1C_2N_2$ = 114.538	
$\measuredangle H_3C_3C_4$ = 121.848	$\measuredangle C_2N_2C_3$ = 122.514	
$\measuredangle C_5C_4C_1$ = 119.425	$\measuredangle N_2C_3C_4$ = 123.320	
$\measuredangle H_6C_5C_4$ = 111.674	$\measuredangle C_3C_4C_1$ = 116.914	
	$\measuredangle C_4C_1N_1$ = 116.360	

(b) G2

$\updownarrow O_1H_2$ = 5.091	$\measuredangle H_5C_5C_4$ = 110.664	
$\updownarrow H_1H_3$ = 4.878	$\measuredangle H_4C_5C_4$ = 111.327	
$\updownarrow O_2C_5$ = 5.609	$\measuredangle H_4C_5H_5$ = 108.651	
$\measuredangle O_1C_1N_1$ = 120.504	$\measuredangle H_5C_5H_6$ = 106.247	
$\measuredangle H_1N_1C_2$ = 116.071	$\measuredangle H_6C_5H_4$ = 108.806	
$\measuredangle O_2C_2N_2$ = 121.999	$\measuredangle C_1N_1C_2$ = 125.693	
$\measuredangle H_2N_2C_3$ = 120.072	$\measuredangle N_1C_2N_2$ = 115.888	
$\measuredangle H_3C_3C_4$ = 122.494	$\measuredangle C_2N_2C_3$ = 121.955	
$\measuredangle C_5C_4C_1$ = 118.748	$\measuredangle N_2C_3C_4$ = 122.836	
$\measuredangle H_6C_5C_4$ = 110.979	$\measuredangle C_3C_4C_1$ = 117.667	
	$\measuredangle C_4C_1N_1$ = 115.931	

(c) G3

Figure 5.20: Bond-lengths, in Å, and angles, in degree, of thymine in equilibrium geometry (G1) and in clusters: ACDEF (G2) and ABCDE (G3). The double arrows indicate a length between the two atoms listed.

geom	1 π^*	2 π^*	3 π^*	4 π^*
Thy G1	2.91 eV	4.97 eV	9.10 eV	16.14 eV
Thy G2	2.83 eV	4.87 eV	9.08 eV	16.12 eV
Thy G3	2.64 eV	4.61 eV	8.82 eV	16.13 eV

Table 5.5: The shapes and energies of the first four π^* orbitals of thymine in three different geometries.

The SE and SEP results give qualitatively the same picture: the water molecules affect the geometry of thymine, due to these changes the resonances are stabilized. The only exception is the fourth resonance, of mixed shape–core-excited character, which is destabilized for the Thy G2 system. The

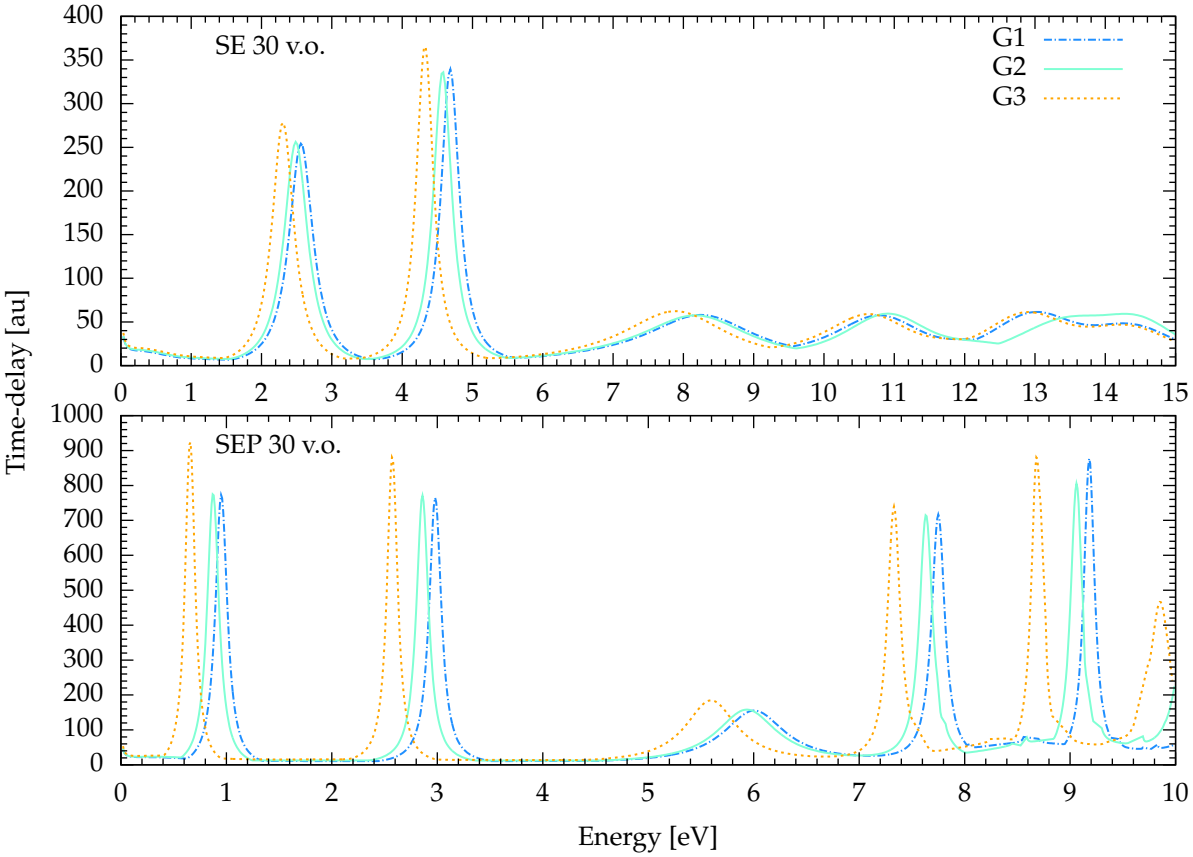

Figure 5.21: Time-delay for thymine in three different geometries (see main text for the explanation of the symbols 'G1', 'G2' and 'G3'). The calculations have been performed for the scattering model and number of v.o. indicated on the panels.

model	v.o.	Δ^{E_r}	1 π^*	2 π^*	3 π^*	4 π^*
SE	10	E_r^{G2}-E_r^{G1}	-0.08	-0.11	-0.07	0.13
		E_r^{G3}-E_r^{G1}	-0.26	-0.36	-0.36	-0.18
SEP	20	E_r^{G2}-E_r^{G1}	-0.08	-0.11	-0.07	-0.10
		E_r^{G3}-E_r^{G1}	-0.30	-0.30	-0.38	-0.42
	30	E_r^{G2}-E_r^{G1}	-0.09	-0.12	-0.07	-0.12
		E_r^{G3}-E_r^{G1}	-0.30	-0.40	-0.41	-0.42

Table 5.6: Shift in the resonance positions of thymine in the geometry corresponding to the clusters ABCDE and ACDEF (G2 and G3) with respect to isolated thymine in its equilibrium geometry (G1). The number of v.o. used in the calculations is indicated in the table.

big change of the behaviour of the resonance with mixed shape–core-excited character comes form the fact that the SE calculations do not include some v.o. necessary to describe the resonance accurately. Comparing the SE results obtained using 20 v.o. for Thy G2 and Thy G1 (not presented in the table and figure) gives the same trend for each of the resonances (also for the fourth mixed shape–core-excited resonance). The shifts between the resonances of Thy G2 and Thy G1 are the same for calculations at SE and SEP level using 20 v.o. and only slightly different for the SEP calculations using 30 v.o. The changes in the resonance shifts of Thy G3 and Thy G1 between methods are small. As we already mentioned, the SEP resonance shifts are not very reliable since we do not have a method

to ensure that the polarization is described at the same level for both systems. However, in this case we compare similar systems: they differ only by bond-lengths of their atoms and most of their orbitals are similar. Therefore, we can be more confident that that polarization of investigated systems is described at a similar level. The SEP resonance shifts presented here seem to be more reliable than the ones presented in the next section. We can state that the changes in the thymine geometry due to the presence of water stabilize all presented resonances in both clusters for both scattering methods. However, the indirect effects have stronger influence on the resonances of the ACDEF than ABCDE cluster.

5.4.2 DIRECT EFFECTS

In order to investigate the direct effects of water in the system we analyse changes in the resonance characteristics in the clusters with respect to isolated thymine in the geometry which it has in the cluster. Figure 5.22 illustrates which systems are compared in order to investigate direct effects.

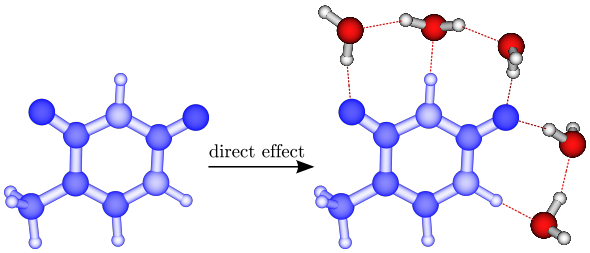

Figure 5.22: In the investigation of direct effects results for isolated thymine in the geometry which it has in the cluster are compared with those for the cluster. The blue colour of thymine indicates that the geometry of thymine is as in the cluster.

As we already stated in section 5.3.3, the effects of water on the Thy resonances are approximately additive (the shift does not always add quantitatively) for clusters with 2 and 3 H_2O molecules. We also noticed that the effect on resonance positions is stronger when Thy acts as a hydrogen donor than when Thy acts as a hydrogen acceptor. Since in both ABCDE and ACDEF clusters, Thy acts as a hydrogen acceptor for three water molecules and donor for two, one might expect the effect to approximately cancel out. The top panel of figure 5.23 shows that this is the case for the first peak in the SE time-delay of the ABCDE cluster: the position of the first π^* resonance of Thy G2 is almost the same as for the cluster ABCDE. The second π^* resonance of the ABCDE cluster is stabilised with respect to the resonance of Thy G2. The third resonance is not present in the cluster, due to the fact that the third π^* orbital is not included amongst the 10 v.o. used in the SE calculations (this is because amongst the chosen v.o. of the cluster are also water orbitals, therefore the third π^* orbital is missing in the cluster calculations but is present amongst the first 10 v.o. of isolated thymine). The shift of the two pure shape π^* resonance positions is consistent with energy differences between first two π^* orbitals of the clusters: ABCDE and ACDEF, and those of isolated thymine: Thy G2 and Thy G3 (see appendix D, table D.1).

In the bottom panel of figure 5.23, the SEP calculations performed with 20 v.o. for Thy G2 and 30 v.o. for the ABCDE cluster are presented. We compare these numbers of virtual orbitals, as the 20

v.o. of isolated Thy are included amongst the 30 v.o. of Thy-$(H_2O)_5$ (i.e. amongst the 30 v.o. we can identify 20 orbitals which also appear for isolated Thy and 10 additional orbitals which correspond to water). This is one of the approaches used in chapter 4 to compare two systems at SEP level. We can see that the trend remains the same as for calculations at the SE level. The position of the first resonance is almost the same, whereas the second resonance is stabilised in the cluster. The third resonance is also slightly stabilized; the resonances above 7 eV are destabilized (the narrow sharp spikes in the SEP graphs at higher energies are pseudo-resonances).

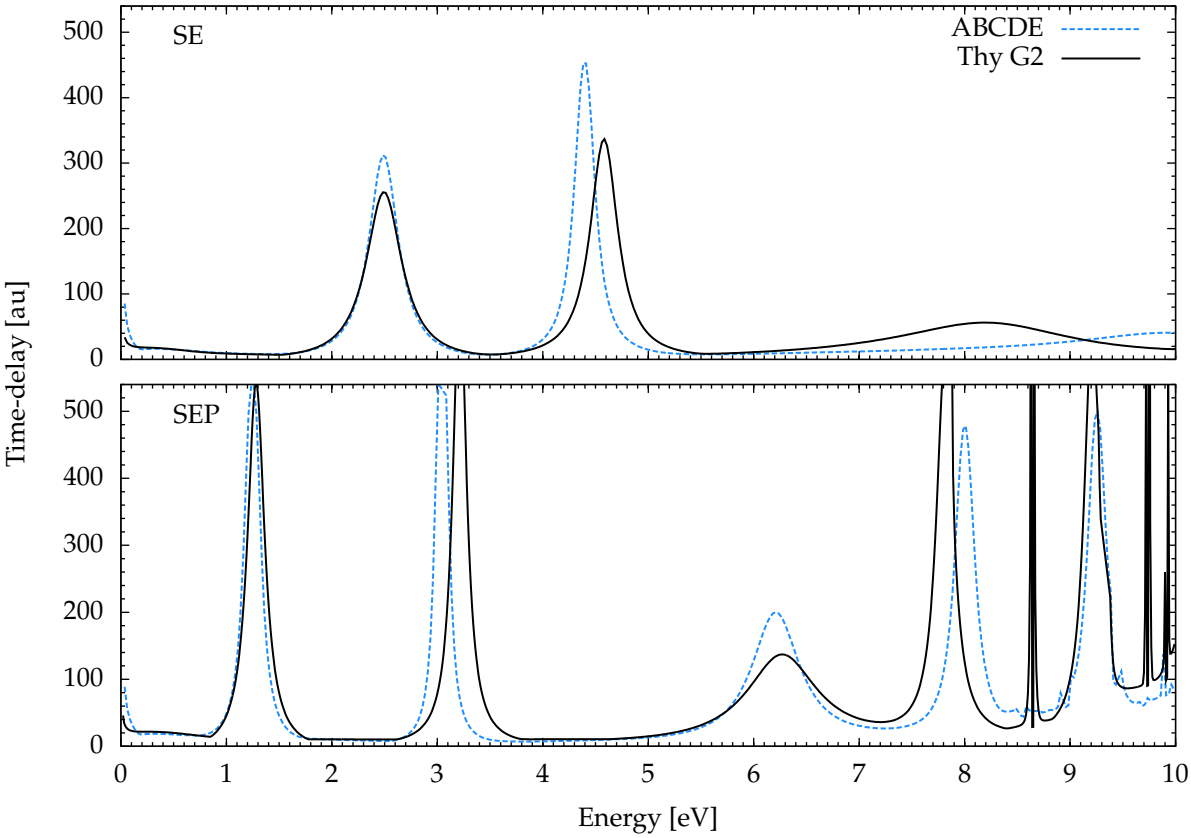

Figure 5.23: Time-delay for Thy-$(H_2O)_5$ ABCDE and isolated Thy G2 at SE level with 10 v.o. (top panel) and at SEP with 20 v.o. for Thy G2 and 30 v.o. for Thy-$(H_2O)_5$ ABCDE (bottom panel).

The resonance positions of Thy G3 and the ACDEF cluster and their shifts are not the same as for Thy G2 and ABCDE cluster. However, the results for SE and SEP calculations are consistent, as in case of indirect effects. The SE time-delay presented in the top panel of figure 5.24 and SEP time-delay presented in the bottom panel of figure 5.24 show that the position of the first, third and fourth π^* resonances is slightly destabilized, whereas the second π^* resonance of the cluster is stabilized, the fifth resonance visible amongst the pseudo-resonances is also slightly stabilized.

The resonance shifts for both clusters are collected in table 5.7. Since the third resonance is not present in the SE time-delay graph (the third π^* orbital into which electron is trapped is not amongst the 10 v.o. of the cluster which are included in the calculation), we analyse only the first and second

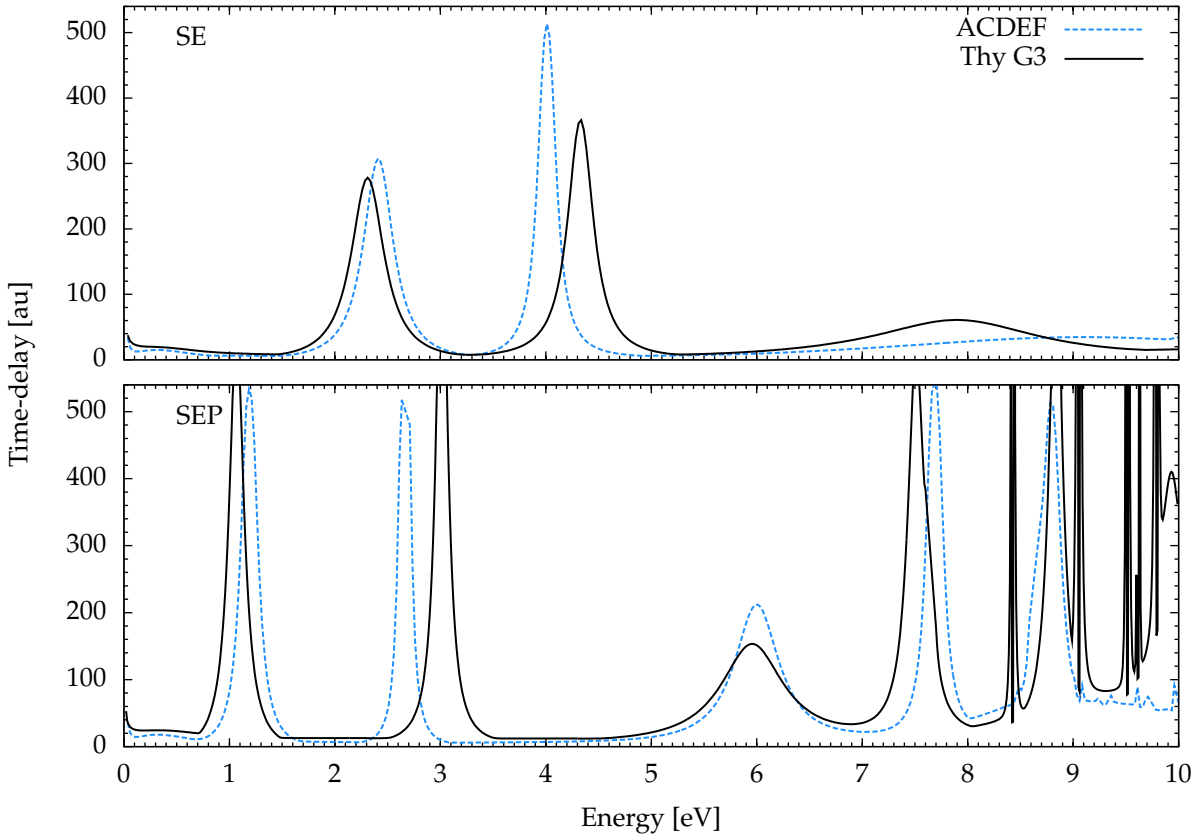

Figure 5.24: Time-delay for Thy-$(H_2O)_5$ ACDEF and isolated Thy G3 at SE level with 10 v.o. (top panel) and at SEP with 20 v.o. for Thy G3 and 30 v.o. for Thy-$(H_2O)_5$ ACDEF (bottom panel).

π^* resonance. Table 5.7 (and figures 5.23 and 5.24) illustrates that the direct effects do not influence resonances in the same way (unlike the indirect effects, which stabilized all resonances for both clusters). The shift of the first resonance of ABCDE cluster with respect to Thy G2 is not significant, whereas the first resonance of ACDEF cluster is destabilized. The second resonance for both clusters is stabilized. The direct effects have stronger influence on resonances of the ACDEF than ABCDE cluster (indirect effects alike).

model	v.o.	Δ^{E_r}	1 π^*	2 π^*
SE	10	E_r^{ABCDE}-E_r^{G2}	0.005	-0.18
		E_r^{ACDEF}-E_r^{G3}	0.11	-0.31
SEP	20	E_r^{ABCDE}-E_r^{G2}	-0.03	-0.17
		E_r^{ACDEF}-E_r^{G3}	0.14	-0.35

Table 5.7: Shift in the resonance positions of clusters ABCDE and ACDEF with respect to isolated thymine in geometry G2 and G3, respectively. The number of v.o. used in the calculations is indicated in the table.

The fact that the second resonance is affected more strongly by water than the first one can be understood by analysing the first and second π^* orbitals of the clusters (we have already used this approach in sections 5.3.2 and 5.3.3), illustrated in table 5.8 (the orbitals can also be find in appendix D, table D.1: orbitals number 59, 61 and 59, 60 for cluster ABCDE and ACDEF, respectively). We can

see that the second π^* orbital has more density close to those water molecules which are hydrogen donors than the first π^* orbital. The differences in the first π^* resonance shift between the two clusters can also be understood by comparing the orbitals. In cluster ABCDE two of the water molecules which act as a hydrogen donor are close to the first π^* orbital, whereas for the cluster ACDEF this is the case for only one water molecule. Therefore the first π^* resonance of the ACDEF cluster is destabilized, while the position of the first resonance of cluster ABCDE hardly changes (see table 5.7). The differences in the second π^* resonance shift between the two clusters is harder to explain by looking at the second π^* orbital, since the same number of water molecules which are hydrogen donors are close to the second π^* orbital. Therefore, the reasons may be distance between thymine and water (stronger hydrogen bonds in ACDEF cluster).

cluster	1 π^*	2 π^*
Thy-$(H_2O)_5$ ABCDE	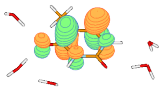	
Thy-$(H_2O)_5$ ACDEF	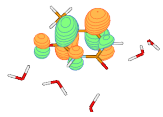	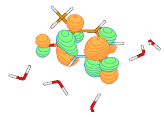

Table 5.8: The shapes and energies of the 1st and 2nd π^* orbitals of ABCDE and ACDEF clusters.

5.4.3 TOTAL EFFECTS

In order to investigate the total effect of water on thymine, we compare thymine clusters with isolated thymine in its equilibrium geometry (illustrated in figure 5.25).

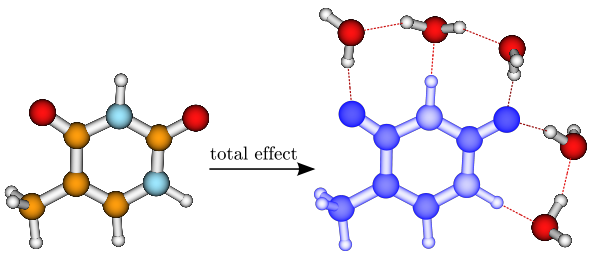

Figure 5.25: In the investigation of total effects results for isolated thymine in its equilibrium geometry are compared with those for the cluster. The picture of thymine in 'natural' colours indicates that thymine is in its equilibrium geometry, the blue colour indicates the geometry of thymine in the cluster.

The total effect is the sum of the indirect and direct effects. Therefore if we sum the resonance shifts caused by the indirect (see table 5.6) and direct effects (see table 5.7), we get the total shifts (see table 5.9).

Analysing table 5.6 or figure 5.21, we noticed that in general the indirect effect of water stabilized the resonances. Table 5.7 or figure 5.23 and 5.24 show that direct effects at SE level have very little effect on the position of the first ABCDE resonance, destabilize the first ACDEF resonance and stabilize the second one for both geometries.

model	v.o.	Δ^{E_r}	1 π^*	2 π^*
SE	10	E_r^{ABCDE}-E_r^{G2}	-0.075	-0.29
		E_r^{ACDEF}-E_r^{G3}	-0.15	-0.67
SEP	20	E_r^{ABCDE}-E_r^{G2}	-0.11	-0.28
		E_r^{ACDEF}-E_r^{G3}	-0.16	-0.65

Table 5.9: The resonance shifts of clusters ABCDE and ACDEF with respect to isolated Thy in its equilibrium geometry (G1). The number of v.o. used in the calculations is indicated in the table.

The total effects of water on the resonances of the Thy-$(H_2O)_5$ ABCDE cluster are illustrated in figure 5.26. To analyse these effects we compare Thy G1 with the ABCDE cluster. At both SE and SEP level the first and second resonances are stabilized. The situation is similar for the cluster ACDEF at SE and SEP levels, as illustrated in figure 5.27. For both clusters and isolated Thy the SE calculations have been performed with 10 v.o. and the SEP calculations with 30 v.o. for clusters and 20 v.o. for isolated Thy. The two pure shape π^* resonance shifts for both clusters at SE and SEP level are collected in table 5.9.

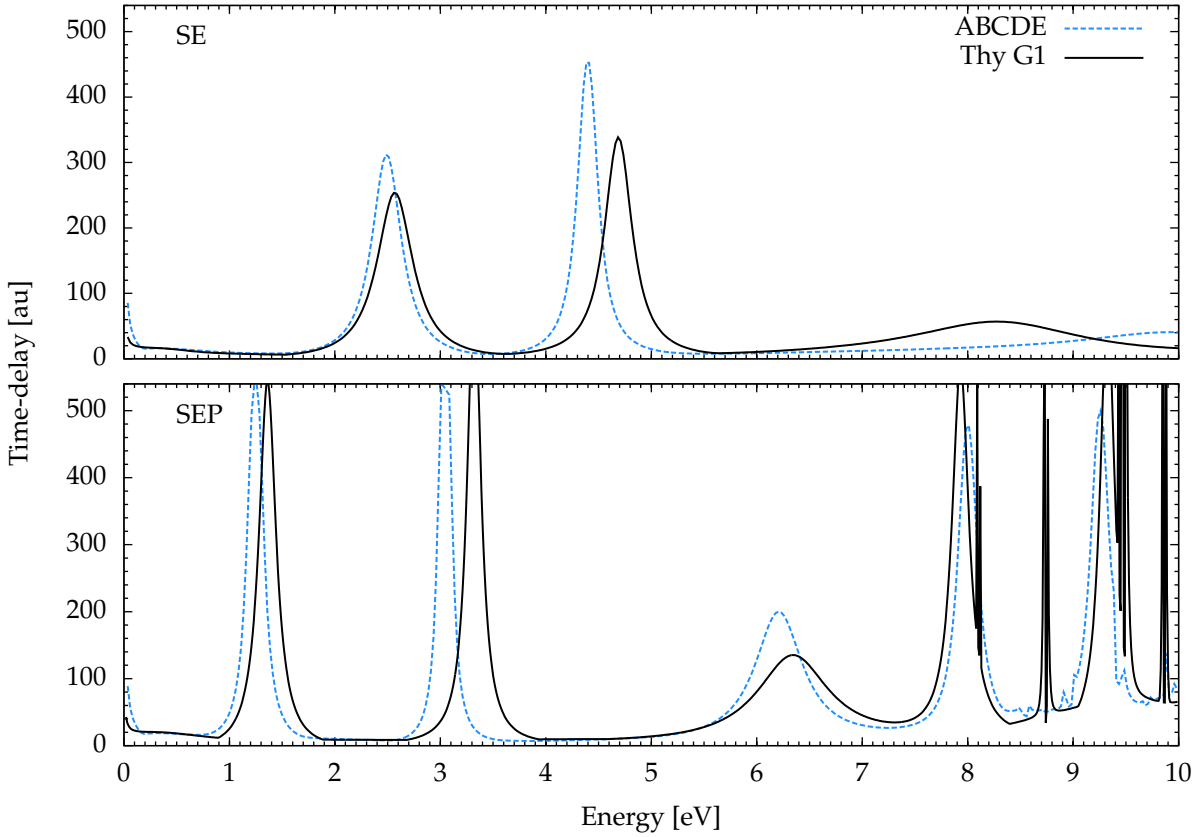

Figure 5.26: Time-delay for Thy-$(H_2O)_5$ ABCDE and isolated Thy G1 at SE level with 10 v.o. (top panel) and at SEP with 20 v.o. for Thy G1 and 30 v.o. for Thy-$(H_2O)_5$ ABCDE (bottom panel).

The role of indirect and direct effects on resonance positions is not always the same. Moreover they do not influence all resonances in the system in the same way. Although the indirect effects stabilize the two pure shape π^* resonances, the second one is slightly stronger affected than the first one at the SE and SEP levels for both clusters (the exception is the resonance shift of the ACDEF

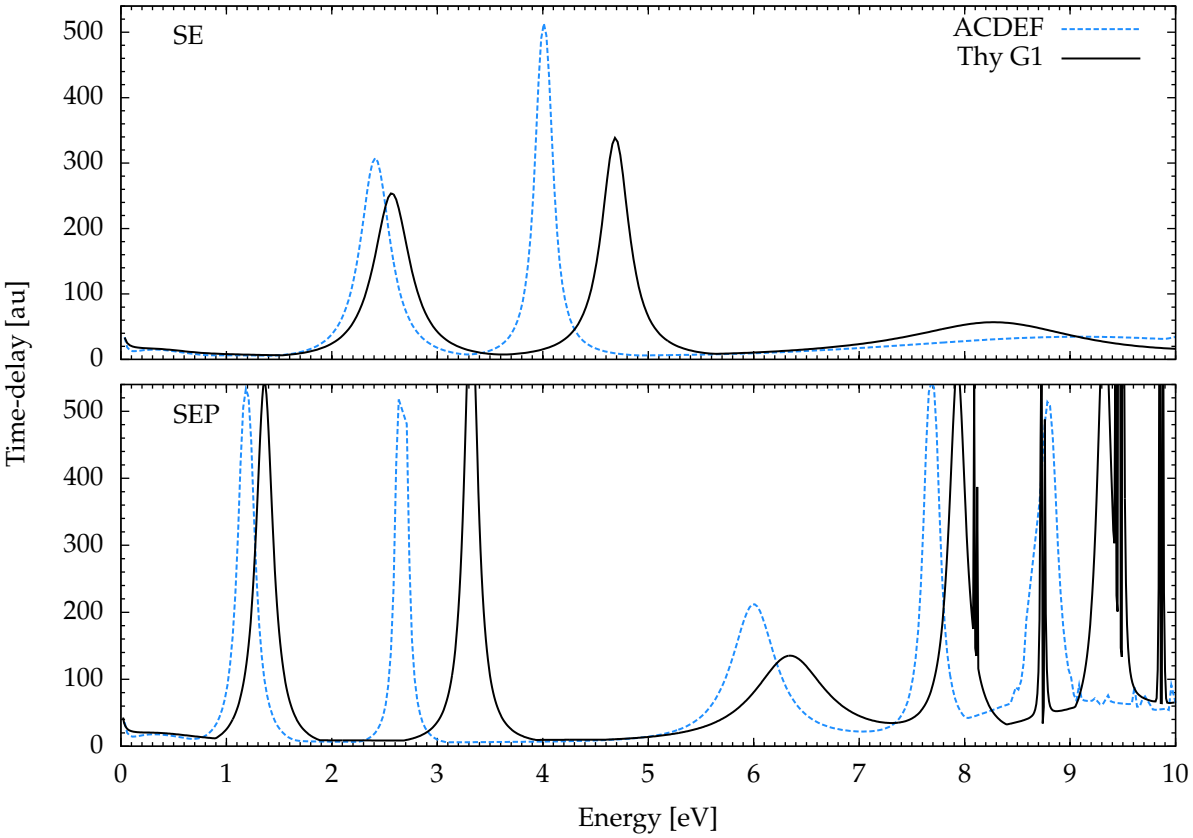

Figure 5.27: Time-delay for Thy-$(H_2O)_5$ ACDEF and isolated Thy G1 at SE level with 10 v.o. (top panel) and at SEP with 20 v.o. for Thy G1 and 30 v.o. for Thy-$(H_2O)_5$ ACDEF (bottom panel).

cluster for SEP calculations using 20 v.o.: the shifts of first and second π^* resonances are the same). The influence of the direct effect on the second resonance is also stronger than for the first resonance (regardless of the sign of the shift, i.e. the second resonance is stabilized more than the first is destabilized). The same trend can be noticed analysing the total effect: both pure shape π^* resonances are stabilized but the second resonance is affected more strongly by the presence of water. The total effects have a stronger influence on resonances of the ACDEF than ABCDE cluster (indirect and direct effects alike). Most of the differences in the resonance shifts between the two clusters come from the different geometry of Thy (indirect effects, see table 5.6).

Our results show that the influence of water on the resonance positions does not have the same effect for each resonance in the cluster. The resonance shift depends on many conditions, for instance, whether water acts as the acceptor or donor in the H-bond, how many water molecules are in the cluster, what the binding sites are, how much the binding water to Thy changes its geometry. The changes in the resonance position of the two clusters are not large. Only the second resonance of the ACDEF cluster shifts more than 0.5 eV towards lower energies. The resonance shifts of both clusters are approximately equal to the energy differences of the π^* orbitals of the clusters with respect to isolated Thy G1. SE and SEP results give qualitatively the same picture of the water influence on resonance de-/stabilization.

5.4.4 COMPARISON WITH PRIOR RESEARCH

M. Smyth *et al.* have performed VEA and DEA calculations for N_2-H (see figure 5.20) fragmentation, for uracil and thymine, surrounded by five water molecules, based on the nonlocal complex potential and multiple scattering theories [51, 154, 155]. This allowed them to obtain the DEA cross section for hydrogen detachment, which is strongly enhanced by presence of a water cluster. They explained the strong enhancement of the DEA cross section by two effects: lowering of the resonance position of thymine/uracil and the increase of the resonance lifetime, both due to interaction with the water molecules. They performed the VEA calculations only for the first π^* (A') resonance, whereas G. A. Gallup and I. I. Fabrikant [62] determined that the resonance which leads to N_2-H fragmentation is a very wide σ^* resonance and N_1-H (see figure 5.20) fragmentation is due to the coupling between the σ^* and the second π^* (A'') resonance. M. Smyth *et al.* assumed that the other resonances also behave in the same way as the one calculated by them.

M. Smyth *et al.* also calculated vertical attachment energies for the first π^* resonance of isolated thymine (our Thy G1) and three clusters of Thy-H_2O (our Aeq, Beq, Deq); these values together with Thy-$(H_2O)_5$ (our ABCDE) and our resonance positions are collected in table 5.10. The SE calculations give absolute resonance positions much higher in energy since this is the most basic approximation. Also, our SEP results for absolute resonance positions are not reliable as we have not included enough virtual orbitals in our calculations. Therefore, the comparison of our results will be qualitative and not quantitative: we analyse how the cluster's resonance positions change with respect to the isolated Thy. In the table we only present the SEP results for Thy G1 with 20 v.o. and Thy-$(H_2O)_5$ with 30 v.o. (the reason for comparison of the SEP calculation for these specific number of v.o. has been explained in section 5.3.1). We do not present here our results for Thy-H_2O since we only have SEP calculations with 10 v.o. available. As we have already explained in chapter 4, the comparison of resonance positions between different systems at the SEP with the same number of v.o. may not give reliable results, as for each cluster we may be including different levels of polarization.

		Thy G1	Aeq	Beq	Deq	ABCDE
VEA	Smyth *et al.*	0.43	0.30	0.16	0.22	0.11
1 π^* res.	SE	2.56	2.65	2.31	2.67	2.49
	SEP	1.36				1.25

Table 5.10: Vertical electron attachment (VEA) and energy of the first π^* resonance (1 π^* res.) of isolated Thy, Thy-H_2O for geometries Aeq, Beq and Deq and Thy-$(H_2O)_5$ ABCDE. The results of Smyth *et al.* are taken from [79]. Our results are calculated at SE level with 10 v.o. and SEP with 20 v.o. for Thy G1 and 30 v.o. for cluster ABCDE .

By analysing Smyth *et al.*'s results collected in table 5.10, we can see that water decreases the VEA. In the Thy-H_2O clusters the VEA strongly depends on the binding site at which water is attached to

Thy, but in each case the VEA is smaller than that of isolated thymine. For Thy-$(H_2O)_5$, the VEA changes (decreases) by -0.32 eV. Our calculations for the first resonance for Thy-$(H_2O)_5$ also show a lowering of its position but the stabilisation is less strong than the one calculated by Smyth *et al.* At the SE level the resonance shifts by -0.07 eV; the SEP results also give a shift much smaller than the Smyth *et al.*'s (about -0.11 eV). The behaviour of the first resonance shifts for Thy-H_2O for our calculations are also different from Smyth *et al.*'s ones. The energy of the resonance for clusters Aeq and Deq increases, i.e. we observe destabilization of the resonances. Our calculations show that the effect on resonance positions depends on the water acceptor/donor character in the cluster (which has already been shown also in work [27, 140]) and with respect to this can destabilize or stabilize resonances. We also noted in the previous sections that water does not have the same effects on each resonance (the size and sign of the shift does not have to be the same for every resonance) in the same system. That is in contradiction to the assumption made by Smyth *et al.* that water has always the same stabilizing effects on each resonance (i.e. they stated that water always stabilize all resonances) and that the resonance shift is the same for each resonance in the system like the 1 π^* resonance calculated by them.

The strongly enhanced cross section for the fragmentation process obtained by Smyth *et al.* is not in agreement with the latest experiment carried out by Kočišek *et al.* [78]. However, the experimental results are for hydrogen detachment from both nitrogen atoms, while the Smyth *et al.* calculations only for one. Kočišek *et al.* performed experiments for small clusters of thymine/uracil with water – microhydrated nucleobases. The size of the clusters was controlled by controlling the pressure in the chamber to produce only clusters with a small number of water molecules. However, the experimental set-up did not allowed them to determine the proportion of clusters of different sizes. They performed the measurements for two values of molecular beam pressure; this allowed them to compare the results for a mixture with larger concentration of smaller cluster than the other.

The experiment shows that microhydration leads to production of different DEA fragments than the isolated nucleobases. The presence of water molecules prevents the hydrogen fragmentation process. Kočišek *et al.* gave two possible explanations for that outcome: first, changes to the resonance caused by the hydration; second, "a redistribution of internal energy by water (caging) and stabilization of the intact anion" [78] (uracil$^-$/Thy$^-$). They pointed out that Smyth *et al.*'s work [79] does not predict significant changes in the resonance characteristic and therefore concluded that the most probable explanation is the caging effect. However, Smyth *et al.*'s results present significant changes in resonance position (almost 75%) and lifetime (around 40%) influenced by the present of water. Actually, our results show that water does not change resonance characteristics significantly (see figure 5.26). Therefore, our results support the proposed explanation of changing fragmentation channels by caging effects.

The Kočišek *et al.* experiment indicates that the presence of water molecules in the systems has another role in the DEA process than de-/stabilization of the resonance, i.e. can prevent the dissociative fragment from detaching and by energy transfer it can detach itself. Therefore, these experimental results are not in contradiction to our results but introduce a different role of water on the DEA process.

5.4.5 THYMINE WITH POLARIZED ORBITALS

The results for systems in which water is described using the polarized continuum model in one case and as point charges in the second case (introduced at the beginning of this chapter) are presented in figure 5.28. The calculations for the system in which water is described as point charges (Thy-char) have been performed only for the ACDEF cluster. The polarized continuum model (PCM) and point charges model describe the effect of water on thymine.

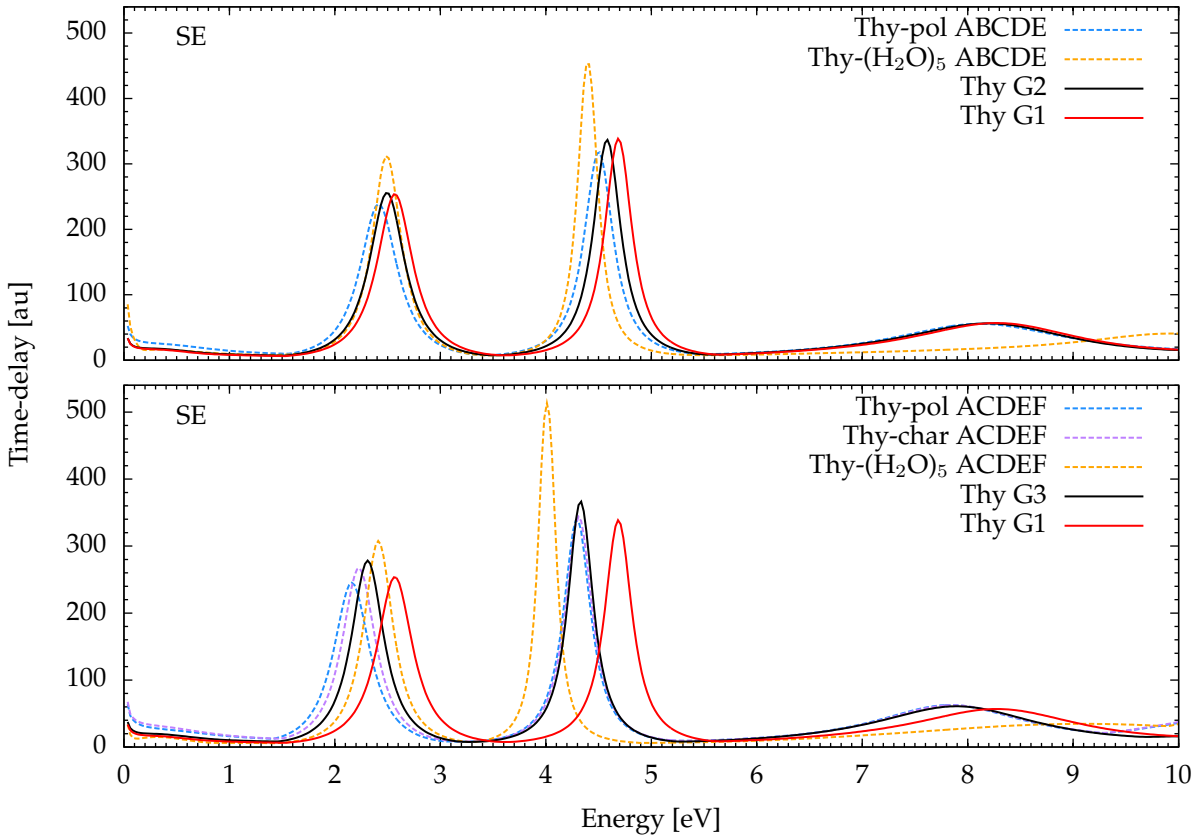

Figure 5.28: The time-delay for Thy-pol and Thy-$(H_2O)_5$ in geometry ABCDE (top panel) and time-delay for Thy-pol, Thy-char and Thy-$(H_2O)_5$ in geometry ACDEF (bottom panel) at SE level with 10 v.o. In both panels are also plotted time-delays for isolated Thy G1 and G2 at SE level with 10 v.o.

The thymine in the clusters Thy-pol ABCDE, Thy-pol ACDEF and Thy-char ACDEF has the same geometry as in the cluster ABCDE, ACDEF, respectively. Therefore, the indirect effects are the same as in section 5.4.2. From figure 5.28, we can analyse the direct effects (comparing Thy-pol/Thy-char

with Thy G2 or G3) and total effects (comparing Thy-pol/Thy-char with Thy G1). The direct effects are not significant; the resonances of Thy-pol ABCDE are slightly stabilized with respect to Thy G2. We can also notice stabilization of the first resonance of Thy-pol and Thy-char ACDEF with respect to Thy G3, however the position of the second resonance remains almost the same. Therefore, we can state that the total effects are mostly indirect effects, i.e. the changes in resonance positions between Thy-pol/Thy-char and Thy G1 are mostly caused by the change in geometry of thymine in Thy-pol/Thy-char, and not by modified orbitals. This is not the case for *ab initio* calculations for Thy-$(H_2O)_5$. Although, the positions of the first resonance are similar for Thy-pol ABCDE and Thy-$(H_2O)_5$ ABCDE, the positions of the second resonance differ more prominently: the Thy-$(H_2O)_5$ ABCDE resonance is more stabilized than the Thy-pol one. Both the 1^{st} and 2^{nd} π^* resonance of the cluster ACDEF differ substantially from those of Thy-pol/Thy-char ACDEF. In terms of direct effects, the first resonance is destabilized for cluster ACDEF (see table 5.7), while for Thy-pol ACDEF is stabilized. In terms of total effects the Thy-$(H_2O)_5$ ACDEF first resonance is less stabilized than the Thy-pol/Thy-char ACDEF one. However, the second π^* resonance of Thy-$(H_2O)_5$ ACDEF is stabilized much more significantly than the one of Thy-pol/Thy-char ACDEF, in terms of direct and total effects. We can also see (more clearly in the case of ACDEF Thy-pol/Thy-char and ACDEF Thy-$(H_2O)_5$) that the resonance positions of Thy-pol/Thy-char are closer to the resonance positions of isolated Thy than of Thy-$(H_2O)_5$.

The fact that the direct effect on Thy-pol are not significant and do not have the same trend as the one for Thy-$(H_2O)_5$ may suggest that the PCM does not describe the influence of water on the system correctly. On the other hand, in the SE calculations for Thy-pol the polarization effects have been included (polarized orbital have been used in the calculation), therefore comparing the SE results for Thy-pol with our SE results for isolated Thy and Thy-$(H_2O)_5$, may not be accurate. However, we know that inclusion of polarization effects in R-matrix calculation always stabilizes resonances and qualitatively does not change the resonance shifts (as shown in sections 5.4.1-5.4.3). Assuming that inclusion of same amount of polarization would stabilize the two pure shape π^* resonance equally, it is possible the position of the first resonance for Thy-pol could be the same as the one for the clusters, but differences between the positions of the second resonances for Thy-pol and Thy-$(H_2O)_5$ would be even larger than the one observed in figure 5.28. Therefore it is more likely that the reason for the differences in results for Thy-pol and Thy-$(H_2O)_5$ systems is that PCM do not describe accurately the total effect of water on thymine. This means that our expectation of being able to replace the computationally expensive and time-consuming calculations including all molecules in the cluster by much simpler ones using polarized orbitals is unlikely to yield good results.

5.5 SUMMARY

In this chapter we investigated how water influences the resonance position in Thy-$(H_2O)_n$, n = 1, 2, 3, 5, with focus on pure π^* resonances. Although both thymine and pyridine are ring molecules they form clusters which are fairly different in structure (see figures 4.18 and 5.18). In pyridine clusters water concentrates near to nitrogen and only one water is bound to the ring, whereas the water molecules in thymine clusters are located around the ring with different binding sites and acceptor/donor characters. Therefore the scattering results presented in this chapter are fairly different from those presented in chapter 4. Unlike pyridine cluster calculations, the thymine ones allowed us to investigate the role of water as a hydrogen acceptor and the effect of more than one water molecule bound to the ring. These results show that the conclusions deduced by T. C. Freitas *et al.* [27] for formic acid clusters also hold for all thymine clusters presented in this chapter. Moreover, we observed that the effect of water on the resonances positions is additive.

We mostly focused on Thy-$(H_2O)_5$ clusters for which we presented a detailed study for indirect, direct and total effects of water on thymine. We observed that the indirect effect stabilized thymine resonances (both in ABCDE and ACDEF geometry), while in the previous chapter we showed the opposite effect on pyridine resonances. However, we noticed for all investigated molecules that comparing the same molecule in equilibrium geometry and the one in the cluster, gives a resonance position lower in energy for the system with longer bond-lengths (bigger volume). There is no qualitative picture to explain the water indirect effect on de-/stabilization of the resonances, unlike to direct effects, for which the de-/stabilization of the resonances is explained by water acceptor/donor character.

The direct effects more strongly influence the second π^* resonance than the first one, unlike in pyridine clusters, where the first π^* resonance is affected more strongly than the second one. The different effects on π^* resonances can be correlated with the shape of the π^* orbitals into which electron is trapped. If the electronic density of the π^* orbital is located close to the water molecule the resonance shift is affected more strongly. The direction of the shift also seems to depend on which of the water atoms is closer to the molecule: if hydrogen is closer to the molecule the resonance is stabilized, and in case of oxygen it is destabilized. In the clusters with more then one water molecule, the effects of each water are competitive and not always obvious.

The total effects of water on ABCDE and ACDEF clusters on both π^* resonances is stabilization as it was the case for pyridine clusters. However our calculations for smaller thymine clusters showed that the presence of water does not always have to stabilize resonances. We also showed that resonances in the system are not always affected by water in the same way. Therefore our calculations

are in contradiction to some assumption and conclusion presented by M. Smyth *et al.* [79]. Moreover our calculations show that the presence of water does not have as strong an effect on resonance shifts as presented in the paper of M. Smyth *et al.* Our results support Kočišek *et al.*'s hypothesis about caging effect [78] preventing hydrogen fragmentation loss (see section 5.4.4 for more details). Finally, our calculations in which water effects on thymine are described using the polarized continuum model do not give the same results as *ab initio* calculations. Therefore the time-consuming and computationally expensive *ab initio* calculations cannot be replaced with the simplest ones.

6

CONCLUSIONS AND OUTLOOK

The main focus of this work was to investigate collisions of low-energy electrons with small molecular clusters, i.e. biological molecules bound with one, up to five water molecules, and the influence of water on resonance characteristics. To study these influences *ab initio* R-matrix calculations have been performed.

In order to investigate how resonance characteristics are modified by the presence of water, the isolated molecules have been studied. Therefore, we investigated isolated pyridine and thymine and their clusters with water molecules. Due to the fact that, at the time, there were no available calculations of low-energy electron collision from isolated pyridine (and, to our knowledge, no other inelastic calculations are yet available), this system has been studied in detail by us. In this work we performed calculation for pyridine using the SE, SEP and CC approximations (see chapter 3). We presented elastic and inelastic integral and differential cross sections, resonance energies and widths and characterised the resonances' parent states. To determine the resonance characteristics we used the time-delay analysis, which we found to be the most useful tool for identifying and characterizing resonances. We found a large number of resonances, most of which had not been characterized before. We compared our pyridine results with those obtained in our group for pyrimidine. In most cases, the pyrimidine results are qualitatively similar to pyridine ones: the cross sections have similar shape (see section 3.3 and appendix B) and many resonances have parent states of the same symmetries (see section 3.4).

The pyridine resonances have been compared to those of Pyr-H_2O at SE, SEP and CC level. At SE and SEP levels we compared the two pure shape π^* resonances (as only these resonances can be fully described using these models), while at CC level all resonances up to 10 eV have been compared. All

resonances which appear for pyridine are also present for Pyr-H_2O. Results for the CC calculations (presented in section 3.3.3) with a low number of virtual orbitals shows that not all resonances stabilize due to water presence. However, the results for calculations with more than 20 v.o. present stabilization for all resonances. We conclude that for Pyr both shape and core-excited resonances are shifted towards lower energy when a single water molecule attaches to it.

We also analysed our SE results for Pyr-$(H_2O)_n$, n = 1, 2, 3, 5, in terms of indirect, direct and total effect of water on the resonances. Water influences resonance positions in two ways: by changing the geometry of the molecule to which it is bound (indirect effect) and by the explicit presence of water in the system, excluding change of molecule geometry (direct effect). In terms of indirect effect, water destabilizes pyridine resonances (in each pyridine cluster the shift is the same), however the direct and total effects of water stabilize the resonances. Water affects slightly more the first pure π^* resonance than the second one. We explain that by the shape of the π^* orbitals: the first π^* orbital has more density close to the water than the second one.

Including more water in the cluster, does not change the direction of the shifts for the pure shape π^* resonances at SE level. However, the resonances for Pyr-$(H_2O)_n$, n = 2, 3 are less stabilized than Pyr-H_2O resonances, while, the Pyr-$(H_2O)_5$ shape resonances are more stabilized than Pyr-H_2O. In each of the clusters only a single water molecule is directly bound to the ring by nitrogen, each additional water is bound to another water molecule. The resonance positions of the clusters seem to be correlated with their dipole moment (see section 4.4).

Calculations for low-energy electron collisions with isolated thymine using the R-matrix method at SE, SEP and CC level have been already performed by A. Dora *et al.* [16]. Therefore, in this work we only presented the calculations for isolated thymine which are needed to compare with thymine clusters. Namely, calculations at SE and SEP level for isolated thymine and Thy-$(H_2O)_n$, n = 1, 2, 3, 5 have been performed. Due to the computational demands of these calculations and very long computational time, no CC calculations have been performed. Also, for the same reasons, the SEP calculations have not been performed with the number of virtual orbitals which would give resonance energies close to experimental values. Thereby, the SEP results presented in this work do not give reliable resonance positions for isolated Thy and Thy-$(H_2O)_5$. The purpose of these calculations was to investigate role of water on resonance positions and examine if the same qualitative picture is obtained both at SE and SEP level. Thy-$(H_2O)_n$, n = 1, 5 have been investigated in terms of indirect, direct and total effects for both scattering models. However, in Thy-H_2O indirect effects are negligible, thus direct effects are equal to the total effects in these systems. The systems: Thy-$(H_2O)_n$, n = 2, 3 have been investigated in terms of direct effects only (as we did not posses the equilibrium geometries for those systems). The broadest investigation has been done for Thy-$(H_2O)_5$, as theses results could be compared to another calculations performed by M. Smyth *et al.* [79] and experimental

results for microsolvated thymine carried out by J. Kočišek *et al.* [78].

Investigation of the pyridine and thymine clusters in terms of indirect effects at SE level shows that these effects may play a different role in each system. Water influences the pyridine geometry in a way that destabilize resonances, whereas in Thy-$(H_2O)_5$ indirect effects stabilize the resonances.

The direct effects obtained at SE level are consistent between all systems presented in this work, and they depend on the role of the water binding to the molecule: water acting as a hydrogen donor stabilizes the resonance positions, while water acting as a hydrogen acceptor destabilizes the resonance positions. This dependence of acceptor/donor character of water on the resonance position was first deduced by T. C. Freitas *et al.* [27], who investigated formic acid bound to one and two water molecules. The investigation of Thy-$(H_2O)_n$, n = 1, 2, 3, 5, extended their conclusion to ring molecules and to clusters up to five water molecules (since in Pyr-$(H_2O)_n$, n = 1, 2, 3, 5 only one water is directly bound to the ring, in the same position and orientation for all clusters, we can only investigate the role of single water acting as a hydrogen donor). We also found that the effect of water on the resonances positions is additive. Therefore, in the system with several water molecules, where some of them act as a hydrogen donor and the others act as acceptor, these effects can cancel out. We also noticed that in the direct effects destabilization is stronger than stabilization. Although the direction of the shift for all pure shape π^* resonances depends on the water role as a donor or acceptor, the effects are not equally strong for each resonance. By looking at the π^* orbitals into which the incoming electron is trapped, we found a correlation between orbital density and resonance shift: if the electronic density of the orbital that the scattering electron occupies is localised close to the water molecules the shifts are stronger than when the orbital density is not close to the water molecules.

For clusters with more than one water, where some are hydrogen donors and some hydrogen acceptors, the direction of the resonance shifts in the same system may be different. This situation can be observed for Thy-$(H_2O)_5$ (see, section 5.4.2). Since each water molecule does not shift both resonances by the same amount, the combination of effects from all water molecules can give the opposite effect for each resonance.

The total effects are a sum of indirect and direct effects. The direct effects are correlated whether water is bound as a proton donor or acceptor in the cluster, however not indirect effects. Therefore, in principle the outcome of these effects does not have to depend on water acceptor/donor character. For pyridine clusters the direct effects are stronger than indirect effects, therefore as the total effect we observe a stabilization of resonances in these systems. In Thy-$(H_2O)_5$, however, both indirect and direct effects stabilize the second resonance but the first resonance is stabilized by indirect effect and slightly destabilized by direct effects. As a total effect we observe stabilization of both shape resonances in Thy-$(H_2O)_5$ clusters.

The investigation of Thy-$(H_2O)_n$, n = 1, 2, 3, 5 in terms of indirect, direct and total effects at SEP

level are qualitatively consistent with the observation at SE level. However, since we are not able to ensure how much polarizability is included in our calculations, we are not sure if we are comparing like-with-like. And therefore, we are not confident that the resonance shifts influenced by presence of water are reliable.

Calculations to determine how much of the polarization effects are included in the calculations for both compared systems have been undertaken in this work. Our first approach was to estimate the polarizability of the investigated systems and then include the same percentage of polarizability for both. We tested isolated pyridine and isolated formic acid. In the first case, to obtain resonance positions close to experimental values, we needed to overestimated the experimental value of polarizability. However, in the case of formic acid, with the polarizability under the experimental value the right resonance position can be obtained. Due to the fact the results for these systems are not consistent we suspect that either the program does not calculate the polarizability correctly or our understanding of the problem is not correct or complete. One way or another, at this stage, we are not able to use this method to determine the number of virtual orbitals needed to be used in our calculations in order to compare scattering data for the cluster with that for isolated molecule confidently.

The second approach to this problem was to only include the virtual orbitals in the calculations of the isolated molecule which are also present in the cluster calculations. Since the identification of the orbitals is not always straightforward and we do not know if we describe enough polarizability of water this method does not guarantee that the polarization effects are described in the same level for both system. We also do not possess any experimental data for the clusters we studied (or any other) to ensure whether the calculations with the number of virtual orbitals chosen in this way give the right position of resonances. Nevertheless, this method is the best we can do right now to compare SEP and CC calculations for various systems.

Future work should try to accomplish the challenge of finding the recipe of how many virtual orbitals should be included in the cluster calculations. This would allow us to predict actual resonance position. A more challenging future task is to find a method which can determine the number of virtual orbitals (polarization) needed in the calculations to obtain the accurate resonance position for any system.

Future work should also include thymine clusters calculations at CC level, in order to investigate of the water effect also on core-excited resonances. Performing calculations at SEP level with a higher number of virtual orbitals than those presented in this work would give a better description of the shape π^* resonances. Using larger CAS model for Pyr-H_2O system would improve the description of the presented resonances for this system. Since DEA also strongly depends on the resonance width, the future studies should focus on the characterisation of this parameter.

Our work shows that the presence of water in the investigated systems has an effect on the resonance characteristic. Kočišek *et al.*'s experiment [78] (discussed in section 5.4.4 of chapter 5) proved that water significantly influences the DEA processes (it prevents the hydrogen fragmentation process in thymine and uracil). However, the possible explanation of the changes in DEA influenced by the presence of water suggests a different role of water on DEA than de-/stabilization of resonances. Nevertheless, our research contributes to filling in the gaps in knowledge about water effects on biological molecules (pyridine and thymine). We confirmed the influence of water on resonance stabilization and destabilization. We found that the effects of water on the resonances are approximately additive. We also show that in contradiction to Smyth *et al.*'s assumption [79] water does not always stabilize all resonances. Finally we explained that molecule bound to water may change its geometry which also has an influence on resonance characteristics.

The work on pyridine is a first step towards understanding the effect of core-excited resonances in DNA damage by looking at their constituents and prototypes. Our investigation of microhydration shows the effect is still not well understood. Although we shown that the changes to the resonances in Thy-$(H_2O)_5$ are not huge, their effect on DEA (and also, the effect of changes to the lifetime, which were not investigated in this work) may be important. Much still needs to be done to gain a deeper understanding of the mechanism by which low energy electrons damage DNA and how this mechanism could be modified and controlled.

SOFTWARE

A.1 UKRMOL SUITE

The software used before the UKRmol+ suite has been developed, is called the UKRmol suite. It is divided into two subsets of programs: UKRmol-in and UKRmol-out [107]. The subsets correspond, respectively, to the inner and outer region in the R-matrix method. Additionally some of the UKRmol-in programs are also used to perform target calculations. The programs used to carry out the target calculations are illustrated in figure A.1 and those ones used to perform the scattering inner region calculations are shown in figure A.2. The flowchart for the scattering outer region calculations is illustrated in figure A.3.

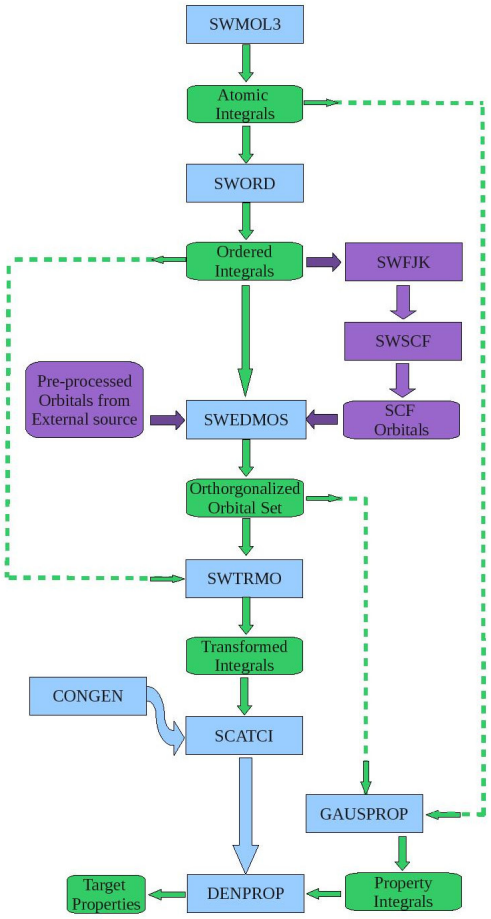

Figure A.1: A flowchart of the programs called in target calculations. The blue boxes indicate programs in the suite. The green boxes indicate the main output/input of the different programs. The purple boxes indicate alternative options to produce molecular orbitals in the calculation [107].

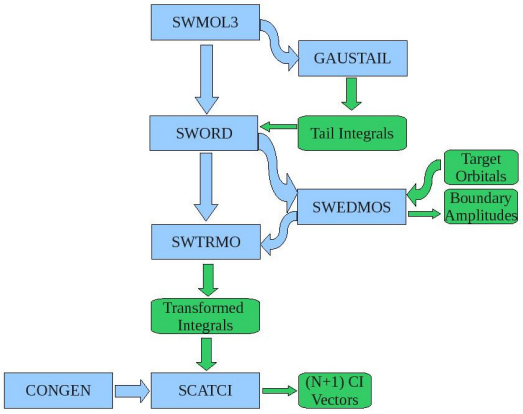

Figure A.2: A sequence of programs called in the inner region calculations (the meaning of boxes is as same as figure A.1).

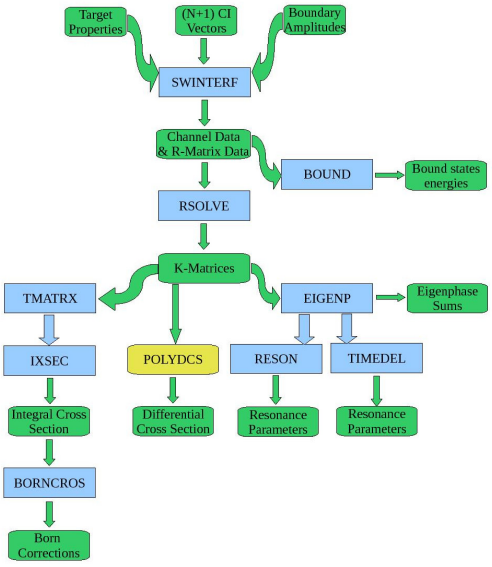

Figure A.3: A sequence of programs called in the outer region calculations (the meaning of boxes is as same as figure A.1).

A.2 RUNNING THE UKRMOL AND UKRMOL+ SUITE

In chapter 2, section 2.6 are discussed programs essential to perform R-matrix calculations. The programs need input files (additionally some of them also need pre-processed data files); preparing the input manually was very time-consuming and it was easy for the user to make mistakes. The input files usually need two kinds of data: settings which are established by the user, depending on the kind of calculation one runs, and data which can be found in the standard output files, of the

programs run at the earlier stages. Therefore, in order to simplify the setting up of the calculations, in the script, the user only needs to specify parameters which depend on the calculation one runs, i.e. geometry of molecule, basis set, scattering method, etc. The script then generates the input files itself and invokes the programs in the right order. It also extracts relevant data from some output files and saves them in files in a format more useful for the user, i.e. it saves cross section, eigenphases sum and time-delay data in a format which can be used without any changes by plotting software. Additionally, the script sums the cross section results obtained for each irreducible representation for all states and gives a total cross section (the scattering region results are obtained for each irreducible representation separately, thus sometimes it is useful to combine them).

The script is written in perl but no knowledge of it is needed to run it. Users familiar with perl or other programming languages (e.g. python), can modify the script to their specific needs. Many functionalities of the script have been added since it was created and plenty of new features can be still included. The script is written to give a lot of flexibility to the user, enough to perform all the calculations presented in this work. The same script may invoke either the UKRmol or UKRmol+ suites. It may execute each of the programs mentioned above in the appropriate sequence to obtain scattering results, or, when needed, it may invoke either only one program or a part of the sequence, e.g. it allows one to perform calculations only for the target. If, for some reason, the user needs to modify input files manually, it is possible to 'switch off' the automatic generation of the input.

The script allows one to run calculations for almost any target; the limitation, however, comes from the software itself and also from memory limitation of the machine used to perform the calculations. The basis set for which calculations are carried out is specified in script by name but the user has to make sure that the required files containing the basis set exist. UKRmol+ users have also the choice to give only the name of the basis set without putting it explicitly into a file. The target can be described using the HF or CASSCF methods. Users can specify how many and explicitly which of target orbitals are frozen and how many and which are in the active space. For the target, by default, some properties of the molecule are calculated but additionally the polarizability can also be obtained by specifying it in the script*.

For the scattering calculations, one can choose among SE, SEP or CC models. Continuum basis sets for different R-matrix radii are provided in separate files (in the same way as for the molecular basis sets). Users may choose the R-matrix radius (the script also allows one to run RADDEN in order to make this choice) and the maximum value of partial waves (ℓ_{max}) for which calculations are to be carried out. Since, it is possible to create more than one different continuum for the same R-matrix radius, the name of a file containing the continuum basis for the same R-matrix radius and ℓ_{max} may be distinguished by the use of a suffix (for the time being, the default suffixes are: 'old'

*Performing calculation to obtain polarizability for one of the molecule, a bug in DENPROP was discovered and reported.

and 'new' for two different continuum orbitals of the same R-matrix radius)[†]. Moreover, users must also input the scattering energy range, the energy step and several other parameters.

The script itself takes care of putting all files in appropriate directories. It creates a directory named after the calculated target (the user specifies the name in the script). The next folder is created and named depending on the user's settings. The name contains the name of the basis set, an acronym for scattering method, number of frozen orbitals, number of active orbitals, number of virtual orbitals, number of target states included in the calculation, R-matrix radius, maximum number of partial waves, as mentioned above, suffix of file containing the continuum basis set, precision of SCATCI-INTEGRALS binaries (blank if not needed) and suffix (an arbitrary string, which may be empty). For instance, for one specific pyridine calculation the directory created has the name: "pyridine/cc-pVDZ.SE.16frozen.5active.20virtual.1states.r15.L5.old.quadru_prec". Although the name of the directory is very long, it prevents accidentally overwriting previous calculations run for different settings. In that case, if the user runs calculations for exactly the same set of settings and does not want to overwrite the previous calculation, the two directories can be distinguished by changing the suffix of the directory (option in the script is called 'suffix') and thus preventing overwriting. In summary, the script takes care that all the user's calculations for one target are in the same directory and groups calculations by chosen settings.

The whole script is divided into a few files, only one of them contains the user settings. For the time being, there is no user manual of the script but since it is written in an intuitive way with many comments for each variable, it should be clear enough for the user. The main contribution to developing the script by the author of this thesis was the adding of several new features. These are: enabling the use of CASSCF type of orbitals, option to calculate the polarizability of the target; option to run complementary programs like RADDEN or HAMDIAG. In addition the parallization of the script was implemented, to enable to perform outer region calculations for each irreducible representation at the same time. Also the possibility to run the script on different machines (i.e. the Linux system at the OU and ARCHER) was added, and, more importantly, the script was adapted in order to run the UKRmol+ suite.

[†]Although the files containing the GTOs basis sets for the free particle for UKRmol and UKRmol+ are the same, due to technical reasons, they have different names. For UKRmol each basis set with different R-matrix radius and ℓ_{max} value is put in separate file, where for UKRmol+ they are only group by different R-matrix radius.

B

BENZENE, PYRIDINE, PYRIMIDINE

B.1 BENZENE, PYRIDINE AND PYRIMIDINE HF ORBITALS

Table B.1 presents HF orbitals for benzene, pyridine and pyrimidine determined with the compact basis set (cc-pVDZ), listed in increasing energy order. The changes in orbital shape between the three molecules are not significant, but the corresponding orbitals are not always in the same order. Generated by MOLDEN with the contour parameter: space = 0.0500.

	Benzene		Pyridine		Pyrimidine	
No.	Orbital	Sym.	Orbital	Sym.	Orbital	Sym.
1	-11.2412 Ha 	1 a_g	-15.5676 Ha 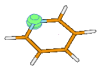	1 a_1	-15.5781 Ha 	1 b_2
2	-11.2407 Ha 	1 b_{1u}	-11.2792 Ha 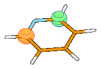	1 b_2	-15.5781 Ha 	1 a_1
3	-11.2407 Ha 	1 b_{2u}	-11.2791 Ha 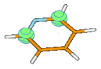	2 a_1	-11.3195 Ha 	2 a_1

4	-11.2395 Ha 	2 a_g	-11.2653 Ha 	3 a_1	-11.3051 Ha 	3 a_1
5	-11.2395 Ha 	1 b_{3g}	-11.2474 Ha 	2 b_2	-11.3050 Ha 	2 b_2
6	-11.2390 Ha 	2 b_{1u}	-11.2474 Ha 	4 a_1	-11.2555 Ha 	4 a_1
7	-1.1448 Ha 	3 a_g	-1.2541 Ha 	5 a_1	-1.3076 Ha 	5 a_1
8	-1.0109 Ha 	2 b_{2u}	-1.0865 Ha 	6 a_1	-1.1921 Ha 	3 b_2
9	-1.0109 Ha 	3 b_{1u}	-1.0300 Ha 	3 b_2	-1.0732 Ha 	6 a_1
10	-0.8201 Ha 	2 b_{3g}	-0.8552 Ha 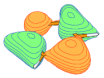	7 a_1	-0.8925 Ha 	4 b_2
11	-0.8201 Ha 	4 a_g	-0.8526 Ha 	4 b_2	-0.8871 Ha 	7 a_1
12	-0.7031 Ha 	5 a_g	-0.7160 Ha 	8 a_1	-0.7341 Ha 	8 a_1
13	-0.6412 Ha 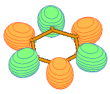	4 b_{1u}	-0.6551 Ha 	5 b_2	-0.6957 Ha 	5 b_2

14	-0.6130 Ha 	3 b_{2u}	-0.6509 Ha 	9 a_1	-0.6486 Ha 	9 a_1
15	-0.5833 Ha 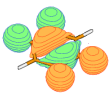	4 b_{2u}	-0.5934 Ha 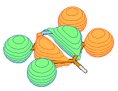	6 b_2	-0.5922 Ha 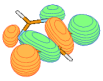	6 b_2
16	-0.5833 Ha 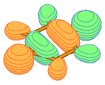	5 b_{1u}	-0.5730 Ha 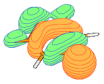	10 a_1	-0.5825 Ha 	10 a_1
17	-0.4968 Ha 	1 b_{3u}	-0.5360 Ha 	1 b_1	-0.5703 Ha 	1 b_1
18	-0.4905 Ha 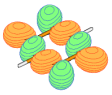	3 b_{3g}	-0.5155 Ha 	7 b_2	-0.4707 Ha 	11 a_1
19	-0.4905 Ha 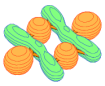	6 a_g	-0.4154 Ha 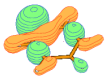	11 a_1	-0.4165 Ha 	1 a_2
20	-0.3327 Ha 	1 b_{2g}	-0.3797 Ha 	2 b_1	-0.4131 Ha 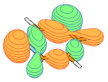	7 b_2
21	-0.3327 Ha 	1 b_{1g}	-0.3439 Ha 	1 a_2	-0.3748 Ha 	2 b_1
22	0.1358 Ha 	1 a_u	0.1155 Ha 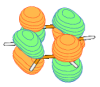	3 b_1	0.1018 Ha 	2 a_2
23	0.1358 Ha 	2 b_{3u}	0.1297 Ha 	2 a_2	0.1170 Ha 	3 b_1

24	0.1821 Ha 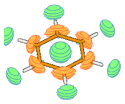	7 a_g	0.1825 Ha 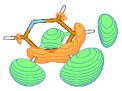	12 a_1	0.1852 Ha 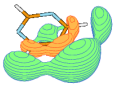	12 a_1
25	0.2198 Ha 	6 b_{1u}	0.2143 Ha 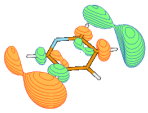	8 b_2	0.2211 Ha 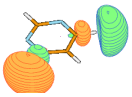	8 b_2
26	0.2198 Ha 	5 b_{2u}	0.2286 Ha 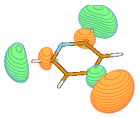	13 a_1	0.2302 Ha 	13 a_1
27	0.2550 Ha 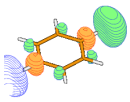	8 a_g	0.2525 Ha 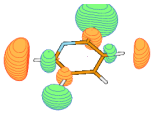	9 b_2	0.2462 Ha 	14 a_1
28	0.2550 Ha 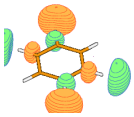	4 b_{3g}	0.2593 Ha 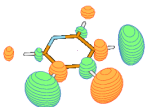	14 a_1	0.3243 Ha 	4 b_1
29	0.2716 Ha 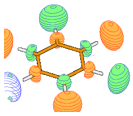	7 b_{1u}	0.3381 Ha 	4 b_1	0.3784 Ha 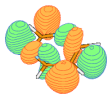	9 b_2
30	0.3479 Ha 	2 b_{2g}	0.3810 Ha 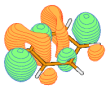	15 a_1	0.3788 Ha 	15 a_1
31	0.4353 Ha 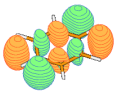	5 b_{3g}	0.4326 Ha 	10 b_2	0.4690 Ha 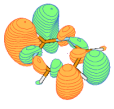	10 b_2
32	0.4353 Ha 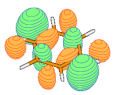	9 a_g	0.4637 Ha 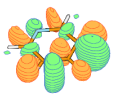	16 a_1	0.4928 Ha 	16 a_1
33	0.4667 Ha 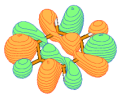	8 b_{1u}	0.4704 Ha 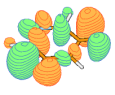	11 b_2	0.5078 Ha 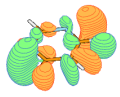	11 b_2

34	0.4667 Ha 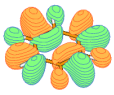	6 b_{2u}	0.5529 Ha 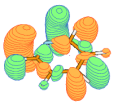	12 b_2	0.5324 Ha 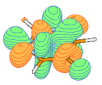	17 a_1
35	0.5861 Ha 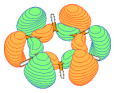	7 b_{2u}	0.5754 Ha 	17 a_1	0.6447 Ha 	18 a_1
36	0.5876 Ha 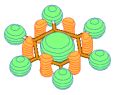	10 a_g	0.6333 Ha 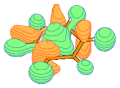	18 a_1	0.6531 Ha 	5 b_1
37	0.6681 Ha 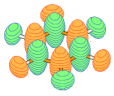	9 b_{1u}	0.6680 Ha 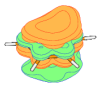	5 b_1	0.6905 Ha 	12 b_2
38	0.6813 Ha 	3 b_{3u}	0.6840 Ha 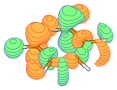	13 b_2	0.7120 Ha 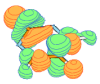	19 a_1
39	0.7127 Ha 	11 a_g	0.7195 Ha 	3 a_2	0.7159 Ha 	6 b_1
40	0.7329 Ha 	3 b_{2g}	0.7228 Ha 	19 a_1	0.7237 Ha 	20 a_1
41	0.7329 Ha 	2 b_{1g}	0.7234 Ha 	14 b_2	0.7261 Ha 	3 a_2
42	0.7386 Ha 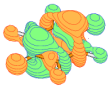	10 b_{1u}	0.7260 Ha 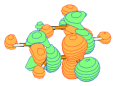	20 a_1	0.7411 Ha 	13 b_2
43	0.7386 Ha 	8 b_{2u}	0.7346 Ha 	6 b_1	0.8137 Ha 	7 b_1

44	0.7393 Ha 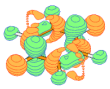	12 a_g	0.7885 Ha 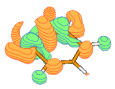	21 a_1	0.8145 Ha 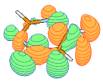	14 b_2
45	0.7393 Ha 	6 b_{3g}	0.8025 Ha 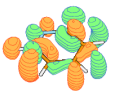	15 b_2	0.8265 Ha 	21 a_1
46	0.7395 Ha 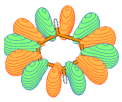	7 b_{3g}	0.8131 Ha 	4 a_2	0.9170 Ha 	22 a_1
47	0.8227 Ha 	4 b_{3u}	0.8456 Ha 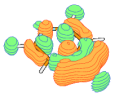	22 a_1	0.9387 Ha 	15 b_2
48	0.8227 Ha 	2 a_u	0.8494 Ha 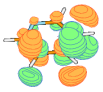	7 b_1	0.9432 Ha 	23 a_1
49	0.8524 Ha 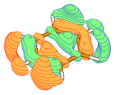	11 b_{1u}	0.8741 Ha 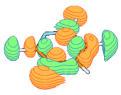	16 b_2	0.9768 Ha 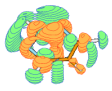	24 a_1
50	0.8524 Ha 	9 b_{2u}	0.9396 Ha 	17 b_2	1.0593 Ha 	16 b_2
51	0.8859 Ha 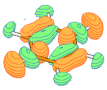	13 a_g	0.9644 Ha 	23 a_1	1.0673 Ha 	25 a_1
52	0.8859 Ha 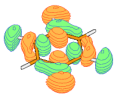	8 b_{3g}	0.9894 Ha 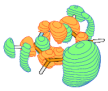	24 a_1	1.0743 Ha 	8 b_1
53	0.9088 Ha 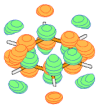	4 b_{2g}	1.0580 Ha 	8 b_1	1.0899 Ha 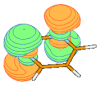	4 a_2

54	0.9835 Ha 	12 b_{1u}	1.0826 Ha 	18 b_2	1.1378 Ha 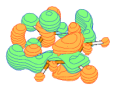	26 a_1
55	0.9972 Ha 	14 a_g	1.0838 Ha 	25 a_1	1.1541 Ha 	17 b_2
56	1.0498 Ha 	5 b_{3u}	1.1352 Ha 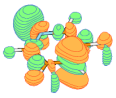	26 a_1	1.1861 Ha 	5 a_2
57	1.1039 Ha 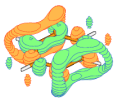	10 b_{2u}	1.1607 Ha 	9 b_1	1.1871 Ha 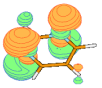	9 b_1
58	1.1039 Ha 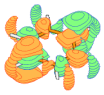	13 b_{1u}	1.1644 Ha 	5 a_2	1.2263 Ha 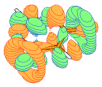	18 b_2
59	1.1202 Ha 	9 b_{3g}	1.1920 Ha 	19 b_2	1.2479 Ha 	27 a_1
60	1.1498 Ha 	3 b_{1g}	1.2126 Ha 	27 a_1	1.2944 Ha 	10 b_1

Table B.1: HF orbitals of benzene, pyridine and pyrimidine. The numbers in first columns for each molecule (No.) indicate the number of orbitals. In the second columns for each molecules (Orbital) is given energy in Hartree and shape of orbitals. The numbers in third columns (Sym.) indicate number of orbital per symmetry and its irreducible representation.

B.2 COMPARISON OF CROSS SECTIONS

In order to compare how the presence of nitrogen influences the position of resonances, the SE and SEP cross sections of benzene, pyridine, pyrimidine systems are presented in figure B.1 and B.2, respectively. Due to the fact that benzene has higher symmetry, D_{6h}, than these azabenzenes, C_{2v}, the first two resonances in benzene are degenerate and therefore indistinguishable. The degenerate resonances are formed by trapping the incoming electron into the lowest empty π^* orbitals of the

same energy. In table B.1, it can be seen that orbitals number 22 and 23 are the first unoccupied orbitals (LUMO) and have the same energy. It is important to notice that the benzene orbitals have been calculated using the D_{2h} point group, however benzene belongs to the D_{6h} point group; this is because MOLPRO does not perform calculations for higher symmetries than D_{2h}. The symmetry a_u in D_{2h} may correspond either to a_{1u} or e_{2u} in D_{6h} point group and b_{3u} in D_{2h} correspond to b_{2u} in D_{6h}.

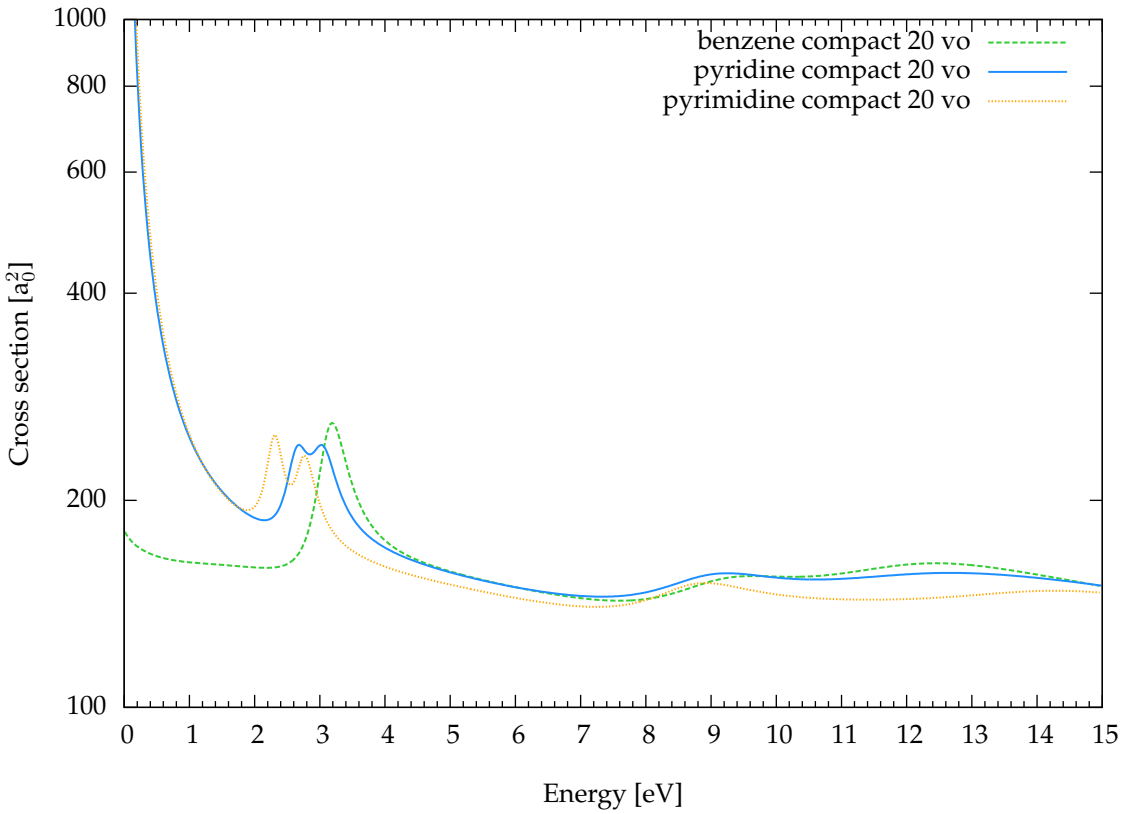

Figure B.1: Integral elastic cross sections for electron scattering from benzene, pyridine and pyrimidine, calculated using 20 virtual orbitals and $\ell_{max} = 5$ with the compact basis set at SE level.

The inclusion of nitrogen in the benzene ring destroys the symmetry and degeneracy of the resonances. The presence of nitrogen in pyridine lowers the energy of most of its orbitals and destroy the degeneracy of 22th and 23th orbitals presented in the table B.1. The additional nitrogen in pyrimidine increases the difference in orbital energies. This is consistent with the positions of the resonances as seen in the SE cross sections in figure B.1. Adding more nitrogen atoms in the ring not only lowers the position of the two lowest resonances but also separate them more. The huge difference between benzene and azabenzenes cross section from 0 eV to around 3 eV are due to the fact that benzene does not posses dipole moment.

Results obtained at SEP level for three different systems are more difficult to compare because, at the moment, there is no method to determine and control how much polarization is included in the

calculations. Nevertheless, since the three systems are very similar, and, as long as the corresponding orbitals are included in the calculations for the three systems (see, table B.1), comparison of the SEP cross sections may give some insight in the scattering process.

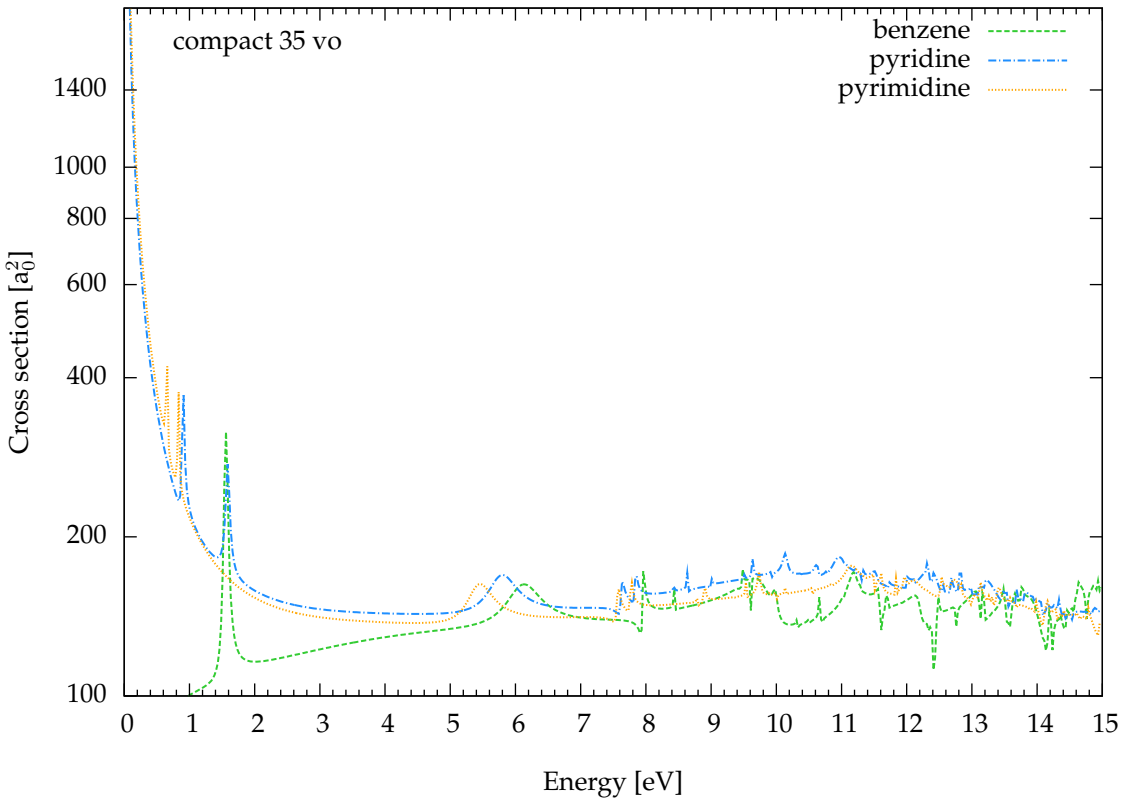

Figure B.2: Integral elastic cross sections for electron scattering from benzene, pyridine and pyrimidine, calculated using 35 virtual orbitals and $\ell_{max} = 5$ with the compact basis set at SEP level.

Analysing SEP cross sections in figure B.2, we can still observe that replacing carbon with nitrogen lower the position of resonances. Nevertheless, the separation of the first two resonances is not getting bigger with increased number on nitrogen atoms. The first benzene resonance still remind degenerate, but the difference between the position of first and second resonance for pyridine is bigger ($\sim$ 0.7 eV) than for pyrimidine ($\sim$ 0.2 eV).

The structures of benzene, pyridine and pyrimidine are similar and therefore the low-energy electron scattering for these systems give fairly similar results (with explained differences in cross section at low energies for molecules with and without dipole moment). The difference between benzene and pyridine cross section is more significant than between the pyridine and pyrimidine one. It is expected that replacing one atom in the homogeneous carbon ring, gives bigger effect than replacing one carbon in inhomogeneous ring. The presence of one nitrogen in the 6-membered ring lowers the symmetry of the system and therefore destroys the degeneracy of the first π^* orbital and lower its energy.

C

PYRIDINE-WATER

C.1 PYR-H_2O, PYR AND WATER HF ORBITALS

Table C.1 presents HF orbitals for pyridine-water, pyridine and water determined with the compact basis set (cc-pVDZ), listed in increasing energy order. Generated by MOLDEN with the contour parameter: space = 0.0500.

Pyridine-water			Pyridine			Water		
No.	Orbital	Sym.	No.	Orbital	Sym.	No.	Orbital	Sym.
1	-20.5097 Ha 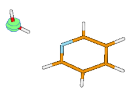	1 a′				1	-20.5473 Ha 	1 a_1
2	-15.5807 Ha 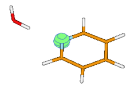	2 a′	1	-15.5676 Ha 	1 a_1			
3	-11.2884 Ha 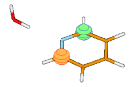	1 a″	2	-11.2792 Ha 	1 b_2			
4	-11.2884 Ha 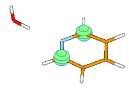	3 a′	3	-11.2791 Ha 	2 a_1			

5	-11.2727 Ha 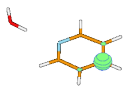	4 a′	4	-11.2653 Ha 	3 a_1			
6	-11.2542 Ha 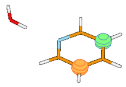	2 a″	5	-11.2474 Ha 	2 b_2			
7	-11.2542 Ha 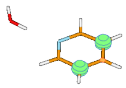	5 a′	6	-11.2474 Ha 	4 a_1			
8	-1.3051 Ha 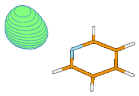	6 a′				2	-1.3405 Ha 	2 a_1
9	-1.2809 Ha 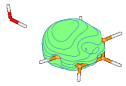	7 a′	7	-1.2541 Ha 	5 a_1			
10	-1.1035 Ha 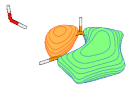	8 a′	8	-1.0865 Ha 	6 a_1			
11	-1.0485 Ha 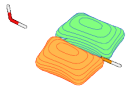	3 a″	9	-1.0300 Ha 	3 b_2			
12	-0.8713 Ha 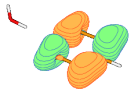	4 a″	11	-0.8526 Ha 	4 b_2			
13	-0.8695 Ha 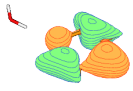	9 a′	10	-0.8552 Ha 	7 a_1			
14	-0.7347 Ha 	10 a′	12	-0.7160 Ha 	8 a_1			

15	-0.6747 Ha 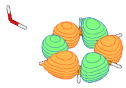	5 a″	13	-0.6551 Ha 	5 b_2			
16	-0.6693 Ha 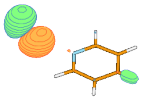	11 a′				3	-0.7094 Ha 	3 a_1
17	-0.6614 Ha 	12 a′	14	-0.6509 Ha 	9 a_1			
18	-0.6088 Ha 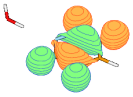	6 a″	15	-0.5934 Ha 	6 b_2			
19	-0.5875 Ha 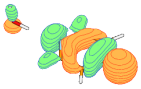	13 a′	16	-0.5730 Ha 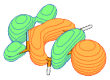	10 a_1			
20	-0.5575 Ha 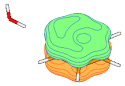	14 a′	17	-0.5360 Ha 	1 b_1			
21	-0.5353 Ha 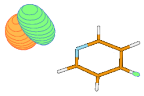	15 a′				4	-0.5640 Ha 	4 a_1
22	-0.5299 Ha 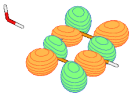	7 a″	18	-0.5155 Ha 	7 b_2			
23	-0.4582 Ha 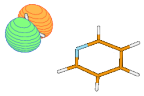	8 a″				5	-0.4931 Ha 	1 b_2
24	-0.4292 Ha 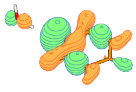	16 a′	19	-0.4154 Ha 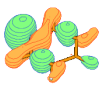	11 a_1			

25	-0.3966 Ha 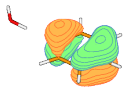	17 a′	20	-0.3797 Ha 	2 b_1			
26	-0.3579 Ha 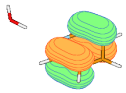	9 a″	21	-0.3439 Ha 	1 a_2			
27	0.1060 Ha 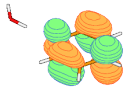	18 a′	22	0.1155 Ha 	3 b_1			
28	0.1211 Ha 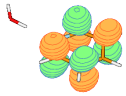	10 a″	23	0.1297 Ha 	2 a_2			
29	0.1728 Ha 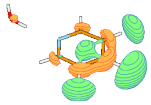	19 a′	24	0.1825 Ha 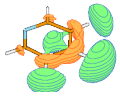	12 a_1			
30	0.2072 Ha 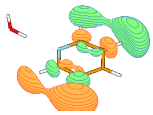	11 a″	25	0.2143 Ha 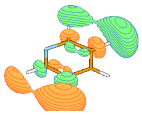	8 b_2			
31	0.2090 Ha 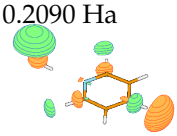	20 a′	26	0.2286 Ha 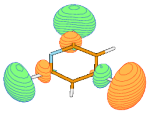	13 a_1			
32	0.2376 Ha 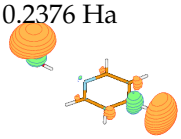	21 a′				6	0.1878 Ha 	5 a_1
33	0.2464 Ha 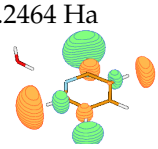	12 a″	27	0.2525 Ha 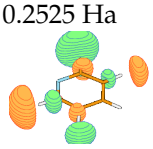	9 b_2			
34	0.2596 Ha 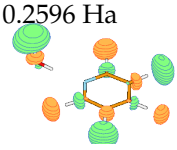	22 a′	28	0.2593 Ha 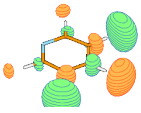	14 a_1	7	0.2575 Ha 	6 a_1

35	0.3323 Ha 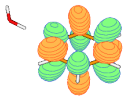	23 a′	29	0.3381 Ha 	4 b_1			
36	0.3391 Ha 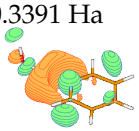	24 a′	30	0.3810 Ha 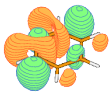	15 a_1			
37	0.4257 Ha 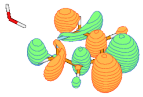	13 a″	31	0.4326 Ha 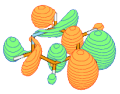	10 b_2			
38	0.4295 Ha 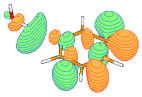	25 a′	32	0.4637 Ha 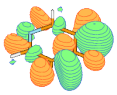	16 a_1			
39	0.4628 Ha 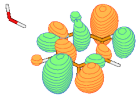	14 a″	33	0.4704 Ha 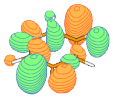	11 b_2			
40	0.4737 Ha 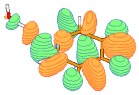	26 a′						
41	0.5363 Ha 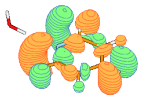	15 a″	34	0.5529 Ha 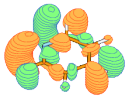	12 b_2			
42	0.5639 Ha 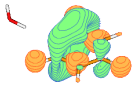	27 a′	35	0.5754 Ha 	17 a_1			
43	0.6257 Ha 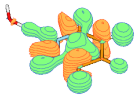	28 a′	36	0.6333 Ha 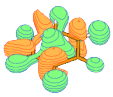	18 a_1			
44	0.6548 Ha 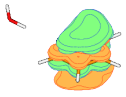	29 a′	37	0.6680 Ha 	5 b_1			

45	0.6797 Ha 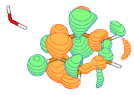	16 a″	38	0.6840 Ha 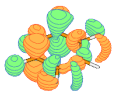	13 b_2			
46	0.7060 Ha 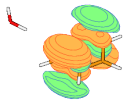	17 a″	39	0.7195 Ha 	3 a_2			
47	0.7156 Ha 	30 a′	40	0.7228 Ha 	19 a_1			
48	0.7161 Ha 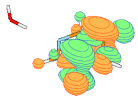	18 a″	41	0.7234 Ha 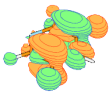	14 b_2			
49	0.7207 Ha 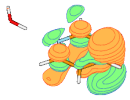	31 a′	43	0.7346 Ha 	6 b_1			
50	0.7243 Ha 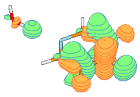	32 a′	42	0.7260 Ha 	20 a_1			
51	0.7978 Ha 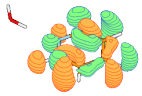	19 a″	45	0.8025 Ha 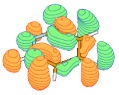	15 b_2			
52	0.7996 Ha 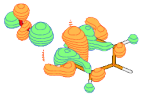	33 a′	44	0.7885 Ha 	21 a_1	8	0.8049 Ha 	7 a_1
53	0.8021 Ha 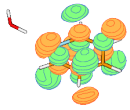	20 a″	46	0.8131 Ha 	4 a_2			
54	0.8132 Ha 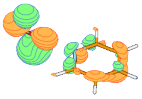	34 a′				8	0.8049 Ha 	7 a_1

55	0.8385 Ha 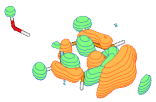	35 a′	47	0.8456 Ha 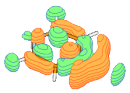	22 a_1			
56	0.8431 Ha 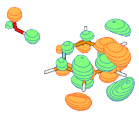	36 a′	48	0.8494 Ha 	7 b_1			
57	0.8685 Ha 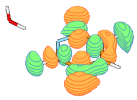	21 a″	49	0.8741 Ha 	16 b_2			
58	0.8979 Ha 	37 a′				9	0.8545 Ha 	8 a_1
59	0.9372 Ha 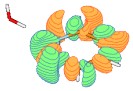	22 a″	50	0.9396 Ha 	17 b_2			
60	0.9627 Ha 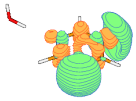	38 a′	51	0.9644 Ha 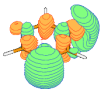	23 a_1			
61	0.9860 Ha 	39 a′	52	0.9894 Ha 	24 a_1			
62	1.0451 Ha 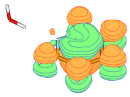	40 a′	53	1.0580 Ha 	8 b_1			
63	1.0729 Ha 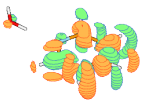	23 a″	54	1.0826 Ha 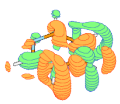	18 b_2			
64	1.1098 Ha 	41 a′	56	1.1352 Ha 	26 a_1			

65	1.1244 Ha 	42 a′	55	1.0838 Ha 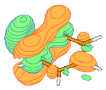	25 a_1			
			57	1.1607 Ha 	9 b_1			
66	1.1568 Ha 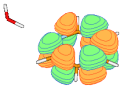	24 a″	58	1.1644 Ha 	5 a_2			
67	1.1724 Ha 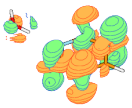	25 a″	59	1.1920 Ha 	19 b_2			
68	1.2011 Ha 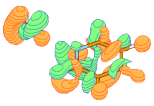	43 a′	60	1.2126 Ha 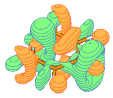	27 a_1			
69	1.2077 Ha 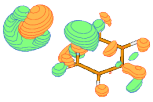	44 a′				10	1.1612 Ha 	9 a_1
70	1.2147 Ha 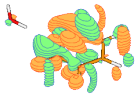	26 a″	61	1.2211 Ha 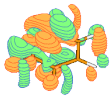	20 b_2			
71	1.2352 Ha 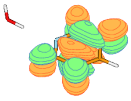	27 a″	62	1.2427 Ha 	6 a_2			
72	1.2509 Ha 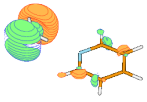	28 a″				11	1.2009 Ha 	2 b_2
73	1.2662 Ha 	45 a′	63	1.2708 Ha 	10 b_1			

74	1.2871 Ha 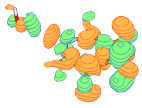	46 a′	64	1.3073 Ha 	28 a_1			
75	1.3248 Ha 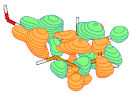	29 a″	65	1.3435 Ha 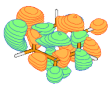	21 b_2			
76	1.3390 Ha 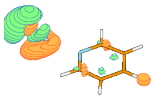	47 a′				12	1.2505 Ha 	10 a_1
77	1.3600 Ha 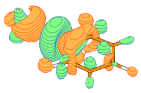	48 a′						
78	1.3625 Ha 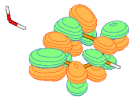	30 a″	66	1.3692 Ha 	7 a_2			
79	1.4286 Ha 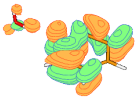	49 a′	67	1.4337 Ha 	11 b_1			
80	1.4801 Ha 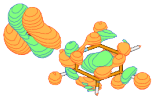	50 a′				13	1.4628 Ha 	11 a_1
81	1.4949 Ha 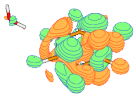	51 a′	68	1.4971 Ha 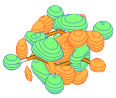	29 a_1			
82	1.5297 Ha 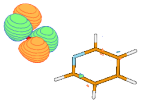	31 a″				14	1.4719 Ha 	3 b_2

Table C.1: HF orbitals of pyridine-water, pyridine and water. The numbers in first columns for each molecule (No.) indicate the number of orbitals. In the second columns for each molecules (Orbital) is given energy in Hartree and shape of orbitals. The numbers in third columns (Sym.) indicate number of orbital per symmetry and its irreducible representation.

C.2 POLARIZABILITY

Below we present our results for an approach described in section 4.1.3 of chapter 4 (to find out the optimal number of virtual orbitals to include in our calculations by looking at how the polarizability changes depending on the number of virtual orbitals). The results are illustrated in figure C.1. The graph shows the dependence of the resonance energies on the polarizability and the number of virtual orbitals used in the calculations. It can be seen that the best agreement with the experimental resonance positions for pyridine (red dashed line) is for 35 v.o. and polarizability of 70.41 a_o^3. This value is bigger than the experimental value of polarizability: 64.10 a_o^3 [147, 148] (purple constant line) and the reference calculated value of 60.00 a_o^3 [145] (purple dashed line). Unfortunately, to the best of our knowledge an experimental value of Pyr-H_2O polarizability has not been published. The only reference value is the calculated value of 68.16 a_o^3 [145] (see table 4.1 or figure C.1). Since we only know the calculated value of polarizability for Pyr-H_2O our idea was to calculate a percent of how much more polarizability we include in our calculations in accordance to the reference calculated value of pyridine polarizability. Then we could assume that we should include of the same percentage more polarizability than the reference calculated value for Pyr-H_2O. However, our calculations for formic acid (see figure C.2) show that we obtain good agreement with the experimental resonance position (red dashed line) including less polarizability (17.68 a_o^3) than the experimental value (22.4 a_o^3 [112], purple dashed line). Moreover, the formic acid polarizability, as a function of number of virtual orbitals, presented in figure 4.3 in section 4.1.3 does not reach the experimental value of polarizability. The results for Pyr and FA are inconsistent, therefore there is no straightforward link between polarizability and the right energy of resonances. Consequently, we cannot derive any prediction of how much polarizability included in Pyr-H_2O calculations will give the right resonance positions based on information for Pyr.

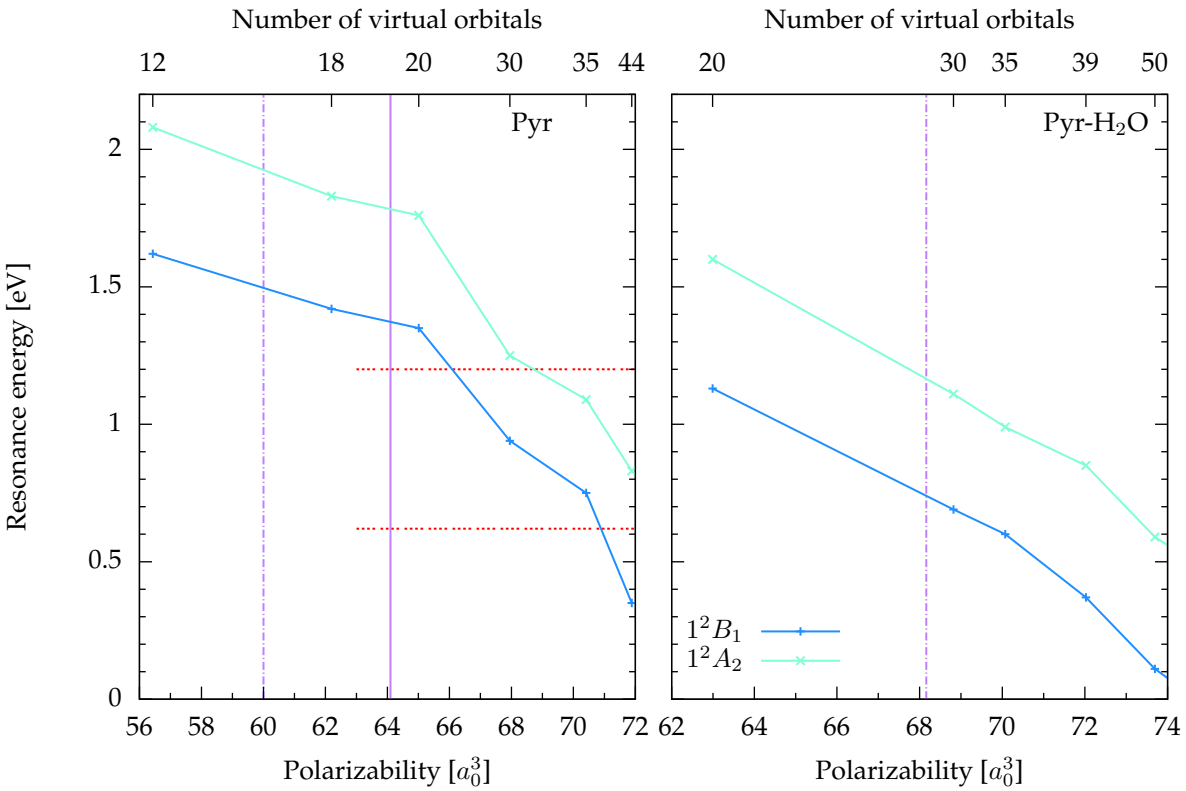

Figure C.1: Energy (vertical axis) of the $1\ ^2B_1$ and $1\ ^2A_2$ resonances as a function of the number of virtual orbitals used in the calculations (upper axis) and polarizability described (bottom axis). The systems are indicated in the panel. The horizontal red dashed lines indicate the experimental resonance energies (only in the pyridine graph). The vertical purple dotted dashed lines indicate the accurate calculated value of the polarizability taken from the literature [145]. The vertical purple constant line indicates the experimental polarizability [147, 148].

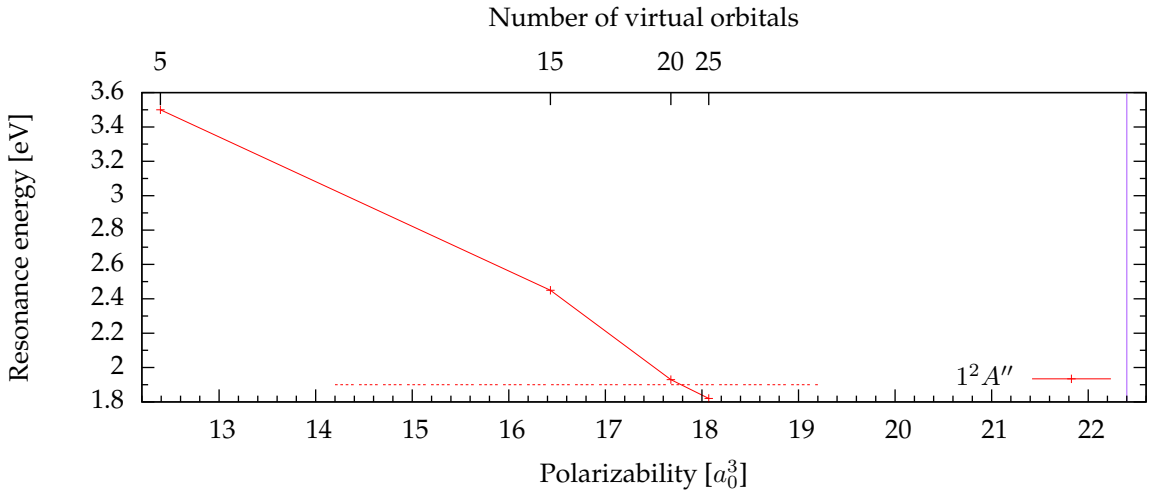

Figure C.2: Energy (vertical axis) of the $1\ ^2A''$ formic acid resonance as a function of the number of virtual orbitals used in the calculations (upper axis) and polarizability described (bottom axis). The horizontal red dashed lines indicate the experimental resonance energies. The vertical purple line indicates the experimental polarizability [112].

D

THYMINE-WATER

D.1 THY AND THY-$(H_2O)_5$ HF ORBITALS

Table D.1 presents HF orbitals for Thy G2, Thy G3, Thy-$(H_2O)_5$ ABCDE and Thy-$(H_2O)_5$ ACDEF determined with the compact basis set (cc-pVDZ), listed in increasing energy order. Generated by MOLDEN with the contour parameter: space = 0.0500.

The orbitals for thymine in equilibrium geometry (G1) are virtually identical in shape to those of Thy G2 therefore they are not presented here. However, the Thy G1 orbital energies are higher than those of Thy G2.

No.	Thy G2	No.	Thy-$(H_2O)_5$ ABCDE	No.	Thy G3	No.	Thy-$(H_2O)_5$ ACDEF
		1	-20.5615 Ha 			1	-20.5649 Ha 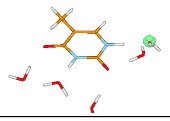
		2	-20.5521 Ha 			2	-20.5600 Ha 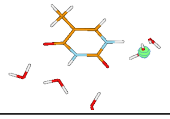
1	-20.5354 Ha 	3	-20.5518 Ha 	1	-20.5386 Ha 	3	-20.5531 Ha 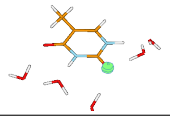

		4	-20.5516 Ha 			4	-20.5474 Ha 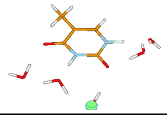
		5	-20.5497 Ha 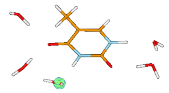			5	-20.5441 Ha 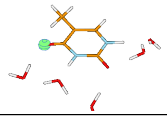
2	-20.5315 Ha 	6	-20.5427 Ha 	2	-20.5309 Ha 	6	-20.5429 Ha 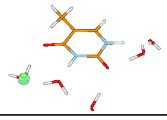
		7	-20.5168 Ha 			7	-20.5291 Ha 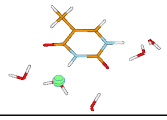
3	-15.6449 Ha 	8	-15.6233 Ha 	3	-15.6497 Ha 	8	-15.6305 Ha 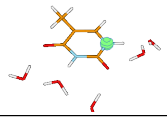
4	-15.6290 Ha 	9	-15.6160 Ha 	4	-15.6389 Ha 	9	-15.6138 Ha 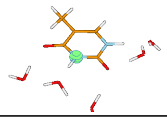
5	-11.4152 Ha 	10	-11.4158 Ha 	5	-11.4194 Ha 	10	-11.4273 Ha 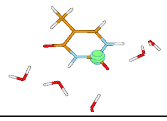
6	-11.3739 Ha 	11	-11.3880 Ha 	6	-11.3834 Ha 	11	-11.3860 Ha 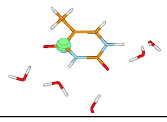
7	-11.3319 Ha 	12	-11.3272 Ha 	7	-11.3385 Ha 	12	-11.3322 Ha 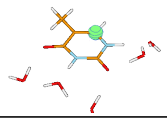
8	-11.2589 Ha 	13	-11.2527 Ha 	8	-11.2665 Ha 	13	-11.2610 Ha 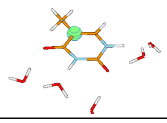
9	-11.2440 Ha 	14	-11.2349 Ha 	9	-11.2487 Ha 	14	-11.2460 Ha 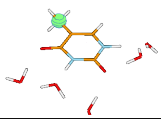

10	-1.4286 Ha 	15	-1.4333 Ha 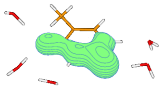	10	-1.4102 Ha 	15	-1.4213 Ha 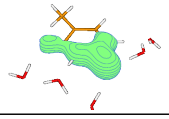
11	-1.3817 Ha 	16	-1.4039 Ha 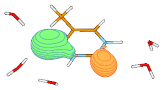	11	-1.3721 Ha 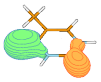	16	-1.3853 Ha 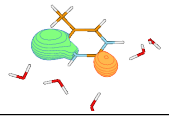
		17	-1.3522 Ha 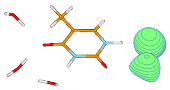			17	-1.3487 Ha 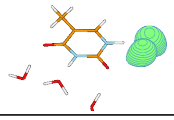
		18	-1.3450 Ha 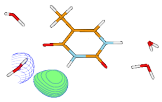			18	-1.3304 Ha 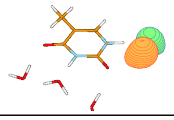
		19	-1.3338 Ha 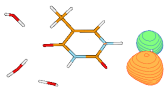			19	-1.3279 Ha 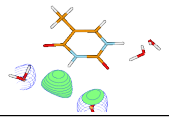
		20	-1.3283 Ha 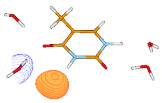			20	-1.3210 Ha 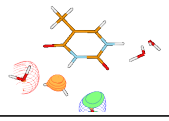
12	-1.3079 Ha 	21	-1.3044 Ha 	12	-1.2935 Ha 	21	-1.3043 Ha 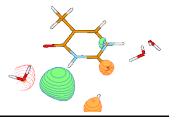
		22	-1.3015 Ha 			22	-1.2948 Ha 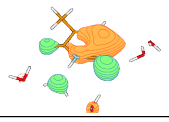
13	-1.2428 Ha 	23	-1.2371 Ha 	13	-1.2368 Ha 	23	-1.2261 Ha 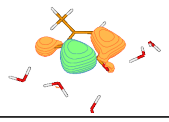
14	-1.1070 Ha 	24	-1.1030 Ha 	14	-1.1039 Ha 	24	-1.1004 Ha 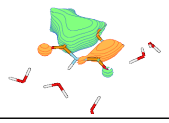
15	-0.9691 Ha 	25	-0.9622 Ha 	15	-0.9664 Ha 	25	-0.9632 Ha 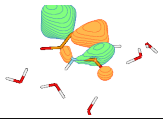

16	-0.9171 Ha 	26	-0.9142 Ha 	16	-0.9117 Ha 	26	-0.9071 Ha 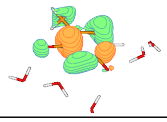
17	-0.8924 Ha 	27	-0.8896 Ha 	17	-0.8878 Ha 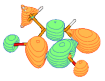	27	-0.8827 Ha 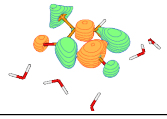
19	-0.7684 Ha 	28	-0.7702 Ha 	18	-0.7630 Ha 	28	-0.7627 Ha 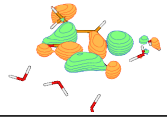
18	-0.7695 Ha 	29	-0.7645 Ha 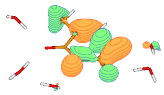	19	-0.7615 Ha 	29	-0.7612 Ha 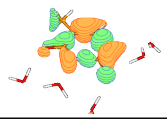
		30	-0.7320 Ha 			30	-0.7256 Ha 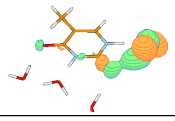
		31	-0.7255 Ha 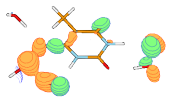			31	-0.7111 Ha 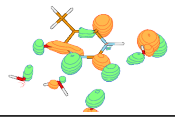
		32	-0.7124 Ha 			32	-0.7045 Ha 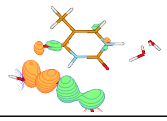
		33	-0.7098 Ha 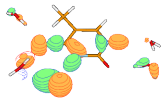			33	-0.7009 Ha 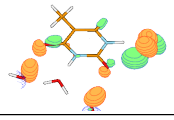
20	-0.7058 Ha 	34	-0.6981 Ha 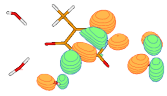	20	-0.6998 Ha 	34	-0.6927 Ha 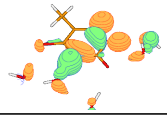
		35	-0.6811 Ha 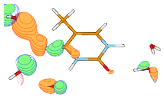			35	-0.6780 Ha 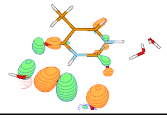
21	-0.6663 Ha 	36	-0.6640 Ha 	21	-0.6635 Ha 	36	-0.6630 Ha 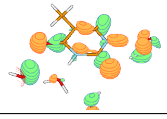

22	-0.6654 Ha 	37	-0.6598 Ha 	22	-0.6584 Ha 	37	-0.6541 Ha 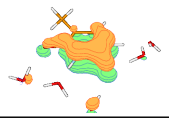
23	-0.6300 Ha 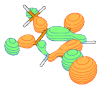	38	-0.6381 Ha 	23	-0.6170 Ha 	38	-0.6323 Ha 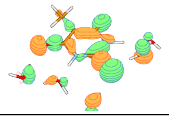
24	-0.6047 Ha 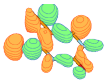	39	-0.6163 Ha 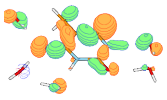	24	-0.6048 Ha 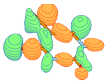	39	-0.6134 Ha 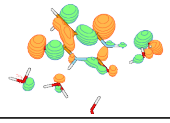
		40	-0.5935 Ha 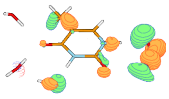			40	-0.5983 Ha 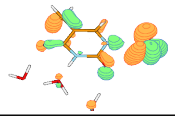
25	-0.5856 Ha 	41	-0.5856 Ha 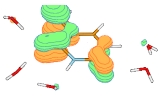	25	-0.5827 Ha 	41	-0.5846 Ha 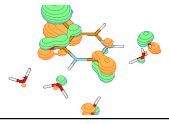
		42	-0.5823 Ha 			42	-0.5786 Ha 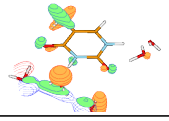
26	-0.5671 Ha 	43	-0.5663 Ha 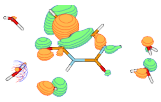	26	-0.5648 Ha 	43	-0.5659 Ha 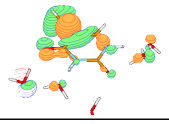
27	-0.5530 Ha 	44	-0.5583 Ha 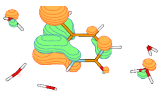			44	-0.5571 Ha 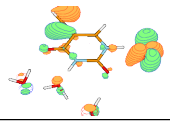
		45	-0.5566 Ha 			45	-0.5522 Ha 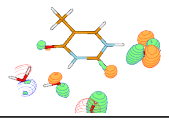
28	-0.5468 Ha 	46	-0.5494 Ha 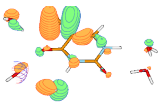	27	-0.5497 Ha 	46	-0.5485 Ha 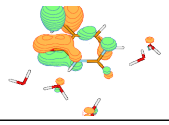
		47	-0.5435 Ha 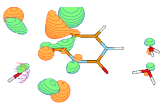	28	-0.5470 Ha 	47	-0.5452 Ha 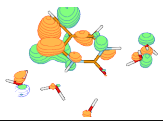

		48	-0.5307 Ha 			48	-0.5313 Ha 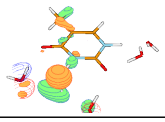
		49	-0.5084 Ha 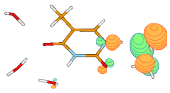			49	-0.5062 Ha 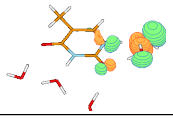
29	-0.5064 Ha 	50	-0.5036 Ha 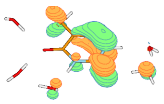	29	-0.4989 Ha 	50	-0.5023 Ha 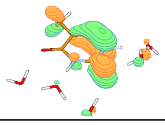
		51	-0.4986 Ha 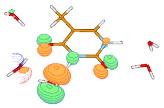			51	-0.4982 Ha 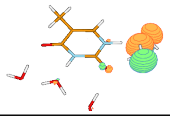
		52	-0.4927 Ha 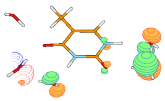			52	-0.4929 Ha 
		53	-0.4925 Ha 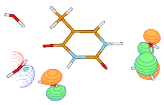			53	-0.4801 Ha 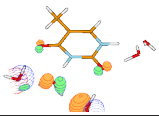
30	-0.4682 Ha 	54	-0.4718 Ha 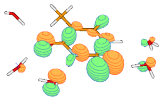			54	-0.4776 Ha 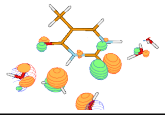
		55	-0.4610 Ha 	30	-0.4625 Ha 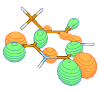	55	-0.4636 Ha 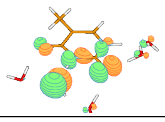
31	-0.4353 Ha 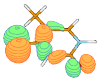	56	-0.4524 Ha 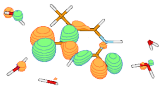	31	-0.4367 Ha 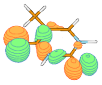	56	-0.4434 Ha 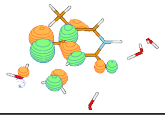
32	-0.4219 Ha 	57	-0.4336 Ha 	32	-0.4201 Ha 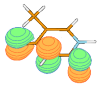	57	-0.4274 Ha 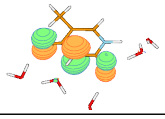
33	-0.3473 Ha 	58	-0.3442 Ha 	33	-0.3479 Ha 	58	-0.3470 Ha 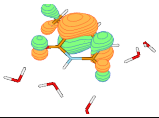

34	0.1041 Ha 	59	0.1033 Ha 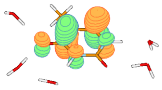	34	0.0970 Ha 	59	0.0997 Ha 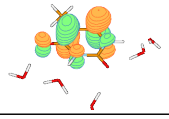
35	0.1494 Ha 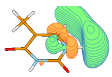	60	0.1695 Ha 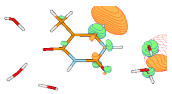	36	0.1693 Ha 	60	0.1555 Ha 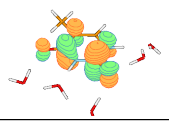
36	0.1789 Ha 	61	0.1721 Ha 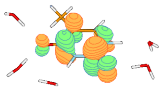	35	0.1464 Ha 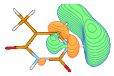	61	0.1701 Ha 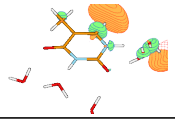
		62	0.1856 Ha 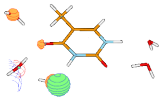	37	0.1823 Ha 	62	0.1847 Ha 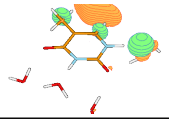
37	0.1870 Ha 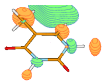	63	0.1909 Ha 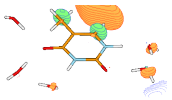			63	0.1975 Ha 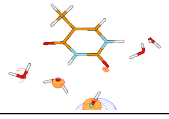
38	0.2063 Ha 	64	0.2085 Ha 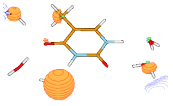	38	0.1968 Ha 	64	0.2069 Ha 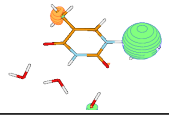
		65	0.2168 Ha 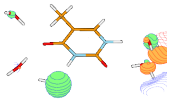			65	0.2101 Ha 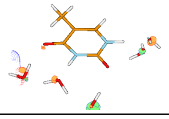
		66	0.2268 Ha 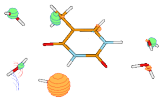			66	0.2189 Ha 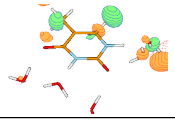
39	0.2272 Ha 	67	0.2423 Ha 	39	0.2241 Ha 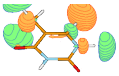	67	0.2575 Ha 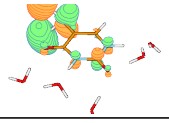
40	0.2610 Ha 	68	0.2674 Ha 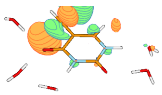	40	0.2575 Ha 	68	0.2603 Ha 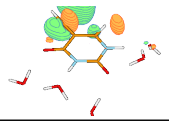
41	0.2680 Ha 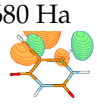	69	0.2853 Ha 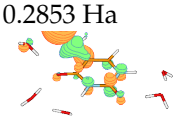	41	0.2634 Ha 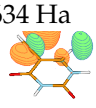	69	0.3002 Ha 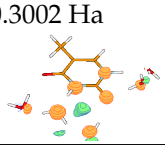

		70	0.3199 Ha 			70	0.3106 Ha 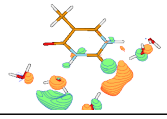
		71	0.3354 Ha 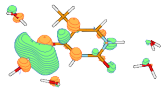	42	0.3240 Ha 	71	0.3249 Ha 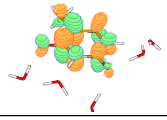
42	0.3336 Ha 	72	0.3398 Ha 	43	0.3534 Ha 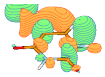	72	0.3342 Ha 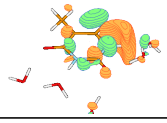
43	0.3583 Ha 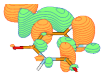	73	0.3531 Ha 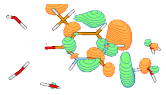			73	0.3540 Ha 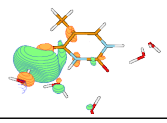
		74	0.3586 Ha 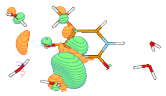			74	0.3639 Ha 
		75	0.3757 Ha 			75	0.3756 Ha 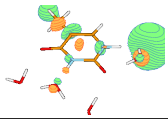
		76	0.3824 Ha 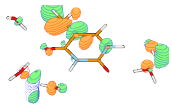			76	0.4008 Ha 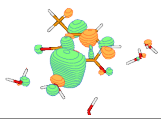
		77	0.3986 Ha 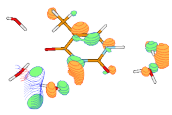			77	0.4160 Ha 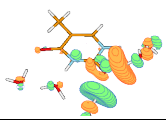
		78	0.4259 Ha 			78	0.4294 Ha 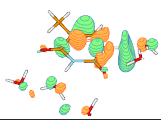
44	0.3904 Ha 	79	0.4430 Ha 	44	0.3830 Ha 	79	0.4372 Ha 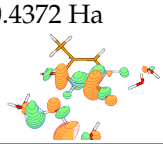
45	0.4104 Ha 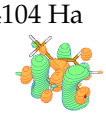	80	0.4500 Ha 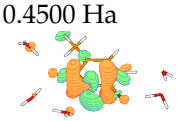	45	0.3998 Ha 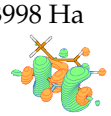	80	0.4459 Ha 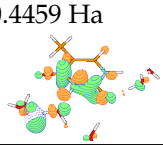

46	0.4144 Ha 	81	0.4701 Ha 	46	0.4113 Ha 	81	0.4661 Ha 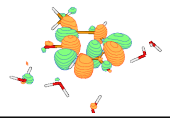
47	0.4531 Ha 	82	0.4913 Ha 	47	0.4444 Ha 	82	0.4818 Ha 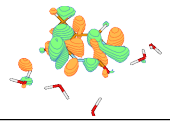
48	0.4836 Ha 	83	0.5042 Ha 	48	0.4824 Ha 	83	0.4928 Ha 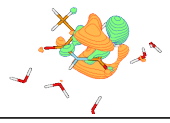
49	0.5016 Ha 	84	0.5107 Ha 	49	0.4937 Ha 	84	0.5153 Ha 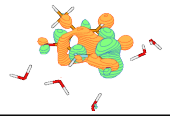
50	0.5240 Ha 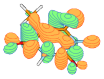	85	0.5388 Ha 	50	0.5145 Ha 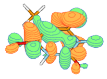	85	0.5351 Ha 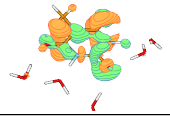
51	0.5717 Ha 	86	0.5763 Ha 	51	0.5701 Ha 	86	0.5742 Ha 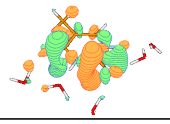
52	0.5923 Ha 	87	0.5980 Ha 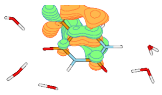	52	0.5926 Ha 	87	0.5971 Ha 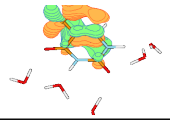
53	0.6386 Ha 	88	0.6411 Ha 	53	0.6385 Ha 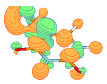	88	0.6427 Ha 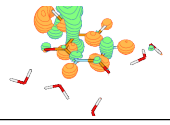
54	0.6445 Ha 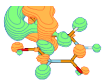	89	0.6604 Ha 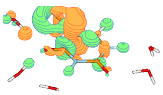	54	0.6404 Ha 	89	0.6447 Ha 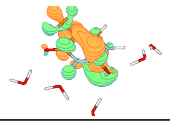
55	0.6688 Ha 	90	0.6751 Ha 	55	0.6588 Ha 	90	0.6671 Ha 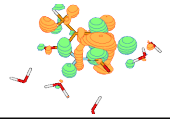
56	0.6743 Ha	91	0.6850 Ha	56	0.6671 Ha	91	0.6814 Ha

57	0.6973 Ha	92	0.7101 Ha	57	0.6896 Ha	92	0.6933 Ha
58	0.7361 Ha	93	0.7323 Ha			93	0.7156 Ha
		94	0.7363 Ha	59	0.7432 Ha	94	0.7262 Ha
		95	0.7489 Ha	58	0.7352 Ha	95	0.7353 Ha
59	0.7476 Ha	96	0.7566 Ha	60	0.7472 Ha	96	0.7477 Ha
		97	0.7626 Ha			97	0.7572 Ha
		98	0.7809 Ha			98	0.7716 Ha
60	0.7508 Ha	99	0.8045 Ha			99	0.7888 Ha
61	0.7809 Ha	100	0.8180 Ha	61	0.7739 Ha	100	0.8018 Ha
62	0.8175 Ha	101	0.8253 Ha	62	0.8092 Ha	101	0.8103 Ha
63	0.8517 Ha	102	0.8301 Ha	63	0.8288 Ha	102	0.8176 Ha

Table D.1: HF orbitals of Thy G2, Thy G3, Thy-$(H_2O)_5$ ABCDE and ACDEF. The numbers in the columns 'No.' indicate the number of orbitals for each of the system.

BIBLIOGRAPHY

[1] http://objects.povworld.org/cgi-bin/dl.cgi?dna.pov.

[2] L. Sanche, "Investigation of ultra-fast events in radiation chemistry with low-energy electrons," *Rad. Phys. Chem.*, vol. 34, no. 1, pp. 15 – 33, 1989.

[3] L. Sanche, "Low energy electron-driven damage in biomolecules," *Eur. Phys. J. D.*, vol. 35, pp. 367–390, August 2005.

[4] E. Alizadeh and L. Sanche, "Precursors of solvated electrons in radiological physics and chemistry," *Chem. Rev.*, vol. 112, pp. 5578–5602, 2012.

[5] L. Sanche, "Nanoscale Dynamics of Radiosensitivity: Role of Low Energy Electrons," in *Radiation Damage in Biomolecular system* (G. García and M. C. Fuss, eds.), Springer, 2012.

[6] S. M. Pimblott and J. A. LaVerne, "Production of low-energy electrons by ionizing radiation," *Rad. Phys. Chem.*, vol. 76, no. 8–9, pp. 1244 – 1247, 2007. Proceedings of the 11th Tihany Symposium on Radiation Chemistry.

[7] C. Burrows and J. Muller, "Oxidative nucleobase modifications leading to strand scission," *Chem. Rev.*, vol. 98, pp. 1109–1151, May 1998.

[8] W. Pogorzelski and T. Tullius, "Oxidative strand scission of nucleic acids: Routes initiated by hydrogen abstraction from the sugar moiety," *Chem. Rev.*, vol. 98, pp. 1089–1107, May 1998.

[9] B. Boudaïffa, P. Cloutier, D. Hunting, M. A. Huels, and L. Sanche, "Resonanant formation of DNA strand breaks by low-energy (3 to 20 eV) electrons," *Science*, vol. 287, pp. 1658–1660, 2000.

[10] B. Michael and P. O'Neill, "Molecular biology - a sting in the tail of electron tracks," *Science*, vol. 287, pp. 1603–1604, March 2000.

[11] F. Martin, P. Burrow, Z. Cai, P. Cloutier, D. Hunting, and L. Sanche, "Dna strand breaks induced by 0-4 ev electrons: The role of shape resonances," *Phys. Rev. Lett.*, vol. 93, p. 068101, August 2004.

[12] H. Jakubowski, "Structure & Reactivity in Chemistry. Introduction to Biomolecules." http://employees.csbsju.edu/hjakubowski/classes/ch125/IB3_IMF_Nucleic_Acids.html.

[13] http://employees.csbsju.edu/hjakubowski/classes/ch125/deoxynucleotidemonomers.gif.

[14] http://www.sci-news.com/genetics/science-duons-code-dna-01618.html.

[15] R. L. Johnston, *Atomic and Molecular Clusters*. London and New York: Taylor & Francis, 2002.

[16] A. Dora, L. Bryjko, T. van Mourik, and J. Tennyson, "R-matrix study of elastic and inelastic electron collisions with cytosine and thymine," *J. Phys. B: At. Mol. Opt. Phys.*, vol. 45, p. 175203, September 2012.

[17] Z. Mašín, J. D. Gorfinkiel, D. B. Jones, S. M. Bellm, and M. J. Brunger, "Elastic and inelastic cross sections for low-energy electron collisions with pyrimidine," *J. Chem. Phys.*, vol. 136, p. 144310, April 2012.

[18] Z. Mašín and J. D. Gorfinkiel, "Shape and core excited resonances in electron collisions with diazines," *J. Chem. Phys.*, vol. 137, p. 204312, November 2012.

[19] C. Winstead, V. Mckoy, and S. d. Sanchez, "Interaction of low-energy electrons with the pyrimidine bases and nucleosides of DNA," *J. Chem. Phys.*, vol. 127, p. 085105, August 2007.

[20] C. Winstead and V. McKoy, "Interaction of low-energy electrons with the purine bases, nucleosides, and nucleotides of DNA," *J. Chem. Phys.*, vol. 125, no. 24, p. 244302, 2006.

[21] Z. Mašín, *Resonance formation in electron collision with pyrimidine-like target*. PhD thesis, The Open University, Milton Keynes, October 2012.

[22] J. Fabian and E. Lewars, "Azabenzenes (azines) - The nitrogen derivatives of benzene with one to six N atoms: Stability, homodesmotic stabilization energy, electron distribution, and magnetic ring current; a computational study," *Can. J. Chem.*, vol. 82, no. 1, pp. 50–69, 2004.

[23] Z. Mašín and J. D. Gorfinkiel, "Elastic and inelastic low-energy electron collisions with pyrazine," *J. Chem. Phys.*, vol. 135, p. 144308, October 2011.

[24] Z. Mašín and J. D. Gorfinkiel, "Resonance formation in low energy electron scattering from uracil," *Eur. Phys. J. D.*, vol. 68, no. 5, p. 112, 2014.

[25] F. Filsinger, J. Küpper, G. Meijer, J. L. Hansen, J. Maurer, J. H. Nielsen, L. Holmegaard, and H. Stapelfeldt, "Pure Samples of Individual Conformers: The Separation of Stereoisomers of Complex Molecules Using Electric Fields," *Angew. Chem. Int. Ed.*, vol. 48, p. 6900–6902, 2009.

[26] B. Barc, M. Ryszka, J. Spurrell, M. Dampc, P. Limão-Vieira, R. Parajuli, N. J. Mason, and S. Eden, "Multi-photon ionization and fragmentation of uracil: Neutral excited-state ring opening and hydration effects," *J. Chem. Phys.*, vol. 139, no. 24, p. 244311, 2013.

[27] T. C. Freitas, K. Coutinho, M. Varella, M. A. P. Lima, and S. Canuto, "Electron collisions with the $HCOOH(H_2O)_n$ complexes ($n = 1, 2$) in liquid phase: The influence of microsolvation on the π^* resonance of formic acid," *J. Chem. Phys.*, vol. 138, no. 174307, p. 174307, 2013.

[28] P. Sulzer, S. Ptasińska, F. Zappa, B. Mielewska, A. R. Milosavljevic, P. Scheier, T. D. Märk, I. Bald, S. Gohlke, M. A. Huels, and E. Illenberger, "Dissociative electron attachment to furan, tetrahydrofuran, and fructose 044304," *J. Chem. Phys.*, vol. 125, no. 4, pp. 1–7, 2006.

[29] L. Sanche, "Primary interactions of low energy electrons in condensed matter," in *Excess Electrons in Dielectric Media* (C. Ferradini and J.-P. Jay-Gerin, eds.), vol. 26, ch. 1, pp. 1–42, CRC Press, 1991.

[30] J. R. Taylor, *Scattering Theory: The Quantum Theory of Nonrelativistic Collisions*. New York: Dover Publications Inc., 2006.

[31] M. Shukla and J. Leszczynski, *Radiation Induced Molecular Phenomena in Nucleic Acids: A Comprehensive Theoretical and Experimental Analysi*. Springer Science & Business Media, 2008.

[32] L. G. Christophorou, "The Lifetimes of Metastable Negative Ions," in *Advances in Electronics and Electron Physics* (L. Marton, ed.), vol. 46, Academic Press, 1978.

[33] M. Weyland, *Atomic excitation and molecular dissociation by low energy electron collisions*. PhD thesis, The Ruperto-Carola University of Heidelberg, 2016.

[34] K. Aflatooni, G. Gallup, and P. Burrow, "Electron attachment energies of the DNA bases," *J. Phys. Chem. A*, vol. 102, pp. 6205–6207, July 1998.

[35] R. Abouaf and H. Dunet, "Structures in dissociative electron attachment cross-sections in thymine, uracil and halouracils," *Eur. Phys. J. D.*, vol. 35, no. 2, pp. 405–410, 2005.

[36] P. D. Burrow, G. A. Gallup, A. M. Scheer, S. Denifl, S. Ptasińska, T. Mark, and P. Scheier, "Vibrational Feshbach resonances in uracil and thymine," *J. Chem. Phys.*, vol. 124, pp. 124310–124317, March 2006.

[37] G. Hanel, B. Gstir, S. Denifl, P. Scheier, M. Probst, B. Farizon, M. Farizon, E. Illenberger, and T. Mark, "Electron attachment to uracil: Effective destruction at subexcitation energies," *Phys. Rev. Lett.*, vol. 90, p. 188104, May 2003.

[38] S. Denifl, S. Ptasińska, G. Hanel, B. Gstir, M. Probst, P. Scheier, and T. Mark, "Electron attachment to gas-phase uracil," *J. Chem. Phys.*, vol. 120, pp. 6557–6565, April 2004.

[39] A. Scheer, K. Aflatooni, G. Gallup, and P. Burrow, "Bond breaking and temporary anion states in uracil and halouracils: Implications for the DNA bases," *Phys. Rev. Lett.*, vol. 92, p. 068102, February 2004.

[40] A. Scheer, C. Silvernail, J. Belot, K. Aflatooni, G. Gallup, and P. Burrow, "Dissociative electron attachment to uracil deuterated at the N-1 and N-3 positions," *Chem. Phys. Lett.*, vol. 411, pp. 46–50, August 2005.

[41] K. Aflatooni, A. Scheer, and P. Burrow, "Dissociative electron attachment in uracil: Total anion yield," *Chem. Phys. Lett.*, vol. 408, pp. 426–428, June 2005.

[42] R. Abouaf, J. Pommier, and H. Dunet, "Electronic and vibrational excitation in gas phase thymine and 5-bromouracil by electron impact," *Chem. Phys. Lett.*, vol. 381, pp. 486–494, November 2003.

[43] S. Denifl, S. Ptasińska, M. Probst, J. Hrušák, P. Scheier, and T. D. Märk, "Electron attachment to the gas-phase DNA bases cytosine and thymine," *J. Phys. Chem. A*, vol. 108, no. 31, pp. 6562–6569, 2004.

[44] S. Ptasińska, S. Denifl, B. Mróz, M. Probst, V. Grill, E. Illenberger, P. Scheier, and T. D. Märk, "Bond selective dissociative electron attachment to thymine.," *J. Chem. Phys.*, vol. 123, no. 12, p. 124302, 2005.

[45] H. Abdoul-Carime, M. A. Huels, F. Bruning, E. Illenberger, and L. Sanche, "Dissociative electron attachment to gas-phase 5-bromouracil," *J. Chem. Phys.*, vol. 113, pp. 2517–2521, August 2000.

[46] S. Denifl, S. Matejcik, B. Gstir, G. Hanel, M. Probst, P. Scheier, and T. Mark, "Electron attachment to 5-chloro uracil," *J. Chem. Phys.*, vol. 118, pp. 4107–4114, March 2003.

[47] S. Denifl, S. Matejcik, S. Ptasinska, B. Gstir, M. Probst, P. Scheier, E. Illenberger, and T. Mark, "Electron attachment to chlorouracil: A comparison between 6-ClU and 5-ClU," *J. Chem. Phys.*, vol. 120, pp. 704–709, January 2004.

[48] S. Ptasińska, E. Alizadeh, P. Sulzer, R. Abouaf, N. Mason, T. Mark, and P. Scheier, "Negative ion formation by low energy electron attachment to gas-phase 5-nitrouracil," *Int. J. Mass Spec.*, vol. 277, pp. 291–295, November 2008.

[49] R. Abouaf, S. Ptasińska, and D. Teillet-Billy, "Low energy electron impact on gas phase 5-nitrouracil," *Chem. Phys. Lett.*, vol. 455, pp. 169–173, April 2008.

[50] C. König, J. Kopyra, I. Bald, and E. Illenberger, "Dissociative Electron Attachment to Phosphoric Acid Esters: The Direct Mechanism for Single Strand Breaks in DNA," *Phys. Rev. Lett.*, vol. 97, p. 018105, July 2006.

[51] L. G. Caron and L. Sanche, "Low-energy electron diffraction and resonances in DNA and other helical macromolecules," *Phys. Rev. Lett.*, vol. 91, p. 113201, 2003.

[52] L. Caron and L. Sanche, "Diffraction in resonant electron scattering from helical macromolecules: A- and B-type DNA," *Phys. Rev. A*, vol. 70, p. 32719, 2004.

[53] L. Caron and L. Sanche, "Temporary electron localization and scattering in disordered single strands of DNA," *Phys. Rev. A*, vol. 73, pp. 062707–7, June 2006.

[54] S. Tonzani and C. Greene, "Low-energy electron scattering from DNA and RNA bases: Shape resonances and radiation damage," *J. Chem. Phys.*, vol. 124, p. 054312, February 2006.

[55] C. Winstead and V. McKoy, "Resonant interactions of slow electrons with DNA constituents," *Rad. Phys. Chem.*, vol. 77, pp. 1258–1264, 2008.

[56] A. Kumar and M. Sevilla, "The role of π, $\sigma*$ excited states in electron-induced DNA strand break formation: A time-dependent density functional theory study," *J. Am. Chem. Soc.*, vol. 130, pp. 2130–+, February 2008.

[57] Y.-F. Wang and S. X. Tian, "Shape resonance states of the low-energy electron attachments to DNA base tautomers," *Phys. Chem. Chem. Phys.*, vol. 13, no. 13, p. 6169, 2011.

[58] F. A. Gianturco and R. R. Lucchese, "Radiation damage of biosystems mediated by secondary electrons: Resonant precursors for uracil molecules," *J. Chem. Phys.*, vol. 120, no. 16, pp. 7446–7455, 2004.

[59] C. Winstead and V. McKoy, "Low-energy electron collisions with gas-phase uracil," *J. Chem. Phys.*, vol. 125, pp. 174304–8, November 2006.

[60] F. A. Gianturco, F. Sebastianelli, R. R. Lucchese, I. Baccarelli, and N. Sanna, "Ring-breaking electron attachment to uracil: Following bond dissociations via evolving resonances," *J. Chem. Phys.*, vol. 128, pp. 1–9, May 2008.

[61] T. Takayanagi, T. Asakura, and H. Motegi, "Theoretical study on the mechanism of Low-Energy dissociative electron attachment for uracil," *J. Phys. Chem. A*, vol. 113, pp. 4795–4801, April 2009.

[62] G. A. Gallup and I. I. Fabrikant, "Vibrational Feshbach resonances in dissociative electron attachment to uracil," *Phys. Rev. A*, vol. 83, pp. 1–7, January 2011.

[63] F. Kossoski, M. H. F. Bettega, and M. T. D. N. Varella, "Shape resonance spectra of uracil, 5-fluorouracil, and 5-chlorouracil," *J. Chem. Phys.*, vol. 140, no. 2, p. 024317, 2014.

[64] A. Dora, J. Tennyson, L. Bryjko, and T. Van Mourik, "R-matrix calculation of low-energy electron collisions with uracil," *J. Chem. Phys.*, vol. 130, no. 16, p. 164307, 2009.

[65] A. Dora, L. Bryjko, T. Van Mourik, and J. Tennyson, "Low-energy electron scattering with the purine bases of DNA/RNA using the R-matrix method," *J. Chem. Phys.*, vol. 136, no. 2, pp. 1–9, 2012.

[66] X. Bao, J. Wang, J. Gu, and J. Leszczynski, "DNA strand breaks induced by near-zero-electronvolt electron attachment to pyrimidine nucleotides," *Proceedings of the National Academy of Sciences of the United States of America*, vol. 103, pp. 5658–5663, April 2006.

[67] L. Caron and L. Sanche, "Diffraction in resonant electron scattering from helical macromolecules: Effects of the DNA backbone," *Phys. Rev. A*, vol. 72, no. 3, p. 32726, 2005.

[68] S. Tonzani and C. H. Greene, "Radiation damage to DNA: Electron scattering from the backbone subunits," *J. Chem. Phys.*, vol. 125, no. 9, p. 094504, 2006.

[69] C. Winstead and V. McKoy, "Interaction of slow electrons with methyl phosphate esters," *Int. J. Mass Spec.*, vol. 277, no. 1-3, pp. 279–283, 2008.

[70] H. Xie, R. Wu, F. Xia, and Z. Cao, "Effects of electron attachment on C5'-O5' and C1'-N1 bond cleavages of pyrimidine nucleotides: A theoretical study. ," *J. Comp. Chem.*, vol. 29, pp. 2025–2032, September 2008.

[71] B. Boudaïffa, P. Cloutier, D. Hunting, M. A. Huels, and L. Sanche, "Resonanant formation of DNA strand breaks by low-energy (3 to 20 eV) electrons," *Science*, vol. 287, pp. 1658–1660, 2000.

[72] X. Pan, P. Cloutier, D. Hunting, and L. Sanche, "Dissociative Electron Attachment to DNA," *Physical Review Letters*, vol. 90, p. 208102, may 2003.

[73] X. Pan and L. Sanche, "Mechanism and site of attack for direct damage to DNA by Low-Energy electrons," *Phys. Rev. Lett.*, vol. 94, p. 198104, May 2005. Copyright (C) 2009 The American Physical Society; Please report any problems to prola@aps.org.

[74] R. Panajotovic, F. Martin, P. Cloutier, D. Hunting, and L. Sanche, "Effective cross sections for production of single-strand breaks in plasmid DNA by 0.1 to 4.7 eV electrons.," *Radiation Research*, vol. 165, p. 452–459, April 2006.

[75] M. A. H. du Penhoat, M. A. Huels, P. Cloutier, J. P. Jay-Gerin, and L. Sanche, "Electron stimulated desorption of h- from thin films of thymine and uracil," *J. Chem. Phys.*, vol. 114, pp. 5755–5764, April 2001.

[76] P. Levesque, M. Michaud, W. Cho, and L. Sanche, "Absolute electronic excitation cross sections for low-energy electron (5-12 eV) scattering from condensed thymine," *J. Chem. Phys.*, vol. 122, p. 224704, June 2005.

[77] X. Pan and L. Sanche, "Dissociative electron attachment to DNA basic constituents: The phosphate group," *Chemical Physics Letters*, vol. 421, no. 4-6, pp. 404–408, 2006.

[78] J. Kočišek, A. Pysanenko, M. Fárník, and J. Fedor, "Microhydration Prevents Fragmentation of Uracil and Thymine by Low-Energy Electrons," *J. Phys. Chem. Lett.*, pp. 3401–3405, 2016.

[79] M. Smyth, J. Kohanoff, and I. Fabrikant, "Electron-induced hydrogen loss in uracil in a water cluster environment," *J. Chem. Phys.*, vol. 140, p. 184313, May 2014.

[80] L. Sanche, "Low-Energy Electron Damage to DNA and its Basic Constituents," *Physica Scripta*, vol. T68, pp. C108–C112, 2003.

[81] L. Caron, L. Sanche, S. Tonzani, and C. H. Greene, "Diffraction in low-energy electron scattering from DNA: Bridging gas-phase and solid-state theory," *Physical Review A - Atomic, Molecular, and Optical Physics*, vol. 78, no. 4, pp. 1–13, 2008.

[82] I. Baccarelli, I. Bald, F. a. Gianturco, E. Illenberger, and J. Kopyra, "Electron-induced damage of DNA and its components: Experiments and theoretical models," *Phys. Rep.*, vol. 508, no. 1-2, pp. 1–44, 2011.

[83] J. Younkin, L. Smith, and R. Compton, "Semi-empirical calculations of π-electron affinities for some conjugated organic molecules," *Theoretica chimica acta*, vol. 41, no. 2, pp. 157–176, 1976.

[84] R. N. Compton, C. P. Section, Y. Yoshioka, and K. D. Jordan, "Comment on Semiempirieal Calculations of ˜Eleetron Affmities," *Theoretica Chimica Acta*, vol. 260, pp. 259–260, 1980.

[85] I. Nenner and G. J. Schulz, "Temporary negative ions and electron affinities of benzene and *N*-heterocyclic molecules: pyridine, pyridazine, pyrimidine, pyrazine, and striazine," *J. Chem. Phys.*, vol. 62, p. 1747, 1975.

[86] A. Modelli and P. Burrow, "Electron-transmission study of the temporary anion states of substituted pyridines," *J. Electron Spec.*, vol. 32, no. 3, pp. 263 – 276, 1983.

[87] C. Winstead and V. McKoy, "Low-energy electron scattering by pyrazine," *Physical Review Letters*, vol. 98, no. 11, pp. 6–9, 2007.

[88] I. I. Fabrikant, S. Caprasecca, G. A. Gallup, and J. D. Gorfinkiel, "Electron attachment to molecules in a cluster environment," *J. Chem. Phys.*, vol. 136, p. 184301, May 2012.

[89] F. Bowman, *Introduction to Bessel Functions*. New York: Dover Publications Inc., 2003.

[90] R. Mehrem, "The plane wave expansion, infinite integrals and identities involving spherical Bessel functions," *Appl. Math. Comp.*, vol. 217, no. 12, pp. 5360–5365, 2011.

[91] B. Średniawa, *Mechanika kwantowa*. Warszawa: Państwowe Wydawnictwo Naukowe, 1978.

[92] P. G. Burke, *R-Matrix Theory of Atomic Collisions: Application to Atomic, Molecular and Optical Processes*. Springer, 2011.

[93] J. M. Blatt and V. F. Weisskopf, *Theoretical Nuclear Physics*. Springer Science & Business Media, 2012.

[94] A. U. Hazi, "Behavior of the eigenphase sum near a resonance," *Phys. Rev. A*, vol. 19, pp. 920–922, 1979.

[95] F. T. Smith, "Lifetime matrix in collision theory," *Phys. Rev.*, vol. 118, pp. 349–356, April 1960.

[96] I. Baccarelli, F. Sebastianelli, F. A. Gianturco, and N. Sanna, "Modelling dissociative dynamics of biosystems after metastable electron attachment: the sugar backbones," *Eur. Phys. J. D.*, vol. 51, pp. 131–136, January 2009.

[97] I. Shimamura, E. Bröandas, C. Nicolaides, and J. Sabin, "Chapter 4 -Quasi-Bound states of electronic and positronic Few-Body systems: Analysis of multichannel scattering information," in *Advances in Quantum Chemistry* (E. B. Cleanthes A. Nicolaides and J. R. Sabin, eds.), vol. Volume 63, pp. 165–245, Academic Press, 2012.

[98] E. P. Wigner and L. Eisenbud, "Higher angular momenta and long range interaction in resonance reactions," *Phys. Rev.*, vol. 72, no. 1, pp. 29–41, 1947.

[99] P. G. Burke and K. A. Berrington, eds., *Atomic and Molecular Processes, an R-matrix Approach*. Bristol: Institute of Physics Publishing, 1993.

[100] P. Burke, W. Robb, D. Bates, and B. Bederson, "The R-Matrix theory of atomic processes," *Adv. At. Mol. Phys.*, vol. 11, pp. 143–214, 1976.

[101] J. Tennyson, "Electron - molecule collision calculations using the R-matrix method," *Phys. Rep.*, vol. 491, pp. 29–76, 2010.

[102] C. Bloch, "Une formulation unifiée de la théorie des réactions nucléaires," *Nucl. Phys.*, vol. 4, p. 503, 1957.

[103] T. Helgaker, P. Jørgensen, , and J. Olsen, *Molecular Electronic-Structure Theory*. England: John Willey & Sons, 2000.

[104] A. Dora, J. Tennyson, L. Bryjko, and T. van Mourik, "R-matrix calculation of low-energy electron collisions with uracil," *J. Chem. Phys.*, vol. 130, p. 164307, 2009.

[105] Basis set Exchange. `https://bse.pnl.gov/bse/portal`.

[106] A. Szabo and N. S. Ostlud, *Modern Quantum Chemistry. Tntroduction to Advanced Electronic Structure Theory*. New York: Dover Publications Inc., 1996.

[107] J. M. Carr, P. G. Galiatsatos, J. D. Gorfinkiel, A. G. Harvey, M. A. Lysaght, D. Madden, Z. Mašín, M. Plummer, J. Tennyson, and H. N. Varambhia, "UKRmol: a low-energy electron- and positron-molecule scattering suite," *Eur. Phys. J. D.*, vol. 66, no. 3, p. 58, 2012.

[108] Z. Maší and J. D. Gorfinkiel, "Towards an accurate representation of the continuum in calculations of electron, positron and laser field interactions with molecules," *J. Phys. Conf. Ser.*, vol. 490, no. 1, p. 012090, 2014.

[109] A. Faure, J. D. Gorfinkiel, L. a. Morgan, and J. Tennyson, "GTOBAS: fitting continuum functions with Gaussian-type orbitals," *Computer Phys. Comm.*, vol. 144, no. 2, pp. 224–241, 2002.

[110] "Forge Advanced Server." `http://ccpforge.cse.rl.ac.uk/gf/`.

[111] N. Sanna and F. A. Gianturco, "Differential cross sections for electron/positron scattering for polyatomic molecules," *Computer Phys. Comm.*, vol. 114, pp. 142–167, 1998.

[112] R. D. Johnson III Editor, "NIST Standard Reference Database Number 101." `http://cccbdb.nist.gov/`, August 2011.

[113] M. Schreiber, M. R. Silva-Junior, S. P. A. Sauer, and W. Thiel, "Benchmarks for electronically excited states: CASPT2, CC2, CCSD, and CC3," *J. Chem. Phys.*, vol. 128, pp. 134110–25, April 2008.

[114] R. D. Nelson Jr., D. R. Lide, and A. A. Maryott, "Selected values of electric dipole moments for molecules in the gas phase," tech. rep., NSRDS-NBS10, 1967.

[115] C. G. Gray and K. E. Gubbins, *Theory of molecular fluids. Volume 1: Fundamentals*, vol. 1. Clarendon Press, Oxford, 1984.

[116] P. G. Szalay, T. Mueller, G. Gidofalvi, H. Lischka, and R. Shepard, "Multiconfiguration self-consistent field and multireference configuration interaction methods and applications," *Chem. Rev.*, vol. 112, pp. 108–181, January 2012.

[117] J. P. Doering and J. H. Moore, "Observation of a Singlet—Triplet Transition in Gas Phase Pyridine by Ion and Electron Impact," *J. Chem. Phys.*, vol. 56, no. 5, p. 2176, 1972.

[118] L. Goodman, "n $\rightarrow$ π^* transitions in the azines," *J. Mol. Spectr.*, vol. 6, pp. 109–137, 1961.

[119] A. Bolovinos, P. Tsekeris, J. Philis, E. Pantos, and G. Andritsopoulos, "Absolute vacuum ultraviolet absorption spectra of some gaseous azabenzenes," *J. Mol. Spec.*, vol. 103, no. 2, pp. 240–256, 1984.

[120] A. Sieradzka, F. Blanco, M. C. Fuss, Z. Mašín, J. D. Gorfinkiel, and G. García, "Electron scattering from pyridine," *J. Phys. Chem. A*, vol. 118, pp. 6657–6663, August 2014.

[121] A. S. Barbosa, D. F. Pastega, and M. H. F. Bettega, "Shape resonances in the elastic scattering of slow electrons by pyridine," *Phys. Rev. A*, vol. 88, p. 022705, August 2013.

[122] F. A. Gianturco and A. Jain, "The theory of electron-scattering from polyatomic-molecules," *Phys. Rep*, vol. 143, pp. 347–425, 1986.

[123] K. Regeta, M. Allan, C. Winstead, V. McKoy, Z. Mašín, and J. D. Gorfinkiel, "Resonance effects in elastic cross sections for electron scattering on pyrimidine: Experiment and theory," *J. Chem. Phys.*, vol. 144, no. 2, p. 024301, 2016.

[124] H. Murai, Y. Ishijima, T. Mitsumura, Y. Sakamoto, H. Kato, M. Hoshino, F. Blanco, G. García, P. Limão-Vieira, M. J. Brunger, S. J. Buckman, and H. Tanaka, "A comprehensive and comparative study of elastic electron scattering from OCS and CS_2 in the energy region from 1.2 to 200 eV," *J. Chem. Phys.*, vol. 138, p. 054302, 2013.

[125] J. R. Brunton, L. R. Hargreaves, S. J. Buckman, F. B. G. García, O. Zatsarinny, K. Bartschat, and M. J. Brunger, "Anomalously large low-energy elastic cross sections for electron scattering from the CF_3 radical," *Chem. Phys. Lett.*, vol. 568-569, p. 55, 2013.

[126] P. Palihawadana, J. P. Sullivan, S. J. Buckman, Z. Mašín, J. D. Gorfinkiel, F. Blanco, G. García, and M. J. Brunger, "A joint theoretical and experimental study for elastic electron scattering from 1,4-dioxane," *J. Chem. Phys.*, vol. 139, p. 014308, 2013.

[127] M. C. Fuss, A. G. Sanz, F. Blanco, J. Carlos Oller, P. Limao-Vieira, M. J. Brunger, and G. Garcia, "Total electron-scattering cross sections from pyrimidine as measured using a magnetically confined experimental system," *Phys. Rev. A*, vol. 88, p. 042702, October 2013.

[128] M. C. Fuss, A. G. Sanz, F. Blanco, P. Limao-Vieira, M. J. Brunger, and G. Garcia, "Differential and integral electron scattering cross sections from tetrahydrofuran (THF) over a wide energy range: 1-10 000 eV," *Eur. Phys. J. D.*, vol. 68, p. 161, June 2014.

[129] A. Zecca, L. Chiari, G. García, F. Blanco, E. Trainotti, and M. J. Brunger, "Total cross sections for positron and electron scattering from pyrimidine," *J. Phys. B: At. Mol. Opt. Phys.*, vol. 43, no. 21, p. 215204, 2010.

[130] M. Hoshino, M. Horie, H. Kato, F. Blanco, G. Garcia, P. Limao-Vieira, J. P. Sullivan, M. J. Brunger, and H. Tanaka, "Cross sections for elastic scattering of electrons by CF3Cl, CF2Cl2, and CFCl3," *J. Chem. Phys.*, vol. 138, p. 214305, June 2013.

[131] H. Kato, A. Suga, M. Hoshino, F. Blanco, G. Garcia, P. Limao-Vieira, M. J. Brunger, and H. Tanaka, "Elastic cross sections for electron scattering from GeF4: Predominance of atomic-F in the high-energy collision dynamics," *J. Chem. Phys.*, vol. 136, p. 134313, April 2012.

[132] A. G. Sanz, M. C. Fuss, F. Blanco, Z. Mašín, F. Gorfinkiel, Jimena D.and Carelli, F. Sebastianelli, F. A. Gianturco, and G. García, "Electron scattering cross section calculations for polar molecules over a broad energy range," *Appl. Radiat. Isot.*, vol. 83, pp. 57–67, 2014.

[133] G. Blackman, R. Brown, and F. Burden, "Microwave spectrum, dipole moment, and nuclear quadruple coupling constants of pyrimidine," *J. Mol. Spec.*, vol. 35, no. 3, p. 444, 1970.

[134] J. Franz and F. A. Gianturco, "Low-energy positron scattering from gas-phase pyrimidine: A quantum treatment of the dynamics and a comparison with experiments," *Phys. Rev. A*, vol. 88, p. 042711, October 2013.

[135] C. Winstead and V. McKoy, "Resonant channel coupling in electron scattering by pyrazine," *Phys. Rev. Lett.*, vol. 98, p. 113201, March 2007.

[136] C. Winstead and V. Mckoy, "Low-energy electron scattering by pyrazine," *Phys. Rev. A*, vol. 76, p. 012712, July 2007.

[137] Z. Mašín and J. D. Gorfinkiel, "Shape and core excited resonances in electron collisions with diazines," *J. Chem. Phys.*, vol. 137, no. 20, p. 204312, 2012.

[138] J. Tennyson and C. J. Noble, "RESON – A program for the detection and fitting of Breit-Wigner resonances," *Comput. Phys. Commun.*, vol. 33, pp. 421–424, 1984.

[139] K. Regeta, M. Allan, Z. Mašín, and J. D. Gorfinkiel, "Absolute cross sections for electronic excitation of pyrimidine by electron impact," *J. Chem. Phys.*, vol. 144, no. 1, p. 024302, 2016.

[140] E. M. De Oliveira, T. C. Freitas, K. Coutinho, M. T. Márcio, S. Canuto, M. A. P. Lima, and M. H. F. Bettega, "Communication: Transient anion states of phenol...(H2O) n (n = 1, 2) complexes: Search for microsolvation signatures," *J. Chem. Phys.*, vol. 141, no. 5, p. 051105, 2014.

[141] S. Schlücker, R. K. Singh, B. P. Asthana, J. Popp, and W. Kiefer, "Hydrogen-Bonded Pyridine–Water Complexes Studied by Density Functional Theory and Raman Spectroscopy," *J. Phys. Chem. A*, vol. 105, pp. 9983–9989, November 2001.

[142] M. C. Sicilia, C. Muñoz Caro, and A. Niño, "Theoretical Analysis of Pyridine Protonation in Water Clusters of Increasing Size," *ChemPhysChem*, vol. 6, no. 1, pp. 139–147, 2005.

[143] A. Dkhissi, L. Adamowicz, and G. Maes, "Density Functional Theory Study of the Hydrogen-Bonded Pyridine–H_2O Complex: A Comparison with RHF and MP2 Methods and with Experimental Data," *J. Phys. Chem. A*, vol. 104, no. 10, pp. 2112–2119, 2000.

[144] S. Clough, Y. Beers, G. Klein, and L. Rothman, "Dipole moment of water from Stark measurements of H2O, HDO, and D2O," *J. Phys. Chem.*, vol. 59, no. 5, pp. 2254–2259, 1973.

[145] E. Fileti, K. Coutinho, T. Malaspina, and S. Canuto, "Electronic changes due to thermal disorder of hydrogen bonds in liquids: Pyridine in an aqueous environment," *Phys. Rev. E*, vol. 67, p. 061504, June 2003.

[146] D. R. Lide, *Handbook of Chemistry and Physics*. CRC Press, Boca Raton, FL, 1994.

[147] B. Shanker and J. Applequist, "Polarizabilities of nitrogen heterocyclic molecules from atom monopole dipole interaction theory," *J. Phys. Chem.*, vol. 100, pp. 3879–3881, March 1996.

[148] C. Lefevre, R. Lefevre, B. Rao, and M. Smith, "Molecular polarisability - ellipsoids of polarisability for certain fundamental heterocycles," *J. Chem. Soc.*, no. March, pp. 1188–1192, 1959.

[149] R. Ditchfield, N. Ostlund, J. Murrell, and M. Turpin, "Comparison of the sum-over-states and finite perturbation theories of electrical polarizability and nuclear spin-spin coupling," *Mol. Phys.*, vol. 18, no. 4, pp. 433–440, 1970.

[150] M. Jones and J. Tennyson, "On the use of pseudostates to calculate molecular polarizabilities," *J. Phys. B: At. Mol. Opt. Phys.*, vol. 43, p. 045101, February 2010.

[151] S. Kim, S. E. Wheeler, and H. F. Schaefer, "Microsolvation effects on the electron capturing ability of thymine: Thymine-water clusters," *J. Chem. Phys.*, vol. 124, no. 20, pp. 1–8, 2006.

[152] S. Kim and H. F. Schaefer, "Effects of microsolvation on uracil and its radical anion: uracil(H2O)n (n = 1-5).," *J. Chem. Phys.*, vol. 125, no. 14, p. 144305, 2006.

[153] S. Kim and H. F. Schaefer, "Effects of microsolvation on the adenine-uracil base pair and its radical anion: adenine-uracil mono- and dihydrates," *J. Phys. Chem. A*, vol. 111, no. 41, pp. 10381–10389, 2007.

[154] D. Bouchiha, L. G. Caron, J. D. Gorfinkiel, and L. Sanche, "Multiple scattering approach to elastic low-energy electron collisions with the water dimer," *J. Phys. B: At. Mol. Opt. Phys.*, vol. 41, no. 4, p. 045204, 2008.

[155] S. Caprasecca, J. D. Gorfinkiel, D. Bouchiha, and L. G. Caron, "Multiple scattering approach to elastic electron collisions with molecular clusters," *J. Phys. B: At. Mol. Opt. Phys.*, vol. 42, no. 9, p. 095205, 2009.

[156] J. Tomasi, B. Mennucci, and R. Cammi, "Quantum mechanical continuum solvation models," *Chemical Reviews*, vol. 105, no. 8, pp. 2999–3093, 2005.

[157] N. Hush and A. Cheung, "Ionization potentials and donor properties of nucleic acid bases and related compounds," *Chem. Phys. Lett.*, vol. 34, no. 1, pp. 11–13, 1975.

[158] D. Dougherty, K. Wittel, J. Meeks, and S. Mcglynn, "Photoelectron-spectroscopy of carbonyls - ureas, uracils, and thymine," *J. Am. Chem. Soc.*, vol. 98, no. 13, pp. 3815–3820, 1976.

[159] M. Preuss, W. Schmidt, K. Seino, J. Furthmuller, and F. Bechstedt, "Ground- and excited-state properties of DNA base molecules from plane-wave calculations using ultrasoft pseudopotentials," *J. Comp. Chem.*, vol. 25, pp. 112–122, January 2003.

[160] I. Kulakowska, M. Geller, B. Lesyng, and K. Wierzchowski, "Dipole moments of 2, 4-diketopyrimidines: Part II: Uracil, thymine and their derivatives," *Biochimica et Biophysica Acta (BBA) - Nucleic Acids and Protein Synthesis*, vol. 361, pp. 119–130, August 1974.

[161] C. Adamo and V. Barone, "Toward reliable density functional methods without adjustable parameters: The PBE0 model," *J. Chem. Phys.*, vol. 110, pp. 6158–6170, April 1999.